

**HERSTELLUNG KERAMISCHER MIKROSTRUKTUREN UND DEREN EINFLUSS
AUF KNOCHENZELLEN**

FABRICATION OF CERAMIC MICROPATTERNS AND THEIR IMPACT ON BONE
CELLS

Vom Fachbereich Produktionstechnik

der

UNIVERSITÄT BREMEN

zur Erlangung des Grades

Doktor-Ingenieur

genehmigte

Dissertation

von

M.Sc. Marzellus Matthias Maurus große Holthaus

Gutachter:

Prof. Dr.-Ing. Kurosch Rezwan

Prof. Dr.-Ing. Lutz Mädler

Tag der mündlichen Prüfung: 22.09.2011

Overview

The main objective of this study is to elucidate a possible method of producing ceramic calcium phosphate micropatterns ranging from 5 to 100 μm . Additionally the influence on human osteoblast cells has been tested in vitro with patterned surfaces, fabricated with some of these techniques.

Today, micropatterned ceramic surfaces are of great interest for fundamental materials research as well as for high-end industrial processes, whereas the fabrication of ceramic patterns in the sub-100 μm range is still rather a challenge. Therefore, in the context of this thesis, six different patterning techniques have been applied in order to generate ceramic patterns. Three of these patterning methods, namely, microtransfer molding (μTM), modified micromolding (m- μM) and Aerosol-Jet[®] printing, generated patterns by the use of aqueous ceramic suspensions. The other methods, to wit, CNC-micromachining, laser ablation and direct laser interference patterning (DLIP), removed material from solid ceramic substrates to generate micropatterned surfaces. The patterning techniques have been evaluated concerning their capability of fabricating ceramic patterns. Several different aspects, such as the achieved pattern edge contour or the smallest producible pattern size, have been regarded.

It can be summarized from this that all applied patterning techniques are useful to fabricate ceramic micropatterns smaller than 100 μm . Further, it was found that the choice of patterning technique limits the scope of the produced pattern properties such as the desired pattern accuracy, quality or size. Using modified micromolding, patterns as small as 5 μm with vertical sidewalls can be fabricated within some days of production. The molded micropatterns feature very high accuracy with only low technical efforts needed at the same time. A faster processing can be achieved with the use of Aerosol-Jet[®] printing, but the pattern accuracy then is lower while the costs for equipment are much higher. CNC micromachining resulted in ceramic patterns of about 100 μm with the costs for the equipment being quite high. Solely re-sintering of machined patterns resulted in widths of 75 μm . However, CNC-machining is a fast patterning process for various solid ceramics. The laser treatment techniques imply high costs for the technical equipment, yet the production time required is short. Direct interference patterning, for example, offers a fast and accurate patterning of ceramic surfaces within only some hours of production. Thus, altogether, the quest for a suitable patterning technique is a balancing act between, on the one hand, general process properties, such as costs for equipment or production time, and, on the other hand, desired pattern properties.

Another objective of this study has been the investigation of the influence of ceramic patterns

on human osteoblasts (HOB). Tests with defined levels of randomized hydroxyapatite surface roughness caused no significant changes in the osteoblast viability (WST-1 and collagen type I production) in-vitro. In addition, tests with specific micropatterning were carried out. First tests with osteoblast-like tumorous osteosarcoma cells (MG-63) showed a distinct cell orientation on ceramic Aerosol-Jet[®] printed micropatterned lines of 10 to 60 μm in width. Due to a lack of edge contour and accuracy further in-vitro testing on better defined micromolded patterns were made with normal HOB cells. This investigation has revealed that ceramic hydroxyapatite-based patterns ranging from 16 μm to 77 μm in widths have a strong influence on the contact guidance of the HOB. In short, less viable cells were measured on the basis of patterned compared to non-patterned samples. In doing so, the cells showed distinct orientations between 0° and 15° in reference to the pattern direction, whereas fewer cells were measured inside the microchannels as compared to on top of the pattern struts. Both effects were stronger on smaller pattern widths than on larger ones.

Überblick

Die Hauptziele dieser Arbeit bestanden darin, mögliche Herstellungsmethoden keramischer Kalziumphosphatmikrostrukturen im Bereich von 5 bis 100 μm zu erläutern. Deren Einfluss auf humane Osteoblasten wurde mit strukturierten Oberflächen, hergestellt mithilfe einiger dieser Methoden, in-vitro getestet.

Mikrostrukturierte keramische Oberflächen sind heutzutage von großem Interesse in der Grundlagenforschung von Materialien sowie in hochtechnisierten Industrieprozessen, wobei die Herstellung von Strukturen kleiner als 100 μm immer noch eine große Herausforderung darstellt. Im Rahmen dieser Arbeit wurden sechs verschiedene Strukturierungsmethoden angewendet, um keramische Mikrostrukturen herzustellen. Drei dieser Methoden, und zwar „microtransfer molding“ (μTM), „modified micromolding“ ($\text{m-}\mu\text{M}$) und „Aerosol-Jet[®] printing“, stellten dabei Mikrostrukturen unter Verwendung wässriger keramischer Suspensionen her. Die anderen Methoden, „CNC-micromachining“, „laser ablation“ und „direct laser interference patterning“ (DLIP), trugen Material von keramischen Festkörperproben ab, um mikrostrukturierte Oberflächen herzustellen. Die Strukturierungstechniken wurden hinsichtlich ihrer Fähigkeit zur Herstellung keramischer Mikrostrukturen bewertet. Mehrere Kriterien, wie die erzielten Konturen der Strukturanten oder die kleinsten herstellbaren Strukturen, wurden dabei berücksichtigt.

Zusammenfassend kann gesagt werden, dass sich alle angewendeten Strukturierungsmethoden dazu eignen, keramische Mikrostrukturen kleiner als 100 μm herzustellen. Es wurde darüber hinaus herausgefunden, dass die Wahl der Strukturierungsmethode die Bandbreite der hergestellten Struktureigenschaften, wie Strukturgenauigkeit, -qualität oder -größe, begrenzt. Bei der Verwendung von „modified micromolding“ können Strukturen von nur 5 μm mit vertikalen Seitenwänden innerhalb weniger Tage hergestellt werden. Die so hergestellten Strukturen weisen eine sehr hohe Genauigkeit auf, wobei ein nur geringer technischer Aufwand betrieben werden muss. Eine schnellere Strukturierung kann mittels „Aerosol-Jet[®] printing“ erzielt werden, jedoch sind hier die Anschaffungskosten weitaus höher. „CNC micromachining“-produzierte keramische Mikrostrukturen von ca. 100 μm und die Anschaffungskosten sind vergleichsweise hoch. Lediglich ein Nachsintern resultierte in Strukturbreiten von 75 μm . Trotzdem ist „CNC micromachining“ ein schnelles Verfahren zur Strukturierung verschiedener keramischer Materialien. Die Laserverfahren haben allesamt hohe Anschaffungskosten, aber die Produktionszeit verringert sich durch ihren Einsatz erheblich. „Direct laser interference patterning“ bietet eine schnelle und präzise Strukturierung von keramischen Oberflächen

innerhalb weniger Stunden. Die Suche nach einer geeigneten Strukturierungsmethode ist dabei immer ein Spagat einerseits zwischen allgemeinen Eigenschaften wie Anschaffungskosten oder Produktionszeit und andererseits den gewünschten Mikrostruktureigenschaften.

Ein weiteres Ziel dieser Arbeit bestand in der Untersuchung des Einflusses keramischer Hydroxylapatit-basierter Strukturen auf humane Osteoblasten (HOB). In-vitro-Versuche mit definierten, zufälligen Hydroxylapatit-Oberflächenrauheiten erwirkten keine signifikanten Unterschiede in der Osteoblastviabilität (WST-1 und Kollagen I Produktion). Zudem wurden Versuche mit definierten Mikrostrukturen durchgeführt. Erste Versuche mit tumorösen osteoblast-ähnlichen Zellen (MG-63) zeigten eine klare Ausrichtung der Zellen auf keramischen Aerosol-Jet[®] gedruckten Linien mit Breiten von 10 bis 60 µm. Wegen Mangel an Kantenkonturen und Genauigkeit wurden weitere in-vitro Versuche an besser definierten gegossenen Mikrostrukturen (Modified Micromolding) mit normalen HOB durchgeführt. Diese haben gezeigt, dass 16 bis 77 µm breite Hydroxylapatit-basierte Strukturen einen starken Einfluss auf die Zellausrichtung haben. Im Allgemeinen gab es weniger lebende Zellen auf mikrostrukturierten Oberflächen als auf nicht-strukturierten. Die Zellen zeigten eine klare Ausrichtung zwischen 0° und 15° in Abhängigkeit von der Strukturrichtung, wobei weniger Zellen in den Mikrokanälen als auf den Mikrostrukturen gemessen wurden. Beide Effekte waren in kleineren Mikrostrukturen stärker ausgeprägt als in größeren.

Contents

OVERVIEW

ÜBERBLICK

1.	INTRODUCTION AND AIMS OF THIS THESIS	10
1.1	CELL-MATERIAL INTERFACES	10
1.2	BIOCERAMICS	13
1.3	AIMS OF THIS THESIS	15
2.	MICROPATTERNING OF CERAMIC SURFACES.....	17
2.1	PRINCIPLES AND STATE OF THE ART OF CERAMIC MICROPATTERNING	17
2.1.1	<i>Molding techniques.....</i>	<i>18</i>
2.1.2	<i>Conventional molding techniques via soft-lithography.....</i>	<i>18</i>
2.1.3	<i>Modified micromolding (m-μM)</i>	<i>24</i>
2.1.4	<i>Rapid Prototyping.....</i>	<i>28</i>
2.1.4.1	<i>Maskless material deposition by aerosol jet printing.....</i>	<i>29</i>
2.1.5	<i>Micromachining.....</i>	<i>31</i>
2.1.5.1	<i>Precision machining by Computer Numerical Control Machining.....</i>	<i>31</i>
2.1.5.2	<i>Microgrinding via grinding papers.....</i>	<i>34</i>
2.1.6	<i>Laser treatment.....</i>	<i>35</i>
2.1.6.1	<i>Laser ablation.....</i>	<i>35</i>
2.1.6.2	<i>Direct laser interference patterning.....</i>	<i>37</i>
2.2	SURFACE CHARACTERIZATION.....	40
2.2.1	<i>Measurement of surface texture</i>	<i>40</i>
2.2.2	<i>Roughness analysis</i>	<i>41</i>
2.2.3	<i>Measurement of micropattern geometry</i>	<i>43</i>
3.	EXPERIMENTAL RESULTS OF CERAMIC MICROPATTERNING	44
3.1	MICROTRANSFER MOLDING AND MODIFIED MICROMOLDING OF CERAMIC SUSPENSIONS.....	45
3.1.1	<i>Versatile crack-free ceramic micropatterns made by a modified molding technique.....</i>	<i>49</i>
3.1.2	<i>Orientation of osteoblasts on hydroxyapatite-based microchannels.....</i>	<i>60</i>
3.2	AEROSOL-JET [®] PRINTING OF HYDROXYAPATITE SUSPENSIONS	80
3.2.1	<i>Aerosol-Jet[®] printing of hydroxyapatite suspensions for bone cell growth studies.....</i>	<i>80</i>
3.3	MICROMACHINING	90
3.3.1	<i>Micromachining of ceramic surfaces: hydroxyapatite and zirconia</i>	<i>90</i>
3.3.2	<i>Monitoring osteoblast viability on hydroxyapatite with adjusted submicron and micron surface roughness by using proliferation reagent WST-1.....</i>	<i>114</i>
3.4	LASER TREATMENT	131
3.4.1	<i>Laser ablation of hydroxyapatite surfaces</i>	<i>131</i>
3.4.2	<i>Laser interference patterning of hydroxyapatite surfaces.....</i>	<i>133</i>
4.	COMPARISON OF MICROPATTERNING METHODS FOR CERAMIC SURFACES	146

Contents

5.	CONCLUSION	163
6.	OUTLOOK.....	165
7.	REFERENCES	167
8.	APPENDICES.....	188
8.1	FABRICATION OF MICROPATTERNED FREESTANDING CERAMIC FILMS THROUGH M- μ M.....	188
8.2	SUPPORTING DATA FOR 3.1.1 VERSATILE CRACK-FREE CERAMIC MICROPATTERNS MADE THROUGH M- μ M:	190
8.3	SUPPORTING DATA FOR “ORIENTATION OF OSTEOLASTS ON HYDROXYAPATITE-BASED MICROPATTERNS”	193
8.4	SUPPORTING DATA FOR 3.3.1 “MICROMACHINING OF CERAMIC SURFACES: HYDROXYAPATITE AND ZIRCONIA”	196
8.5	ADDITIONAL MICROGRAPHS	197

Acknowledgements

CURRICULUM VITAE

PUBLICATIONS

1. Introduction and aims of this thesis

1.1 Cell-material interfaces

Tissue consists of viable cells, therefore it is in permanent synthesis and degradation to heal defects and to prevent loss of quality. Bone tissue is a mineralized tissue that gives various mechanical and metabolic functions to the skeleton. In the case of bone tissue, bone-forming osteoblasts are involved in the bone synthesis, whereas bone-resorbing osteoclasts are responsible for the bone degradation. Both play the main role in the life cycle of the skeleton regulating its mass continually (Teitelbaum, 2000; Ducky et al., 2000).

With a bone implant, e.g. a dental implant or a hip prosthesis, being inserted into the patient's body a distinct reaction will be caused by the surrounding tissue. However, if the implant material is toxic, tissue necrosis and death of the surrounding tissue will occur, making a removal of the implant obligatory (Wintermantel, 2000).

If the implant surface is inert, a layer of non-adherent connective tissue will encapsulate the implant, which might cause a rejection of the implants. The ingrowth of inert surfaces can be remarkably improved by using porous inert materials. As pore sizes in natural cortical bone usually range from 1 to 100 μm and from 200 to 400 μm in trabecular bone (LeGeros, 2002), best ingrowth results are found for porous implants with interconnecting pores from 100 to 150 μm . These pore sizes are supposed to be sufficient to allow the vascularisation of blood vessels and a mechanical stabilization of the implant (Wintermantel, 2000). However, the growth of human osteoblasts into periodic microchannels or micropatterns with well-defined accuracy and different sizes is still not fully understood.

If the implant surface is bioactive, cells and generated tissue are adherent to the implant surface via chemical bonding at the interface. The interfacial bonding strength and the mechanisms of the bonding depend on the inserted material and the surrounding tissue. In the case of bioactive bone implants, a layer of bone apatite-like material or carbonate hydroxyapatite is synthesized on the implant surface. The chemical composition of this layer is very similar to the crystal structure of the naturally mineralized bone (LeGeros, 2002; Wintermantel, 2000).

If the implant material is non-toxic and degradable, the surrounding tissue will degrade and replace the implant. The speed of the biological degradation, then, depends on the material's composition, solubility, size and geometry. For example, cylindrical implants made of β -tricalcium phosphate (β -TCP) were degraded by 55% after 24 months of implantation in

rabbits. Same implants made of hydroxyapatite (HA) were degraded by 5% under identical conditions (Lu et al., 2002).

The bioactive calcium orthophosphate ceramic (CaP) hydroxyapatite is an important material which has been used in all experiments for this doctoral thesis. HA is utilised as a bioactive coating for metal implants. It is similar in composition to mineralized bone apatite and is able to promote cellular functions leading to the formation of a uniquely strong bone-tissue-HA interface. In addition, HA is osteoconductive, which allows for the provision of an appropriate scaffold or template for bone formation. Hydroxyapatite with an appropriate 3D geometry is able to bind and concentrate bone morphogenetic proteins. Furthermore, HA might be osteoinductive, which describes the capability of osteogenesis, and can be an effective carrier of bone cell seeds (LeGeros, 2002; Anselme, 2000).

In many studies, it has been found that chemical and topographical modifications of various materials affect different cell functions, depending on topographical geometry and size. Thus, Reichert et al. have demonstrated the impact of topography on the attachment of fibroblast cells which usually do not show any adherent contact to polytetrafluoroethylene (PTFE) surfaces. After laser micropatterning of the PTFE, the fibroblasts became attached to the PTFE surfaces (Reichert et al., 2007). Especially the alignment of cells in reference to micropattern formation has been reported by several researchers (Kirmizidis et al., 2009; Walboomers et al., 1999; Kaiser et al., 2006; Berry et al., 2004; Lu and Leng, 2003; Lu and Leng 2009; Tan and Saltzman, 2004; Perizzolo, 2001). Walboomers et al., for instance, reported an increased fibroblast alignment with decreasing groove widths from 10, 5, 2, and 1 μm (depths of 0.5 μm) on polystyrene substrates.

Randomized surface texturing (e.g. roughening of HA) has been studied by different research groups with various cell types. Depending on the investigated parameters the randomized CaP texturing can have a significant influence on the cell behaviour and metabolism (Ball et al., 2008; Deligianni et al., 2001; Hayashi et al., 1994).

The effects of defined CaP surface topographies (e.g. microgrooves) has so far been investigated in only very few studies (Lu and Leng, 2003; Lu and Leng 2009; Tan and Saltzman, 2004; Perizzolo, 2001). A main reason for this is certainly the difficult fabrication of defined ceramic micropatterns. Most reports on this deal with coatings, e.g. HA deposited by magnetron sputtering or by direct mineralization of HA on pre-patterned silicon wafer

substrates (Lu and Leng, 2003; Lu and Leng, 2009; Tan and Saltzman, 2004; Perizzolo, 2001). However, the effect of systematically changed micropatterns in the sub-100 μm range with high accurate patterns has not yet been studied using solid HA-based ceramic samples and human osteoblasts.

1.2 Bioceramics

Bioceramics are ceramic materials and glasses which are biocompatible and used in medical applications. Common bioceramics are oxidic ceramics, such as alumina (Al_2O_3), zirconia (ZrO_2) and silica (SiO_2), or non-oxidic ceramics such as hydroxyapatite. The former, i.e. oxidic bioceramics, are bio-inert (Wintermantel, 2002). Stabilized zirconia and alumina have a fracture toughness of $6.1 \text{ MPa}\cdot\text{m}^{1/2}$ and $4.2 \text{ MPa}\cdot\text{m}^{1/2}$, respectively (Bradt et al., 2005). Due to their high hardness and fracture toughness, stabilized alumina (ZTA: zirconia-toughened alumina) and stabilized zirconia (Y-TZP: yttria-stabilized zirconia and Mg-PSZ: Mg-partially stabilized zirconia) have been used as load-bearing implants, e.g. in hip-prosthesis, for almost four decades (Wintermantel, 2002). Moreover, alumina and zirconia were used in the experimental section of this thesis for the fabrication of micropatterns, e.g. via modified micromolding.

One important group of bioceramics are calcium orthophosphates (CaP), which inhibit twelve known non-ion-substituted calcium orthophosphates (Elliott, 1994). They are composed of three major chemical elements: calcium, with an oxidation state of +2; phosphorus, with an oxidation state of +5; and oxygen, with an oxidation state of -2, as a part of the orthophosphate anions. These materials are stabilized by a network of orthophosphate PO_4 groups (Dorozhkin, 2007).

CaPs are natural minerals and are biocompatible due to a chemical similarity to the mineral component of biological calcified tissue. They represent the inorganic part of mammal teeth, bones and antlers. Most calcium orthophosphates are stable in alkaline solutions pH 7 to 12, but are soluble in acids with pH 0 to 7 (Dorozhkin, 2007). This makes them absorbable in acidic conditions, which is important for possible in-vivo insertions into bone tissue, because osteoclast cells decrease the pH down to 3 to 4 locally in order to resorb bone tissue (Lucht, 1972; Ducey et al., 2000). In addition, the solubility between pH 0 and 7 should be kept in mind in order to prevent acidic conditions during the manufacture of micropatterns, as e.g. by using aqueous slurries of calcium phosphates for molding processes. CaPs are commercially available as synthetic materials with different grades of purity and various physical forms such as powders with different grain sizes, cements, composites with polymers and differently shaped blocks (LeGeros, 2002).

From the biomedical point of view, hydroxyapatite ($\text{Ca}_{10}(\text{PO}_4)_6(\text{OH})_2$), fluorapatite ($\text{Ca}_{10}(\text{PO}_4)_6\text{F}_2$), and β -tri-calcium phosphate ($\beta\text{-Ca}_3(\text{PO}_4)_2$) are the most commonly used calcium orthophosphates. An overview of the properties of these three important CaPs is given in **Tab. 1**.

Tab. 1: Material properties of medical relevant calcium orthophosphates according to Dorozhkin, 2007.

Compound	Abbreviation	Formula	Ca/P ratio	Density (g/cm ³)	Crystal system	pH stability at 25 °C in aqueous solution
β-tri-calcium phosphate	β-TCP	β-Ca ₃ (PO ₄) ₂	1.50	3.08	rhombohedral	n.a.
fluorapatite	FA or FAp	Ca ₁₀ (PO ₄) ₆ F ₂	1.67	3.20	hexagonal	7-12
hydroxyapatite	HA or HAp	Ca ₁₀ (PO ₄) ₆ (OH) ₂	1.67	3.16	hexagonal or monoclinic	9.5-12

In the experimental section of the present thesis, only hydroxyapatite was utilised as a calcium phosphate ceramic. The melting point of hydroxyapatite is at 1650 °C (Ha et al., 1994), but it thermally degrades and reconstitutes to other calcium orthophosphate structures at a temperature of about 1350 °C. Beyond this temperature it converts into α- and β-tri-calcium phosphate, which is critical for the sintering of HA and for micropatterning processes with thermal impacts, e.g. laser treatment.

An advantage of hydroxyapatite consists in its ability to provide an implant for new bone formation and support of osteoblast adhesion and proliferation (LeGeros, 2002; Anselme, 2000). Due to this osteoconductive behaviour HA is used as a coating on e.g. dental implants, hip-protheses or as a bone grafting material (Salmang und Scholze 2006.). As HA's fracture toughness is low and does not exceed 1.0 MPa.m^{1/2} it is not used as a load-bearing implant material (human bone 2-12 MPa.m^{1/2}) (Suchanek, 1996).

1.3 Aims of this Thesis

The main objective behind this doctoral thesis is to explore processing techniques for the fabrication of ceramic surfaces featuring small structures and patterns with dimensions in the sub-100 μm range. The explored techniques should be used to fabricate micropatterns and evaluate their ability and feasibility for the production of well-defined accurate ceramic patterns. The ceramic materials of interest were so-called bioceramics, as e.g. alumina, zirconia and hydroxyapatite, which are biocompatible and state of the art in various medical applications. The main focus in the fabrication of these micropatterns and in the biological study of this thesis has been put on the calcium phosphate hydroxyapatite. These micropatterns should be used in in-vitro cell experiments with human osteoblasts (HOB) and osteoblast-like osteosarcoma cells (MG-63). The findings from these fundamental investigations are aimed to understand osteoblast behaviour on micropatterned ceramic surfaces and may improve the bioactivity of medical implants, such as ceramic-coated dental implants, in future.

The doctoral thesis at hand is divided up into eight main sections. The first one will give an overview of some general problems occurring at the interface of an inserted implant (1.1) as well as further information about the ceramic materials used in the experiments (1.1). Furthermore, the main objectives will be briefly described, (1.3) highlighting thus the fundamental background of this study.

In the second section the principles of various micropatterning techniques appropriate for the fabrication of ceramic patterns will be introduced. The first subsection of it will be divided into four parts, namely, soft-lithography (2.1.1), rapid prototyping (2.1.4), micromachining (2.1.5) and laser treatment (2.1.6). The second subsection gives a detailed overview of the state of the art of ceramic micropatterning, shows examples of recently published literature, and outlines possible surface characterizations according to the well-established standards in this discipline (1.1).

The third section, then, will illustrate the experimental fabrication of ceramic micropatterns through the use of the techniques mentioned in section 2, including results from non-published pre-testing as well as from published data. This section comprises micromolding techniques via soft-lithography (3.1), rapid prototyping via Aerosol-Jet[®]-printing (3.2), and micromachining (3.3) and laser treatment of ceramic surfaces (3.4).

The fourth section will be a review on the feasibility of fabrication of ceramic micropatterns regarding the tested technologies (4). A detailed discussion of the advantages and

disadvantages of each applied technology will also be included. Section five, then, is to provide a conclusion drawn from the results of this thesis (5). In section six an outlook in order to pave the way for future studies in the field of ceramic research (6) will be given. In section seven, all the references used in the work on this thesis will be listed (7), and in section eight, finally, the appendices to this paper (8) will be delivered, with some additional information, e.g. micrographs, diagrams and further notes and comments.

2. Micropatterning of ceramic surfaces

2.1 Principles and state of the art of ceramic micropatterning

The development and continuous improvement of surface micro and nanopatterning has been the focus in material research for the last two decades and reviewed by a large number of researchers (Xia et al., 1998; Heule et al., 2003; Geissler and Xia, 2004; Gates et al, 2005; ten Elshof et al. 2010, Xia et al. 2011). For the surface patterning of ceramic materials, mainly two different strategies can be applied. First of all, there is the possibility of machine-aided ceramic micropatterning with a high effort of technical equipment such as laser surface treatment, injection molding of microparts, slip pressing, or casting of micro devices and micromachining of surfaces by, among others, Computer Numerical Control (CNC). Apart from that, there is also the possibility of using low cost methods such as soft-lithography. Beyond doubt, the results of the machine-aided methods are quite convincing. Thus, Bauer et al. reported on the reliable method for the fabrication of micro parts with high accuracy on edges and surface detail when using ceramic slip pressing. Thereby, alumina arrays of more than a thousand columns have been fabricated with smooth sidewalls and sharp edges. The thus produced patterns were 455 μm high and 115 μm wide (Bauer et al., 1999). Other researchers reported about reproducible results from the fabrication of micro devices via ceramic injection molding (CIM), in particular with low pressure injection molding (LPIM) of ceramic feedstocks. Various ceramic materials, such as alumina, hydroxyapatite and zirconia, have been used to reliably produce micropatterned components of a few cm^2 in size (**Fig. 1**) (Fanelli et al., 1989; Knitter et al., 2001; Piotter et al., 2003).

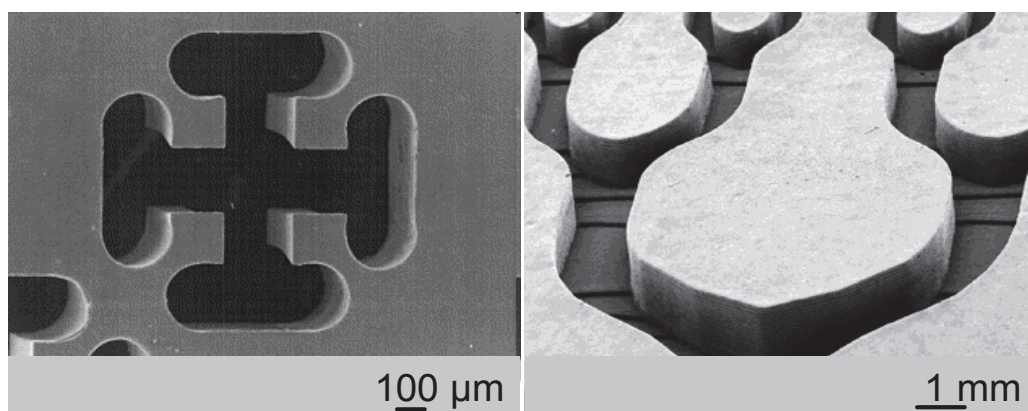


Fig. 1: Left: taken from Bauer et al., 1999: SEM micrograph of an Al_2O_3 micropattern made through ceramic slip pressing. Right: taken from Knitter et al., 2001: SEM micrograph of an Al_2O_3 fluid distributor made through low pressure ceramic injection molding.

Summarizing the above-mentioned studies, machine-aided processes have proved to yield excellent results. One main advantage of this is the potential fabrication of a high number of items at a time. On the other hand, the most limiting factor in all this consists still in the difficulty to produce patterns or micro components much smaller than 100 μm .

Due to the ambition of ceramic micropatterning with low technical effort as well as low producing costs and very high accuracy (even $\ll 100 \mu\text{m}$) at the same time, ceramic molding via soft-lithographic techniques will be presented in the following chapter.

2.1.1 Molding techniques

Micromolding (μM), or replica molding (μRM), is the basic principle for all soft-lithography techniques. It is used to fabricate a negative duplication, e.g. a soft PDMS mold, of a silicon wafer with a positive surface pattern (**Fig. 2**). Thereby, the relief structures or patterns and shapes of a master surface can be casted and duplicated. This method enables multiple copies with nanoscale resolution in a reliable and simple process route.

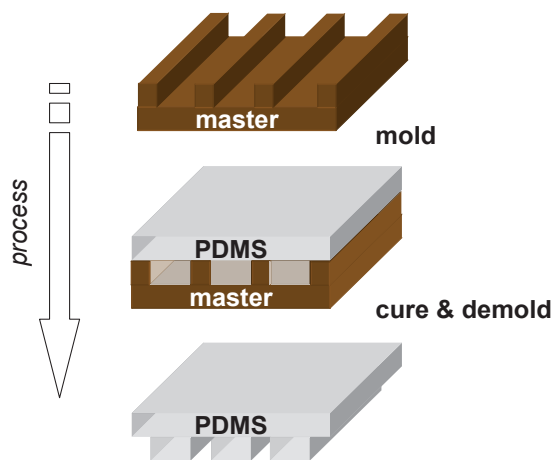


Fig. 2: Replication of a structured Si-wafer via PDMS

2.1.2 Conventional molding techniques via soft-lithography

In the field of micropatterning and microfabrication, the soft-lithography is a process route that is inexpensive and, at the same time, applicable with low expenditure of time. This non-photolithographic process is based on replica-molding, allowing the fabrication of micro devices or surface nano and micro structuring. As no complex devices or machines are needed, this technique is accessible to a wide range of users. During the process an

elastomeric fluid is used to replicate the surface relief of a master structure. Very often, the master is fabricated by a photolithographic process on a silicon wafer or by CNC micromachining, laser machining or etching of a polymer or metal block (Su et al., 2002; Xia & Whitesides, 1998). The elastomeric fluid is usually supplied as a two-part kit, containing a liquid silicone rubber base and a curing agent or catalyst. After mixing, the elastomeric liquid has to be poured over the master surface where it becomes solid and cross-linked due to a chemical reaction between the hydrosilane groups and the vinyl groups (Semlyen, 1994). This solidification process can be controlled on the basis of the mixing ratio and the hardening temperature. Usually, the hardening time decreases with increasing temperatures. Compared to rigid molds, the use of elastomeric soft molds makes it easier to release fragile small patterns and is much more inexpensive than the original master surface. After replication of the expensive and sensible original master surface (e.g. Si-wafer), the economic and stable soft mold acts as a new master surface for further molding processes. One of the most widely used elastomers for molding is polydimethylsiloxane (PDMS) Sylgard[®] 184 from Dow Corning (Wiesbaden, Germany). This silicone elastomer is optical transparent, does not swell in humid conditions, is thermally stable to about 186 °C, and supplies a surface with a low, interfacial-free energy (Xia & Whitesides, 1998). This molded negative copy of the master surface is called stamp and can be easily removed from the master surface, in most of the cases. Thereby, the master can be equipped with a nano-sized topography or even with complex, micro-sized quasi-3D pattern geometries.

The adhesion between the elastomeric stamp and the master surface can be reduced by the use of anti-sticking agents such as BGL-GZ-83 (PROFACTOR GmbH, Steyr-Gleink, Austria) or else by wetting the master before molding. The lateral resolution for the replication via PDMS is strongly dependent on the pattern height or depth. Schmidt and Michel as well as Odom et al. reported a lateral resolution of <100 nm by casting parallel line-like patterns and cylindrical pillows via PDMS Sylgard[®] or even 30 nm by using composite layers of different polymeric materials (Schmidt and Michel, 2000; Odom et al., 2002).

Due to its hydrophobic surface state, the PDMS stamp should be treated with, for example, oxygen plasma in order to increase the moisture inside the patterns. Otherwise, the small patterns will not be covered or filled by the ceramic suspension (so-called “ink”) homogeneously, which in turn downgrades the patterning results. Likewise, the aspect ratio between pattern height and width is of great importance. If the pattern width is too large compared to the height, the PDMS will sag on the substrate due to its own weight. If the

pattern height is much larger than the width, the PDMS patterns will collapse and stick together (Fig. 3).

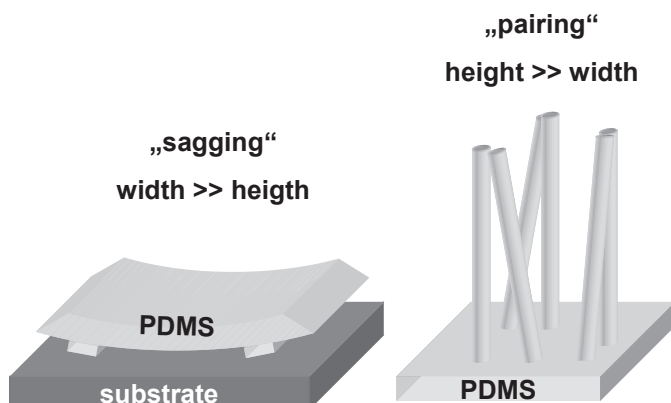


Fig. 3: Deformation of PDMS due to inauspicious aspect ratio

Zhang et al. have found that molded PDMS nanopatterns mainly collapse owing to the adhesive force when the aspect ratio is above 6, whereas those from more rigid molding materials (polyurethane and epoxy) collapse laterally at a much higher aspect ratio, namely, larger than 12 (Zhang et al., 2006).

The soft-lithography strategy exhibits different methods for the replication of structured master surfaces via PDMS stamps. This technique was made in mention and predominantly shaped by the group of George M. Whitesides with almost 500 publications in the last twenty years. Therefore, three different techniques for the fabrication of ceramic micropatterns will be of interest in the following chapter and have been extensively reported on by many researchers. These methods are microcontact printing (μ CP), microtransfer molding (μ TM), and micromolding in capillaries (MIMIC).

Microcontact printing (μ CP)

The most widely used technique for the replication of surface topographies via soft mold stamps is probably that of microcontact printing. Hereby, the replicated relief of a master surface is formed on the surfaces of substrates through contact via a structured PDMS stamp. The printed nano or micropatterns can be made of various materials such as biological molecules and proteins (Bernard et al., 2000; Dusseiller, 2005; de la Fuente et al., 2006), metal oxides, or ceramic particles (Clem, 1997; Heule, 2004;) (Fig. 4). When using μ CP, a thin layer is printed on the substrate, where the printed ink and the substrate can be made of

two different materials. Through repetition of the printing procedure with different shaped stamps or different ink materials or change of the stamp position, more than one material and micropattern geometry can be generated on the substrate surface (Bernard et al., 2000; Tien et al., 2001). By printing ceramic suspensions onto a ceramic substrate, often a discrete separation between the substrate and the printed ceramic patterns occurs after drying. In this case, the bonding at the ceramic-ceramic interface can be increased e.g. by sintering.

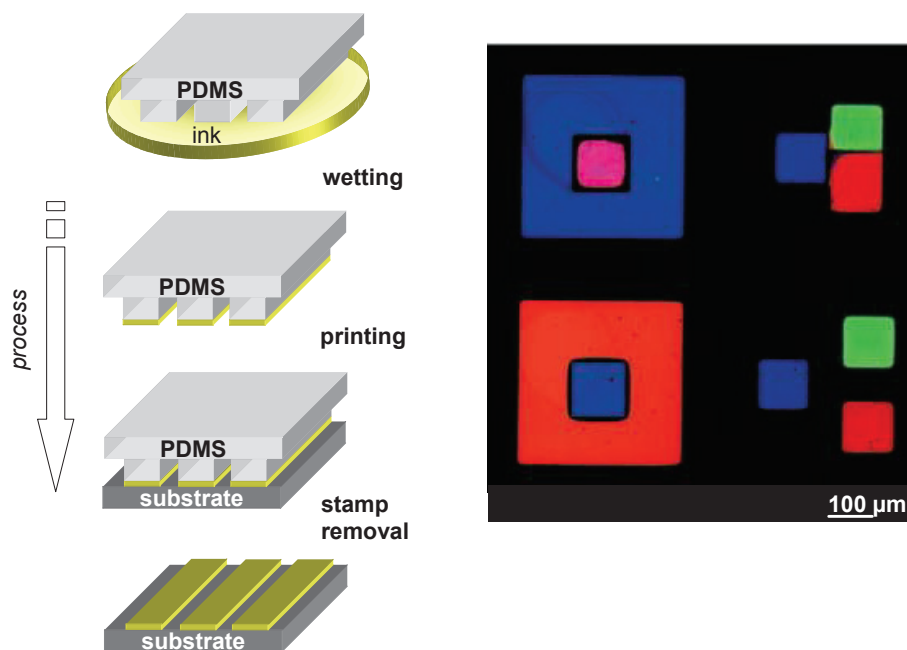


Fig. 4: Left: micro-contact printing (μ CP) process. Right: taken from Tien et al., 2001: microscopic image of three fluorescently labelled proteins printed on a glass surface by multilevel μ CP

Microtransfer molding (μ TM)

Microtransfer molding was firstly introduced by the group around George M. Whitesides (Zhao et al, 1996). By the use of microtransfer molding, a thin film of a liquid ink is filled into the patterns of a soft mold made of, for instance, PDMS. The excessive ink is then removed by scraping with a flat glass slide or a plane piece of PDMS. Then, the filled mold is deposited on the substrate surface. After drying it, the mold can be peeled off or lifted with care (**Fig. 5**).

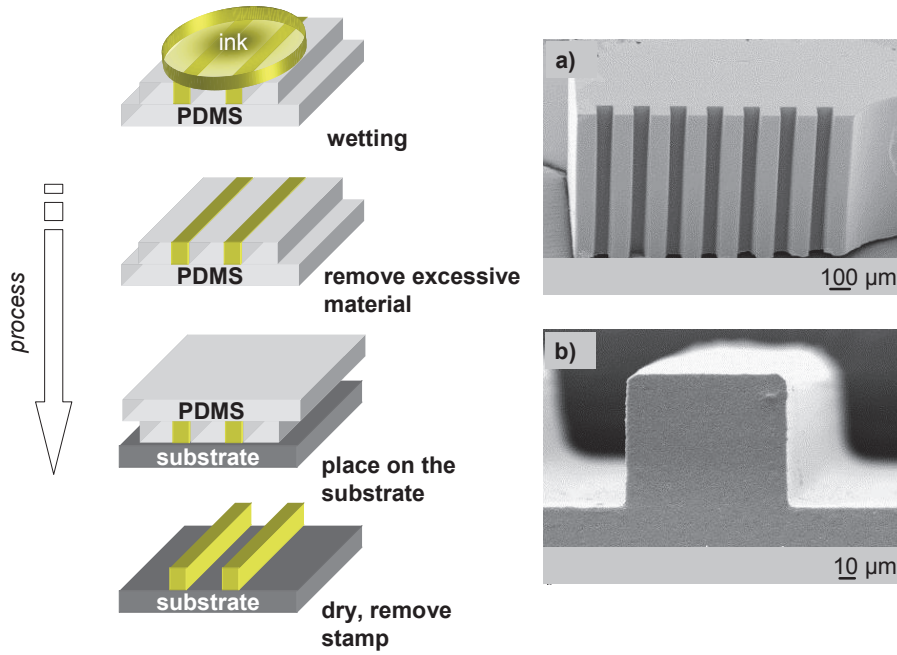


Fig. 5: Left: microtransfer molding (μ TM) process; right: taken from Zhang et al., 2006: non-sintered ceramic Al_2O_3 structures made by μ TM (a); enlarged side view of one ceramic structure (b)

The lower surface energy of the PDMS mold, as compared to the surface energy of the substrate, allows the patterned ink to remain on the substrate during the removal of the stamp. This process is described in the model by Khan et al., where γ_{ink} is the surface energy of the liquid ink, γ_{mold} the surface energy of the PDMS mold, $\gamma_{substrate}$ the surface energy of the substrate, and α the aspect ratio of the mold (height vs. width) (Khan et al. 2009, Martin and Aksay, 2004):

$$\gamma_{ink} < \gamma_{mold} < \frac{1}{(2\alpha + 1)} \gamma_{substrate}$$

eq. 1

The μ TM process is adaptable for various substrate materials and inks. In many cases it is used for the patterning of polymeric materials. Also, the fabrication of multiple-layer structures has been reported (Zhao et al, 1996; Lee et al., 2005). Zhang et al. and Su et al. reported on the production of miniaturized engine components such as teeth structures and micro-gear wheels made of ceramic alumina suspensions. Defects in the molding quality can be avoided by centrifuging the filled mold. Thereby, the green body density and the edge definition of the micro gears increase, resulting from a higher strength of the green bodies (**Fig. 5**) (Zhang et al. 2007; Zhang et al., 2004; Su et al, 2002). A variety of materials, e.g.

metals, biological materials such as proteins and hydrogels with cells, have been patterned by several research groups using μ TM (Bailey et al., 2000; Cavallini et al., 2001; Tang et al., 2003; Thibault et al., 2006; Talei Franzes et al., 2006).

Micromolding in capillaries (MIMIC)

The MIMIC process was also first presented by the group of George M. Whitesides, in 1996. With this method, a micropatterned PDMS mold is placed on a plane substrate surface and fixated by applying gentle pressure on the mold. Afterwards, a droplet of a fluid, low-viscous ink is pipetted in front of the mold with contact to it. Due to capillary action the ink is soaked into the micropatterns where it dries until the removal of the mold (Kim et al., 1996). MIMIC has been used for different materials; for example, Ahn et al. reported the fabrication of ceramic Al_2O_3 microstruts on the basis of silicon wafers with widths between 10 and 100 μm (Ahn et al., 2008) (**Fig. 6**). In their application of MIMIC, Beh and Xia used polymeric precursors to fabricate polycrystalline ceramic microstructures from ZrO_2 and SnO_2 (Beh and Xia, 1999). In the same year, Beh et al. showed the generation of conducting polymeric microstructures (Beh et al., 1999). Furthermore, also biomolecules can be utilised with MIMIC. The patterning of fluorescently labelled immunoglobulin was reported on by Delamarche et al. (1997).

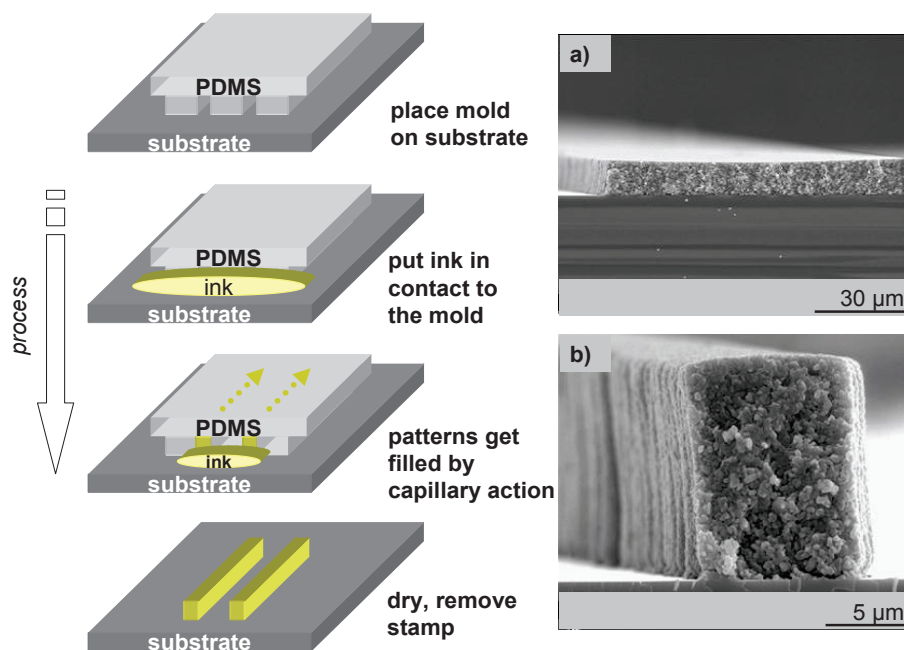


Fig. 6: Left: micromolding in capillaries (MIMIC) process. Right: taken from Ahn et al., 2008: SEM micrograph of a cross-section of a ceramic Al_2O_3 100 μm pattern on a Si-wafer surface (a); micropattern with a width of 10 μm on a Si-wafer (b). Patterns were fabricated via MIMIC

Altogether, MIMIC is a helpful tool in the patterning of surfaces with various materials. However, there are two main disadvantages of MIMIC, to wit, the impossibility to replicate isolated patterns and, second, the decrease in the infiltration rate of the ink with an increasing length of the microchannel (ten Elshof et al., 2010).

2.1.3 Modified micromolding (m- μ M)

Micropatterning via m- μ M was introduced by Rezwan's group in 2010 and has been demonstrated for several ceramic materials in the course of the preparation of the present doctoral thesis (Holthaus et al., 2010). The modified micromolding technique belongs to the soft-lithography family. By applying m- μ M, a microstructured Si-wafer is casted through a fluid elastomer such as PDMS Sylgard[®] 184 or Wirosil[®]. After curing inside the master mold, the elastomer can be removed from the master surface. Subsequently, the soft mold has to be sealed and an aqueous ceramic suspension can be filled into the molding chamber (**Fig. 7**).

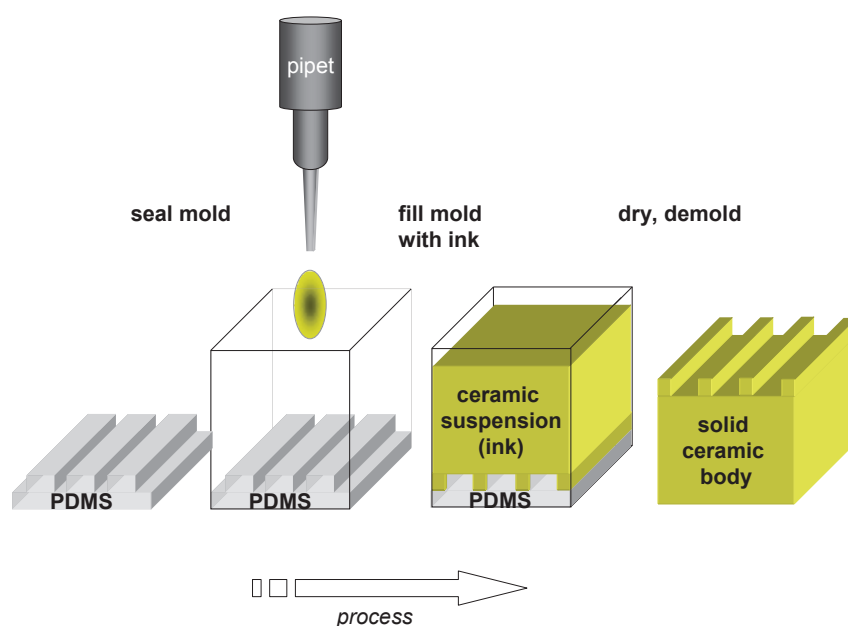


Fig. 7: Modified-micromolding (m- μ M) process

During the drying process the ceramic particles are homogenously dispersed throughout the fluid ceramic suspension. Gravity lets the particles sink down to the bottom of the micropatterned mold, while water from the fluid ceramic suspension is continuously evaporating. Due to the mold geometry the evaporation only takes place to one side. After a complete drying of the ceramic green body, the micropatterned sample can be carefully removed from the mold. The sedimentation and drying of molded samples is illustrated in **Fig. 8**. According to Reed (1995), this sedimentation of the spherical ceramic particles in

aqueous suspension can be described as follows: a ceramic particle with a diameter of a and a density of D_p in a viscous fluid of viscosity η_L of lower density D_L accelerates and then sinks, at a constant terminal velocity v , down to the bottom of the mold.

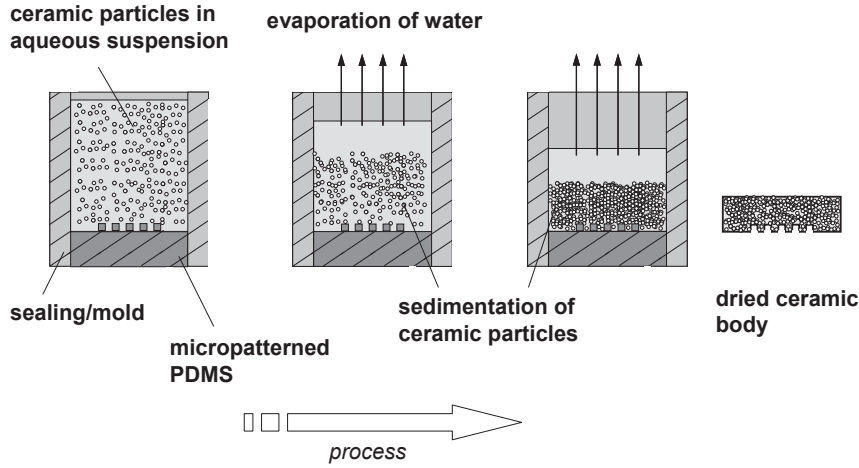


Fig. 8: Cross-sectional view: principle of the sedimentation and drying process of a ceramic suspension during m- μ M

According to the Stokes equation depicted in **Fig. 9**, the terminal velocity v is related to the diameter of the ceramic particle:

$$v = a^2 (D_p - D_L) \frac{g}{18\eta_L}$$

eq. 2

with the acceleration g due to gravity effects.

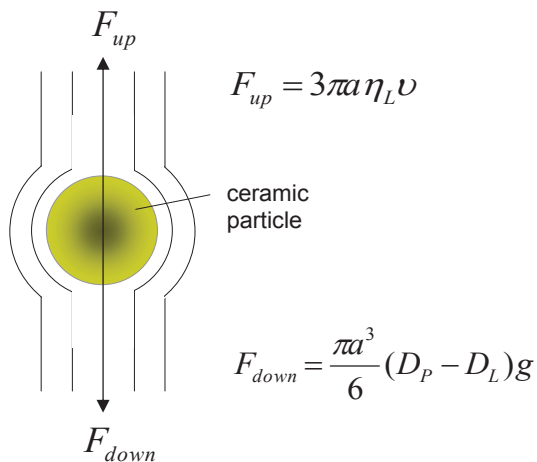


Fig. 9: Illustration of the equilibrium of forces during the sedimentation of a spherical ceramic particle in a Newtonian fluid with laminar flow; taken from Reed, 1995 (modified)

A particle of a diameter a needs to sink a distance of a length H for the time t which can be calculated from **eq. 3**. This means that for a ceramic alumina particle released in water (density of 1 g/cm³ and viscosity of 1 kg/(s*m) at 20 °C), the time for travelling 1 cm is about 1 minute for a 10 µm particle, but about 2 hours for a 1 µm particle. For a 150 nm alumina particle with a density of 3.98 g/cm³, as it was used in the experimental chapter 3.1, the theoretical time to sink to the bottom of a mold with 1 cm height is even 3.2 days.

$$t = \frac{18H\eta_L}{a^2(D_p - D_L)g}$$

eq. 3

The drying process starts as soon as a micropatterned mold is filled with an aqueous ceramic suspension. In this thesis, the drying of molded samples was applied in a controlled manner by the use of a climatic chamber. In the saturated ceramic suspension, liquid consisting of water and liquid from the dispersant or binder is removed through evaporation from the external surface, as depicted in **Fig. 8**. The drying rate, which is defined as the weight loss per time, increases on heating when the rel. humidity in the climatic chamber is less than 100%. If the evaporation surface area and the evaporation rate are constant, the drying rate will be constant, too. The mass loss of water due to evaporation R_E is given in **eq. 4** (Reed, 1995):

$$R_E = K_E(P_w - P_o)$$

eq. 4

with the evaporation constant K_E , which is dependent on air flow conditions in the climatic chamber, the vapour pressure of the liquid suspension at the evaporation temperature P_w as well as the partial pressure of liquid in the surrounding atmosphere P_o inside the chamber. The thus evaporated liquid at the sample surface is then re-filled in interparticle liquid transport processes via diffusion and capillary flow. Adsorbed binder molecules were mixed to the ceramic suspension in order to prevent cracking. These binder molecules are bound to the particles and resist the migration/transport with the liquid, so that they remain in their position. Non-bound binder molecules and particles as well as dissolved salts will follow this migration to the evaporation surface area, which in turn results in an inhomogeneous density and material distribution inside the sample. The practical drying rate R_{CR} can be described as in **eq. 5** above (Reed, 1995):

$$R_{CR} = \frac{W_1 - W_2}{At}$$

eq. 5

where W_1 describes the content of liquid before drying and W_2 is the content of liquid after drying for a time t and a surface area of evaporation A .

Usually, shrinkage during the drying process of a molded sample takes place because of the removal of liquid between the ceramic particles and the decreasing interparticle separation. If the shrinkage rate is homogenous within the material and the intensity of shrinkage is adequate, no cracks or fissures will occur. However, cracks at the sample surface may appear when material near the surface evaporation area becomes too brittle and the differential shrinkage results in stresses as high as the greenbodies' tensile strength. Differential shrinkage can be defined as an inhomogeneous shrinkage caused, among other things, by gradients in particle size or junctures between differently oriented particles. In addition, vapor inside small pores can increase these stresses during drying (Reed, 1995).

Contrary to conventional soft-lithographic methods, a solid micropatterned ceramic body is fabricated by using m- μ M instead of a micropatterned thin film which is placed on a plane substrate. Another advantage, e.g. compared to MIMIC, is the possibility to produce various pattern geometries such as microchannels and struts, holes, cylinders and different isolated microstructure formations.

The results from the molding of ceramic suspensions are presented in chapter 3.1, "Microstamping and micromolding of ceramic suspensions."

2.1.4 Rapid Prototyping

By using rapid prototyping (RP) a computer-generated 3D model is fabricated rapidly from a computer aided drawing. However, the real fabrication of a rapid prototype involves a number of steps that have to be accomplished before the 3D model can be generated. There is a variety of existing RP techniques which have been introduced throughout the last three decades, having been subject to continuous optimisation. In most cases, they are already well-established in industrial processes and usable for polymers and metals with high precision and accuracy even in the micron range (Bertsch et al. 2000; Varadan et al., 2001). RP processes are, for instance, selective laser sintering (SLS), stereolithography (SLA), freeform multijet solidification (MJS), laminated object manufacturing (LOM), fused deposition or extrusion free-forming, inkjet printing, aerosol jet printing, and injection molding (IM) (Hull, 1986; Greulich et al., 1995; Subramanian et al., 1995; Tari et al., 1998; Tseng and Tanaka, 2001; Mette et al., 2007; Yu et al., 2007). Independently of the material deployed, rapid prototyping processes should inhibit a fast fabrication of samples from a functional model to a small batch series within a short time period. RP may involve the fabrication of adequate ceramic micro components or just the finishing of various surfaces with a ceramic material. Ideally, the process chain combines an inexpensive and accurate but flexible way of processing ceramic suspensions, feedstocks, or powders. Ceramic micro fabrication can be integrated into a rapid prototyping process chain as successfully shown via low pressure injection molding of ceramic feedstocks by Bauer et al. (1999) and Knitter et al. (2001) (see **Fig. 1**). Contrary to metals and polymers, rapid or direct fabrication of ceramic materials in the micro range is still not established and rather difficult, but it has become much more usable and accurate throughout the last ten years. For instance, Wozniak et al. developed a highly loaded UV curable nanosilica dispersion which is suitable for stereolithography applications (Wozniak et al., 2009). Hansch et al. reported of the fabrication of screen-printed yttria-stabilized zirconia honeycomb structures ($D \sim 2 \text{ mm}$) with a layer thickness of less than $20 \text{ }\mu\text{m}$ (Hansch et al., 2009).

The layer-wise deposition of highly loaded colloidal ceramic slurries was shown by Cesarano et al. as well as by other research groups by using “robocasting”. This technique allows a freeform fabrication for dense ceramics, as e.g. Al_2O_3 and composites with less than 2 volume percent of organic additives by extrusion of slurry. Thereby, ceramic slurries can be shaped into complex geometries with thick solid sections as well as with thin-walled sections with high aspect ratios (Cesarano et al., 1997; Cesarano et al., 1999; Tuttle et al., 2001).

Another RP technique for ceramics materials is that of inkjet printing, where liquid droplets of ceramic suspensions are ejected through inkjet nozzles onto predetermined positions. Several researchers have already used ceramic suspension and precursors in inkjet printing to produce ceramic micron or sub-millimetre patterns (Mott and Evans, 2001; Zhao et al., 2003; Song et al., 2004; Oh et al., 2010). Song et al., for example, reported about the manufacture of grid patterns in the sub-millimetre range printed with various ceramics such as alumina and zirconia (Song et al., 2004). Even biomolecules and cells have been used for inkjet printing; thus, e.g. Xu et al. have illustrated the printing of pre-designed ring patterns of viable hamster and rat cells onto a hydrogel-based substrate (Xu et al., 2005).

However, the horizontal and lateral resolutions are in general limited to the range of 100 μm for these RP techniques, suffering from problems in the process reliability or from changes in the ceramic properties. One rapid prototyping method, which was also applied for this thesis, is aerosol jet printing, whose principles will be introduced in the following chapter.

2.1.4.1 Maskless material deposition by aerosol jet printing

Aerosol jet printing, also known as maskless mesoscale materials deposition (M^3D), is a direct write printing technique for the precise deposition of different materials on various planar or curved substrates without using any masks. The characteristics and details of an aerosol jet by Optomec Inc. (Albuquerque, USA) will be given in this chapter, as it is used in experimental set-ups in chapter 3.2, “Aerosol-Jet[®]-printing of hydroxyapatite suspensions”. This printing device is computer-aided as CAD-drawings (computer aided design) can be used to deposit the ink material on specific positions in various geometries. One ink droplet has a diameter of about 1 to 5 μm , which is equivalent to a volume of a few femtolitres. The horizontal resolution of printed structures or geometries is 10 μm , whereas the lateral resolution can be in the nano range. The feed velocity or printing speed is customizable up to 200 mm/s. Liquid materials to be deposited, such as colloidal particles in aqueous suspension, must have a viscosity between 0.7 and 1000 mPas (Hedges et al., 2005; Zöllmer et al., 2006; Mette et al., 2007; Sears et al., 2007).

During the aerosol jet process an atomizer module converts the liquid and colloidal suspension into an aerosol by using an ultrasonic transducer or pneumatic nebuliser. The aerosol is then aerodynamically focused by a sheath gas stream in a second module which is called flow guidance deposition head. This module forms a co-axial flow between the aerosol stream and the sheath gas stream. At the exit of the deposition head, the aerosol leaves the module through an abrasive resistant, ceramic nozzle, and the aerosol droplets are

deposited on the substrate where a pattern or structure is generated. The distance between the printer nozzle and the substrate is adjustable to up to 5 mm. The precise printing of the patterns can be either controlled through the movement of the flow guidance head while the substrate is fixed or else by the change of the substrate position via a computer-controlled stage (Hedges et al., 2005; Zöllmer et al., 2006) (**Fig. 10**).

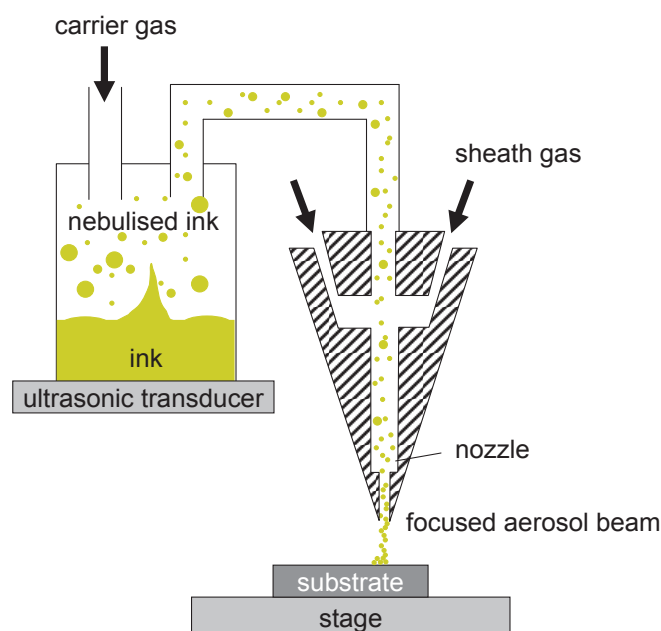


Fig. 10: Aerosol-Jet®-printing process, modified sketch according to Maiwald et al., 2010

The patterns are generated through a layer-wise material deposition, which allows the fabrication of 3D parts or pattern geometries. A continuous-wave Nd:YAG laser is integrated in another module (not shown in the sketch) which can be used for the post-treatment of the generated particles, as e.g. sintering of ceramic micropatterns. This treatment allows a local heat treatment without affecting the surrounding substrate material. Using this aerosol jet technique, the printing of various materials and biomolecules has been effected. Maiwald et al. reported a multilayer deposition of inks containing nanoscale silver particles for the fabrication of a conductive meander structure and isolating polymers for sensor applications (Maiwald et al., 2010). The fabrication of aerosol jet-printed ceramic alumina honeycomb patterns with average diameters of 430 μm and wall heights of 10 μm has been shown by Treccani et al. (Treccani et al., 2009). Grunwald et al. used fluorescently labelled DNA as well as labelled proteins bovine serum albumin (BSA) and horseradish peroxidase (HRP) for aerosol printing of spot formations with single diameters of 9 μm and lines with widths between 10 and 20 μm (Grunwald et al., 2010). These results show the versatility of this rapid aerosol printing technique.

2.1.5 Micromachining

All processes where electrical machines are needed to fabricate micropatterns or micro components are called micromachining techniques. Micromachining belongs to the group of solid freeform fabrication (SFF) and comprises the direct fabrication of complexly shaped materials, such as e.g. polymers, metals and ceramics, without the use of molds or masks. During the machining process, material is abrasively removed from a solid material substrate, for instance by means of a rotating milling tool. Common micromachining processes are drilling, reaming, threading, milling, and grinding. Most of these processes such as micromilling or microgrinding belong to the rapid prototyping technologies mentioned above. Industrial machining techniques are usually CAD-driven, which means that geometrical information, e.g. the virtual object of a micro device, is pre-processed by means of software. This object is then manufactured by a computer-aided machine as a solid finished component (Cawley et al., 1999; Tay et al., 2003). Computer-numerical control-based milling and grinding and machine-assisted roughening and polishing will be presented as they were used in the experimental set-ups of this thesis.

2.1.5.1 Precision machining by Computer Numerical Control Machining

In the beginning of automated machining, most machining processes were manually operated. Nowadays, computer numerical control (CNC) machining is widely used in industrial as well as in research processing routes. CNC milling is the automated, controlled and accurate processing of solid materials via an electrical machine tool (device) and a rotational cutter (tool). Milling machines are grouped into two basic machine forms, i.e. in a vertical and a horizontal form, which corresponds to the orientation of the main spindle. During the cutting process the workpiece is held stationary as the cutting tool moves axially to cut the material. Furthermore, the milling machine moves the workpiece radially against the rotating tool or cutter. The tool, then, cuts using its sides as well as its tip. The contact force during machining should remove particles from the surface layer without causing fracture of the workpiece. The failure rate of the fracturing is high when the workpiece is brittle and fragile or when the strength and the tool force for machining are high (Reed, 1995). Cooling liquid or lubricant can be used to remove excessive material from the grinding zone and to reduce or avoid thermal effects.

The cutting tool movement as well as the position of the workpiece are precisely controlled with an accuracy in the sub-micron and even in nano range. Important machining settings are

the applied feed velocity (v_f) and the rotational speed (n). The tool characteristics influence the machining results strongly. Tools made of various materials, shapes and diameters are commercially available. Thus, tools made of TiAlN coated with tungsten carbide were used for milling, and grinding pins made of a solid steel body electroplated with diamond grains were utilized for grinding in the experimental section of this thesis since they are hard enough to cut ceramics.

Processing with milling machines can be performed with a large number of operations per day and the workpiece shape can feature simple, e.g. planar, as well as complex, e.g. 3D, geometries. The CNC-machining processes in this thesis were operated with the so-called end milling cutters, i.e. with ball-nose end mills. As illustrated in **Fig. 11**, the shape of these milling tools is a semisphere. Ball-nose end mills are often used when cutting molds, dies as well as on solid workpieces with complex surfaces in various fields of applications such as in automotive, dental and aerospace industries via the machining with six-axis robots (Dormer-Tools, 2005; Xu and Newman, 2006; Olabi et al., 2010).

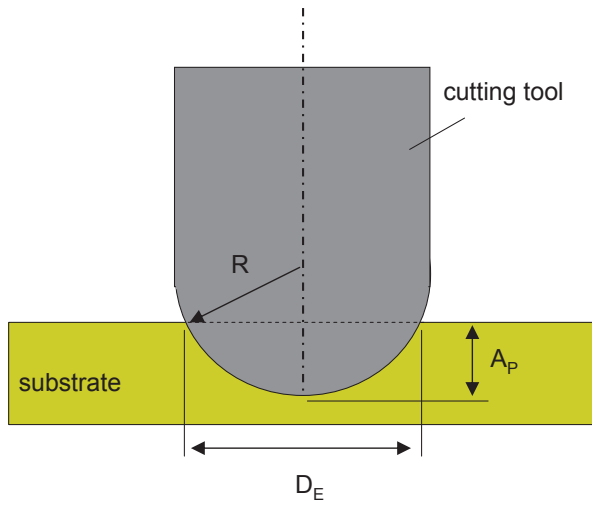


Fig. 11: The cutting process with a ball-nose end milling tool. Important parameters are effective diameter D_E , radius of the cutting tool R and the axial depth-of-cut A_p . Modified sketch according to Dormer-Tools, 2005.

The effective diameter D_E is the main factor used for the prediction or calculation of the required spindle speed. It is defined as the actual radius of the cutting tool R at the axial depth-of-cut line A_p :

$$D_E = 2 * \sqrt{R^2 - (R - A_p)^2} \quad \text{eq. 6}$$

The effective diameter replaces the cutting tool diameter when calculating the effective cutting speed for ball-nose end milling processes:

$$V_c = \frac{(\pi * D_E * n)}{1000} \quad \text{eq. 7}$$

There, V_c stands for the effective cutting speed, D_E is the effective diameter, and n is the rotational speed. The CNC machining of microchannels can be easily described. When a cutting tool with a ball-nose end mill is used to machine a surface in groove-like patterns, an uncut strut is created between the two cutting passes. The height of these struts is called cusp height H_c (Fig. 12).

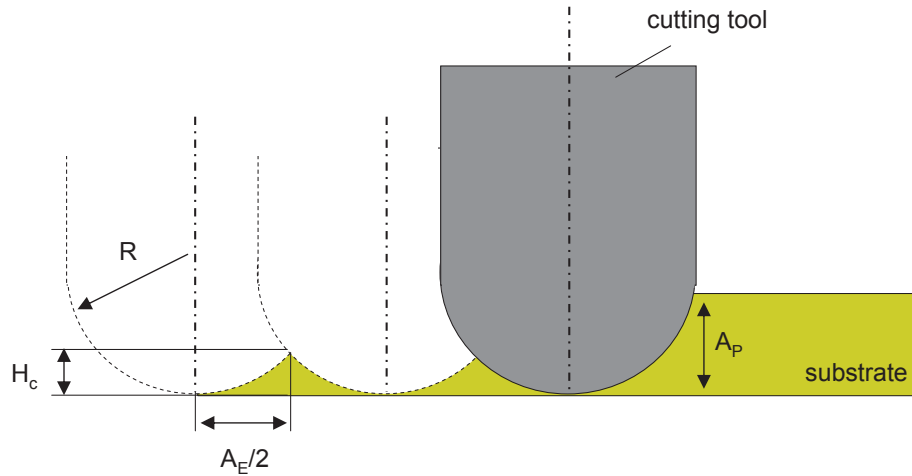


Fig. 12: Schematic illustration of uncut struts between three machined groove-like patterns. Radius of the cutting tool R , axial depth-of-cut A_p , cusp height H_c and the step-over value between two cutting passes A_E . Modified sketch according to Dormer-Tools, 2005.

The cusp height can be calculated as follows:

$$H_c = R - \sqrt{R^2 - \left(\frac{A_e}{2}\right)^2} \quad \text{eq. 8}$$

The cusp height therefore depends on the tool nose radius R and the step-over value between two cutting passes A_e (Dormer-Tools, 2005).

The automated micromachining of various materials such as polymers and metals is well established in industrial and research processes. The manufacture of complex micropatterns is possible with very high accuracy in the micron range. For example, Filiz et al. have reported a 3D pyramide or mushroom-like microbarbs with different widths ranging from 68 to 174 μm , edge sharpness of 60° and 90°, and angles and heights from 84 to 460 μm . These barbs were made of non-biodegradable 304 stainless steel and poly-methylmethacrylate (PMMA), bioresorbable polylactic acid (PLA), and a fibrin-based plastic (Filiz et al., 2008). Adams et al. reported the micromachining of parallel groove-like patterns with widths of 13 μm and depths of 4 μm on curved PMMA surfaces (Adams et al., 2000). Various examples of precise micromilling can be found in further publications (Friedrich and Vasile, 1996; Takacs et al., 2003).

Contrary to the advantageous machining of metals and polymers, ceramic surfaces are more difficult to machine due to their high hardness and fracture toughness as well as their brittleness. Ceramic parts can be micromachined in industrial processes, e.g. by milling with high reliability and tolerances of a few microns. However, the machining of ceramic, especially of micropatterns such as groove-like patterns smaller than 100 μm in width, is still difficult owing to the size of the cutters (usually a total tool diameter of min. 300 μm).

Nevertheless, the CNC machining of ceramics such as yttria-stabilised zirconia (YTZ) is well established in industrial processes such as in the production of crowns, abutments, bridges, and for making final-fit adjustments on dental restorations (Yin et al., 2003; Su et al., 2008; Sundh and Sjögren, 2008). The milling of ceramic groove-like patterns smaller than 100 μm in width will be further investigated in the experimental section in chapter 3.3.1, “Micromachining of ceramic surfaces: hydroxyapatite and zirconia”.

2.1.5.2 Microgrinding via grinding papers

Very simple and fast micropatterning techniques for the fabrication of unspecific patterns are automated roughening, polishing, and lapping. For the present thesis, roughening and polishing via grinding papers have been studied. The grinding papers are coated with particles of, for example, silicon carbide, zirconia, alumina, or diamond grains. The papers are available in different sizes, shapes and grits, e.g. p80. The grit value “p” describes the amount of abrasive particles which are fixed on the grinding paper per mesh size according to ISO6344. The higher the grit value, the larger will be the average grain size (**Tab. 2**) (ISO6344, 2000; Somiya et al., 2003).

Tab. 2: Exemplary overview of grinding paper grain sizes according to ISO6344

Grinding paper grit	average grain size (μm)
p80	201
p120	125
p180	82
p320	46
p600	26
p2500	8

The grinding via papers occurs through the sliding frictions between the abrasive paper and the solid workpiece. The workpiece can be clamped in a specimen holder or pressed manually onto the rotating planar abrasive surface of the grinding paper. In the region of contact, particles are removed from the material's surface layer by the grains of the paper. This process can be applied to all solid materials for fabricating randomized roughness levels of some microns or even a few nanometres. Removal of excessive material from the grinding zone and reduction of thermal effects can be achieved by the use of lubricants (Somiya et al., 2003, Reed, 1995). The results from experiments with ground ceramic surfaces will be shown in chapter 3.3.2, "Monitoring osteoblast viability on hydroxyapatite with adjusted submicron and micron surface roughness by using proliferation reagent WST-1".

2.1.6 Laser treatment

2.1.6.1 Laser ablation

A laser is a coherent, convergent, and monochromatic beam of electromagnetic radiation with wavelengths ranging from ultraviolet to infrared. Pulsed laser ablation with a solid state laser (e.g. nanosecond Nd:YAG laser), as it was used for the experimental section in chapter 3.4.1, "Laser ablation of hydroxyapatite surfaces", is the removal of material from a substrate surface via short high-intensity laser pulses. The pulsed laser ablation can be classified into a thermal and a non-thermal (photochemical) interaction with the substrate surface. The ablation rate depends on various parameters such as the laser fluence, the wavelength, the pulse duration of the laser beam, the number of pulse repetitions, and the type of excitation and dissipation of the energy within the solid substrate (Bäuerle et al., 2000; Dahotre and Harimkar, 2007). At least a laser, a beam delivery system, and an adequate specimen holder for the sample, as three basic parts of experimental equipment, are required to perform a removal of material with the help of a laser. Additional parts such as lenses can be used to focus the laser beam onto the substrate surface, and filters are able to adjust

the beam power. Via mirrors and flexible optical fibres, the laser beam can be guided to any desired location of the experimental test setup (von Allmen and Blatter, 1995).

In non-thermal ablation processes, the energy of the incident photon causes a direct bond breaking of molecular chains in organic materials. This, in turn, triggers the removal of material by molecular fragmentation without significant heat change or thermal damage of the substrate surface (Dahotre and Harimkar, 2007).

In thermal ablation processes, by contrast, laser-induced heating, melting/boiling and vaporization are the basic occurrences in the irradiated solid substrate. Vaporization means the passage from the solid phase to a vapour phase (gas or plasma) by the emission of atoms or molecules from the extreme outer surface under conditions of electron-phonon coupling. The vaporization process includes sublimation and evaporation (Miotello and Kelly, 1999) (**Fig. 13**). This ablation of material through a laser beam can be processed once a specific energy threshold level has been passed over. The ablation rate, thus the ablation depth per pulse, depends on the material.

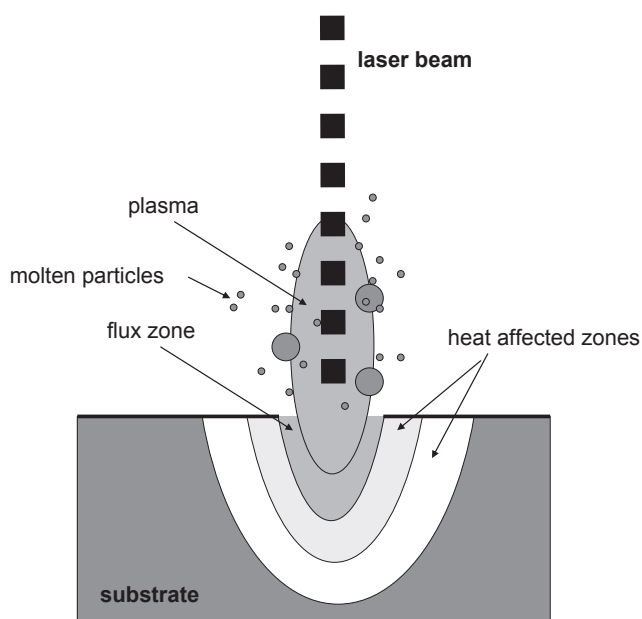


Fig. 13. Schematic illustration of material ablation via a nanosecond laser

Various materials, such as metals, polymers, biological collagen substrates and ceramics, have been micropatterned via pulsed laser beams for research applications as well as for industrial purposes (Ihlemann et al., 1995; Chivkov et al., 1996; Liu et al., 2005; Tiaw et al., 2005). Thereby, very defined and accurate micropatterns have been laser-machined. For example, Ihlemann et al. reported the fabrication of micro holes with diameters of 50 and 100 μm and depths of e.g. 20 μm on Al_2O_3 , MgO and ZrO_2 ceramics by the use of lasers with nanosecond

and femtosecond pulsed lasers. In addition, they reported groove-like patterns with widths of 4 to 5 μm (Fig. 14).

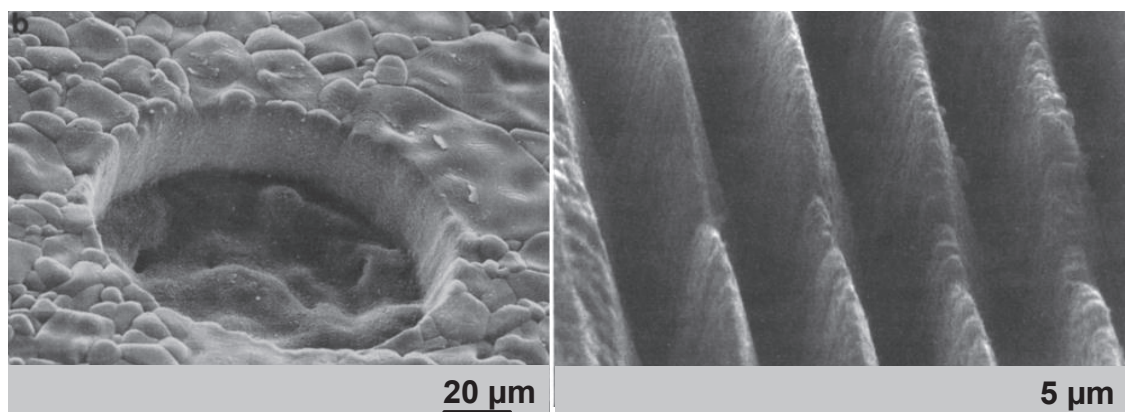


Fig. 14: Laser-ablated micro holes in Al_2O_3 , made at a wavelength of 248 nm and pulse duration of 500 fs with a fluence of 6.1 J/cm^2 with 50 pulses; taken from Ihlemann et al., 1995 (modified)

Results from laser ablation experiments of groove-like HA patterns with a pulsed nanosecond Nd:YAG laser are given in chapter 3.4.1.

2.1.6.2 Direct laser interference patterning

By using direct laser interference patterning (DLIP) a primary beam of a high-power pulsed laser is split into two or more coherent sub-beams via a beam splitter. These sub-beams are guided by mirrors to interfere with each other on a substrate surface in order to fabricate micropatterns. The interference of the sub-beams results in direct, periodical and local heating through photo-thermal mechanisms between, on the one hand, light and, on the other, the substrate material (Mücklich et al., 2006; Lasagni et al., 2006). An exemplary setup for a DLIP process is shown in Fig. 15.

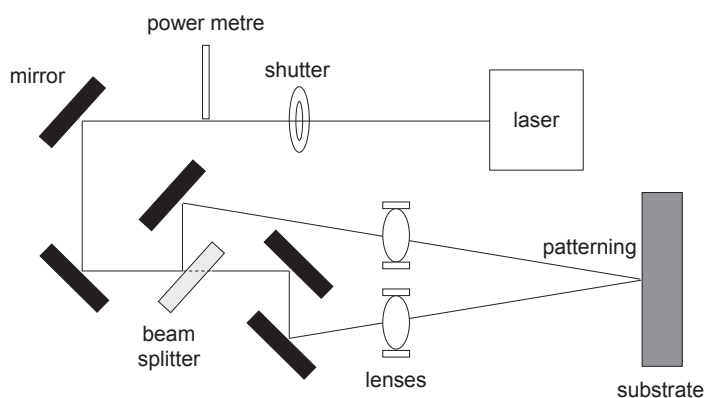


Fig. 15: Possible setup for direct interference patterning using a primary beam which is split into two sub-beams which are focused on the substrate surface where the patterns are fabricated; taken from Lasagni et al., 2006 (modified)

Even by applying one single laser pulse the interference patterning can result in a large area patterning of several cm^2 . The pattern depth and width can be adapted from the nano to the micron range. The geometry of the interference pattern depends on the number of laser pulses, the partial energy, and the geometrical arrangement of optical components from the DLIP setup, thus the guidance of the individual laser beams (Lasagni et al., 2005). The number of laser pulses can be adjusted by means of a mechanical shutter, and the partial energy can be controlled by the power metre. The beam intensity, in turn, can be adjusted independently by focusing via the lenses and mirrors for each individual sub-beam.

Interference patterning is applicable for various materials and substrate shapes; even curved surfaces are able to be patterned by DLIP. The interference patterning of metals (laser interference metallurgy, LIME) and polymers has been reported in various studies (Catrin et al., 2008; Lasagni et al., 2005, Lasagni et al., 2006; Lasagni et al., 2007, Mücklich et al., 2006). Further, Lasagni et al. 2007 report the fabrication of line-like patterns on polyimide with adaptable depth and profile shape by the use of two laser beams and various laser fluence (**Fig. 16**). In the same study, moreover, cylindrical hole-like patterns were fabricated with the aid of three laser beams and several laser fluences.

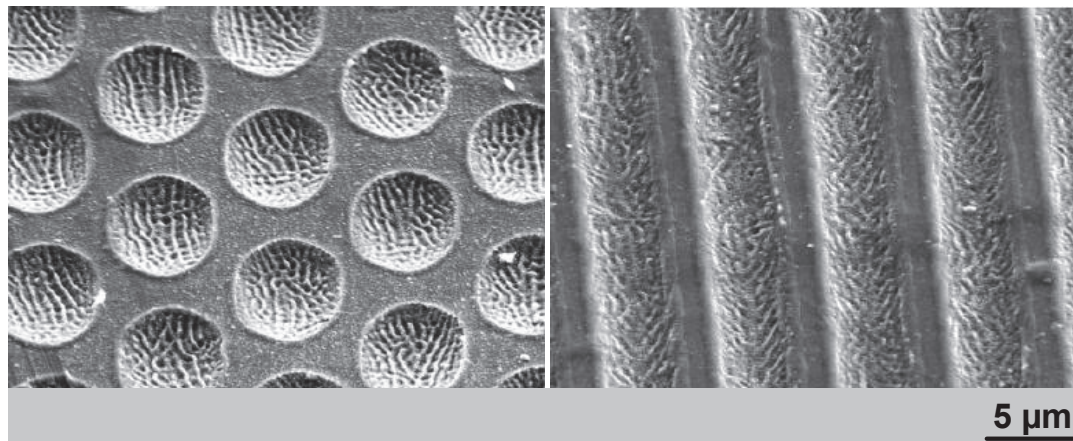


Fig. 16: Polyimide micropatterns made via DLIP. Hole-like patterns (left) and groove-like patterns (right); taken from Lasagni et al., 2007 (modified)

Results of the fabrication of periodic ceramic micropatterning via DLIP are reported only rarely. As one of the few, Segawa et al. (2003) showed the periodic fabrication of 10 μm -wide groove-like patterns on hybrid TiO_2 films on glass substrates. The interference pattern can be calculated and simulated prior to the DLIP process. Assuming that the laser beam is perfectly mono-chromatic and with linear, polarized plane waves, the total electric field E of the pattern can be weighted according to **eq. 9** (Lasagni et al., 2005; Catrin et al., 2008):

$$E = \sum_{j=1}^n E_j = \sum_{j=1}^n E_{j0} e^{-ik \sin \alpha_j (x \cos \beta_j - y \sin \beta_j)}$$

eq. 9

In this relation, all individual sub-beams j in terms of their angles α and β between the sub-beams with respect to the interference plane x, y have to be included. Here, E_{j0} is the amplitude of the beam j , and the wave number k is given in **eq. 10** with the wavelength of the laser beams λ :

$$k = \frac{2\pi}{\lambda}$$

eq. 10

The intensity distribution I of the interference patterning can be calculated as shown in **eq. 11** for the use of two laser beams:

$$I = 2c\epsilon_0 E^2 \cos^2(kx \sin \alpha)$$

eq. 11

with the speed of light in vacuum c and the permittivity of the vacuum ϵ_0 . For the experimental section in chapter 3.4.2, “Laser interference patterning of hydroxyapatite surfaces”, HA surfaces were patterned using DLIP with two laser beams, whereas periodic line-like patterns were finally generated. In the case of these line-like patterns, the period can be adjusted by adapting either the angle α between the two sub-beams or else the wavelength of the laser light (**eq. 12**):

$$p = \frac{\lambda}{2 \sin \alpha}$$

eq. 12

2.2 Surface characterization

2.2.1 Measurement of surface texture

The surface characterization of material surfaces featuring topography-dependent functionality is of crucial importance. Accurate and standardized surface characterization can be made for full 3D areas via non-contact optical imaging or else for single 2D profiles via tactile scanning contact measurements. Because of increasing requirements on functional surfaces, the traditional 2D tactile scanning of surfaces is often not adequate anymore. Problems occur in cases of anisotropic surfaces (**Fig. 17**) where the surface function depends on the direction of the surface texturing, such as implant surfaces featuring groove-like patterns for cell guidance or tribologically stressed surfaces used for minimized friction in bearings (Beck, 2009).

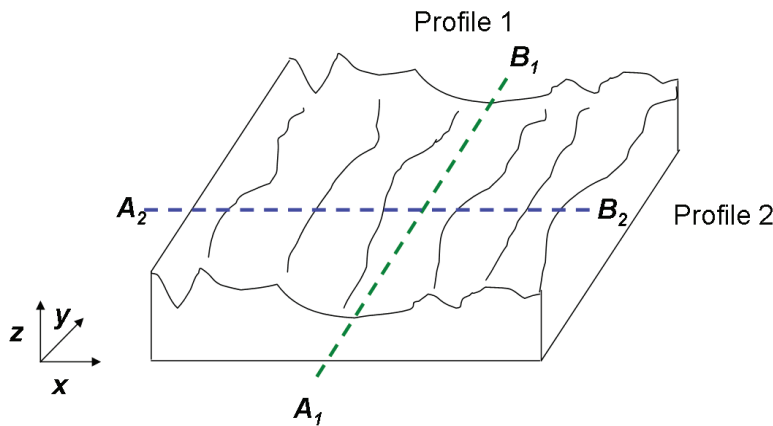


Fig. 17: Example of two different kinds of measuring surface roughness via a 2D profile on an anisotropic surface

The fabricated micropatterns, which will be presented in the experimental section in chapter 3, were topographically analysed by imaging via scanning electron microscopy (SEM) and chromatographic confocal profilometry. Both methods have proven useful to image the geometry of fabricated ceramic micropatterns and to draw further conclusions regarding the surface quality. Contrary to SEM imaging only, it thus was possible to characterize and measure surface parameters, such as roughness, via confocal profilometry in compliance with industrial standards.

Two standards were used to verify the surface parameters, to wit, DIN EN ISO 4287 and ISO 25178. The standard DIN EN ISO 4287 is applicable for single 2D-profile measurements. For example, a single line from point A to point B with a measurement length of 5.6 mm was used to calculate the average surface roughness “Ra” on a 2D profile. Thus, it turns out crucial to

determine how this profile is positioned on the surface between points A and B, e.g. for anisotropic surfaces. This standard was originally introduced for tactile scanning systems. Usually, a symbol is given in the measurement result or image in order to indicate the direction in which the 2D profile has been measured. DIN EN ISO 4287 was used for surface roughness measurements at the beginning of this thesis since it was considered to be state of the art at that time.

ISO 25178 was introduced in 2008 as a draft titled “Geometrical product specification (GPS) - surface texture: areal”. The main advantage of this draft standard ISO 25178 has been the possibility of a quantification of a full size area ($X \times Y$) measured via optical non-contact systems. For example, an area of $635 \times 477 \mu\text{m}^2$ - which corresponds to a single measurement with a 20-fold objective with a confocal profilometry system (Sensofar Plu2300®) from the experimental section in chapter 3 - can be used to calculate the average surface roughness S_a (S for surface) instead of a single 2D profile between two points (**Fig. 17**). In addition, volumetric parameters such as the “real” total surface area are easily measurable using this standard (ISO 25178, DIN EN ISO 4287, Beck, 2009).

2.2.2 Roughness analysis

As mentioned above, two different standards (DIN EN ISO 4287 and ISO 25178) were used in this thesis to measure surface characteristics of the fabricated ceramic surfaces. There are many different roughness parameters in use, but the R_a , R_p , R_v , R_z (2D profiles) and their equivalents S_a , S_p , S_v , S_z (3D area) are the most common. In this study, the four most important parameters were set to be arithmetic average roughness (R_a or S_a), maximum peak height (R_p or S_p), maximum valley depth (R_v or S_v), and the average maximum difference between the highest peak and the deepest valley (R_z and S_z).

On smooth, homogenous surfaces, both standards represent very similar values for measured roughness parameters such as R_a and S_a . Once again, the differences are mainly in the quantification of anisotropic surfaces. The definition of average roughness (R_a) and the average maximum difference between the highest peak and the deepest valley (R_z) is exemplarily given in **Fig. 18**. According to DIN EN ISO 4278, R_z is the average maximum difference between the highest peak and the deepest valley of five neighbouring profile sections on a measurement length l_c (**Fig. 18**). There is no direct mathematical correlation between R_a and R_z . In general, R_a is 1/3 to 1/7 of R_z . The surface parameters R_p , R_v , as well as S_p , S_v are not calculable but only readable from the measured surface profiles.

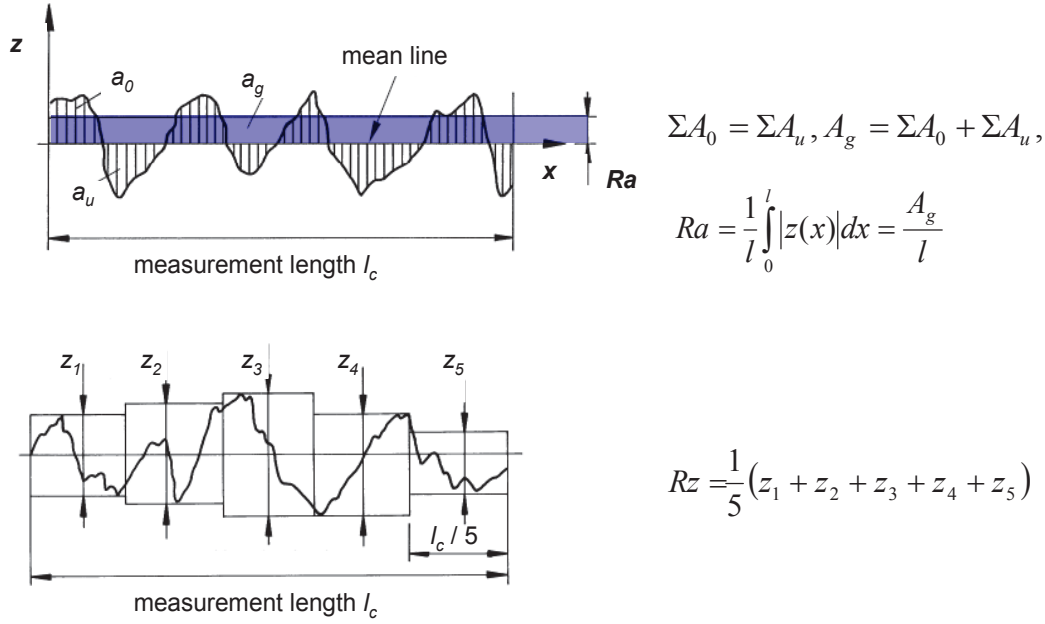


Fig. 18: Definition of the average roughness (Ra) and the average maximum difference between the highest peak and the deepest valley (Rz) according to DIN EN ISO 4278; taken from Wittel et al., 2009 (modified)

Using a modern optical profilometry system it is possible to take 2D-profile measurements according to DIN EN ISO 4287 as well as 3D-area scanning in order to compare collected data from new and old standards. Thanks to this feature it has been possible, in this thesis, to measure both 3D-area surface roughness Sa on homogenous ceramic surfaces as well as the average 2D-profile roughness in micropatterns with the same profilometry system. In future, the draft standard ISO 25178 will have to be transferred to the Deutsches Institut für Normung (DIN) so that it will become standard for industrial surface measurements in Germany in the long run.

Moreover, it is important to notice that the mentioned surface parameters inform about the roughness but do not give all available information about the topography of a surface. Typical topographies as fabricated in the experimental section in chapter 3 are shown in **Fig. 19**.

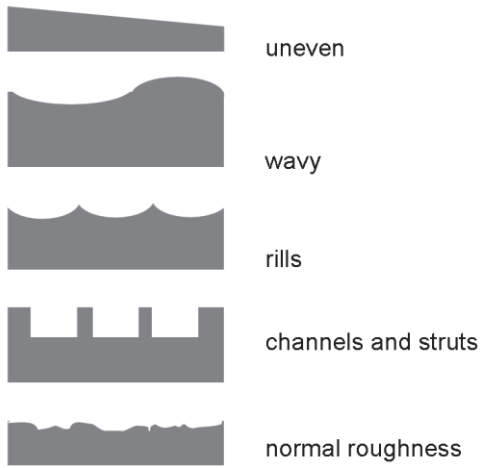


Fig. 19: Cross-sectional drawing of different topographies: uneven, wavy, rills, channels and struts, normal roughness

2.2.3 Measurement of micropattern geometry

The measurements of micropattern widths and depths were realised by means of the chromatographic confocal profilometry system Sensofar Plu 2300[®]. The measurements were not applicable according to any existing standard. Always three neighbouring micropatterns were taken for measurement and their average width or depth was then calculated. While the width was measured at the first position where the fabricated micropattern was detectable, the depth was measured at the deepest point of the fabricated pattern. The same procedure was undertaken for rectangular, V-shaped as well as U-shaped patterns (**Fig. 20**).

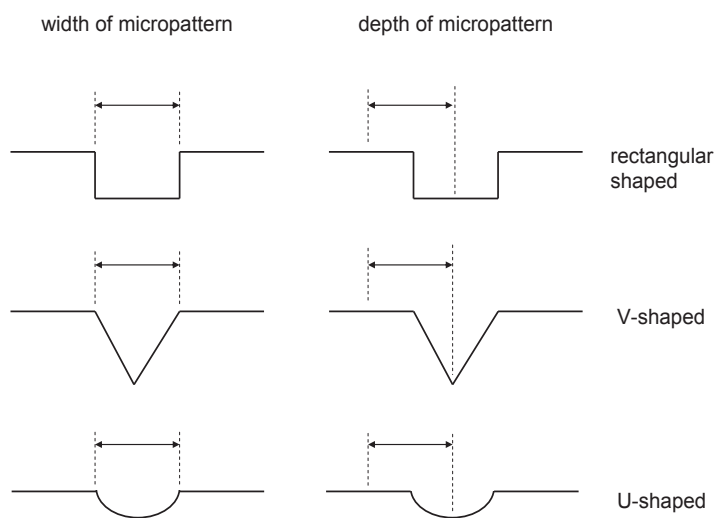


Fig. 20: Definition of micropattern depth and width for three different pattern shapes: rectangular patterns or channels, V-shaped and U-shaped, rill-like patterns

3. Experimental results of ceramic micropatterning

Before the results of the different micropatterning techniques can be reported in this section, a description of the production process of the ceramic suspensions will be given. The same mixed ceramic suspensions were used for Aerosol-Jet[®]-printing, microstamping and micromolding. The procedure was always the following: small amounts (“pinch”) of ceramic powder, e.g. hydroxyapatite, were poured slowly into deionised water (Synergy[®], Millipore) containing a specific amount of polyacrylic acid-based binder (Syntran[®] 8220, Interpolymers) and ammonia solution (25 %, Merck). The liquids were then stirred in a beaker glass while the ceramic powder was added carefully and slowly in order to prevent powder chunks. Syntran[®] and ammonia were taken as a binder-deflocculant system to generate a polymer network around the ceramic particles and for pH and surface charge adjustment. These adjustments generated equal particle surface charges, which in turn caused repulsion between the ceramic particles. This is called electrosterical stabilization in a deflocculated system. By contrast, a heteropolar coagulation of ceramic particles would be originated by an attraction due to opposite surface charges.

In addition, the used suspensions were treated with an ultrasonic horn (Sonifier 450, Branson) in order to destroy possible particle agglomerates (coagulated particles) and to homogenize the ceramic particles in the liquid media. Subsequently, the suspensions were used in the micropatterning processes. The use of this procedure should guarantee that the ceramic particles would be homogeneously dispersed within the liquid at the beginning of the patterning process, e.g. while filling the molds (as stated in the left beaker glass in **Fig. 21**). The particles sank down to the bottom of the beaker glass or mold in the course of time, due to the absence of a full, constant electrosterical stabilization of the particles in the liquid (**Fig. 21**).

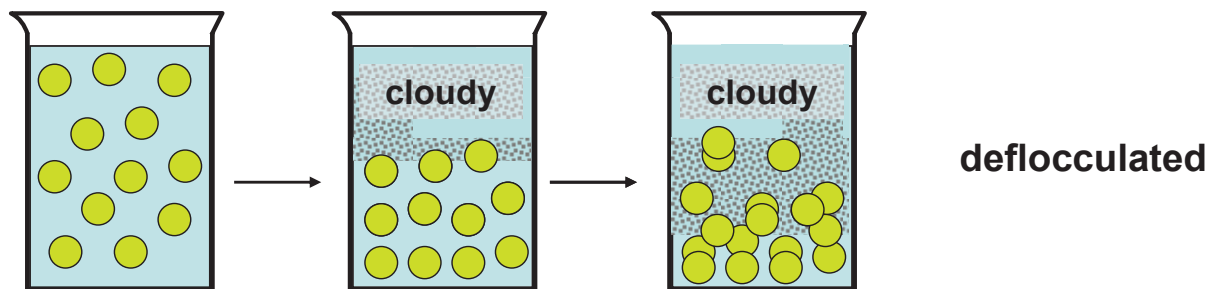


Fig. 21: Sedimentation behaviour of a deflocculated ceramic suspension; taken from Reed, 1995 (modified)

In a dilute coagulated system, all ceramic particles sink rapidly to the bottom of the beaker glass whereas the supernatant liquid above stays clear (i.e. no remaining particles there). In the case of the used ceramic suspensions, the particles sank slowly and the supernatant liquid above was somewhat opaque due to some remaining ceramic particles which had not sunk down to the beaker glass bottom yet.

The addition of the appropriate amount of binder as well as of ammonia for the pH adjustment was experimentally detected by zetapotential measurements. In general, pH ranges in which the zetapotential was most negatively charged (-mV) and where the working pH range was most far away from the isoelectric point (IEP, point where the zetapotential is zero) were chosen to reach highest possible electrosterical stabilization of the ceramic suspensions. Further details about zetapotential measurements are given in section 3.2 and **Fig. 28** below.

3.1 Microtransfer molding and modified micromolding of ceramic suspensions

The following results have been partially published in the “Proceedings of the 2008 International Manufacturing Science and Engineering Conference in Evanston, IL, USA, MSEC2008” by Marzellus grosse Holthaus and Kurosch Rezwan (University of Bremen, Advanced Ceramics) (Holthaus and Rezwan, 2008).

In early tests of the experimental studies of this thesis, a stamping technique was used to fabricate micropatterns. Commercially available calcium phosphate powder (hydroxyapatite, $(\text{Ca}_{10}(\text{PO}_4)_6(\text{OH})_2)$, Riedel-de Haën) with a density of 3.16 g/cm^3 was die-pressed uniaxially with 3.5 kN in order to generate plane cylindrical platelets with diameters of 10 mm each. The particle size median was $0.151 \text{ }\mu\text{m}$ (unimodal distribution, 0.235 std. dev.). The plungers were polished (grit: p2500) with the aim to reduce unintentional structures on the platelet surface. Before each die-pressing process, the plungers were covered with a thin layer of graphite powder (TIMCAL) so as to minimize adhesion between plungers and platelet. Afterwards, the platelets were sintered in a furnace (LHT 04/17, Nabertherm) at $1200 \text{ }^\circ\text{C}$ for two hours. Subsequently, the sintered platelets were micropatterned by using a stamping technique called microtransfer molding technique (μTM).

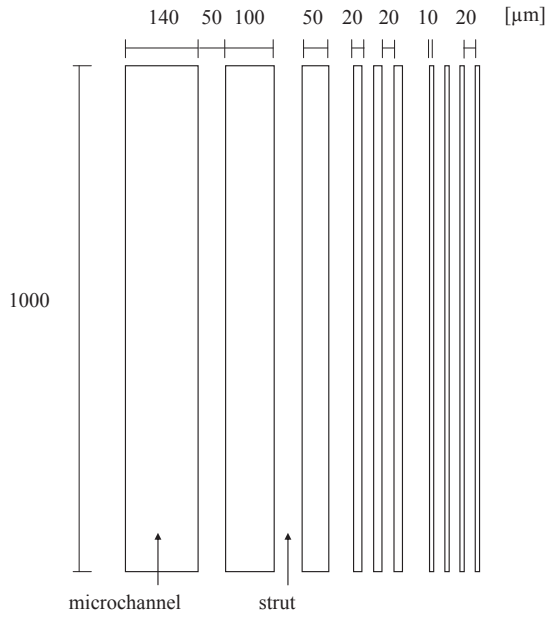


Fig. 22: Sketch of micropatterns for microtransfer molding

The μ -transfer molding of aqueous hydroxyapatite ceramic slurries was used to generate four formations of defined micropatterns with a length of 1000 μm each and a variation in width from 10 to 140 μm . The patterns were replicated via polydimethylsiloxane (PDMS) stamps from a pre-structured silicon wafer with a depth of 10 μm (**Fig. 22**).

After plasma treatment the generated negative micropatterns on the PDMS stamp were coated with a droplet of hydroxyapatite ceramic slurry (13.6 vol. %) and, subsequently, pressed gently on plane ceramic cylindrical samples. After drying at 4 $^{\circ}\text{C}$ for more than 24 hours, the PDMS stamps were removed. Hereafter, the micropatterned samples were sintered in an furnace (Nabertherm) at 1200 $^{\circ}\text{C}$ for two hours (**Fig. 23**).

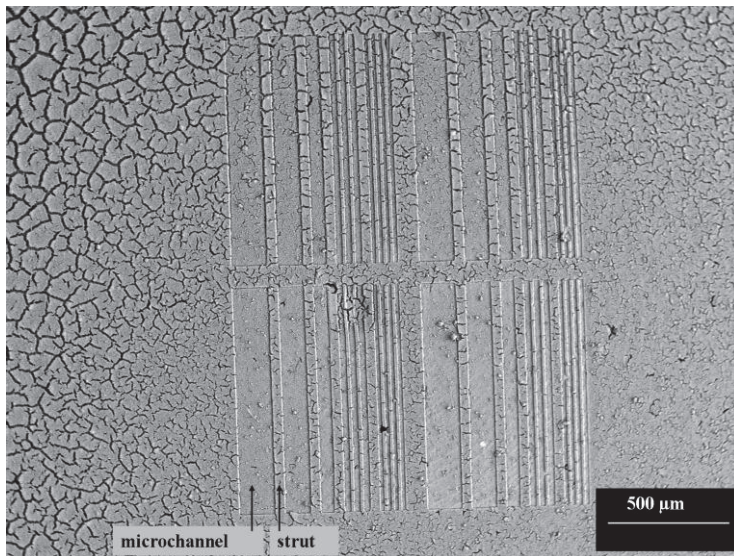


Fig. 23: Sintered ceramic micropatterns. Structures were generated by microtransfer molding via PDMS. Cracks are visible on the surface

The hydroxyapatite material which was stamped onto the surface by microtransfer molding via PDMS stamps looked craggy and fissured after sintering but the microchannels were defined and had clearly visible edges (**Fig. 23**). Fine cracks occurred partially during or after the drying process in which the PDMS stamps had been pressed on the sample surface. Bigger cracks were noticed after the sintering process. The PDMS stamps had a height of 10 micron each. After sintering, the height of the stamped microstructures was about six to eight micron (**Fig. 24**). A XRD analysis of transfer molded and sintered hydroxyapatite samples showed no changes in the crystal structure, thus no traces of β -tri-calcium phosphate (β -TCP) were to be seen on the surface.

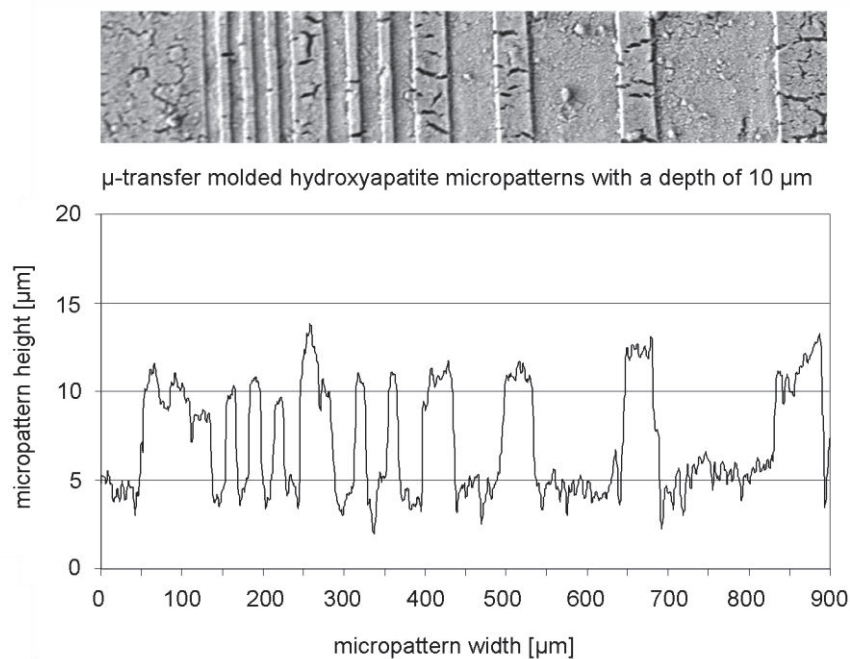


Fig. 24: SEM image (top view) and 2D profile of stamped hydroxyapatite microchannels after sintering

The stamped surface looked very craggy. Fine cracks occurred partially during or after the drying process in which the PDMS stamps were pressed on the sample surface. This was probably a result of the rapid drying. Bigger cracks were noticed after the sintering process, probably due to divergent material shrinkage ratios of pressed ceramic platelet and stamped ceramic material. The PDMS stamps had a height of 10 μm each. After sintering, the height of the stamped microstructures was reduced to about 6 to 8 μm. This loss of height, too, was caused by material shrinkage due to the sintering process.

In an initial testing, the defined stamping of protein solutions was successfully applied by using pre-structured PDMS stamps, an ink pad, and a stamping mechanism for the local deposition of ink without blurring (**Fig. 26**).

Within these first tests it could be demonstrated that microtransfer molding via PDMS stamps is suitable to fabricate calcium phosphate micropatterns and to generate local biofunctionalisation on ceramic surfaces. However, the fabricated patterns still had a lot of cracks. Basic preliminary results with microtransfer molded patterns and osteoblast-like osteosarcoma cells (MG-63) were published in Holthaus and Rezwan, 2008. Thanks to these promising results, molding via PDMS stamps has been the focus of further studies, too, in which the “modified micromolding technique” (m- μ M) was investigated.

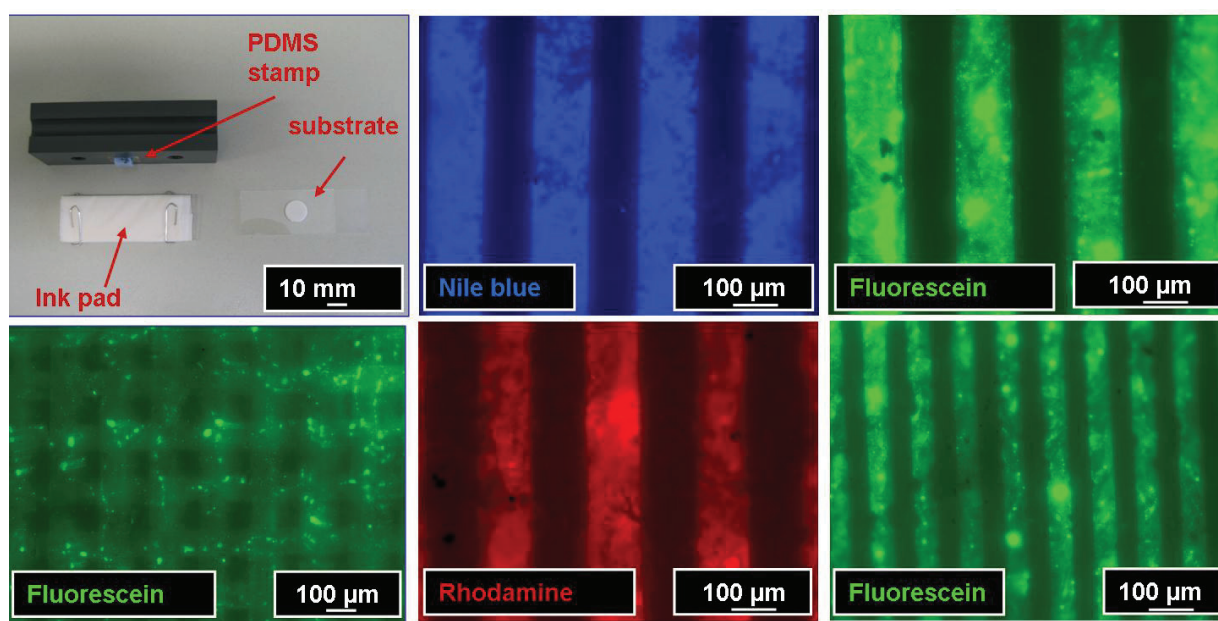


Fig. 25: Upper left: micropatterned PDMS stamp, ink pad with protein solution, and ceramic substrate. The other parts show fluorescent images of stamped protein suspensions on non-patterned alumina surface. Stamping was realised by use of the μ TM technique.

3.1.1 Versatile crack-free ceramic micropatterns made by a modified molding technique

The following results have been published in part in the “Journal of the American Ceramic Society”, in 2010, by Marzellus grosse Holthaus^a, Miron Kropp^b, Laura Treccani^a, Walter Lang^b, and Kurosch Rezwan^a (^aUniversity of Bremen, Advanced Ceramics, ^bUniversity of Bremen, Institute for Microsensors, actuators and systems (IMSAS)) (Holthaus et al., 2010).

Abstract

Crack-free ceramic micropatterns made of oxidic ceramic powders, e.g. alumina, titania, zirconia, and non-oxidic calcium phosphate ceramic powders were fabricated by a novel, simple, and low-cost modified micromolding technique via PDMS stamps (m- μ M). By means of this m- μ M technique it is possible to fabricate monolithic ceramic bodies with a micropatterned surface with very high accuracy on surface detail. Our thus produced micropatterns can take on various geometric shapes, e.g. cylinders, holes, channels and struts, with measurements ranging from 8 to 140 μ m in diameter or widths, and from 8 to 30 μ m in depth or height. In our experiment, these oxidic and non-oxidic ceramic micropatterns could be removed from the molds and dried without any cracks. Even after sintering, these micropatterned samples showed no cracks or fissures. Therefore, this technique has a very high potential for fully automated up-scale fabrication of micropatterned ceramic surfaces.

Introduction

Micropatterned surfaces are of great interest in a variety of research fields and are used in high-end technical applications such as electrical sensor devices, biochemical fluidic system reactors, abrasion-resistant antibacterial surfaces as well as in biological and medical applications (Hu et al., 1999; Zhang and Yu et al., 2006; Kim et al., 2008; Treccani et al., 2009; Wang et al., 2009). The advantages of ceramics as compared to metals or polymers consist in its chemical resistance and inertness, the high hardness, and the temperature resistance (Lemons, 1996; Munz, 1999). However, especially in the micro range advanced ceramics are often difficult to process without cracks, showing at the same time a high accuracy on surface details. Thanks to our novel, simple and low-cost modified micromolding technique via PDMS stamps (m- μ M) we are now able to obtain crack-free ceramic micropatterns made of oxidic ceramic powders, such as alumina, titania, zirconia, and non-oxidic calcium phosphate ceramic powders (**Fig. 26**).

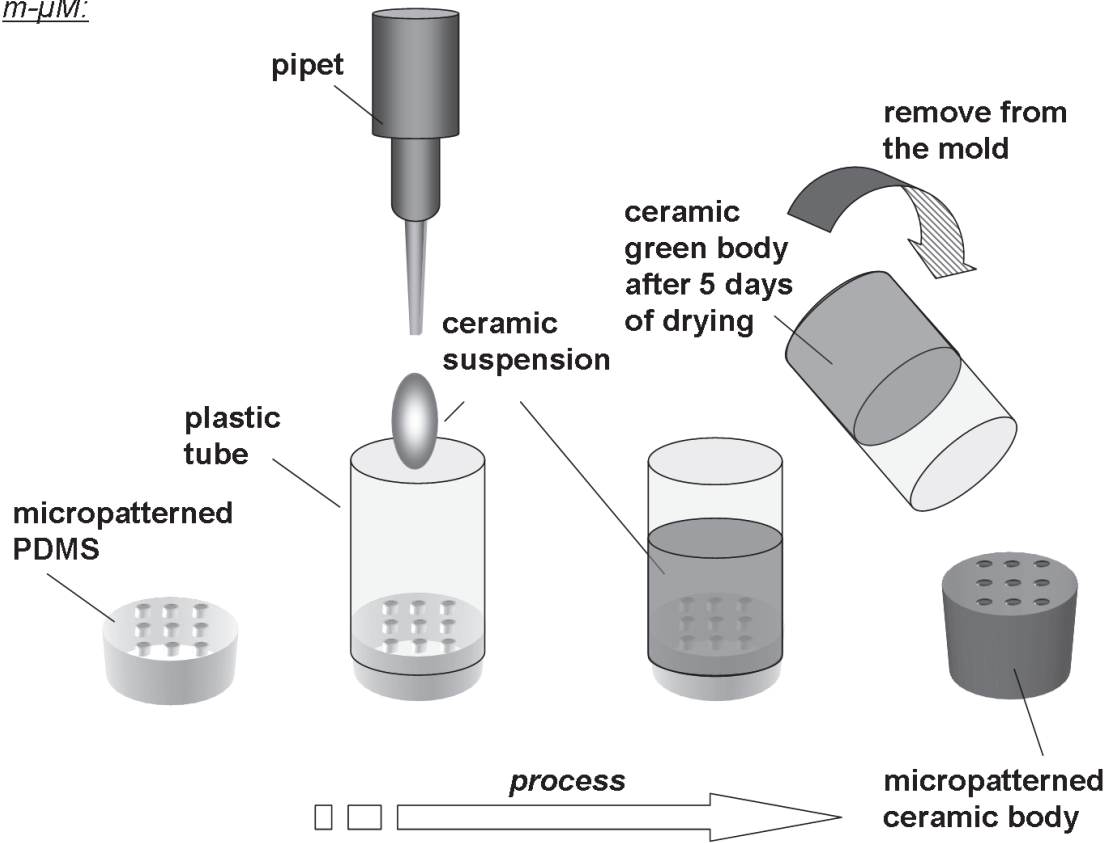
m-μM:

Fig. 26: Fabrication process of ceramic micropatterns. After sealing the micropatterned PDMS stamp with a plastic tube, the ceramic suspension is filled into this plastic tube in order to replicate the surface structure. The micropatterned ceramic bodies can be removed from the mold after five days of drying.

By means of this *m-μM* technique it is now possible to fabricate monolithic ceramic bodies with a micropatterned surface with very high accuracy on surface detail (**Fig. 27**) instead of thin film micropatterns which can be fabricated with well-known techniques such as microtransfer molding (μTM) and capillary force lithography (CFL), conventional micromolding (μM) or replica molding (REM), microcontact printing (μCP), micropatterning via slip pressing, and especially micromolding in capillaries (MIMIC) (Lange, 1989; Xia et al., 1998; Hu et al., 1999; Bauer et al., 1999; Tian et al., 2002; Heule et al., 2004; Khan et al., 2009; Suh et al., 2009). In contrast to the thin film techniques, it is thus feasible to fabricate large-area micropatterned three-dimensional solid ceramic devices. In addition, the shape, size and thickness of the molded ceramic bodies are customizable to several requirements (**Fig. 27**) which emphasises the versatility for large-area micropatterning of this technique. Moreover, this method has a high potential to become fully automated.

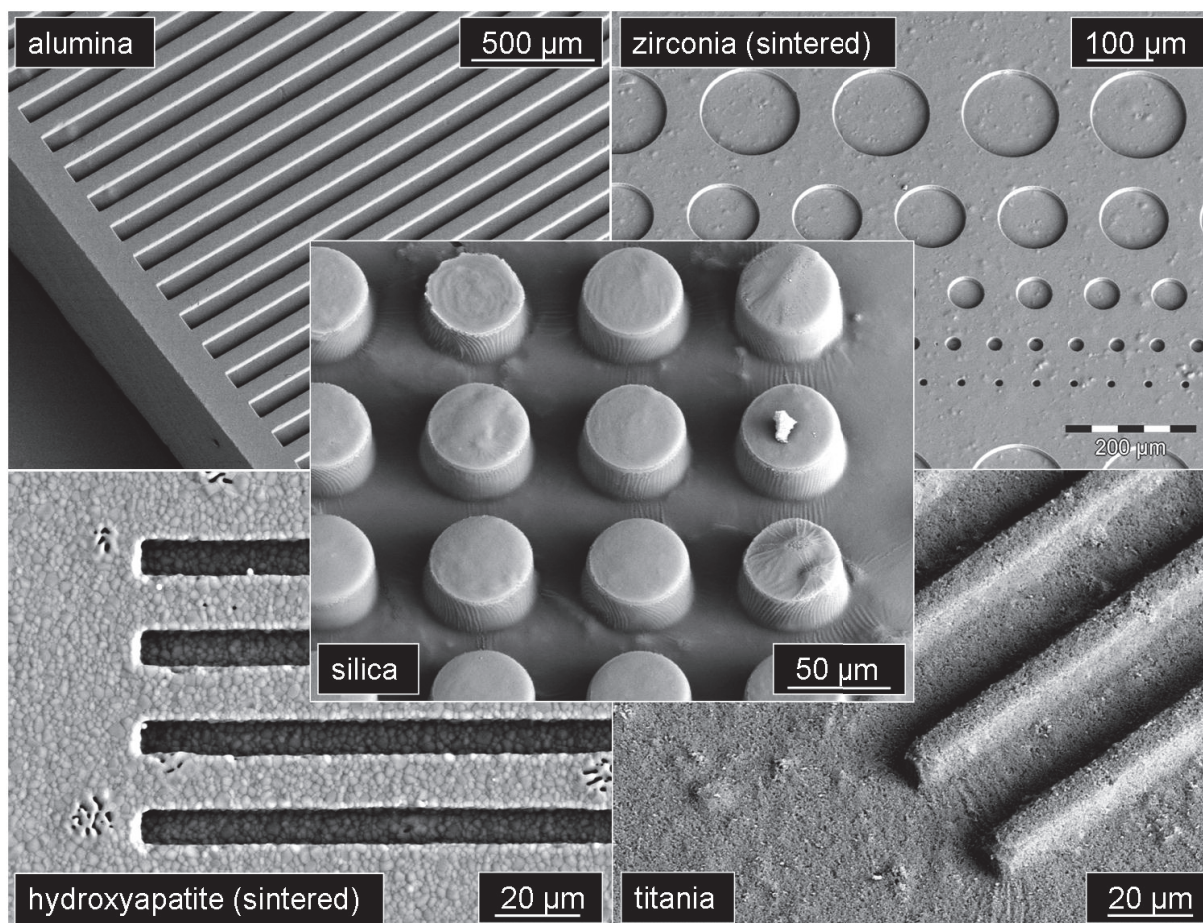


Fig. 27: SEM images of various fabricated ceramic micropatterns, e.g. channels, holes, struts or cylinders. These geometries were applied to different ceramic materials such as alumina, zirconia, hydroxyapatite, silica or titania.

Experimental Procedure

Seven commercially available ceramic powders were used to mix aqueous ceramic suspensions for filling the molds. Five of these powders, namely, hydroxyapatite (04238, Lot: 8345A, Sigma-Aldrich), zirconia (NZ-911, Lot: Z307317P, ABSCO), alumina (TM-DAR, Lot: 7553, Taimei), titania (PT401L, Lot: 0/08, Ishihara) and silica (SiO₂PO15-01, Lot: 090320-01, F.O. Center), had a particle size of approximately 150 nm each. Additionally, two zirconia powders with particle sizes of approximately 26 nm (TZ-3Y-E, Tosoh) and 360 nm (TZ-3YS-E, Lot: S-307752P, Tosoh), each respectively, were used. The specific surface area (BET) of the used powders was measured with a Gemini 2375 (Micromeritics), and the zeta potentials in suspensions with a solid content of 2 vol.% were measured with a DT1200 (Dispersant Technologies).

Preparing the ceramic suspensions: Zetapotential measurements (DT1200, Dispersion Tech.) were carried out in order to characterise the behaviour of the ceramic particles in aqueous surrounding (1 vol%) before preparing the suspensions for the molding processes. Further, suspensions with binder (12 mg /g ceramic) as well as without binder were applied. The binder polyacrylic acid (Syntran[®] 8220, Interpolymer) with a molecular weight of 4000 g/mol was used because it had already worked successfully as a binding polymer in preliminary tests. Thereby, the zetapotentials of hydroxyapatite suspensions with solid contents of 2 vol.% and various additions of binder ranging from 0 to 30 mg Syntran[®]/g ceramic powder were measured. Results showed a lowest zetapotential of -17 mV under addition of 12 mg Syntran[®]/g ceramic powder as compared to without adding a binder with a zetapotential of -12 mV. The addition of 30 mg Syntran[®]/g ceramic powder resulted in a zetapotential of -14 mV. In correlation with the preliminary tests, it was found that the isoelectric point (IEP, the pH value where the charge is zero) shifted to a more acidic pH for each material after addition of Syntran[®] due to the RCOO⁻ groups of the polyacrylic acid. Furthermore, the results showed that all suspensions had negative charges in the alkaline range at pH 10-11 without addition of Syntran[®]. After adding Syntran[®], the charges were even more negative in this alkaline range at pH 10-11 (**Fig. 28**).

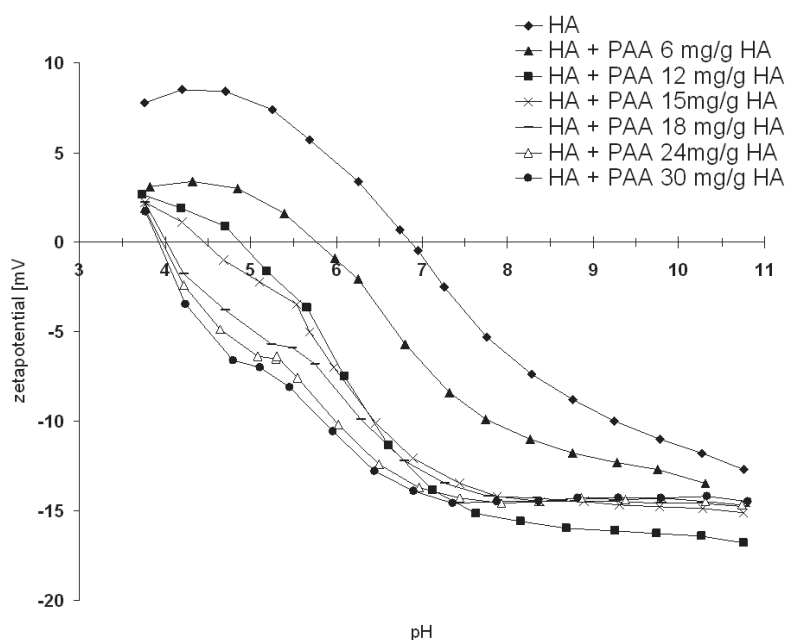


Fig. 28: Diagram shows exemplarily the zetapotentials (pH 3 to 11) of hydroxyapatite suspensions with solid contents of 2 vol.% and various additions of polyacrylic acid based binder Syntran[®] ranging from 0 to 30 mg Syntran[®]/g ceramic powder. The lowest zetapotential (-17 mV) was achieved by adding 12 mg Syntran[®]/g ceramic powder as compared to not adding PAA (-12 mV) and an addition of 30 mg Syntran[®]/g ceramic powder (-14 mV).

Each powder was stirred (RW20, IKA) separately into double deionised water (Synergy, Millipore) in order to obtain suspensions of 10, 15, and 20 vol.% solid loading. Dispersant polyacrylic acid (12 mg/g ceramic powder) was added to all suspensions. Each suspension was adjusted to pH 10-11 by adding ammonium solution (25 vol.%) to achieve an electrosterical stability and prevent an agglomeration of the particles. The ceramic suspensions were then treated with an ultrasonic horn (Sonifier 450, Branson) for three minutes to destroy potential agglomerates after stirring.

Fabrication of non-structured ceramic solid bodies by molding: To find out the best solid contents parameters for the fabrication of crack-free demolded ceramic bodies, cylindrical molds with a diameter of 6.6 mm (96-well microtiter plate, Nunc) were filled with 100, 200, or 300 μ L suspension with solid contents of 10, 15, or 20 vol.%. Due to gravity the particles settled at the bottom of the mold and got densified while the water in the supernatant was evaporating slowly throughout the drying period. After five days at 21-22 °C with 30-43 % relative air humidity, the ceramic bodies were completely dry and got removed from their molds. After demolding, the presence of cracks due to shrinkage was checked visually by means of a microscope (Axio Imager M.1, ZEISS).

Fabrication of micropatterned ceramic solid bodies by micromolding via PDMS stamps (m- μ M): Cylindrically shaped molds with a diameter of 8 mm and micropatterning depths of 10, 20, and 30 μ m were generated via polydimethylsiloxane (PDMS) stamps (Sylgard[®] 184, Dow Corning) from a structured silicon wafer. Before the molding process, the PDMS stamps were hydrophilised in oxygen plasma (Femto, Diener Electronic) by using low pressure plasma with 50 watts generator power for two minutes and an operating pressure of 0.3 mbar. After that plasma treatment, the generated molds were sealed with cylindrical polyethylene tubes. Each mold was filled with 1 ml of ceramic suspension for casting the micropatterns on the PDMS stamps (Fig. 1). The particles settled at the bottom of the micropatterned mold due to gravity and there got densified, while water was evaporating from the supernatant. The samples were dried for five days at 21-22 °C with 30-43 % relative air humidity. Afterwards, the micropatterned samples were removed from their molds and densified in a furnace. With 20 kV the micropatterns were visualised by SEM (Camscan Series 2, Cambridge Instruments), and 2D as well as 3D measurements were made by a 20-fold objective with a profilometer (Pl μ 2300, Sensofar) to characterise the quality and shrinkage caused by the sintering process.

Results and Discussion

By applying this technique we achieved a maximum success rate of 88% of crack-free dried samples for hydroxyapatite with a solid contents of 10 vol%, 25% for zirconia (26 nm) with solid contents of 15 vol%, 100 % for zirconia (150 nm) with solid contents of 10, 15, and 20 vol%, 100 % for zirconia (360 nm) with solid contents of 10, 15, and 20 vol%, 100 % for alumina with solid contents of 15 and 20 vol%, 71% for titania with a solid content of 15 vol.%, and 100 % for silica with a solid content of 15 vol.% (**Fig. 29**). A correlation between the particle sizes and the achieved success rates for crack-free drying cannot be found by comparing the results from three different zirconia powders with particle sizes of 26, 150, and 360 nm, respectively.



Fig. 29: Photograph of molded ceramic bodies made of alumina, zirconia and hydroxyapatite, with various diameters and thicknesses demonstrating the possibility of large surface area micropatterning.

However, a correlation between the surface area (BET), ranging from 6.8 to 68.3 m²/g, and the success rates for crack-free drying seems to be plausible (**supporting data in the appendix**). We assume that a binder concentration of 12 mg/g ceramic is not high enough for hydroxyapatite with a specific surface area of 68.3 m²/g, silica with a specific surface area of 22.6 m²/g, zirconia (particles 26 nm) with a specific surface area of 15.1 m²/g, titania with a specific surface area of 13.1 m²/g, and alumina with a specific surface area of 12.8 m²/g to saturate the whole particle surface with binder molecules in order to avoid cracking during the drying process. These materials showed success rates lower than 100 % after drying. In contrast, success rates of 100 % were achieved with zirconia powders with particle sizes of

150 and 360 nm, which exhibited the smallest surface areas, i.e. $9.7 \text{ m}^2/\text{g}$ and $6.8 \text{ m}^2/\text{g}$, respectively. These materials showed success rates of 100 %. We therefore assume that these particles have been fully coated by binder molecules under addition of 12 mg/g which avoided the cracking. An overview of some exemplary results and particle and suspension characteristics, such as zeta potential measurements, particle sizes, BET surface areas, the Hamaker constants as well as achieved success rates for crack-free drying and demolding, are given in the appendix to this thesis. To check a difference in the packing density further density measurements of the non-sintered zirconia powders (26, 150, and 360 nm) were taken. In doing so, ten measurements per sample were made with helium pycnometry (Accu Pyc 1330, Micromeritics). The density measurements of the non-sintered zirconia powder with particles of 26 nm showed an average density of $6.09 \text{ g/cm}^3 \pm 0.04$. For non-sintered zirconia powder with particles of 150 nm a density of $5.87 \text{ g/cm}^3 \pm 0.03$ was measured, and for zirconia powder with particles of 360 nm a density of $5.98 \text{ g/cm}^3 \pm 0.04$ was measured. Thereby the calculation of the total porosity of the molded zirconia samples which were comparably made with 15 vol.% in 200 μL fillings and 12 mg binder/g ceramic, resulted in 62.38 % (26 nm), 57.19 % (150 nm), and 58.45 % (360 nm). The highest porosity of 62.38 % gave rise to the assumption that the particles agglomerated stronger in the suspension before micromolding, which resulted in a lower final packaging density. The lower zeta potential of -12 mV as compared to zirconia with 150 nm particles (-18 mV) and zirconia with 360 nm particles (-25 mV) confirms the lower electrosterical stability of the suspension at the working pH of 9 to 10.

Due to very high adhesion between the dried samples and the sidewalls of the cylindrical polyethylene plastic tube (not the micropatterned PDMS), it was not possible to remove any crack-free sample made of titania from the molds without destroying the sample. During the trial of demolding the edges of the titania samples, the sample bodies were disconnected from each other. These disconnections were parallel to the sidewalls of the cylindrical plastic molds and thus circular throughout the entire sample. We assume that this effect occurred because of non-visible damages before demolding, e.g. by defects or fine cracks inside the sample bodies. During the demolding process, the titania samples broke circularly and titania material of the samples edges was partially sticking to the sidewalls of the plastic molds after demolding. The entire ceramic body itself, however, did not break. This assumption was affirmed by the presence of circular cracks on clearly visible cracked titania samples after the drying process. We therefore suppose that this unexpected effect can be minimised or completely avoided by deploying anti-sticking agents such as PTFE sprays, as these minimise

the adhesion between PE mold and titania material, or else by the use of cylindrical molds of PTFE. A possible reason for this unexpected sticking effect could be a not optimally chosen concentration of binder, which leads to higher forces between plastic and titania compared to the inner forces in the titania sample.

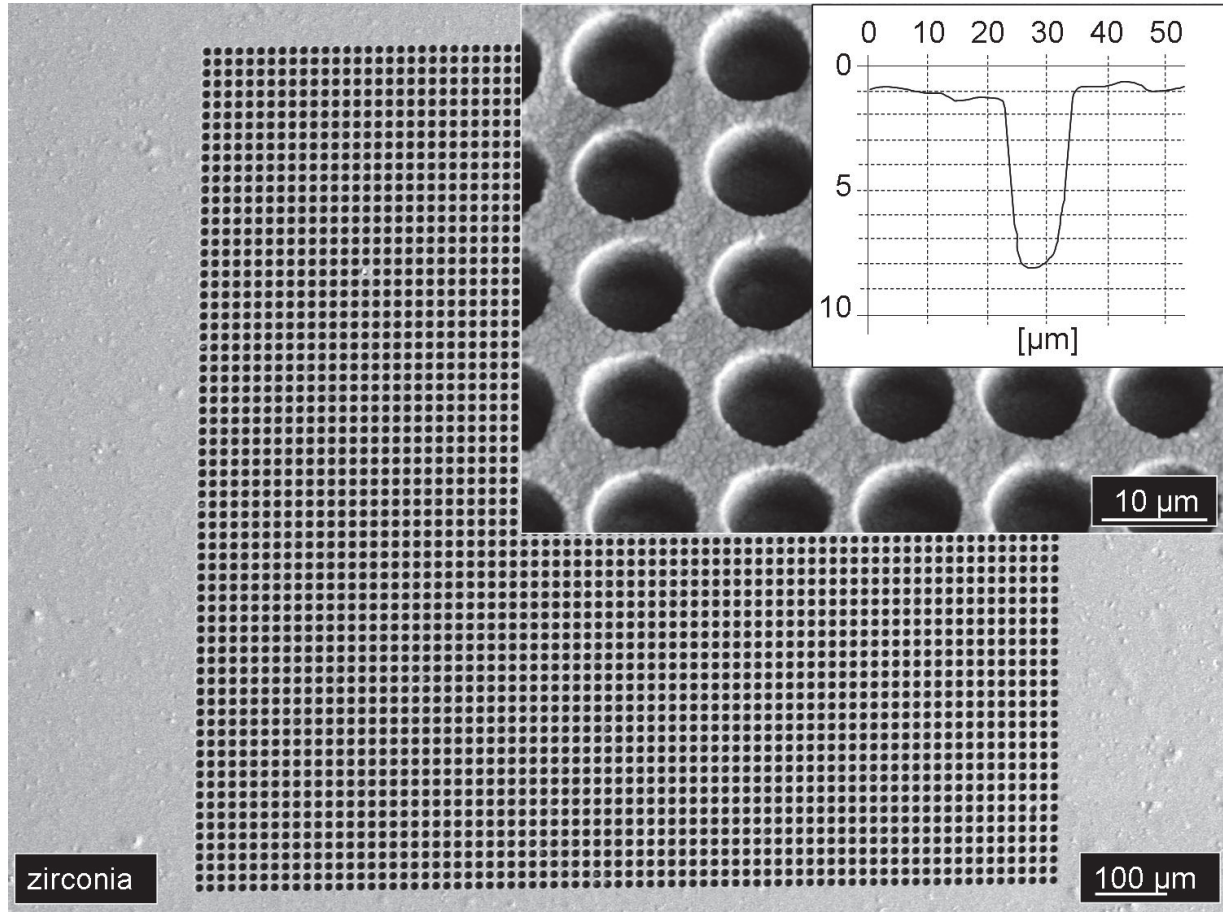


Fig. 30: SEM image of a sintered micropatterned zirconia surface of approx. 1 mm^2 with over 6500 cylindrical holes. These holes have a diameter of about 10 μm and a depth of 8 μm . The graph inset shows a 2d profile measurement of a single cylinder.

The diameters and the heights of the samples were measured with a micrometer gauge before sintering in order to evaluate the shrinkage ratio. Hydroxyapatite samples were densified at 1200 °C , zirconia samples at 1350 °C , alumina samples at 1500 °C , silica samples at 1000 °C , and titania samples at 1250 °C , each for two hours with a heating rate of 50 °K/hour and a cooling rate of 100 °K/hour . Results showed shrinkages of 49 % in volume for hydroxyapatite, 55 % in volume for zirconia (26 nm), 53 % in volume for zirconia (360 nm), and 40 % in volume for silica. The zirconia powder (150 nm) could not be measured after sintering, because a monoclinic non-yttria-stabilised zirconia powder was used which was not sinterable due to crystal phase changes.

Oxidic and non-oxidic ceramic micropatterns, e.g. holes and cylinders with diameters of 10 μm to 140 μm and depths or heights of 10 μm and 30 μm could be removed from the molds and dried without the emergence of cracks. Even after sintering, these micropatterned samples showed no cracks and fissures (**Fig. 27** and **Fig. 30**). It was also possible to fabricate areas of 1 mm^2 with more than 6500 micropatterns, with diameters of 10 μm and depths of about 8 μm , each without cracks and very high accuracy on surface details (**Fig. 30**). The excellent quality is, on the one hand, due to the chosen binder polyacrylic acid, on the other hand because of the geometry of the molds effecting a favourable unidirectional and slow drying process (**Fig. 31**).

m- μM :

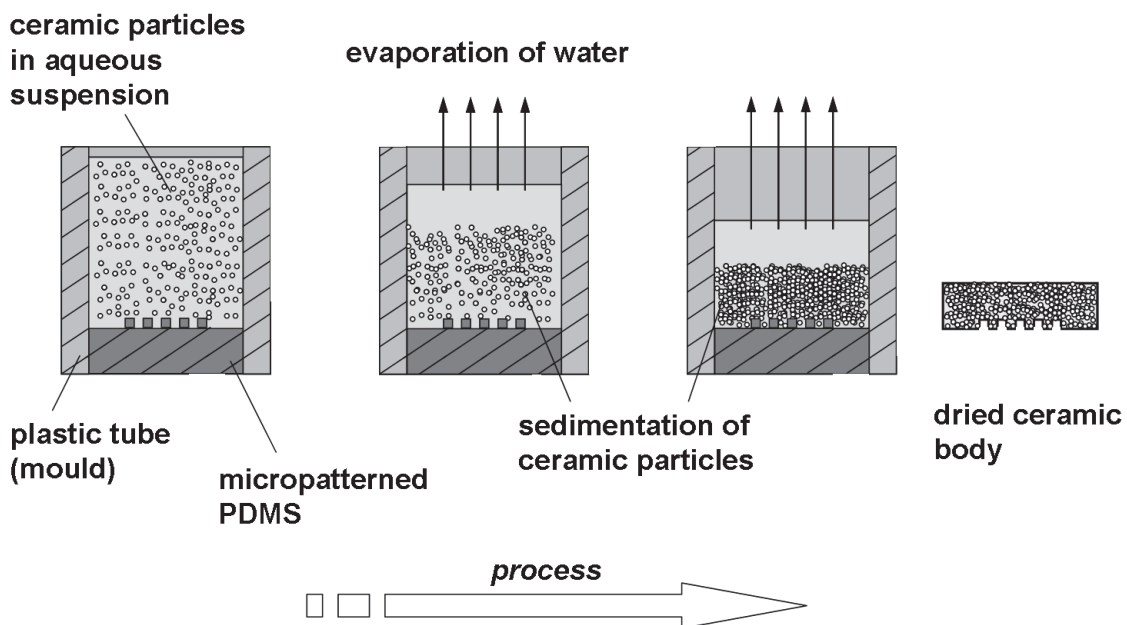


Fig. 31: Drying process of ceramic micropatterns made by modified micromolding (m- μM): at the beginning, the ceramic particles are homogenously dispersed in the aqueous suspension. Due to gravity the particles sink down to the micropatterned bottom of the mold (PDMS stamp) while water is continuously evaporating. The one-sided evaporation of water is completed within five days and the dried micropatterned ceramic body can be removed from the mold.

Samples which did not dry without cracks showed two different kinds of cracking. Hydroxyapatite, alumina, silica and zirconia samples showed a cracking throughout the whole structure as well as the entire sample body. The cracking did not only occur near the micropattern edges or along the micropattern direction, where the mechanical stresses seem to be most concentrated during the drying process (**Fig. 32**).

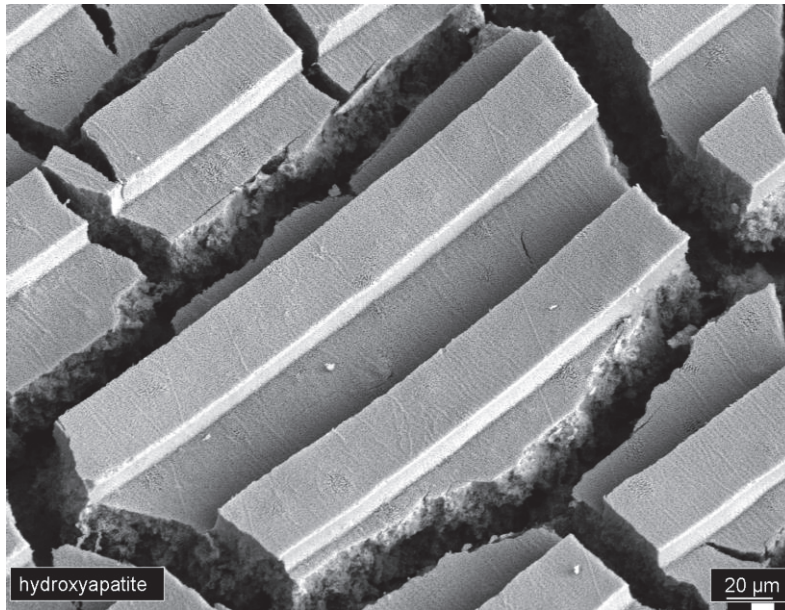


Fig. 32: SEM micrograph of a micropatterned non-sintered hydroxyapatite surface which cracked during the drying process. The micropatterns were fabricated with a suspension with a solid content of 20 vol%. On samples made of alumina, hydroxyapatite, silica and zirconia, cracks emerged throughout the entire sample and in all micropatterns.

Cracks were even visible in the centre of the cylindrical sample. In contrast, cracking on titania samples occurred predominantly circularly, throughout the entire sample body (**Fig. 33**). Because the BET surface area measurements suggested a higher success rate for higher binder concentrations (> 12 mg/g ceramic), an additional test with 24 cylindrical samples of titania suspension (10 vol%, 200 μ L fillings) and the addition of 30 mg Syntran[®]/ g ceramic was conducted in order to test the influence of binder concentration on crack occurrence.

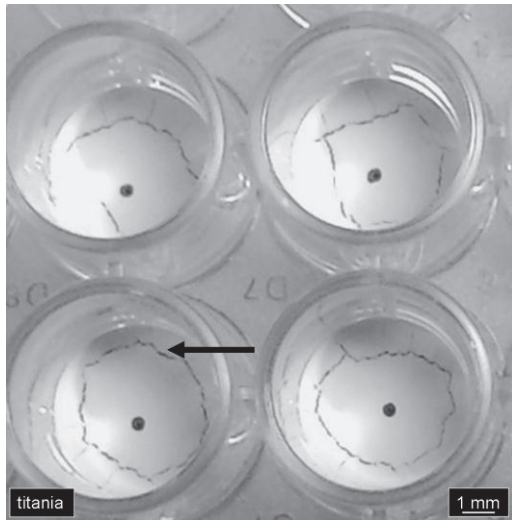


Fig. 33: Top view of four non-sintered titania samples (in their plastic molds) which cracked during the drying process. The samples were fabricated using a suspension with a solid content of 10 vol.% under addition of 12 mg Syntran[®]/g ceramic in 200 μ L fillings. The disconnection between the sample bodies and the sample edges were parallel to the sidewalls of the cylindrical plastic molds, thus circular throughout the entire sample (black arrow bar). The dark grey dots in the centre of the samples were made with a permanent marker.

Results showed a success rate for crack-free drying of 0%. All cracks occurred circular-wise throughout the entire sample. Such a high concentration of binder does not increase the success rate for crack-free drying of titania. This does not mean, however, that there are no concentrations between 12 mg and 30 mg/g ceramic which minimise crack occurrence, but 30 mg is probably too much. Higher binder contents would lead to a higher porosity as well after sintering in the sample body, because more binder would be burned out during the sintering process.

Conclusions

With this simple and low-cost modified micromolding technique (m- μ M) we are now able to produce micropatterns featuring various geometries, e.g. cylinders, holes, channels and struts, with diameters ranging from 8 μ m to 140 μ m and widths from 8 μ m to 30 μ m in depth or height as well as with very high accuracy on surface details. The molding process resulted in an outcome of 25% to 100% dried samples free from cracks, whereas the mean shrinkage ratio from the dried ceramic body to the sintered ceramic body ranged from 40% to 55% in volume, depending on the material. Due to shrinkage it is even possible to fabricate ceramic microgeometries smaller than 10 μ m without any cracks or fissures. Likewise, no cracks occurred in the oxidic or in the non-oxidic ceramic samples during the sintering process.

A relation between the used binder concentrations and their impact on the achieved success rates for crack-free drying could be shown in correlation with the measured BET surface area of the ceramic powders and their calculated porosity of the molded sample bodies. In addition, this method has a high potential to get fully automated for up-scale fabrication of micropatterned ceramic surfaces.

Further investigations using m- μ M have confirmed the versatility and potential of this molding technique. Ceramic micropatterned thin films with freestanding, opened patterns have been successfully fabricated in first experiments. The thus fabricated thin films featured holes with diameters of a minimum of 86 micron and a thickness of 156 μ m, but the molded patterns could feature various geometries, e.g. channels or honeycombs (**Fig. 34**).

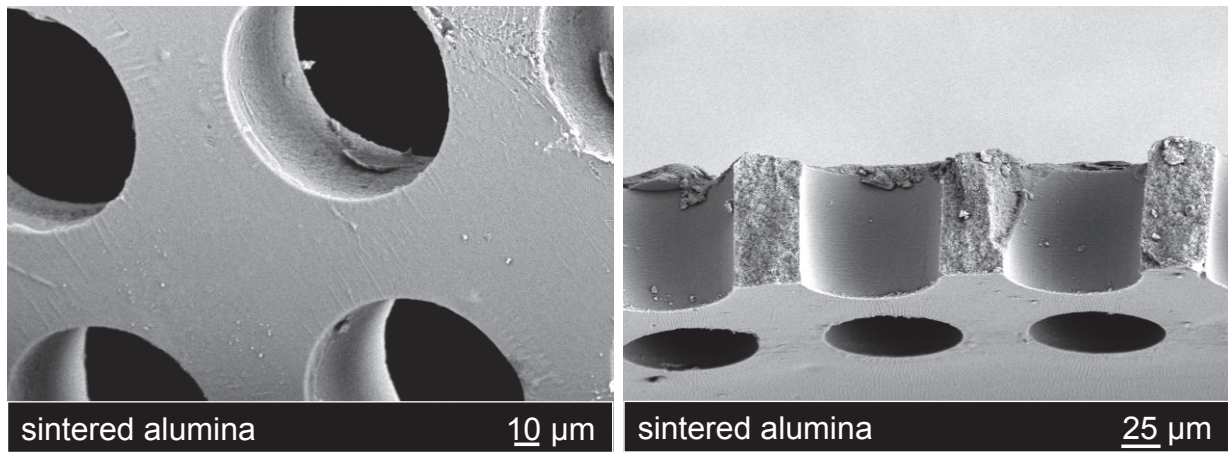


Fig. 34: SEM micrographs of a sintered ceramic thin film (Al_2O_3) with open microholes. This ceramic film has a thickness of 125 μ m and microholes with a diameter of 88 μ m. The micropatterns are well defined with high accuracy and vertical sidewalls (left). Cross section of the fragment (right).

3.1.2 Orientation of osteoblasts on hydroxyapatite-based microchannels

The following results were partially submitted to the journal “Acta Biomaterialia” in 2011 by Marzellus grosse Holthaus, Julia Stolle, Laura Treccani, and Kuroschi Rezwan.

Abstract

The effect of calcium phosphate-based microchannels on the growth and orientation of human osteoblast cells is to be investigated in this study, as substrates hydroxyapatite-based microchannels with high contouring accuracy were fabricated by a novel micro molding technique. Microchannels obtained through this method featured widths ranging from $16.0 \pm$

0.7 μm to $76.6 \pm 1.4 \mu\text{m}$ and to depths from $7.9 \pm 0.8 \mu\text{m}$ to $15.5 \pm 1.3 \mu\text{m}$. Surface and contour characterisation was carried out using X-ray diffraction analysis, SEM imaging and 3D-confocal profilometry. Cell proliferation and alignment on microchannels with different widths were determined after one and after three days, respectively, through fluorescence microscopic imaging and statistically analysed on the basis of Tukey's multiple comparison test. On days 1 and 3 we found for microchannels with 16 and 30 microns, that 70% to 80% of the osteoblasts oriented within an angular range of 0 to 15° relative to the microchannel direction. Interestingly, only 20% of the cells grew inside the microchannels for channel widths of 16 and 30 microns. Substrates with 45, 65, and 76 micron channel widths allowed around 40% of the cells to grow inside. The depth of the microchannel showed hardly any significant impact. All micropatterned surfaces provoked a good cell attachment as flat and spread cell morphologies with lamellipodiae and filopodiae could be already observed after one day. The effect of the microchannels on osteoblast viability was determined with the colorimetric WST-1 assay and the presence of collagen type I assessed by fluorescence analysis. The cell proliferation obtained through WST-1 assay differed insignificantly for all micropatterned samples of varying widths and depths. The assessment of collagen type I yielded the same amounts for all micropatterned samples after 1, 3, and 7 days.

In summary, we can say that the microchannel width of HA-based patterns has a distinct effect on the directed growth of human osteoblast cells, allowing novel design strategies for surfaces of, for instance, dental implants.

Introduction

Substrate surfaces featuring well-defined micropatterns are of great interest and relevance for biosensor applications (Hyun Jong et al., 2010; Lee et al., 2008; Valsesia et al., 2005), fluidic systems (Dusseiller et al., 2005; Velve-Casquillas et al., 2010), antibacterial surfaces (Treccani et al., 2009) as well as for medical implants such as neural cell stimulating implant surfaces (Hsu et al., 2009; Sommani et al., 2007; Turcu et al., 2003) and bone implants (Bowers et al., 1993; Mangano et al., 2010). Ceramic materials are suitable for many of these applications and well established as implant materials nowadays. The non-oxide ceramic hydroxyapatite (HA) is bioactive and, due to its relative low hardness, not used as a load-bearing implant material. However, thanks to its similarity to human bone apatite, HA is used in medical implants such as bone grafting materials or coatings for dental implants for an increased bone in-growth (Dorozhkin, 2009; Wang et al., 2005).

It has been found in different studies that chemical and topographic modifications of polymers and metals affect cell proliferation, depending on pattern geometries and size. For example, Reichert et al. demonstrated the impact of topography on the attachment of Swiss albino mouse fibroblasts (3T3). Cells usually do not show any adherent contact to polytetrafluoroethylene (PTFE) surfaces, but after micropatterning of the PTFE the fibroblasts did indeed attach to the surfaces (Reichert et al., 2007). Especially the alignment of cells in reference to microchannel formation has been reported by several groups (Berry et al., 2004; Kaiser et al., 2006; Kirmizidis and Birch, 2009; Lu and Leng, 2009;2003; Perizzolo et al., 2001; Tan and Saltzman, 2004; Walboomers et al., 1999). For instance, Walboomers et al. reported an increased rat dermal fibroblast (RDF) alignment by decreasing groove widths from 10, 5, 2, and 1 μm (depths of 0.5 μm) on polystyrene substrates.

Contrary to polymer and metals, the effects of ceramic surface topographies have not yet been commented on that often. A randomized calcium phosphate surface texturing, e.g. roughening of HA by grinding papers, has already been studied by different research groups with various cell types. Depending on the investigated parameters, the randomized calcium phosphate texturing can have a significant influence on the cell behaviour and metabolism (Ball et al., 2008; Deligianni et al., 2001; Hayashi et al., 1994). However, cell behaviour to specific and accurate ceramic HA surface micropatterning was reported only by a few researchers (Lu and Leng, 2009;2003; Perizzolo et al., 2001; Tan and Saltzman, 2004). A main reason for this is the difficult fabrication of defined HA micropatterns. Contrary to our study, in the other investigations HA coatings were used, deposited by magnetron sputtering or by direct mineralization of HA on pre-patterned silicon wafer substrates. Nevertheless, the effect of systematically changed micropatterns in the sub-100 μm range using solid HA-based samples on human osteoblasts has not yet been studied well. By using a recently developed method called “modified micro-moulding” (Holthaus et al., 2010), we have fabricated HA microchannels with high shape accuracy.

In this study, we investigate the effect of HA microchannels with widths ranging from 16 to 77 μm on human osteoblast (HOB) proliferation. The objective of this study is to analyse the influence of high quality HA-based microchannels with a well-defined topography on the “contact guidance” of HOB. For this purpose, we used periodic, large-area microchannels fabricated on solid calcium phosphate-based samples. For the patterning process we applied a modification technique that did not change the samples’ surface chemistry or crystal structure in the patterning region.

Materials and Methods

Fabrication of micropatterned ceramic samples

Commercially available ceramic powder was used to mix an aqueous ceramic suspension of 16 vol.% for the fabrication of micropatterned ceramic bodies via modified micromolding (m- μ M) as described in Holthaus et al. 2010. For that purpose, 12.4 g HA powder ($(\text{Ca}_{10}(\text{PO}_4)_6(\text{OH})_2)$, Prod.-No. 04238, Lot: 8345A, Sigma-Aldrich Chemie GmbH, Munich, Germany) was mixed with 20 g of an aqueous silica dispersion (BegoSol K, SiO_2 particle size 8 nm, solid content of 7.5 g colloidal silica, BEGO GmbH, Bremen, Germany). A polyacrylic acid-based dispersant (Syntran[®] 8220, Interpolymer GmbH, Hassloch, Germany) with a ratio of 15 mg Syntran[®] per gram ceramic was added to the suspension. The pH was adjusted to 9 to 10 by adding ammonia solution (25%, Merck, Darmstadt, Germany). The primary particle size of the HA powder was unimodally distributed 151 ± 0.235 nm (DT1200, Dispersant Technologies, Bedford Hills, NY), and the powder density measured via helium pycnometry (Accu Pyc 1330, Micromeritics GmbH, Aachen, Germany) was 3.03 ± 0.04 g/cm³. The molded samples were dried for two days at 30 °C with 30% relative air humidity in a climate chamber (KBF115, Binder GmbH, Tuttlingen, Germany). Afterwards, the micropatterned samples were removed from their molds. The molded samples were then sintered in a furnace (LHT08/17, Nabertherm GmbH, Lilienthal, Germany) at 1200 °C at ambient conditions for two hours. Heating was performed with 50 °C/h, cooling with 100 °C/h. After sintering, all samples were washed for five minutes in double deionised water (Synergy[®], Millipore, resistivity 18 M Ω *cm, Schwalbach, Germany) in an ultrasonic cleaner (1510 Branson[®], Branson Ultraschall, Dietzenbach, Germany) and dried at ambient conditions.

Micropattern dimensions

The bottoms of the molds were made of polydimethylsiloxane stamps (PDMS, Sylgard[®] 184 silicone elastomer, Dow Corning, Wiesbaden, Germany) and featured an area of 1 x 1 cm² of periodic channel-like micropatterns with widths of 20 μ m, 40 μ m, 60 μ m, 80 μ m and 100 μ m, respectively. Molds with two different pattern depths of 10 μ m or 20 μ m were used.

Surface texture imaging

The micropatterns were visualized through SEM (Camscan Series 2, Cambridge Instruments Obducat CamScan Ltd., Cambridgeshire, U.K.) at 20 kV. Prior to SEM imaging the samples

were sputtered with gold (K550, Emitech, Judges Scientific plc, West Sussex, UK). 2D and 3D measurements were achieved through 420-fold magnification with a profilometry system (Plμ 2300, Sensofar Technology, Terrassa, Spain) in order to characterise the quality and shrinkage caused by the sintering process and to measure the average surface roughness according to ISO 4287 (ISO 4287 (1997)). The measurement length for the roughness (Ra) was $L_c = 4 \text{ mm}$.

Non-patterned reference samples

Two kinds of non-patterned ceramic reference samples were fabricated for the experiments. First of all, reference samples (ref.-1) were molded with identical materials and settings as described above, yet without the presence of microchannels at the bottom of the molds. Secondly, reference samples (ref.-2) were die-pressed by using 1.1 g of HA powder. The powder was uniaxially die-pressed with the help of metal plungers and a hydraulic press (Weber Maschinen- und Apparatebau GmbH, Remshalden, Germany) applying a compressive force of 7.5 kN. The sample diameter was $10.0 \pm 0.1 \text{ mm}$ with a thickness of $2.8 \pm 0.2 \text{ mm}$. The non-patterned ceramic samples were sintered using identical conditions as described above. The die-pressed HA samples (ref.-2) were treated with SiC grinding paper (grit p320, WS Flex, Hermes Abrasives Ltd., Virginia Beach, USA) to generate the same surface roughness as measured on the molded non-patterned HA-based samples. Subsequently, Energy Dispersive Spectroscopy (EDS, Camscan Series 2, Obducat CamScan Ltd., Cambridgeshire, United Kingdom), with a detection limit of about 0.1 % of the element's mass, was utilised to detect possible wear residues originating from the SiC grinding papers. The measurements were taken on HA samples (ref.-2) for two different spots with an area of $27 \times 17 \text{ } \mu\text{m}^2$ each. Prior to EDS analysis the samples were washed three times for five minutes respectively in double deionised water in an ultrasonic cleaner and dried at ambient conditions. As a third kind of reference samples, cell culture plastic coverslips with a diameter of 15 mm (Thermanox[®], Nalge NUNC, Rochester, New York, USA) were deployed. Crystal structure analysis X-ray diffraction measurements (XRD, C3000, Seifert, Ahrensburg, Germany) of sintered HA samples were made for molded and die-pressed samples with the aim to determine the crystal structure. Scans with 2θ ranging from 15° to 70° were taken.

Surface wettability

The contact angles (Θ) between sessile droplets (20 μ L) of double deionised water and the ceramic surfaces were measured sixfold (duplicate measurements on $n = 3$ samples) for each kind of micropatterned or non-patterned sample. Macroscopic side view images of the droplets were taken via camera (D3100, Nikon Corp., Kanagawa, Japan). The measurements were taken cross-sectional to the microchannel direction. The contact angles were analysed via Software Image-J (version 1.39u, National Institutes of Health, USA). Prior to the contact angle measurement, the samples were rinsed in isopropanol with analytical grade (Merck, Darmstadt, Germany) and dried at ambient conditions for thirty minutes.

Cell culturing

A total of 390 samples were used for in-vitro testing. After their fabrication, all ceramic samples were sterilised at 180 °C for two hours in a furnace. Prior to the cell experiments all samples were rinsed with double deionised water containing 1% antibiotics/antimycotics (GIBCO Laboratories, Grand Island, NY) and dried in air under ultraviolet light for one hour. Human osteoblast cells (HOB, cryovial, Cat.-No.: 121 0311, Provitro GmbH, Berlin, Germany) with a doubling time of 64 hours were cultivated in their third-culture generation for the in-vitro testing.

Each sample was put into one polystyrene culturing dish (24-well multidish, Nalge NUNC, Rochester, New York, US). Subsequently, the samples were fully immersed in 1 ml of complete DMEM media with high glucose (Dulbecco's Modified Eagle's Medium) and stored at 37 °C, 10% CO₂ and 94.5% RH in an incubator (C200, Labotect Labor-Technik-Göttingen GmbH, Goettingen, Germany) for thirty minutes. The media contained 10% fetal calf serum (FCS) and 1% antibiotics/antimycotics. Afterwards, the media was removed with a sterile pipette and then discarded. Approximately 2×10^4 cells homogenously dispersed in 1 ml DMEM media were added to each well onto the wet samples. The cells were incubated on the various substrates in the same incubator for a period of seven days under static conditions. Sampling points were taken after 24 hours (day 1), 72 hours (day 3), and after 168 hours (day 7). Thermanox[®] cover slides were used as cell culture reference material. Cell relevant chemicals were purchased from Invitrogen GmbH (Darmstadt, Germany).

Cell viability measurement via WST-1 proliferation assay

Proliferation of the HOB cells was analysed by means of a plate reader (Cameleon, HIDEX, Turku, Finland) using a colorimetric WST-1 assay (WST-1, Roche Diagnostics GmbH, Mannheim, Germany). This method is based on the non-radioactive quantification of the cell proliferation via the measurement of the formazan product in viable cells. Supernatants were quantified spectrometrically (OD) at 450 nm with a reference wavelength of 650 nm. Proliferation measurements of $n = 6$ samples for each kind of material per sampling day were applied. The same volume of culture medium and cell proliferation reagent WST-1 was used in the experiment as a background control (absorbance of culture medium plus WST-1 in the absence of cells) for the plate reader. Due to different sample sizes the measured proliferation values of Thermanox[®] were normalised to the sample area of the ceramic samples.

Cell imaging

Fluorescence staining of the osteoblast cells was accomplished with two different fluorescent dyes. Alexa Fluor[®] 488 Phalloidin was used for the cytoskeletons and 4'6'-Diamidino-2-phenylindol (DAPI) was taken for the cell nuclei. Cells were visualized and studied with a fluorescence microscope (Axio Imager M.1, Carl Zeiss GmbH, Jena Germany). Imaging of $n = 3$ comparison specimens for each kind of material and sampling point was applied. The chemicals for cell staining were purchased from Invitrogen GmbH, Darmstadt, Germany.

Staining of collagen type I

Another parameter for cell viability is the production of collagen type I inside the cells. Mouse anti-human collagen as primary antibody and conjugated anti-mouse IgG (Alexa Fluor[®] 546) as secondary antibody were used for a semi-quantitative collagen type I staining inside the cells. This inspection was performed on the basis of the fluorescence microscopic images.

Measurement of cell orientation angle (OA)

The morphological deviation of the cells from the microchannel direction was analysed in fluorescence microscopy images. A virtual axis was placed in each single cell and the cell orientation angle (OA) was measured between 0 and 90° by the use of the software Axio Vision Imaging 4.8 (Carl Zeiss GmbH, Jena, Germany). The definition of OA was the same

as introduced by Brunette in 1986 and used by others (Brunette, 1986; Clark et al., 1990; Lu and Leng, 2003 & 2009). The angle between the long axis of the cell and the channel direction was measured. An osteoblast which was perfectly aligned with the groove would have a value OA of 0° . The possible orientations of the cells were divided into six groups.

N = 3 comparison samples were used (e.g. three samples with pattern widths of 20 μm and depths of 10 μm). For the analysis, n = 4 microscopic images were taken per sample. Each image was of 587,400 μm^2 (890 μm x 660 μm), so that a total quantification area of 2.35 mm^2 per material was investigated. Within the images taken, all present cells were analysed. Non-patterned molded ceramic samples (ref.-1) were taken as reference material.

Measurement of cell positioning

By using fluorescence microscopy it was analysed whether cells grew on top of the micropatterns or inside the microchannels. For this quantitative analysis the same n = 4 images for n = 3 comparison specimens as mentioned above were used.

Statistical analysis

The statistical analysis was performed with the aid of Minitab[®] 16 (Minitab Inc., Pennsylvania, US). A comparison of the experimental data was made in a one-way analysis of variance (ANOVA) with post hoc Tukey's multiple comparison method for assessing whether all sample scenarios show statistically significant differences. A *p*-value of $p < 0.05$ was considered statistically significant. The statistical test was the same as used by other authors for the evaluation of cell orientation (Kirmizidis and Birch, 2009; Lam et al., 2008).

Results

Characterisation of micropatterns and material

Micropattern geometry and topography

Periodic formations of calcium phosphate-based hydroxyapatite microchannels with vertical sidewalls were fabricated via modified micromolding (m- μM). The molds had pattern widths of 20, 40, 60, 80, and 100 μm , respectively. After drying and sintering the molded HA microchannels, the original widths decreased to finally 16.0 ± 0.7 μm (20 μm), 30.3 ± 0.8 μm (40 μm), 45.4 ± 1.2 μm (60 μm), 64.7 ± 2.4 μm (80 μm), and 76.6 ± 1.4 μm (100 μm). The HA pattern depths eventually shrank to 7.9 ± 0.8 μm (10 μm) and 15.5 ± 1.3 μm (20 μm),

respectively (**Fig. 35** and **supporting data in the appendix**) as obtained by 3D profilometry. The measured average surface roughness (R_a) inside the sintered HA-based microchannels was $R_a = 0.358 \pm 0.043 \mu\text{m}$. On top of the sintered patterns an average roughness of $R_a = 0.359 \pm 0.061 \mu\text{m}$ was measured.

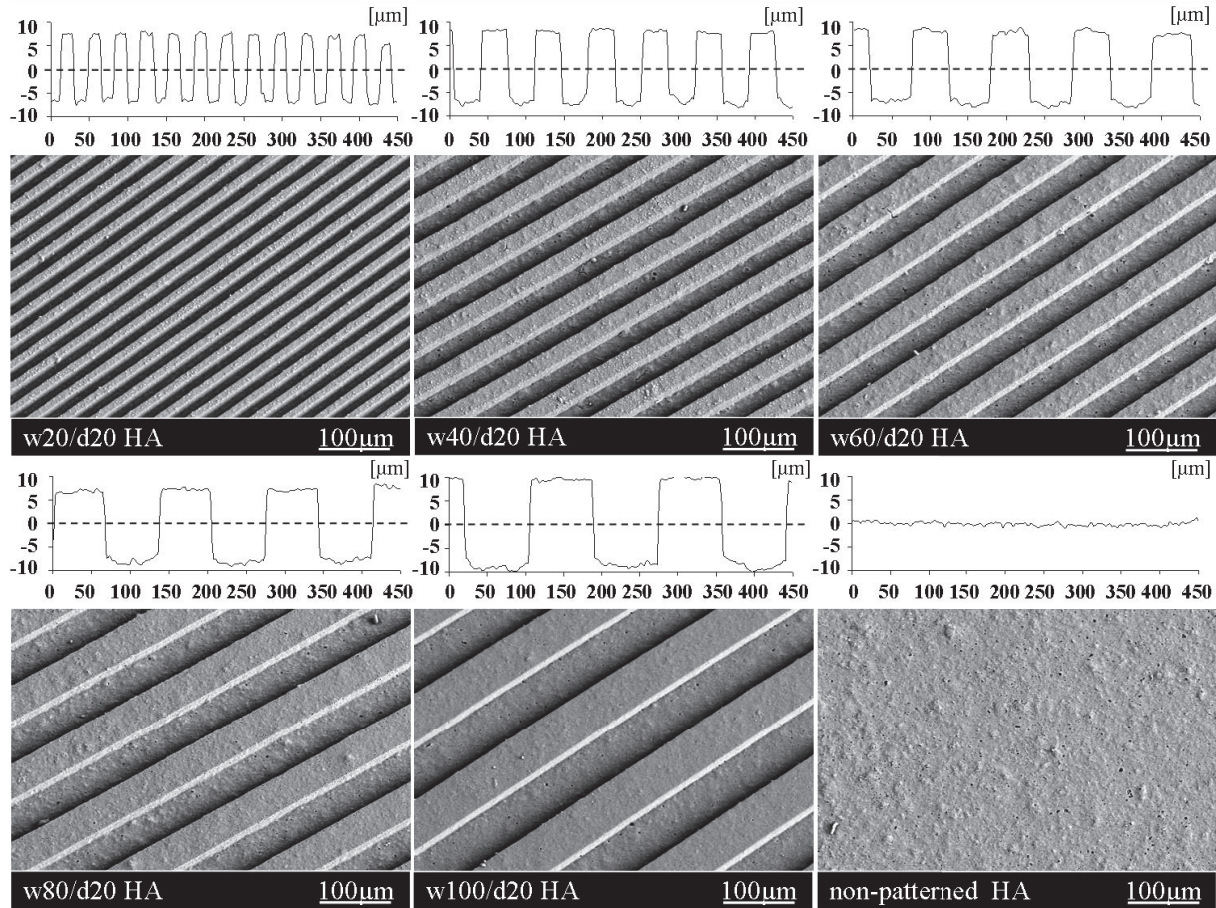


Fig. 35: SEM micrographs and measured 2D profiles of the surface cross section (insets) of micromolded, sintered hydroxyapatite. „w“ and „d“ respectively refer to width and depth of each micropattern.

Crystal structure and detection of residues from grinding

XRD measurements showed the presence of tetragonal silica (cristobalite low), β -tricalcium phosphate and hydroxyapatite on molded HA-based samples, which were mixed with aqueous silica (**supporting data in the appendix**). Pure HA crystal structure was measured on die-pressed HA samples (ref.-2) which were treated with SiC grinding paper (p320) in order to generate an identical surface roughness as measured on the molded HA-based samples. In addition, EDS as well as XRF analysis (not shown) (ref.-2) showed no presence of residues, e.g. Si, from grinding paper after three times of washing for five minutes in deionised water in an ultrasonic cleaner for the prepared samples.

Surface wettability

Contact angles Θ ranging from 89° to 98° were measured on HA-based micropatterns with depths of $10\ \mu\text{m}$. On micropatterns with depths of $20\ \mu\text{m}$ contact angles increased to a minimum of 105° . A distinct alignment of all water droplets with reference to the groove-like pattern direction was observed independently of the microchannel width or depth. The non-patterned HA references had contact angles of 72° (ref.-1) and 20° (ref.-2). Thermanox[®] showed a mean contact angle of 93° (ref.-Th) (**Tab. 3**). Droplets of circular shape were observed on non-patterned surfaces.

Tab. 3: Contact angles of sessile droplets of double deionised water on surfaces

sample	micropattern width (μm)	micropattern depth (μm)	mean contact angle (°)
molded HA micropatterns	20	10	98 ± 2
	40		93 ± 4
	60		89 ± 2
	80		94 ± 5
	100		89 ± 6
	20	20	105 ± 3
	40		105 ± 3
	60		107 ± 4
	80		109 ± 1
	100		114 ± 2
molded HA (ref.-1)	non-patterned		72 ± 6
die-pressed HA (ref.-2)	non-patterned		20 ± 1
Thermanox® (ref.-Th)	non-patterned		93 ± 2

In-vitro tests with osteoblasts

Osteoblast proliferation

After 24 hours of proliferation (day 1) no significant differences in the cell proliferation - detected via cell proliferation WST-1 assay - were detectable, comparing all patterned and non-patterned ceramic samples (ANOVA: Tukey's Multiple Comparison Method). The mean WST-1 proliferation ranged in terms of optical density from $\text{OD} = 0.0130$ to 0.0167 . A significantly higher mean WST-1 proliferation of $\text{OD} = 0.0191$ was measured on the reference material Thermanox[®] (**supporting data in the appendix**).

No significant differences in osteoblast WST-1 proliferation were measured comparing micropatterned and non-patterned ceramic samples after 72 hours (day 3) of in-vitro proliferation. The mean WST-1 proliferations there ranged from OD = 0.0367 to 0.0565. Here, a significantly higher mean osteoblast WST-1 proliferation of OD = 0.0860 was measured on the reference material Thermanox[®] (**supporting data in the appendix**).

After 168 hours (day 7) no significant differences in the mean WST-1 proliferation were measured, comparing all micropatterned ceramic samples. Their mean WST-1 proliferations ranged from OD = 0.0835 to 0.1173. Significantly higher WST-1 proliferation, as compared to all ceramic micropatterned samples with widths smaller than 100 μm (depth 20 μm), was measured on molded non-patterned HA-based samples (ref.-1) and non-patterned die-pressed HA (ref.-2). The highest WST-1 proliferation of OD = 0.2400 was measured on Thermanox[®], which was significantly higher than all micropatterned and non-patterned ceramic samples (**Fig. 36**).

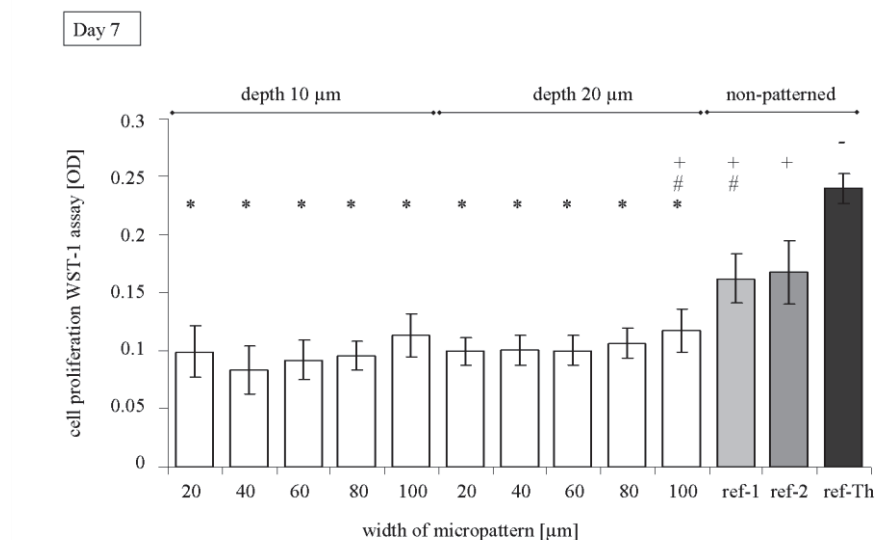


Fig. 36: Dependency of width and depth of micropatterns on the osteoblast WST-1 proliferation measured after seven days. Ref.-1: molded hydroxyapatite, ref.-2: die-pressed pure hydroxyapatite, ref.-Th: Thermanox[®]. Mean values that share a symbol (*/#/+/-) are insignificantly different (ANOVA: Tukey's Multiple Comparison Test).

Collagen type I staining

HOB cells labelled with collagen type I staining (a protein which is important during ossification) showed that collagen was concentrated around the nuclei of the cells for all samples. After one day of proliferation a weak collagen type I signal was detectable on die-pressed HA, turning into a very strong signal after days 3 and 7. Independently of the sampling point, a very strong collagen type I signal was detectable on all molded

micropatterned and molded non-patterned HA-based samples, starting from day 1 on. The collagen type I signal was weak on Thermanox[®] for all sampling points (**Tab. 4**).

Tab. 4: Collagen type I production in osteoblasts; (-) no signal, (+) low signal, (++) distinct signal, (+++) very strong signal. Ref.-1: molded hydroxyapatite, ref.-2: die-pressed pure hydroxyapatite, ref.-Th: Thermanox[®]. Contr.: negative control.

collagen type I production in osteoblast cells														
	width of micropattern (μm)					non-patterned								
	20	40	60	80	100	20	40	60	80	100	ref.-1	ref.-2	ref.-Th	contr.
	depth 10 μm					depth 20 μm								
day 1	+++	+++	+++	+++	+++	+++	+++	+++	+++	+++	+++	+	+	-
day 3	+++	+++	+++	+++	+++	+++	+++	+++	+++	+++	+++	+++	+	-
day 7	+++	+++	+++	+++	+++	+++	+++	+++	+++	+++	+++	+++	+	-

Osteoblast positioning inside or on top of micropatterns

It was checked if the micropatterns' width and depth influence the osteoblast z-positioning, i.e. if cells grow inside the channels or on top of the patterns. Differences in the positioning of the cells in dependency of the pattern width were already detected at day 1 (ANOVA: Tukey's Multiple Comparison Method). On that day, two groupings were found, one of which comprising the two smallest pattern widths (20 and 40 μm) for both depths. Between 26% and 31% of all cells grew inside these channels, though no significant differences were found within this group. The second grouping was constituted of the larger channels with widths of 60 to 100 μm for both depths. Between 42% and 47% of all cells grew inside these channels; no significant differences were found within this grouping either. Channels with widths of 60 μm and depths of 40 μm were statistically related to both groups. Overall, the two groupings showed a significant difference concerning cell positioning. Widths of 60, 80, and 100 μm showed significantly more cells inside the patterns compared to the smaller channel widths of 20 and 40 μm for both depths. For all micropatterned samples it turned out that less cells grew inside the microchannels (37 ± 5 %) compared to the top of the patterns (63 ± 5 %) (**supporting data in the appendix**).

On day 3, significant differences in the cell positioning in terms of pattern widths were still detectable. Comparing the results from these two groupings among each other, some significant differences could be revealed.

Widths of 60, 80, and 100 μm showed significantly more cells inside the patterns (35% to 45%) as compared to widths of 20 and 40 μm (16% to 25%) for both depths. Within each grouping no significant differences were found.

In total, fewer cells grew inside the microchannels ($32\% \pm 5\%$) compared to the top of the patterns ($68\% \pm 5\%$). No significant differences were measured when comparing both pattern depths with the same pattern widths on day 3 (**Fig. 37**).

On day 7, it was not possible to measure the osteoblast positioning because of too high cell quantities and partial presence of single or multilayered cell coverage on the surfaces.

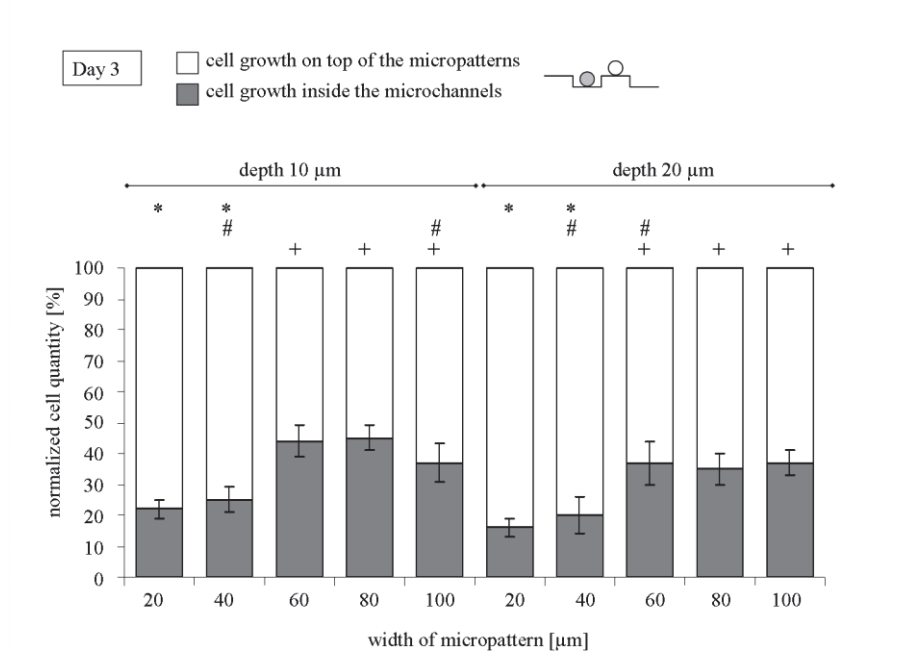


Fig. 37: Distribution of osteoblast cells on different micropatterns in-vitro after three days. Cells adhered either „inside“ the microchannels or „on top“ of the molded hydroxyapatite micropatterns. Cells on $n = 3$ samples were analysed on an area of 2.35 mm^2 each. Mean values that share a symbol (*/#/+) differ only insignificantly (ANOVA: Tukey's Multiple Comparison Test).

HOB orientation and morphology

Phenotypic morphological differences and orientation of the osteoblast cytoskeletons were found when comparing micropatterned HA-based surfaces with non-patterned surfaces (**Fig. 38**). Thereby, the cells aligned with reference to the microchannel direction starting on day 1. This cell alignment was measured and categorised into six groups ranging from 0 to 90° of alignment in order to determine the influence of pattern widths and depth on cell orientation (**Fig. 39**). In so doing, it was found that most osteoblast cells aligned between 0 and 15° with reference to the pattern direction. Owing to its strong relevance (0 to 15°), a statistical loading

of this group was made for two sampling days, i.e. days 1 and 3 (ANOVA: Tukey's Multiple Comparison Method). Detailed results for this 0-15° grouping are given in the following paragraph.

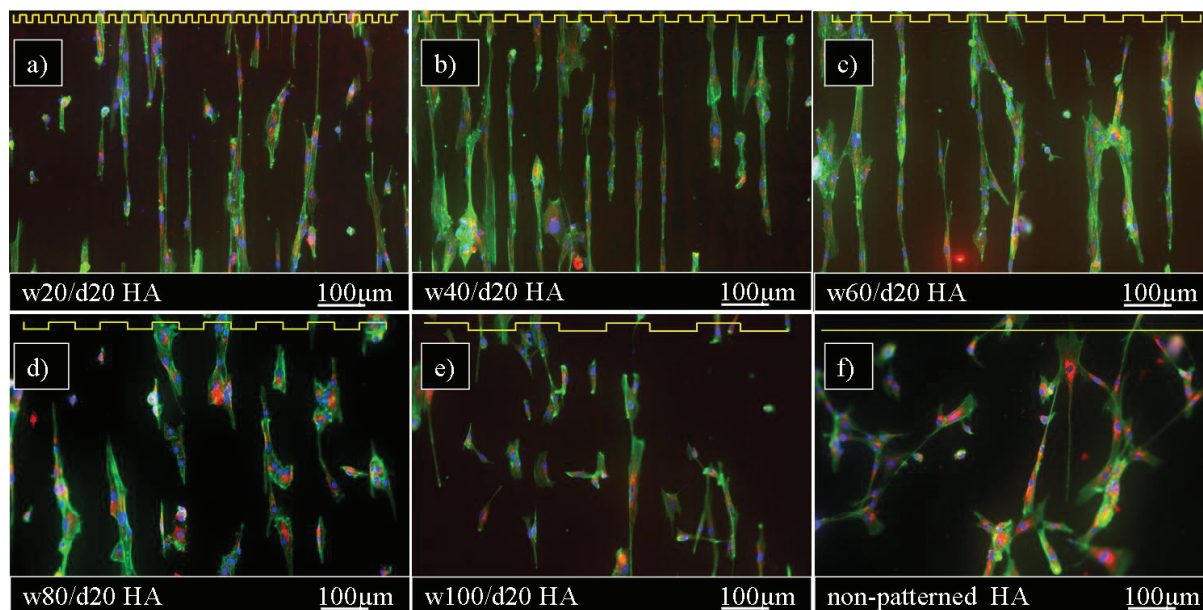


Fig. 38: Fluorescence microscopy images of osteoblast cells (HOB) after three days of proliferation on micropatterned hydroxyapatite samples with different microchannel widths. The position of micropatterns is shown in the form of 2D profiles (yellow insets). Non-patterned HA is shown in f) as a reference. Blue: nucleus, Green: cytoskeleton, Red: collagen type I.

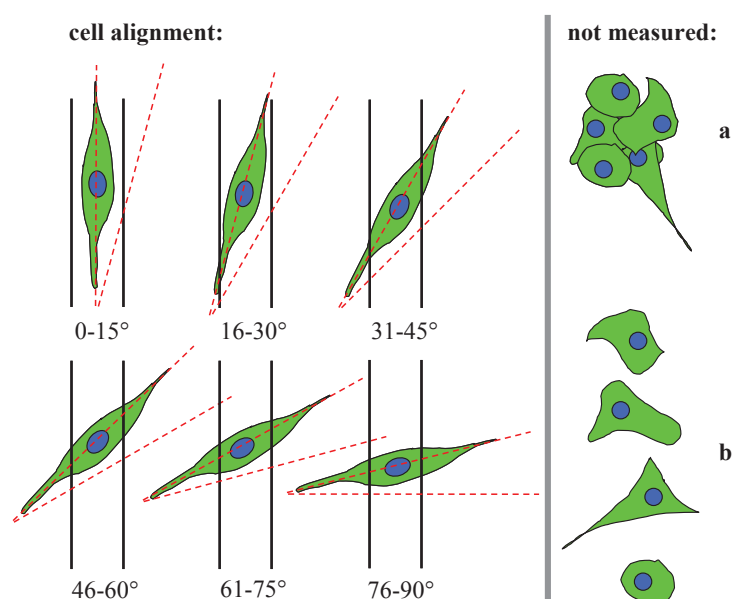


Fig. 39: Osteoblast cell alignment in reference to hydroxyapatite micropattern direction; the aligned cells are divided into six groups within angles between 0 and 90°. Excluded cells are cell bulks (a) and cells with no distinct alignment (b).

On day 1, micropattern with widths of 20 and 40 μm caused an osteoblast alignment in this group (0 to 15°) for 66% to 73% of all cells. The differences in cell alignment between these two pattern widths were insignificant for both fabricated pattern depths. 31% to 47% of all cells aligned between 0 and 15° on HA-based patterns with widths of 60, 80, and 100 μm . The differences in orientation between 60 to 100 μm are insignificant, yet the results are significantly lower compared to 20 and 40 μm wide patterns. This was found for both pattern depths. On non-patterned HA-based samples (ref.-1) in mean 12% of all osteoblasts oriented between 0 and 15°. This value was found to be significantly lower compared to all micropatterned ceramic samples. The mean cell quantity of cells without any specific alignment ranged between 13% and 32% (“not measurable cells”) and increased with increasing pattern widths (**Fig. 40**). All micropatterned as well as non-patterned samples caused a good cell attachment, as flat and spread cell morphologies with lamellipodiae and filopodiae were already present after one day. Overall, the cells’ morphologies on non-patterned surfaces were randomly spread.

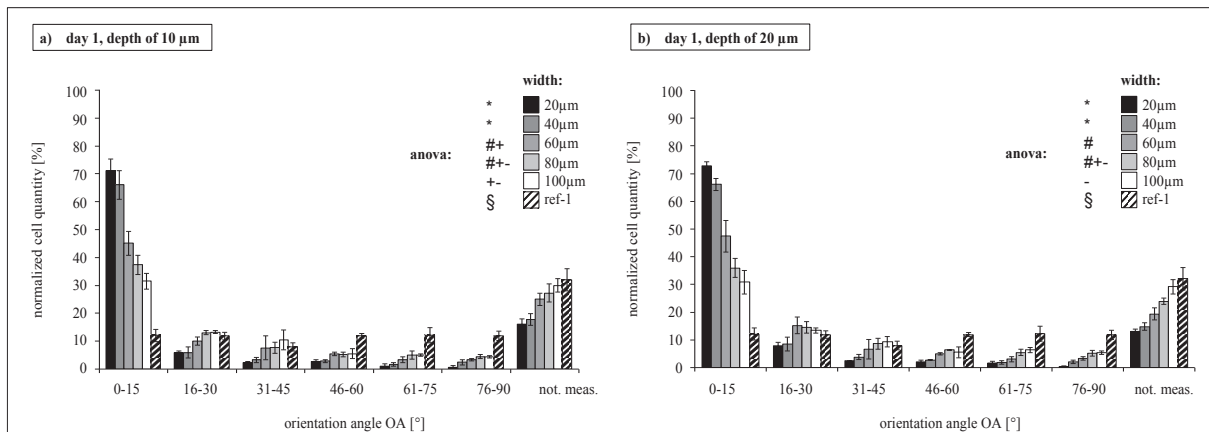


Fig. 40: Osteoblast cell alignment on micropatterned hydroxyapatite with different widths and depths after day 1. Ref-1: non-patterned molded hydroxyapatite. Cells on $n = 3$ samples were analysed on an area of 2.35 mm² each. Mean values that share a symbol (*/#/+/-/§) differ only insignificantly (ANOVA: Tukey’s Multiple Comparison Test).

On day 3, an osteoblast alignment between 0 and 15° was measured for 64% to 79% of all cells on ceramic micropatterns with widths of 20 and 40 μm . The mean cell alignment between the two pattern widths was insignificantly different for both pattern depths. 29% to 47% of all cells oriented between 0 and 15° on patterns with widths of 60, 80, and 100 μm . The differences in alignment for widths between 60 and 100 μm likewise turned out to be insignificant. Compared to widths of 20 and 40 μm , the number of aligned cells was significantly lower, which was found for both pattern depths. On non-patterned HA-based

samples (ref.-1), 13% of all cells aligned between 0 and 15°, which was significantly lower compared to all micropatterned HA samples. The mean cell quantity of osteoblasts without any specific orientation (“not measurable cells”) rose with increasing pattern widths (**Fig. 41**).

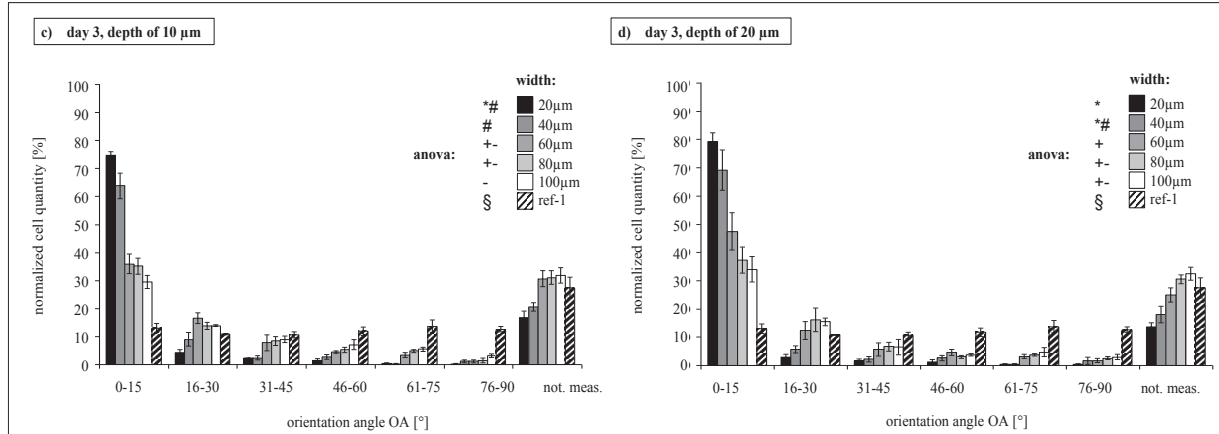


Fig. 41: Osteoblast cell alignment on micropatterned hydroxyapatite with different widths and depths after day 3. Ref-1: non-patterned molded hydroxyapatite. Cells on n = 3 samples were analysed on an area of 2.35 mm² each. Mean values that share a symbol (*/#/+/-/§) are insignificantly different (ANOVA: Tukey’s Multiple Comparison Test). The orientation angles of osteoblast cells on day 7 were not measurable because of too high cell quantities and the formation of single or even multilayered cell coverage on the surfaces.

Additional testing using microscopic live-imaging (Cell TrackerTM Green CMFDA, Prod.-No. C2925, Gibco, New York, US) of viable osteoblast cells revealed that the cells started to align after 3.5 hours on HA-based patterns. Widths of 20 µm with depths of 10 µm were tested (**data not shown**).

Discussion

In this study, the effects of HA-based micropatterned surfaces characterised by five differently sized pattern widths and two pattern depths on human osteoblast cell orientation were assessed under identical conditions over a period of seven days.

The surface roughness Ra measured inside the HA-based microchannels was almost identical compared to the roughness measured on top of the patterns (“inside”: Ra = 0.356 ± 0.043 µm vs. “on top”: Ra = 0.359 ± 0.061 µm). In addition, the average roughness of non-patterned molded HA-based material (Ra = 0.397 ± 0.005 µm) as well as the average roughness of the phase pure die-pressed HA (Ra = 0.391 ± 0.016 µm) was very similar. Compared to the patterned surfaces these roughness values turned out to be significantly higher. We do not

expect any impact on cell proliferation measured with WST-1 reagent, collagen type I production, or influence on cell morphologies due to the small differences in surface roughness. This assumption is based on in-vitro results with osteoblasts on die-pressed HA surfaces with well-defined surface roughness ranging from $R_a = 0.13 \mu\text{m}$ to $3.36 \mu\text{m}$ (**detailed information in chapter 3.3.2**).

The molded HA-based patterns and the molded non-patterned reference sample (ref.-1) were fabricated under addition of silica sol (SiO_2) for better molding results. The role of SiO_2 in bone mineralization processes and the influence of SiO_2 release on the osteoblast environment are still not fully understood. It is reported that the addition of SiO_2 to HA can enhance the bioactivity which is measurable e.g. via the collagen type I production, cell proliferation and number of focal adhesions, yet there are also concentrations which are harmful for cells (Patel et al., 2002; Shie et al., 2011; Thian et al., 2005; Xu and Khor, 2007). In our study, the silica-containing non-patterned HA reference (ref.-1) and the non-patterned pure HA reference (ref.-2) were insignificantly different in the measured cell WST-1 proliferation (ANOVA, Tuckey's multiple comparison test). Thus, we can exclude that a critical SiO_2 concentration or a harmful release of SiO_2 was reached within the first seven days in-vitro. The collagen type I signal was even stronger for SiO_2 -containing HA (ref.-1) compared to pure phase HA (ref.-2) on day 1. This difference might be promoted by the SiO_2 addition. We therefore assume that the soluble SiO_2 and the fast resorbing β -TCP present in the molded HA-based samples (**supporting data in the appendix**) were dissolved in the culture medium and were rapidly available to the osteoblasts on day 1. This might have stimulated the early production of collagen type I. After seven days, a similar collagen type I signal strength was observed on both non-patterned materials.

Wettability was determined via the contact angle Θ . Those ranged from 89° to 114° on micropatterned HA-based samples and 93° on Thermanox[®]; thus, these surfaces are hydrophobic ($\Theta > 90^\circ$). Contact angles of 72° were detected on molded HA and only 20° on die-pressed HA. Hence, both non-patterned ceramic references are hydrophilic ($\Theta < 90^\circ$), whereas their values are significantly different from each other. We do not suppose any significant influence on the cell behaviour (e.g. cell orientation, cell quantity or collagen type I production) due to similar wettability. All samples were fully immersed in DMEM media for thirty minutes directly before fresh media containing cells were put onto the wet samples.

High WST-1 results are an indication for more viable osteoblasts in the samples' culture dish. It was found that the measured WST-1 proliferation was not significantly higher on both non-patterned ceramic reference samples and Thermanox[®], compared to the micropatterned ones starting from the second sampling point (day 3). Therefore, there are less viable cells on all ceramic surfaces compared to Thermanox[®] samples. An indication for metabolic processes inside the cells is the production of collagen type I. Here, all micropatterned samples showed a distinct collagen type I signal starting on day 1, whereas a weak signal was observed for die-pressed HA and Thermanox[®] on day 1. The difference was only observed on that day. Altogether, the results indicate that the samples' topography did not have any influence on the collagen type I production, but had a distinct negative effect on the number of viable cells. This effect could be confirmed through the measurements of the positioning of the cells on the micropatterns. The measurement revealed that there were less cells inside all micropatterns compared to cells grown on top of the microstruts. This effect became stronger by decreasing pattern size. This phenomenon has not been mentioned in comparable studies with osteoblasts or osteoblast-like cells on HA patterns (Lu and Leng, 2009;2003; Perizzolo et al., 2001; Tan and Saltzman, 2004). We suggest that there are some unfavourable conditions, e.g. less exchange of nutritive substances inside these microchannels. Thus, the cells may migrate to the top of the patterns or else the cells may die inside the patterns due to nutritive lagging and detach from the surface. The observed effect was probably a combination of both. Cell migration has often been reported; for example, Kaiser et al. found structure-dependant migration of 3T3 cells on patterned Ti4Al6V surfaces. Thereby, most effectively cell migration was observed on structures with lower depths and large flat tracks between the pattern struts (Kaiser et al., 2006). In our study, cells in small and deep channels (e.g. 20/20 μm) may die and cells in large flat channels (e.g. 100/10 μm) may migrate to the top of the struts.

Our results have shown that the osteoblast oriented strongly in micropattern direction. This was found with an increasing number of aligned cells between $\text{OA} = 0\text{-}15^\circ$ by decreasing pattern width. The effects of micropatterning on cells have been extensively reported by many groups, using various materials and cell types. Kirmizidis et al. found significantly lower focal adhesions per rat calvarial osteoblast (RCO) and also lower alkaline phosphatase on grooved polycarbonate substrates with widths of 10, 15, and 30 μm (depths of 7 μm) compared to flat non-patterned polycarbonate surfaces. In addition, they reported distinct alignments on grooved polycarbonate substrates (Kirmizidis and Birch, 2009). Concerning the alignment, our results for the orientation of osteoblasts on HA micropatterns are similar to

those of Kirmizidis et al. Walboomers et al. determined the rat dermal fibroblast (RDF) behaviour on microgrooved culturing material with widths of 1, 2, 5, and 10 μm (depths of 0.5 μm) with different chemical composition but identical surface channel-like texture. Moreover, an increased cell alignment by decreasing channel widths to 1 μm on polystyrene substrates (PS) was observed (Walboomers et al., 1999). This increased cell alignment with decreasing channel widths matches with our results for HOB on HA patterns.

When comparing our results to studies on cell alignment on sputtered channel-like HA micropatterns, very similar findings and conclusions can be drawn. Thus, for instance, Lu and Leng report pattern-dependent alignment of osteoblast-like cells (SaOS-2) on sputtered channel-like HA patterns. The cells aligned in OA ranging from 10 to 30° and pattern widths between 15 and 40 μm with depth of 10 μm on day 1. On day 3, the cell alignment was less intense with OA of 25 to 40° (Lu and Leng, 2003). The orientation of the SaOS-2 cells is very similar to our results, yet the HOB alignment was not less intense on day 3. SaOS-2 cells are smaller compared to HOB cells; so, presumably, the cell guidance depends on the relation of pattern widths to cell sizes, thus we assume that the larger HOB cells are more influenced by the tested pattern widths. In addition, the sidewalls of our patterns are perpendicular to the bottom of the patterns, whereas Lu and Leng report patterns with tapered sidewalls of 55°. The more rectangular shaped pattern profile in our study might have mediated the cell guidance more strongly. However, the pattern depth did not influence the cell alignment significantly, which is in accordance with Lu and Leng. In a second study, Lu and Leng report the alignment of SaOS-2 on the same HA-coated silicon wafers with pattern widths of 8 and 24 μm and depths of 2, 4, and 10 μm . The osteoblasts responded to channels with widths of 24 μm less intense as compared to widths of 8 μm (Lu and Leng, 2009). Although larger pattern widths, i.e. between 16 to 77 μm , were tested in our study, this effect is still in accordance with our results. Lehnert et al. have found alignment of osteoblasts from calf periost on microgrooved polystyrene surfaces with depth in the sub micron range (50 and 150 nm). Cell alignment was visible after eight hours and more aligned after two days. This is similar to our results with HOB which oriented after 3.5 hours on HA microchannels with depth of 20 μm in an in-vitro live-imaging test (**data not shown**). Even though our study revealed significant differences in the osteoblast alignment as well as in the cell positioning on different HA-based micropatterns, such differences in the cell proliferation (WST-1 assay) or the collagen type I production were not found.

Micropatterning is useful for various biomedical applications such as implants, tissue engineering, cell-based sensors and fundamental cell research. For such applications, the

pattern widths and depths have to be chosen with care if HOB cells are intended to be used. A compromise between chosen pattern widths and depths has to be made to mediate strong HOB cell guidance on the one hand, but also for an effective nutrition support. The results indicate that a pattern depth of 10 μm should not be exceeded when the final pattern widths are smaller than 45 μm . In summary, the present study indicates very strong contact guidance on human osteoblast cells by the use of HA-based microchannels with widths between 16 and 77 μm and depths of 10 and 20 μm .

Conclusions

Hydroxyapatite-based microchannels with vertical sidewalls and sharp pattern ridges were fabricated via modified micromolding (m- μM) to elucidate the role of micropatterns on osteoblast. The cell viability was measured by the use of a colorimetric WST-1 assay and by assessing a collagen type I staining. Moreover, the cell positioning and orientation angle (OA) were analysed on the basis of microscopic images. Finally, the HA-based micropatterns with groove-like channels and struts of different widths and depths were evaluated in-vitro for a period of up to seven days.

The main findings from that have been that osteoblasts orient for 70% to 80% within an angular range of 0 to 15° relative to the microchannel direction for channels with 16 and 30 microns width on days 1 and 3. Only 20% of the osteoblasts grew inside the channels for channel widths of 16 and 30 microns. Microchannels with 45, 65, and 76 channel widths allowed around 40% of the osteoblasts to grow inside; this was found independently of the respective pattern depth. In short, we have found that the width of HA-based microchannels has an important impact on the contact guidance of human osteoblasts.

3.2 Aerosol-Jet[®] printing of hydroxyapatite suspensions

3.2.1 Aerosol-Jet[®] printing of hydroxyapatite suspensions for bone cell growth studies

The following results were partially published in the “Proceedings of the 2008 International Manufacturing Science and Engineering Conference in Evanston, IL, USA, MSEC2008” by Marzellus grosse Holthaus and Kurosch Rezwan (University of Bremen, Advanced Ceramics) (Holthaus and Rezwan, 2008).

A rapid prototyping printing technique was used to fabricate micropatterns. The same quantity of calcium phosphate powder (HA, Riedel-de Haën), as was described in earlier chapters, was die-pressed in order to generate plane cylindrical platelets with diameters of 10 millimetre. These platelets were then sintered in a furnace (LHT 04/17, Nabertherm) at 1200 °C for two hours with a heating rate of 50 °C/h and a cooling rate of 100 °C/h. Afterwards, the sintered HA platelets were micropatterned by means of an Aerosol-Jet[®] printing technique also known as Maskless Mesoscale Materials’ Deposition (M³D).

The non-structured cylindrical samples were micropatterned with Aerosol-Jet[®] printing (Optomec Inc.) and by using an aqueous hydroxyapatite ceramic slurry of 6.6 vol.% stabilized at pH 9.5-10. After slurry deposition, subsequent sintering of the printed micropatterns through an Nd:YAG laser was proceeded. The microstructures had a length of 1000 µm and were printed with various widths between 20 and a maximum of 150 µm (**Fig. 42**).

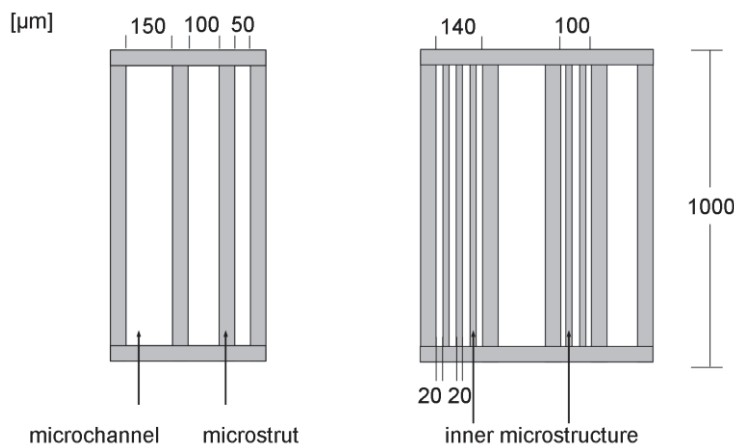


Fig. 42: Sketch of Aerosol-Jet[®]-printed micropattern sizes

Four micropattern formations were printed on each platelet, and two microstructures were deposited on already printed basements, which were also generated with Aerosol-Jet[®]

printing. The printed lines of the basements were generated with a width of 15 μm . The other two microstructures were directly deposited onto the plane platelet surface. Each microstructure (with and without basement) was printed with an inner microstructure within the 100 and 140 μm wide microchannels (**Fig. 43**).

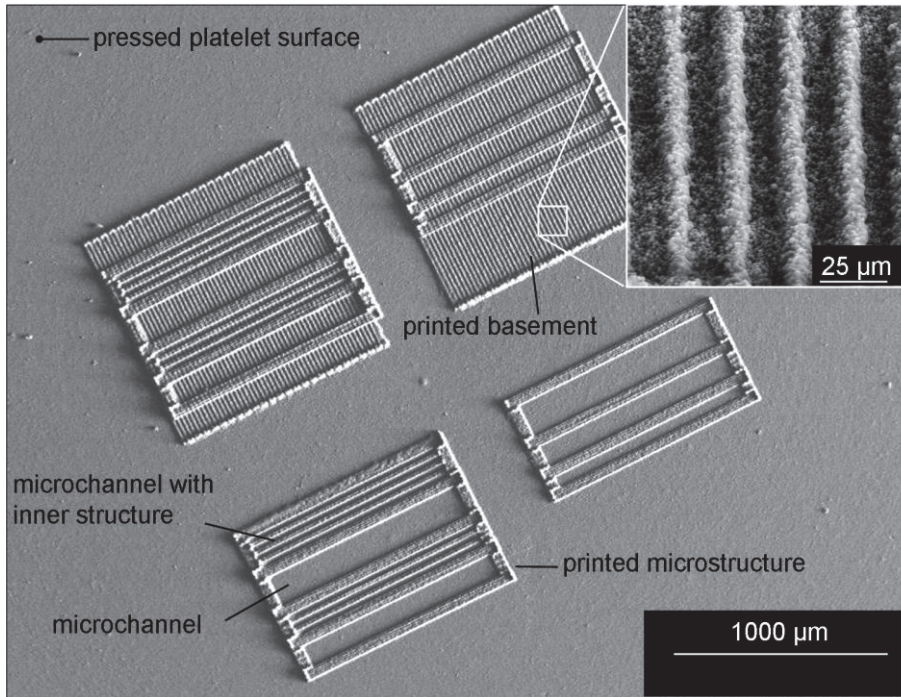


Fig. 43: Four Aerosol-Jet®-printed and laser-sintered ceramic microstructures: two with a printed basement (top) and two without any basement (below). Both microstructures on the left side were printed with inner microstructures of 20 μm width in the 100 and 140 μm wide channels (see also Fig. 42). The detail image shows the magnification of a printed basement.

The microstructure walls had a thickness of 50 μm . Further, the aqueous hydroxyapatite ceramic slurry contained double deionised water, puriss. hydroxyapatite powder (Riedel-de Haën) and was stabilized with a few droplets of ammonia (25%) so as to reach a pH of 9.5-10 (Riedel-de Haën). The printing speed was at 0.5 mm/s. By contrast, the laser sintering power was systematically varied between a selectable minimum of 0.2 and 1.0 watts in order to find the best laser power for sintering.

After the Aerosol-Jet® printing process and after the laser sintering process of 0.25 watts, the generated micropatterns showed a grainy surface. Fine cracks were distinguished within the generated structures. Moreover, single hydroxyapatite particles or agglomerates were visible in SEM images (**Fig. 44**). However, the printed patterns under the grainy surface layer seemed to be sintered or molten. The higher laser powers of > 0.25 watts caused totally molten patterns.

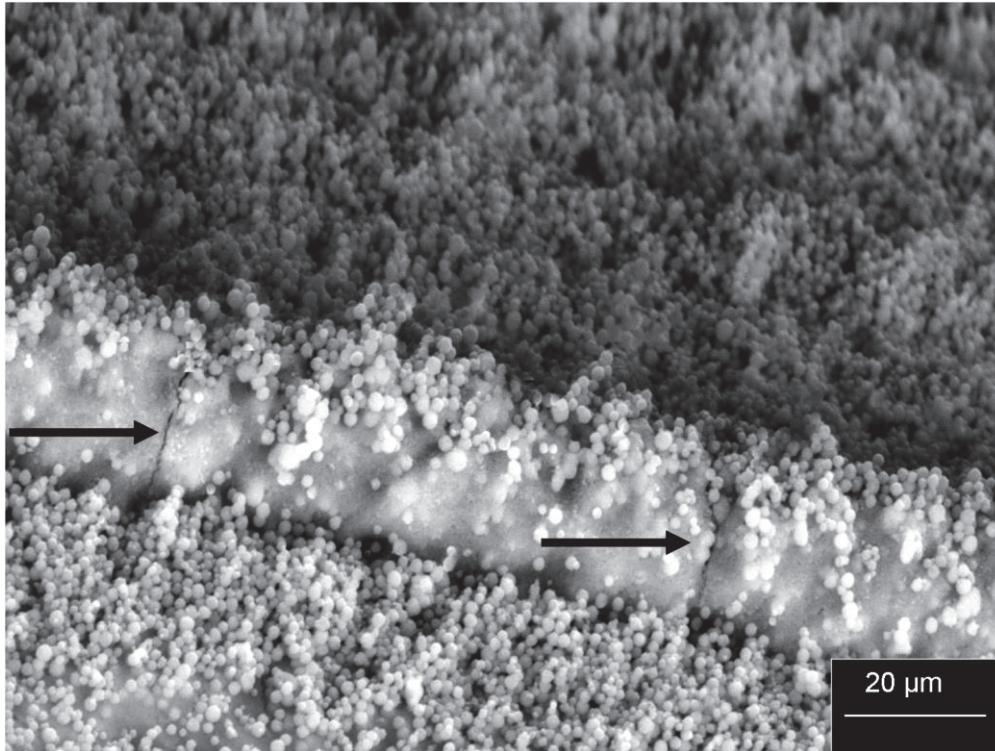


Fig. 44: Aerosol-Jet[®]-printed and laser-sintered strut (0.25 watts; view: angular sidewise) made from hydroxyapatite. Generated strut is partially sintered. Particles or agglomerates are visible. Fine cracks were found (arrows).

The laser-treated hydroxyapatite particles were not fully sintered and showed partially only sinter neck formation. Sintering quality was not stable, so that some parts of the micropatterns were more sintered than others. Likewise the height of the printed micropatterns varied, between 6 to 8 μm (**Fig. 45**). This variation in height was due to inconstant fabrication processes.

Another problem was the difficulty in selecting the sintering power in order to get a constant sintering quality. In doing so, a great disadvantage is the unknown sintering temperature which results from the selected laser power. Also, the crystal phase of the printed and sintered areas is not exactly determinable because of the different sintering quality within these areas. A change in crystal phase may influence cell proliferation. However, XRD analysis of a printed and laser-sintered hydroxyapatite sample showed no traces of β -tri-calcium phosphate (β -TCP) on the printed surface.

Because of these promising results Aerosol-Jet[®]-printed patterns were used for a study on cell growth with tumorous osteoblasts (MG-63).

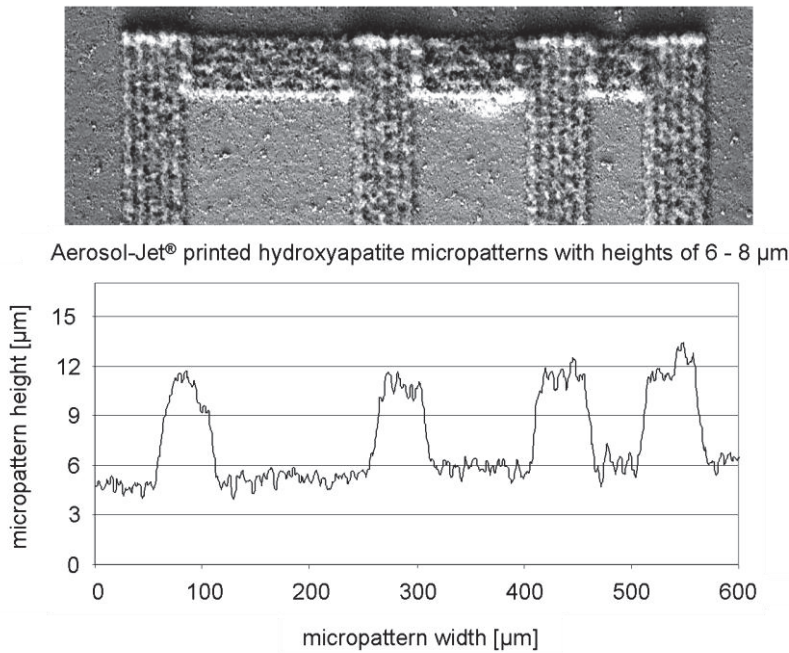


Fig. 45: SEM image (top view) and 2D profile of Aerosol-Jet®-printed micropatterns on plane pressed hydroxyapatite surface (no printed basement and no printed inner structure)

The following results were published in part under the title “Ceramic micropatterns for bone cell growth studies” in the proceedings of the conference “Thüringer Grenz- und Oberflächentage (ThGOT) 2009” in Friedrichroda, Germany, by Marzellus grosse Holthaus^a, Veronika Rutkowski^b, Volker Zöllmer^b, Matthias Busse^b, and Kuroschi Rezwan^a (^aUniversity of Bremen, Advanced Ceramics; ^bFraunhofer Institute for Manufacturing Technology and Advanced Materials, Bremen).

Abstract

Aerosol-Jet®-printed calcium phosphate groove-like micropatterns have been precisely fabricated with widths ranging from 10 to 60 μm. Subsequently, osteoblast-like osteosarcoma cells (MG-63, size 20-100 μm) were seeded on the printed patterns for a period of seven days. It could thus be shown that the osteoblast-like cells grew into 10 μm wide printed patterns, elongating and aligning in accordance with the pattern direction. These first results are of great interest for the defined patterning of implant surfaces with improved osseous integration.

Introduction

The fabrication of implant materials with appropriate mechanical properties and adequate bonding to the surrounding bone tissue is still a challenging enterprise. To achieve these

requirements some implants nowadays are coated with bioactive and osteoconductive calcium phosphate ceramic such as hydroxyapatite (HA). These ceramic-coated implants, e.g. dental implants or hip-prosthesis, are directly inserted into the bone tissue, where they are supposed to persist for several years without loss of bonding at the implant-bone interface. An adequate and good fixation of the implant is achieved when bone cells (osteoblast) adhere at the implant surface subsequently to the implantation. If the surface is biocompatible and sufficiently “attractive”, osteoblasts form new bone tissue which then grows into the implant surface. However, it is still not fully understood how ceramic micropatterns and ceramic porous substrates can enhance the osteoblast adherence and ingrowth. The main objective of this study has been to evaluate the influence of printed ceramic micropatterns ranging from 10 to 60 μm in width on tumorous osteoblast-like cells in-vitro.

Sample fabrication

The same batch of HA calcium phosphate powder as described above was die-pressed in order to generate plane cylindrical platelets with diameters of 10 millimetre each. These platelets were then sintered in a furnace at 1200 $^{\circ}\text{C}$ for two hours with a heating rate of 50 $^{\circ}\text{C}/\text{h}$ and a cooling rate of 100 $^{\circ}\text{C}/\text{h}$. Afterwards, the sintered HA platelets were micropatterned using the Aerosol-Jet[®] printing technique.

Micropatterning via Aerosol-Jet[®] printing

The non-structured cylindrical HA samples were micropatterned through Aerosol-Jet[®] printing (Optomec Inc.) by using an aqueous HA ceramic slurry of 6.6 vol.%. The feed motion of the printer nozzle was 0.5 mm/s. The ceramic slurry was mixed from HA powder and deionised water (Synergy[®], Millipore) and stabilised at pH 9.5-10 with ammonia solution (25%, Merck) so as to prevent particles from rapid sedimentation and agglomeration.

Further, a formation of six micropatterned areas was printed on each calcium phosphate substrate (**Fig. 46**). Each patterned area was of 1 mm². The line-like micropatterns were printed with varying spaces from each other, with the space being called *width* (*w*) and printed with $w = 10, 20, 30, 40, \text{ and } 60 \mu\text{m}$. A non-patterned area of 1 mm² was chosen as a control surface next to the printed areas. This control area was then tagged with a printed frame.

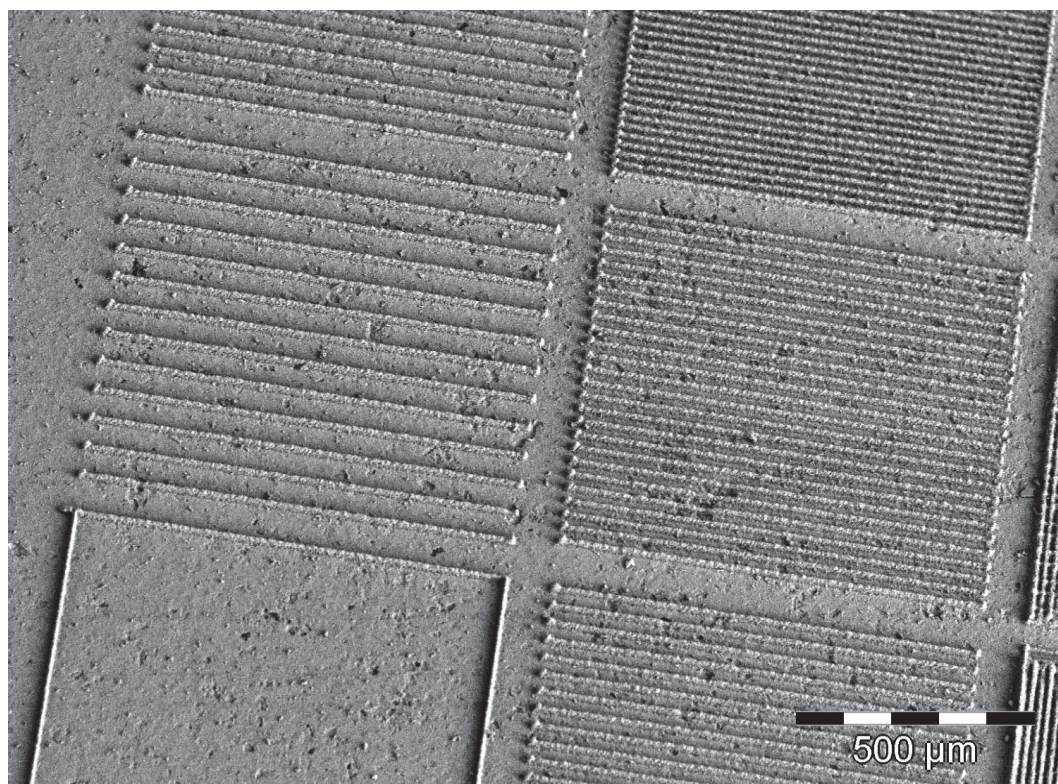


Fig. 46: SEM micrograph of six printed HA micropatterned areas on a HA substrate. Non-patterned control area, $w = 60 \mu\text{m}$, $w = 40 \mu\text{m}$ (from lower left to upper left) and $w = 30 \mu\text{m}$, $w = 20 \mu\text{m}$ and $w = 10 \mu\text{m}$ (from lower right to upper right). Patterns were printed once and laser-sintered (Nd:YAG) with 0.25 watts.

Each printed single line had a width of $10 \mu\text{m}$. The generated patterns were sintered via a Nd:YAG laser at 0.25 watts after the printing process in order to reach the final stability. Sintering speed was at 0.5 mm/s . All patterned samples were fully immersed and rinsed with deionised water so as to remove loose ceramic particles. Heat sterilization was applied at 190°C for two hours at dry conditions.

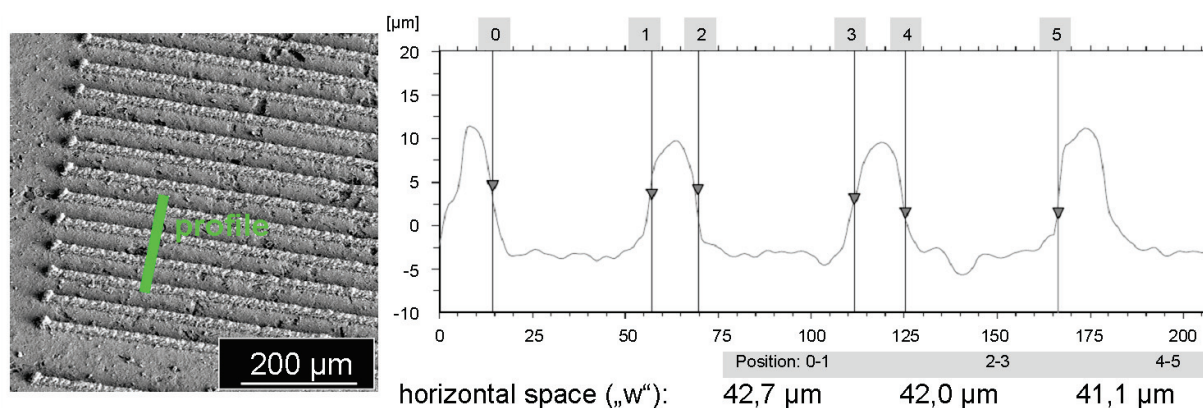


Fig. 47: SEM micrograph of printed HA line-like patterns with a width of $40 \mu\text{m}$ (left). 2D profile with three measurements (position 0-1, 2-3, 4-5) of the horizontal space “w” between printed lines

Cell culturing

Osteoblast-like osteosarcoma cells MG-63 (ATCC) with single cell sizes of 20 to 100 μm were cultivated at standard conditions (37 °C, 10% CO_2 , 94.5 % r.h.) and in complete DMEM media (GIBCO) in an incubator (C200, Labotect) for seven days. The media contained 10% fetal calf serum and 1% antibiotics (Invitrogen). First, the HA samples were washed in DMEM prior to the cell seeding. Subsequently, 1 mL DMEM containing 4×10^4 cells was pipetted onto the sterilized, micropatterned HA samples. In so doing, twelve samples were cultured, with each of them being placed in separate 24-wells (NuncloTM, NUNC). Sampling points were taken after days 1, 3, 5, and 7.

Cell staining and imaging

The cells were fixed onto the substrates via paraformaldehyd (PFA). Cytoskeletons were stained with fluorescent dye phalloidin (Alexa Fluor[®] 488, Invitrogen). Moreover, the cell nuclei were stained via DAPI (4'6'-Diamidino-2-phenylindol, Invitrogen). Afterwards, the samples were washed in phosphate buffered saline (PBS) in order to remove excessive dyes. Microscopy was performed by means of a ZEISS Axio Imager M.1.

Surface characterization

Surface roughness and width of micropatterns were measured via an optical 3D profilometry system (Pl μ 2300, Sensofar). The data thus gained was analysed with the help of the software SensoMap[®] (Sensofar). The roughness values of the non-patterned areas were analysed according to ISO25178. Eventually, SEM imaging was performed at 20 kV (Camsan, Cambridge Instr.). Prior to imaging, the samples were sputtered with gold (Emtech).

Results

The roughness analysis of non-patterned HA control areas resulted in an average roughness of $R_a = 0.87 \mu\text{m}$, with measurements taken on $n = 12$ samples. The predicted micropattern widths of the Aerosol-Jet[®]-printed patterns were precisely achieved with deviations of only a few microns. The adjustment of the aerosol stream was difficult and the stream was inhomogeneous and inconstant during the whole process. The mean differences between the predicted and the measured pattern widths were of $2.2 \mu\text{m}$ (**Fig. 48**).

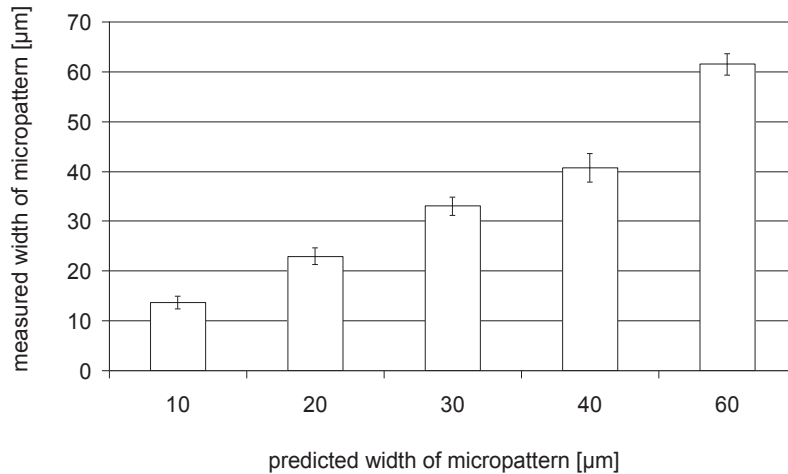


Fig. 48: Predicted width of micropattern vs. measured width of Aerosol-Jet[®]-printed micropatterns

The heights of the printed micropatterns varied strongly, with a measured minimum of 4 μm and a maximum of 17 μm . The heights were measured on micropatterns with widths of 30 μm on $n = 12$ samples. Measurements were taken on $n = 3$ neighbouring printed patterns.

The osteoblast-like osteosarcoma cells proliferated on the micropatterned HA surfaces as well as on the non-patterned surfaces. An increasing cell quantity, regardless of the patterning, was observed in all areas, from day 1 to day 7. Remarkable differences in cell quantity were measured on all samples. A significant difference was measured in the comparison of non-patterned and patterned areas with widths of $w = 20 \mu\text{m}$, whereas the patterned areas showed lower cell quantities (**Fig. 49**). After seven days, no measurements of cell quantity were possible anymore because of too high cell concentration.

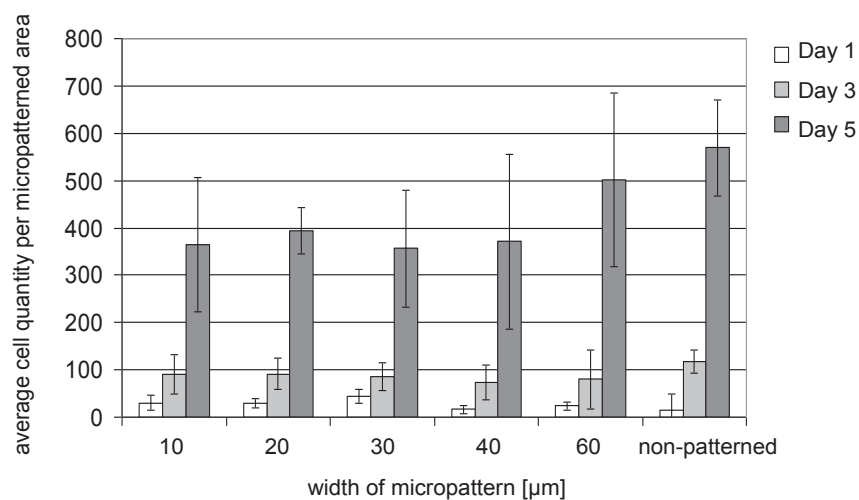


Fig. 49: Cell quantities of osteoblast-like osteosarcoma cells (MG-63) on Aerosol-Jet[®]-printed hydroxyapatite micropatterns

At the first sampling point (day 1), the cells showed spherical cell morphologies on all surfaces. Spherical cells as well as flat, elongated cells were observed at the second sampling point (day 3). At the third sampling point, then, as well as at the fourth sampling point (day 7), almost all cells showed elongated cell morphologies. It was found that the cells aligned in accordance with the micropattern direction. This observation was investigated systematically on samples from day 3, measuring the cell alignment with reference to the printed pattern direction. Spherical cells and cells with no distinct alignment were found to be not measurable. The cell alignment was classified into six groups between 0 and 90°, as shown in **Fig. 50** below.

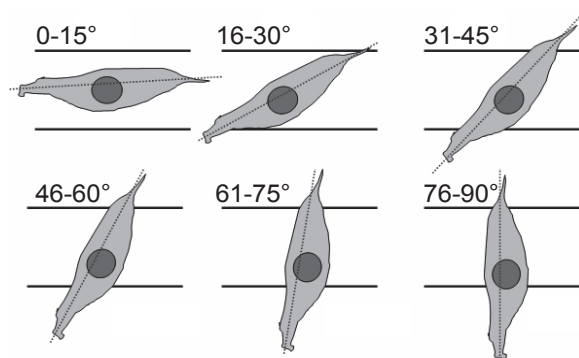


Fig. 50: Classification of cell alignment in accordance with the printed micropattern direction

The measured cells showed a distinct alignment between 0 and 15° on all patterned areas with widths ranging from 10 to 60 μm (**Fig. 52**), yet significant differences between the varying pattern widths were not detectable (**Fig. 51**).

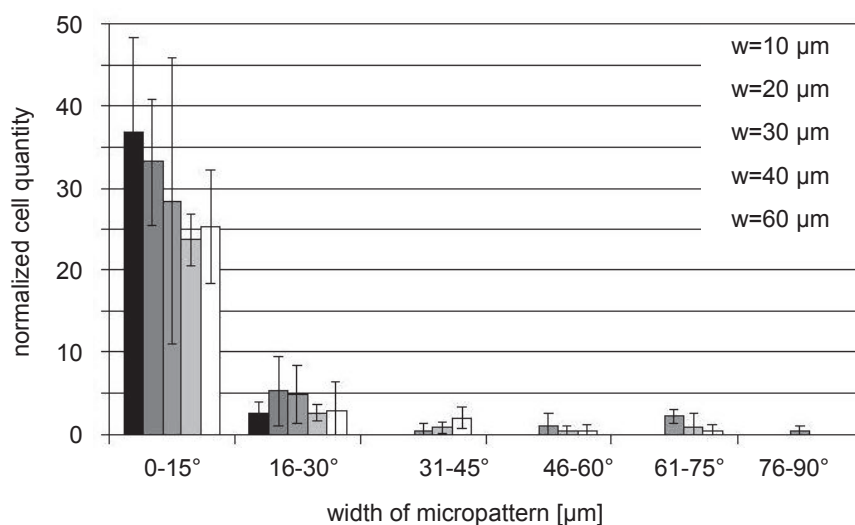


Fig. 51: Osteoblast-like osteosarcoma cell (MG-63) alignment in reference to printed hydroxyapatite micropatterns measured after three days of in-vitro proliferation

Discussion

The Aerosol-Jet[®]-printed micropattern heights (vertical direction) varied between 4 and 17 μm due to inconstant and inhomogeneous aerosol streaming. These inhomogeneously printed pattern heights are assumed to influence the cell alignment. The printing process in pattern width (horizontal direction) turned out well reproducible, with the deviation being only 2.2 μm .

All patterned HA surfaces were found to be as biocompatible as the non-patterned HA surfaces, which was reflected in the identically increasing cell quantity from day 1 to day 7. In addition, all patterned HA surfaces showed insignificant differences in the measured cell alignment.

The cell quantity of 4×10^4 cells at the starting day (day 0) was found to be too high for future tests. A measurement of the cell quantity was not possible on day 7 due to too high cell concentration on all substrates.

The fabrication of hydroxyapatite micropatterns with varying widths ranging from 10 to 60 μm showed that osteoblast-like osteosarcoma cells (MG-63) are able to align even in 10 μm wide micropatterns. A preferred cell alignment of 0 to 15° in accordance with the printed pattern direction was measured regardless of the pattern width (**Fig. 52**).

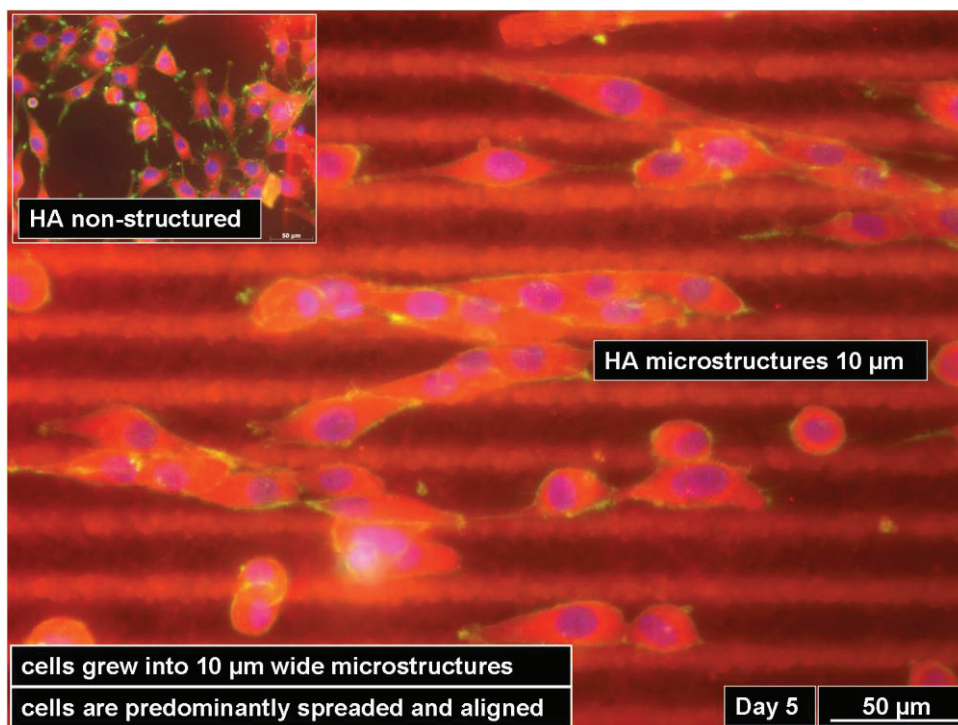


Fig. 52: Microscopic image of osteoblast-like osteosarcoma cells (MG-63) on Aerosol-Jet[®]-printed HA micropatterns with widths of 10 μm . The detail image shows cells on non-patterned HA surface. Blue: nuclei, Green: cytoskeleton, Red: vinculin staining

3.3 Micromachining

3.3.1 Micromachining of ceramic surfaces: hydroxyapatite and zirconia

The following results were accepted for publication in the “Journal of Materials Processing Technologies” in 2011 by Marzellus grosse Holthaus^a, Sven Twardy^b, Julia Stolle^a, Oltmann Riemer^b, Laura Treccani^a, Ekkard Brinksmeier^b, Kurosch Rezwan^{a*} (^aUniversity of Bremen, Advanced Ceramics; ^bUniversity of Bremen, Laboratory for Precision Machining) (Holthaus et al., 2011a).

Abstract

Computerised Numerical Control (CNC) precision machining can be employed as a fast and reproducible method for surface micropatterning. For biomedical applications, an efficient and reproducible micropatterning of zirconia and calcium phosphate-based materials is highly sought in order to guide implant interactions with surrounding biological tissues for better osseous integration. Therefore, CNC precision machining of zirconia and hydroxyapatite substrates is investigated in this study and optimised process parameters are described. By microgrinding and micromilling, microgrooves with a minimum width of 100 µm were obtained and process parameters such as cutting tool diameter and feed velocity discussed. As all samples were sintered prior to the micropatterning process, the influence of the sintering temperature on the pattern quality, size and hardness of the obtained samples is studied. Vickers hardness of the different sintered ceramic surfaces was measured in order to correlate the possible wear impact on the tip of the cutting tools. The stiffness and hardness of the used cutting tools were measured and their effect on the cutting results was discussed. The pattern quality and the average roughness in the machined microgrooves were analysed through 3D profilometry and imaged with SEM. Further, a comparison of the two machining techniques yielded more defined and less fractured micropatterns for microgrinding. The process efficiency for both methods was limited owing to the economic life time of the tool tips. For CNC grinding, life time was downsized due to more pronounced abrasive wear. For both materials, hardness was the crucial process parameter, being adjusted by the sintering temperature. For milling of zirconia, the sintering should not exceed a temperature of 1100 °C in order to minimize tool wear. Likewise, a temperature of less than 1200 °C is suggested for the milling of HA. For sintering temperatures higher than 1200 °C, the machining of both ceramic surfaces was hardly possible. The feed velocity was found not to have a significant influence on the obtained micropattern width. Finally, the preset line pitch of 100 µm was

excellently reached for both applied machining processes. It was found that lower feed velocities and smaller tool diameters caused deeper micropatterns.

Introduction

Processing of material surfaces in the micro range has become the state of the art and has opened new fields of applications and potentials for manufacturing of, for instance, micromolds with well-suited microtopographies (Brinksmeier et al., 2008) or for modification of micro-bio-interfaces for mediating interactions between medical implants and cell tissue (Kirmizidis and Birch, 2009, Lim and Donahue, 2007). Two ceramic materials that are already well established as implant materials are the oxide material yttria-stabilised zirconia (YSZ) and the calcium-phosphate-based material hydroxyapatite (HA). The former exhibits high thermal resistance, hardness and fracture toughness as well as high flexural strength and is chemically inert (Rahaman, 2003, Piconi et al., 2003). Thanks to its mechanical features and its biocompatibility zirconia is used in load-bearing medical applications (Roy and Whiteside, 2010). The non-oxide ceramic hydroxyapatite, by contrast, has lower hardness and is bioactive. It is similar to human bone apatite and is used in medical implants for increased bone in-growth (Dorozhkin, 2009).

In a previous study, we have demonstrated that the surface topography has an effect on the growth of biological cells on micropatterned surfaces (Holthaus and Rezwan, 2009). For this reason, it is necessary to develop machining processes capable of fabricating defined micropatterns with high adaptability. Several techniques for the fabrication of ceramic micropatterns are reported in the literature, such as micromolding of hydroxyapatite, zirconia, alumina, titania and silica (Holthaus et al., 2010), ceramic slip pressing of alumina (Bauer et al., 1999), laser interference patterning of hydroxyapatite and zirconia (Berger et al., 2010), and Aerosol-Jet[®] printing of alumina suspensions (Treccani et al, 2009). Some of these methods feature a very high accuracy and surface details but are, generally speaking, rather slow processes or alter either the material's crystal structure or composition during the process. Micropatterning by grinding and milling, in turn, is highly automatable, fast and reproducible on a large scale. The machining of microdevices or patterns made of polymers and metals are well-known and often reported in the literature. Various geometries in the range of about 10 μm were fabricated with very high accuracy on edges and surface detail. Adams et al. reported the microcutting of parallel microgrooves with widths of 13 μm and depths of 4 μm on curved polymethylmethacrylate (PMMA) surfaces (Adams et al., 2000). Various examples of precise micromilling can be found in further publications, e.g. the

fabrication of microbarbs from non-biodegradable stainless steel, PMMA or bio-resorbable polylactic acid (Pla-Roca et al., 2007), as well as from a fibrin-based plastic (Filiz et al., 2008). Additionally, the micromilling of 62 μm deep trenches with stepped and straight walls in PMMA (Friedrich and Vasile, 1996) was achieved. Takacs et al. reported the machining of metallic 50 μm bars with vertical sidewalls (Takacs et al., 2003). In contrast to these results, the machining of ceramic micropatterns by cutting tools is still not well-established, being very difficult due to the material's brittleness and hardness.

Thus, in this paper we investigate the micromachining of the surfaces of hydroxyapatite and zirconia. The aim of this study is to analyse and optimise process parameters for the fabrication of high-quality micropatterns of small size and with well-defined topography. For this purpose, we used a CNC precision machine tool to either mill or grind the surfaces of the ceramic samples. The thereby achieved quality was then evaluated through SEM imaging and in an optical 3D profilometry analysis.

Experimental procedure

Fabrication of the samples

Plane cylindrical platelets were fabricated by bi-axially die-pressing with 15 kN of 4.5 g of commercially available zirconia powder stabilised with 3 mol% yttria ($\text{Y}_2\text{O}_3\text{:ZrO}_2$, TZ-3YSB-E, Lot: 08M1357, Tosoh Corporation, Tokyo, Japan). The powder had a theoretical density of $6.08 \pm 0.03 \text{ g/cm}^3$ with a particle size of approximately 360 nm. Additionally, 1.7 g commercially available calcium phosphate hydroxyapatite powder (HA, $\text{Ca}_{10}(\text{PO}_4)_6(\text{OH})_2$, Prod.No. 04238, Lot: 8345A, Sigma-Aldrich Chemie GmbH, Munich, Germany) was die-pressed with identical settings. The hydroxyapatite powder had a theoretical density of $3.03 \pm 0.04 \text{ g/cm}^3$ with a particle size of approximately 150 nm. In order to reduce surface defects on the platelets the steel plungers of the die-pressing device were polished with SiC grinding paper (WS Flex, Hermes Abrasives Ltd., Virginia Beach, USA) with a grit of p2500. After die-pressing all samples were sintered in a furnace at ambient conditions (LHT08/17, Nabertherm GmbH, Lilienthal, Germany) for two hours with heating rates of 50 $^\circ\text{C/h}$ and cooling rates of 100 $^\circ\text{C/h}$ until reaching the final stability. Two different sintering temperatures were applied: hydroxyapatite samples were sintered at 1200 $^\circ\text{C}$ and 1350 $^\circ\text{C}$ respectively, while temperatures of 1100 $^\circ\text{C}$ and 1350 $^\circ\text{C}$ were chosen for the zirconia samples.

Subsequently, the sintered platelets were treated with SiC grinding papers (WS Flex, Hermes Abrasives Ltd., Virginia Beach, USA), with grits of p80 to p2500, and finally polished with p4000. For the grinding process, the ceramic platelets were pressed manually on the rotating grinding paper for 45 seconds, with a rotation speed of 150 rpm (Phoenix Alpha, Buehler GmbH, Duesseldorf, Germany). Throughout the process, water was used as a lubricant to remove excessive material and to avoid a heating of the samples. After polishing, each platelet was washed three times for five minutes with double deionised water (Synergy[®], Millipore, resistivity 18 MΩ*cm, Schwalbach, Germany) in an ultrasonic cleaner (1510 Branson[®], Branson Ultraschall, Dietzenbach, Germany).

Vickers hardness measurements

The Vickers hardness HV0.2 (kg/mm²) was measured on sintered, non-patterned ceramic samples via indentation. A quadrilateral diamond pyramid with an apex angle of 136° (Moessner Diamantwerkzeugfabrik GmbH, Pforzheim, Germany) between two opposite faces was pressed onto the specimen surface. The diameters of the indentations were measured in triplicate via an optical profilometer (Plμ 2300, Sensofar Technology, Terrassa, Spain) with 1042-fold and 3125-fold magnification, respectively. The Vickers hardness HV0.2 was then calculated including a standard deviation according to **eq. 13** below (Elssner et al., 1999).

$$HV0.2 = 0.189 \cdot F/D_{\text{ind}}^2$$

eq. 13

with F representing the applied force and D_{ind} the diameter of the indentation.

Fabrication of machined ceramic micropatterns

The manufactured ceramic samples were micropatterned with parallel straight grooves and a CNC precision machine tool (Ultrasonic 20 linear, DMG Sauer GmbH, Stipshausen, Germany), applying a micromilling or a microgrinding cutting tool respectively. Micromilling was carried out using TiAlN coated tungsten carbide cutting tools with a diameter (D) of 300 μm (#20030640603L006, Van Hoorn Hartmetaal BV, Weert, Netherlands) or 500 μm (#20050640603L010), respectively. For microgrinding, cutting tools with a diameter of 300 μm (FRSS4x63/Da0.3–KH1.5–BT0–D46HGVB, Schott Diamantwerkzeuge GmbH, Stadtoldendorf, Germany) were chosen. The grinding pins were made of a solid steel body

electroplated with diamond grains. Both fabrication methods were performed using two different feed velocities (v_f) of 125 mm/min and 250 mm/min. The rotational speed (n) was set to 40 krpm for all machining processes. The final cutting depth (a_p) was reached through a division of cuts, with single cuts with a cutting depth of $5 \pm 2 \mu\text{m}$ being performed in order to avoid tool breakage (**Fig. 53**). The clamping of the circular ceramic samples was achieved using a metal sample holder which fixed the circular samples on three contact points in order to avoid cracking.

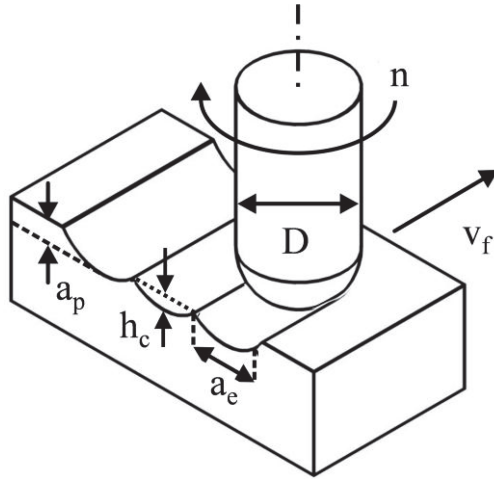


Fig. 53: Parameters for the specification of a micromachining process: diameter of the cutting tool (D), rotational speed (n), feed velocity (v_f), cusp height (h_c), line pitch (a_e), and depth of cut (a_p)

Zirconia samples sintered at 1100 °C were re-sintered at 1350 °C directly after patterning. This re-sintering was realised with the aim to reduce the micropattern size and to increase the final stability of the samples. The same treatment was applied to patterned hydroxyapatite sintered at 1200 °C.

Analysis of micropattern properties

Optical imaging and analysis

In order to analyse the properties of the fabricated grooves in terms of quality and accuracy, the micromachined ceramic surfaces were inspected via 3D measurements with an optical profilometry system (Plu 2300, Sensofar Technology, Terrassa, Spain) with 420-fold magnification. Measurements in duplicate have been conducted for each sample. The size of each single 3D measurement area was $477 \times 1272 \mu\text{m}^2$ containing 884736 measurement data points from which the surface topography was derived. For each area, the depths and widths

of three neighbouring grooves were measured in a randomly chosen 2D cross-section profile perpendicular to the groove direction, and the mean value was calculated via SensoMap Plus Software[®] (Version 5.0.3.4995, Sensofar). Additionally, scanning electron microscopy (SEM) was used at 20 kV with a Camscan Series 2 (Obducat CamScan Ltd., Cambridgeshire, United Kingdom) as an optical control. Prior to imaging, the samples were sputtered with gold (K550, Emitech, Judges Scientific plc, West Sussex, UK).

Furthermore, samples machined with a tool diameter of 300 µm were measured in triplicates with the optical profilometry so as to determine the average surface roughness (Ra) at the bottom area of the micromachined grooves. The measurement length was $L_c = 4$ mm along the feed direction. Neither filters, e.g. median or Fourier, nor restoring of missing data points were utilised for the calculation of the roughness values according to ISO4287 (ISO 4287, 1997). The same measurements were applied to non-patterned HA and $Y_2O_3:ZrO_2$ reference surfaces in order to evaluate the influence of the machining processes on the surface roughness.

Depending on the machining tool diameter (D) and the required line pitch (a_e), the depth of the machined grooves (cusp height h_c) of the fabricated micropatterns can be calculated as in **eq. 14** below (Dormer-Tools, 2005).

$$h_c = \frac{D}{2} - \sqrt{\left(\left(\frac{D}{2}\right)^2 - \left(\frac{a_e}{2}\right)^2\right)}$$

eq. 14

This relation was then used to compare the processed cusp height and groove shape to the theoretically predicted height and shape for the different processing scenarios.

Statistical analysis

The statistical analysis was performed with the aid of the statistic software Minitab[®] 15 (version 15.1.30.0, Minitab Inc.). A comparison of the experimental data was made using the non-parametric statistical hypothesis “Mann-Whitney” test (U-test) for assessing whether two independent processing scenarios show statistically significant differences. A p-value of ≤ 0.05 was considered as statistically significant. In this analysis, the effect of tool diameter, feed velocity, and the sintering temperature was investigated. Strongly different data points (“outliers”) have not been removed from the comparison.

Wear residues and abrasive wear

The presence of wear residues from machining tools was analysed by use of Energy Dispersive Spectroscopy (EDS) with a detection limit of about 0.1% of the elements' mass (Camscan Series 2, Obducat CamScan Ltd., Cambridgeshire, United Kingdom). Measurements were taken on micromilled and microground HA at 1200 °C and on zirconia at 1100 °C on two different spots with an area of $27 \times 17 \mu\text{m}^2$ each $\text{Y}_2\text{O}_3\text{:ZrO}_2$.

Moreover, X-ray Fluorescence analysis (XRF) was performed to detect elements with a high atomic number, e.g. tungsten from the cutting tool material (detection limit of approximately 10 ppm). XRF was carried out using a low pass filter (0-10 keV) and a main filter (0-40 keV) (XL3t900 AnalytiCON Instruments GmbH, Rosbach, v.d. Hoehe, Germany). Here, measurements were taken on two different circular spots, with an area of 7.1 mm^2 each. Prior to the XRF and EDS analysis, the ceramic samples were washed three times for 5 min in deionised water in an ultrasonic cleaner. To detect abrasive wear on the tools the tool tips were imaged by SEM taken at 20 kV with the Camscan SEM.

Cutting tool stiffness

The stiffness of all applied micro tools was measured by use of a multicomponent dynamometer (MiniDyn Type 9256C, Kistler Holding AG, Winterthur, Switzerland). The tips of the clamped cutting tools were moved into feeding direction, against the dynamometer. Further, the given tool deflection and the resulting forces were recorded. Eventually, the stiffness of the whole system was calculated by the slope of force vs. deflection.

Results

Determination of the sample size and Vickers hardness

Die-pressing platelets with a diameter of $30.07 \pm 0.09 \text{ mm}$ and a thickness of $2.5 \pm 0.04 \text{ mm}$ were prepared for both materials. After sintering at 1200 °C, the hydroxyapatite samples shrank to a diameter of $20.83 \pm 0.24 \text{ mm}$ and a thickness of $1.87 \pm 0.03 \text{ mm}$, equalling 88% of the theoretical density. A diameter of $19.99 \pm 0.03 \text{ mm}$ and a thickness of $1.79 \pm 0.01 \text{ mm}$ were obtained at a temperature of 1350 °C, which is equal to 99.8% of the theoretical density. The zirconia platelets yielded a density of 45% of the theoretical density after sintering at 1100 °C. They measured $29.17 \pm 0.06 \text{ mm}$ in diameter and $2.46 \pm 0.04 \text{ mm}$ in thickness.

Sintering at 1350 °C produced 93.1% of the theoretical density. The platelets were 22.84 ± 0.04 mm in diameter and 1.94 ± 0.04 mm in thickness.

For hydroxyapatite, a Vickers hardness of 630 ± 21 HV0.2 was measured for samples sintered at 1350 °C. A sintering temperature of 1200 °C resulted in a hardness of 192 ± 13 HV0.2 for this material. For zirconia samples sintered at 1350 °C, a hardness of 1263 ± 46 HV0.2 was obtained, whereas sintering at a temperature of 1100 °C yielded a hardness of 31 ± 0 HV0.2.

Micromachining of hydroxyapatite

Results from initial tests with hydroxyapatite

Initial tests with a tool diameter of 300 µm using hydroxyapatite samples sintered at 1200 °C showed that the smallest micropatterning width fabricated reproducibly by micromilling was about 100 µm. In order to improve comparability among the various process scenarios, the width of the micropatterns was fixed to this value for all subsequent milling processes with hydroxyapatite and zirconia.

In a second initial testing, the optimal line pitch for the grinding process was investigated for a tool diameter of 300 µm. An analysis of samples machined with a line pitch of 100 µm displayed no patterns, as the resulting cusp height was too low to be perceived by the machine. As a consequence of this observation, a larger line pitch of 200 µm was chosen to machine deeper grooves.

Cusp height and micropattern width of hydroxyapatite

A total of eight different machining scenarios were performed on hydroxyapatite samples. **Tab. 5** provides the summarised values of the measured surface parameters of the milled and ground samples. For a milling tool of 300 µm, the results showed that the two tested feed velocities (125 mm/min and 250 mm/min) have statistically no significant impact on the micropattern width (3a vs. 4a; $p = 0.853$) (supporting data). Similar results were achieved for widths ground with a grinding tool of 300 µm (5a vs. 6a; $p = 0.435$). Grinding with the same tool on HA (1350 °C) showed no significant difference (7 vs. 8; $p = 0.266$) between the two feed velocities on the micropattern width. Only for milling with a tool diameter of 500 µm, a p-value just within the significant range was determined (1a vs. 2a; $p = 0.049$). In this case, the increased feed velocity caused larger pattern widths.

Additionally, the influence of the two feed velocities on the cusp heights was analysed. For milling with a tool of 500 µm, the U-test evaluated a p-value of $p < 0.05$ (1a vs. 2a). The larger

feed velocity resulted in a lower pattern depth. Decreasing the milling tool diameter to 300 μm resulted in an insignificant difference, with $p = 0.533$ (3a vs. 4a). However, grinding with a tool of 300 μm showed different micropattern depths (5a vs. 6a; $p = 0.031$). Likewise for the increased sintering temperature (1350 $^{\circ}\text{C}$) a difference was detected (7 vs. 8; $p < 0.05$). For both grinding scenarios, the increased feed velocity led to smaller pattern depths.

Apart from the feed velocity, the impact of the tool diameter on the micropattern width was investigated as well. For milling with a feed velocity of 125 mm/min, a significant influence of the tool diameter was detected (1a vs. 3a; $p = 0.015$). A larger pattern width was measured for the smaller tool diameter. For an increased feed velocity of 250 mm/min, however, this significance was no longer observed (2a vs. 4a; $p = 0.623$).

Finally, the influence of the two sintering temperatures (1200 $^{\circ}\text{C}$ and 1350 $^{\circ}\text{C}$) on the ground pattern widths and heights was investigated. The differences in the machined widths were insignificant for both feed velocities. Regarding the cusp heights, only for the high feed velocity the values were statistically different (6a vs. 8; $p < 0.05$). Here, the higher sintering temperature caused a lower pattern depth.

To downsize the machined pattern geometries, the HA (1200 $^{\circ}\text{C}$) samples were re-sintered. After re-sintering at 1350 $^{\circ}\text{C}$, shrinkages from 5% to 12% in width and from 4% to 31% in cusp height were observed on milled micropatterns. On ground samples, the re-sintering caused shrinkage in the range from 5% to 8% in width and shrinkage between 15% and 23% in cusp height.

Tab. 5: Parameters for the machining of hydroxyapatite (HA)

ID	Tool	Tool diameter D (μm)	Sinter temp. T ($^{\circ}\text{C}$)	Feed velocity v_f (mm/min)	Depth of micropattern h_c (μm)		Width of micropattern a_s (μm)		deviation (%) a_s theor vs. meas.
					theoretical	measured	theoretical	measured	
ref.1	No patterns		1200						
1 a	Milling	500	1200	125	5.1	4.2 ± 0.6	100	97.2 ± 4.2	-2.8
1 b			re-sintered			2.9 ± 0.5		86.9 ± 2.9	
2 a	Milling	500	1200	250	5.1	3.1 ± 0.8	100	102.9 ± 7.0	2.9
2 b			re-sintered			2.6 ± 1.1		91.8 ± 8.1	
3 a	Milling	300	1200	125	8.5	9.7 ± 1.3	100	100.6 ± 3.8	0.6
3 b			re-sintered			8.5 ± 1.5		88.2 ± 6.8	
4 a	Milling	300	1200	250	8.5	10.1 ± 1.7	100	100.4 ± 2.8	0.4
4 b			re-sintered			9.7 ± 0.9		95.6 ± 2.2	
5 a	Grinding	300	1200	125	38.2	18.5 ± 1.2	200	201.5 ± 1.4	0.75
5 b			re-sintered			14.2 ± 1.3		186.3 ± 4.5	
6 a	Grinding	300	1200	250	38.2	16.5 ± 2.5	200	198.4 ± 6.8	-0.8
6 b			re-sintered			14.0 ± 0.7		188.5 ± 1.0	
7	Grinding	300	1350	125	38.2	18.7 ± 2.1	200	200.6 ± 1.7	0.3
8	Grinding	300	1350	250	38.2	11.7 ± 2.5	200	200.0 ± 1.2	0

re-sintered = micromachined samples were treated at 1350 $^{\circ}\text{C}$ after the machining process

Surface topography of hydroxyapatite

The HA samples (1200 °C) milled with a feed velocity of 125 mm/min exhibited a U-shaped topography. In contrast, the higher feed velocity of 250 mm/min produced a V-shaped surface as shown in **Fig. 54** a and b.

Grinding of HA (1200 °C) delivered sharply edged grooves (rectangle profile) with pattern sidewalls almost vertical and perpendicular to the bottom area. This was observed for both applied feed velocities (**Fig. 54** c and d).

SEM micrographs (magnification 1640-fold; data not shown) showed that there were loose particles and small pores with a size of about 1 μm on machined HA sintered at 1200 °C. In addition, microcracks were visible, too. These features were observed on milled and ground surfaces of HA (1200 °C). Similar surface properties were found for HA 1350 °C for both machining processes. However, fewer loose particles were visible on the surface, which displayed a higher peak to valley ratio.

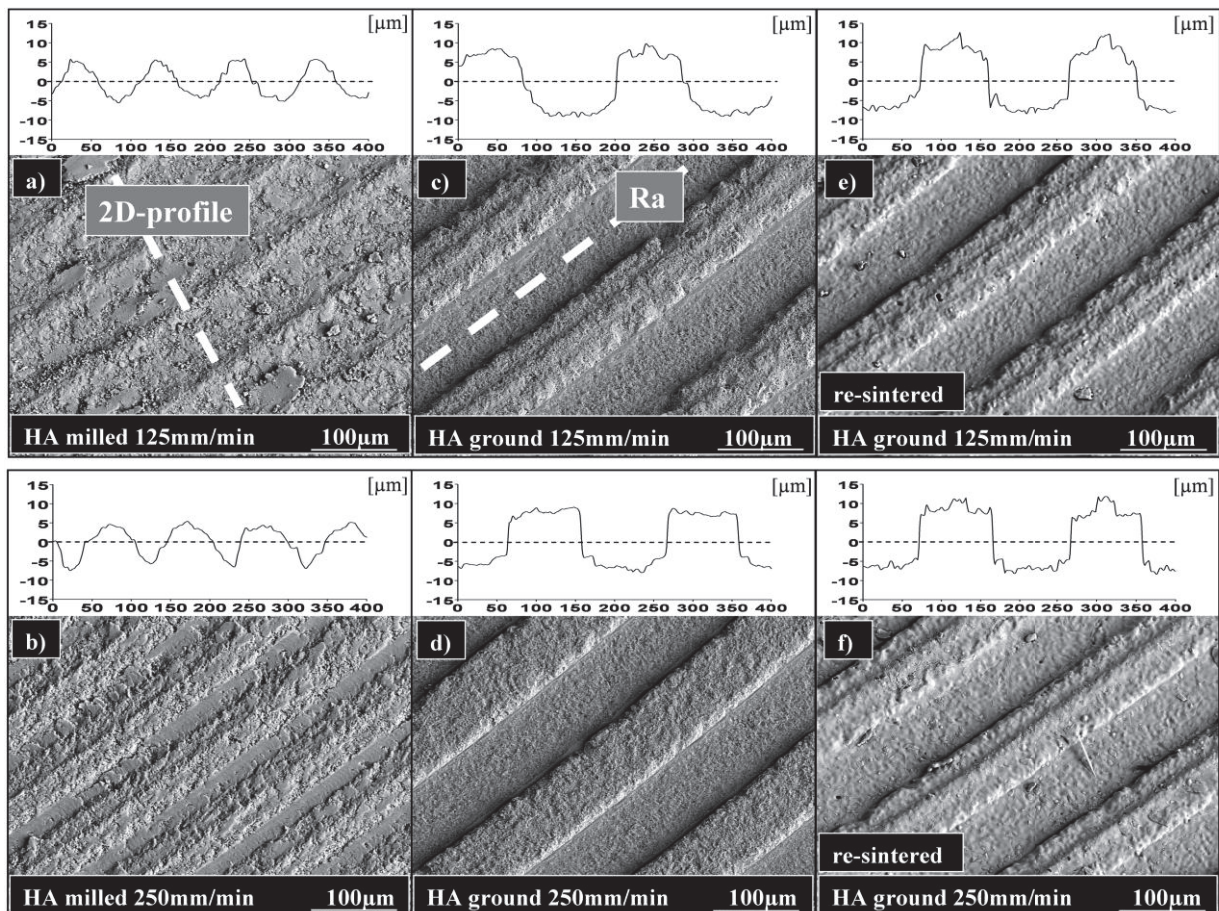


Fig. 54: SEM micrographs (magnification 200-fold) and 2D profile cross-section measurements (white insets) of hydroxyapatite (1200 °C) machined with a tool diameter of 300 μm . The position of a cross section is exemplarily shown in a); the roughness measurements Ra are exemplarily shown in c). a) and b): milled hydroxyapatite; c) and d): ground hydroxyapatite; e) and f): re-sintered samples from c) and d)

The re-sintering of the HA samples changed the surface topography slightly, with the amount of pores being reduced. Through this process the micropattern size decreased, yet there was no visible effect on pattern edges and geometries (**Fig. 54** e and f).

A comparison of the SEM micrographs of the milling and the grinding processes in **Fig. 54** showed that the milled samples are bumpy, chipped and rough, whereas the ground surfaces displayed smoother surfaces. This could be confirmed in surface roughness measurements on HA (1200 °C) milled or ground with a tool of 300 µm in diameter as shown in **Fig. 55**. Non-patterned samples featured a roughness of 0.40 ± 0.07 µm (ref.1), while milled samples had a roughness of 0.48 ± 0.03 µm (3a) and 0.70 ± 0.04 µm (4a) depending on the feed velocity. By grinding, the microgrooves showed a considerably smoother surface of 0.26 ± 0.01 µm (5a) and 0.24 ± 0.01 µm (6a). The re-sintering of the machined samples increased the groove's roughness for all milled samples (3b = 0.71 ± 0.03 µm; 4b = 0.81 ± 0.04 µm) and grinding setups (5b = 0.68 ± 0.08 µm; 6b = 0.71 ± 0.03 µm).

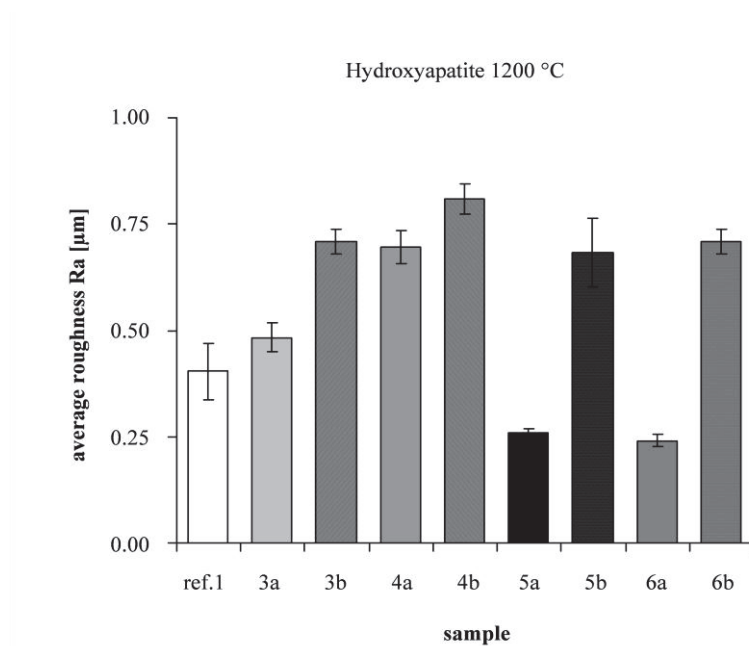


Fig. 55: Average roughness Ra for all samples, measured in the machined microgrooves at the bottom area along the feed direction of micromachined hydroxyapatite. Error bars show the standard deviation. Descriptions of the samples are given in Tab. 5.

Predictability of cusp heights and pattern widths of hydroxyapatite

For all milling processes on HA (1200 °C) a preset micropattern width of 100 µm was set. The milled widths showed a maximum deviation of 2.9% from the pre-selected value. This finding was independent of all other process parameters. An even smaller deviation, i.e. of

0.8%, was achieved by grinding the HA samples sintered at 1200 °C and 1350 °C (**Tab. 5**). The measured values of the cusp heights were evaluated according to **eq. 14**. As depicted in **Fig. 56**, an overlap between the measured values (including error bars) and the predicted ones is found for milling with a feed velocity of 125 mm/min for both tool diameters. The mean value for these two setups is about 12% of the corresponding theoretical value. For the higher feed velocity, a deviation of the mean value of 42% ($D = 500\mu\text{m}$) and 17% ($D = 300\mu\text{m}$), respectively, was found. The theoretical values of the cusp height for microgrooves machined by grinding overestimated the measured heights significantly (deviation > 48 %).

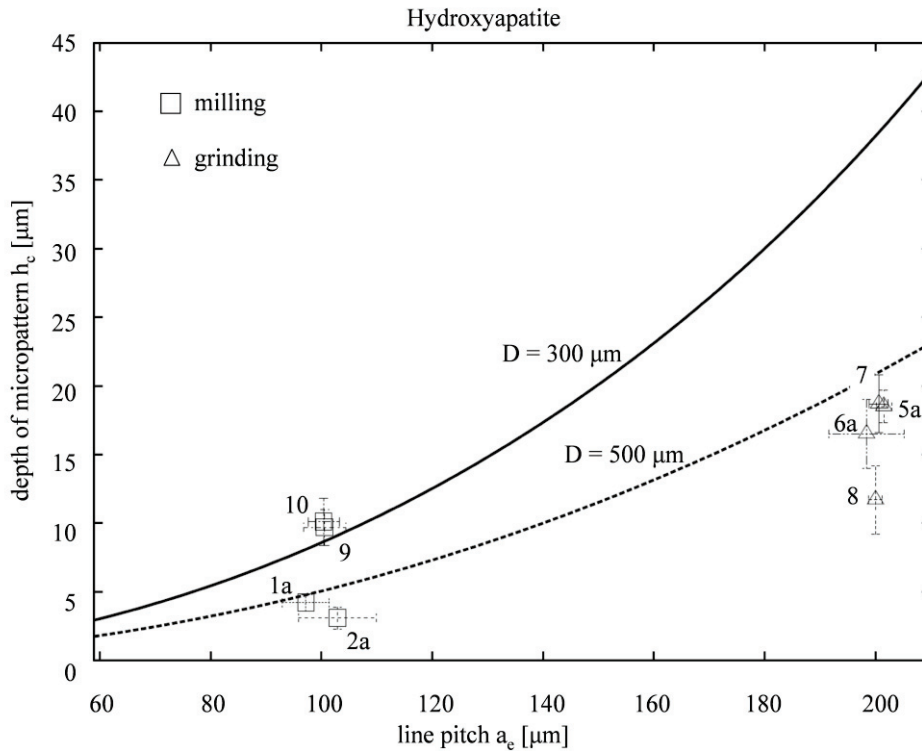


Fig. 56: Micropattern depths (h_c) according to eq. 14 for two different cutting tool diameters (D) versus the line pitch (a_e). Data points show the experimentally obtained results for hydroxyapatite. Error bars show the standard deviation. Descriptions of the samples are given in Tab. 5.

Machining of zirconia

Cusp height and micropattern width of zirconia

For the micromachining of zirconia a total of eight different processing setups were carried out. The summarised values of the measured surface parameters of the milled and ground samples are given in **Tab. 6**. A statistical analysis showed that the obtained pattern widths did not display any difference concerning the two feed velocities. This was true for all tool diameters and sintering temperatures for both machining methods (**supporting data in the**

appendix). In addition, the effect of the two feed velocities on the cusp heights of milled zirconia (1100 °C) was investigated. The results from this showed a difference in the milled cusp heights by using a tool diameter of 500 µm (9a vs. 10a; $p = 0.003$). Decreasing the tool diameter to 300 µm, also the cusp heights were different for the two feed velocities (11a vs. 12a; $p < 0.050$). For both milling tool diameters, the higher feed velocity caused lower pattern depths. On zirconia surfaces sintered at 1350 °C the two feed velocities showed no significant difference in the milled pattern depth (13 vs. 14; $p = 0.220$).

Tab. 6: Micromachining parameters and results for yttria-stabilised zirconia ($Y_2O_3:ZrO_2$)

ID	Tool	Tool diameter D (µm)	Sinter temp. T (°C)	Feed velocity v_f (mm/min)	Depth of micropattern h_c (µm)		Width of micropattern a_w (µm)		deviation (%) a_w theor. vs. meas.
					theoretical	measured	theoretical	measured	
ref.2	No patterns		1100						
9 a	Milling	500	1100	125	5.1	4.7 ± 1.5	100	100.1 ± 1.5	0.1
9 b			re-sintered			2.9 ± 0.3		79.7 ± 1.6	
10 a	Milling	500	1100	250	5.1	3.0 ± 1.8	100	98.4 ± 5.8	-1.6
10 b			re-sintered			3.4 ± 0.6		79.5 ± 1.5	
11 a	Milling	300	1100	125	8.5	8.0 ± 0.6	100	100.6 ± 1.5	0.6
11 b			re-sintered			5.5 ± 0.4	100	78.5 ± 1.4	
12 a	Milling	300	1100	250	8.5	6.9 ± 1.1	100	100.1 ± 2.2	0.1
12 b			re-sintered			4.3 ± 0.3	100	78.1 ± 2.0	
13	Milling	500	1350	125	5.1	1.6 ± 1.1	100	87.1 ± 25.0	-12.9
14	Milling	500	1350	250	5.1	1.0 ± 0.7	100	98.9 ± 13.5	-1.1
15 a	Grinding	300	1100	125	38.2	14.8 ± 1.0	200	200.1 ± 1.3	0
15 b			re-sintered			11.4 ± 0.4		153.7 ± 1.6	
16 a	Grinding	300	1100	250	38.2	14.0 ± 0.6	200	200.0 ± 1.5	0
16 b			re-sintered			10.3 ± 0.7		153.9 ± 1.2	

re-sintered = micromachined samples were treated at 1350 °C after the machining process

The results from grinding with a tool of 300 µm on zirconia (1100 °C) showed a difference in the achieved cusp heights when comparing the two feed velocities (15a vs. 16a; $p = 0.030$), with the higher feed velocity causing in average slightly lower pattern depths.

Beside the feed velocity, the influence of the tool diameter on the micropattern width was investigated, too. For milling with a feed velocity of 125 mm/min, the influence of the tool diameter proved to be not significant (9a vs. 11a; $p = 0.169$). Also the tool diameter showed no influence on pattern widths when milling with the higher feed velocity of 250 mm/min (10a vs. 12a; $p = 0.410$).

Furthermore, it was investigated if the two sintering temperatures (i.e. 1100 °C and 1350 °C) had an influence on the micropattern depth or width of milled zirconia surfaces. The difference in width was found to be insignificant for both feed velocities for milling ($D = 500$ µm) of zirconia (9a vs. 13; $p = 0.174$ and 10a vs. 14; $p = 0.355$). On the other hand, differences were found comparing the milled pattern depths for both feed velocities (9a vs. 13; $p < 0.05$ and 10a vs. 14; $p = 0.001$). Decreased pattern depths were measured for

increased sintering temperatures. The re-sintering at 1350 °C of milled micropatterns on zirconia surfaces caused shrinkages from 19% to 22% in width and from 31% to 38% in pattern depth. One milled sample (10) showed an increase in cusp height of 13% after re-sintering. After re-sintering of ground zirconia samples, shrinkage of 23% in micropattern width and from 23% to 26% in pattern depth was measured.

Surface topography of zirconia

The milling of sintered zirconia (1100 °C) resulted in U-shaped micropattern profile topographies independent of the two feed velocities (**Fig. 57 a and b**). Grinding of zirconia (1100 °C) produced sharply edged micropatterns for the two applied feed velocities (**Fig. 57 c and d**). The pattern shape was neither U- nor V-shaped, and the pattern sidewalls were almost vertical and perpendicular to the bottom area of the ground micropatterns. **Fig. 57 c to f** image clearly the circular tool marks.

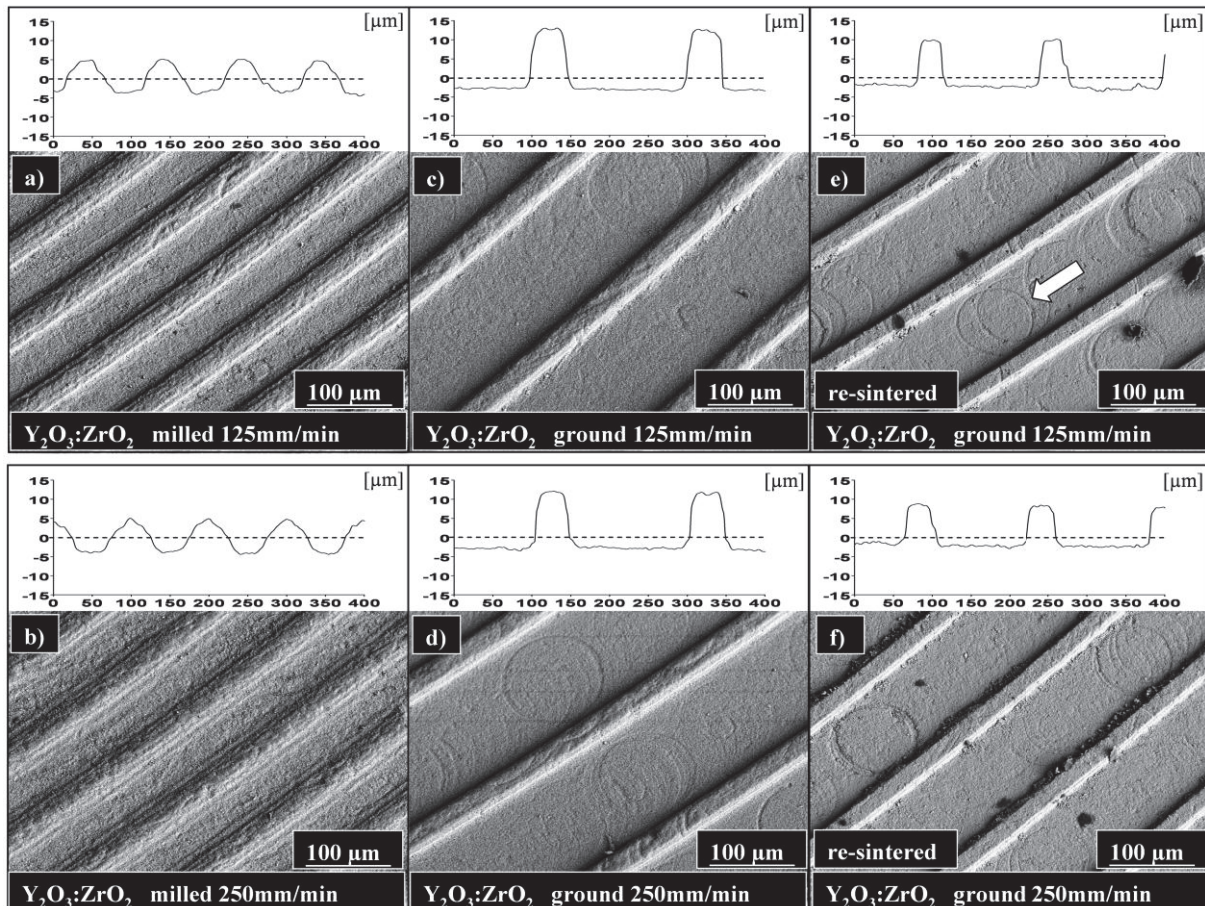


Fig. 57: SEM micrographs and 2D profile cross-section measurements (white insets) of zirconia (1100 °C) machined with a tool diameter of 300 μm; a) and b): milled zirconia; c) and d): ground zirconia; e) and f): re-sintered samples from c) and d). Grey arrow in e) shows a tool mark.

The presence of loose particles is visible on zirconia (1100 °C) in SEM micrographs at a magnification of 1640-fold (data not shown). In addition, the surfaces are highly porous, with pore sizes of about 1 µm. These findings are observable on milled and ground zirconia (1100 °C) samples. No microcracks were found on these surfaces.

On zirconia surfaces (1350 °C) nearly no pores were distinguishable after milling, but many grooves were found on the machined areas. These findings were similar to the results of ground zirconia (1350 °C). Here, a few pores (1 µm) and many grooves were found on the machined areas. The re-sintering at 1350 °C reduced the amount of pores on zirconia (1100 °C). The visible surface characteristics were not changed by re-sintering, yet shrinkage of the micropatterns was found.

Roughness measurements yielded that the differences in roughness of milling and grinding processes are not pronounced as shown in **Fig. 54**. All zirconia samples exhibited a reduced roughness after exposure to the milling or grinding tool as compared to the non-patterned sample (ref. 2).

The re-sintering induced an increase of the coarseness for all zirconia samples. For instance, the roughness value of sample 11a with a roughness of $R_a = 0.15 \pm 0.01$ µm increased to $R_a = 0.25 \pm 0.07$ µm after re-sintering (11b). The machined zirconia samples displayed smoother surface roughness values as compared to the hydroxyapatite samples. Thus, the milling with 125 mm/min on zirconia resulted in $R_a = 0.15 \pm 0.01$ µm (11a). The identical process on hydroxyapatite yielded a R_a of 0.48 ± 0.03 µm (3a).

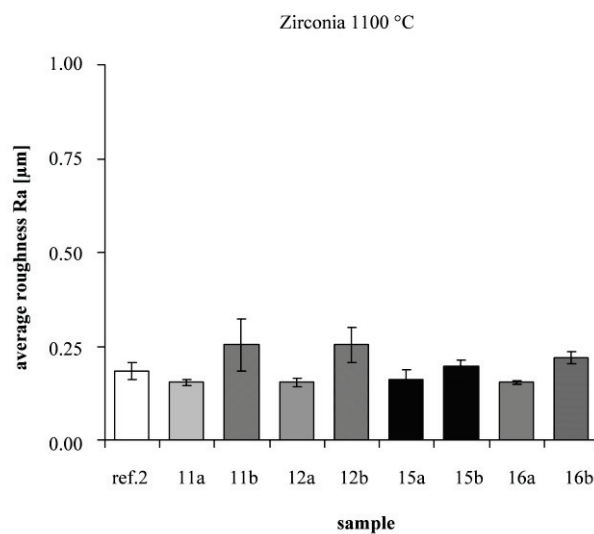


Fig. 58: Average roughness values R_a , measured in the machined microgrooves at the bottom area along the feed direction of micromachined zirconia. Error bars show the standard deviation. Descriptions of the samples are given in Tab. 6.

Predictability of cusp heights and pattern width of zirconia

To evaluate the precision of the milling processes on zirconia (1100 °C), a pre-selected micropattern width of 100 μm was set for the six different milling scenarios. For one milled sample (13) a deviation of 12.9% in micropattern width from the pre-selected one was found, yet in the remaining five testing events the deviation from the pre-selected pattern width was less than 2%. This outcome was independent of all other varied milling parameters. Grinding showed a deviation of merely 0.1% from the preset micropattern width of 200 μm for both tested feed velocities.

The experimentally obtained cusp heights were evaluated according to **eq. 14**. An overlapping between the measured values (including error bars) and the predicted values is given for milling with a tool of 500 μm for both feed velocities, as shown in **Fig. 59**. In detail, the mean value for milling with a feed velocity of 125 mm/min showed a deviation of 7%. However, a deviation of 39% was found for the higher feed velocity of 250 mm/min. This shows that for the higher feed velocity only outliers are responsible for the overlap.

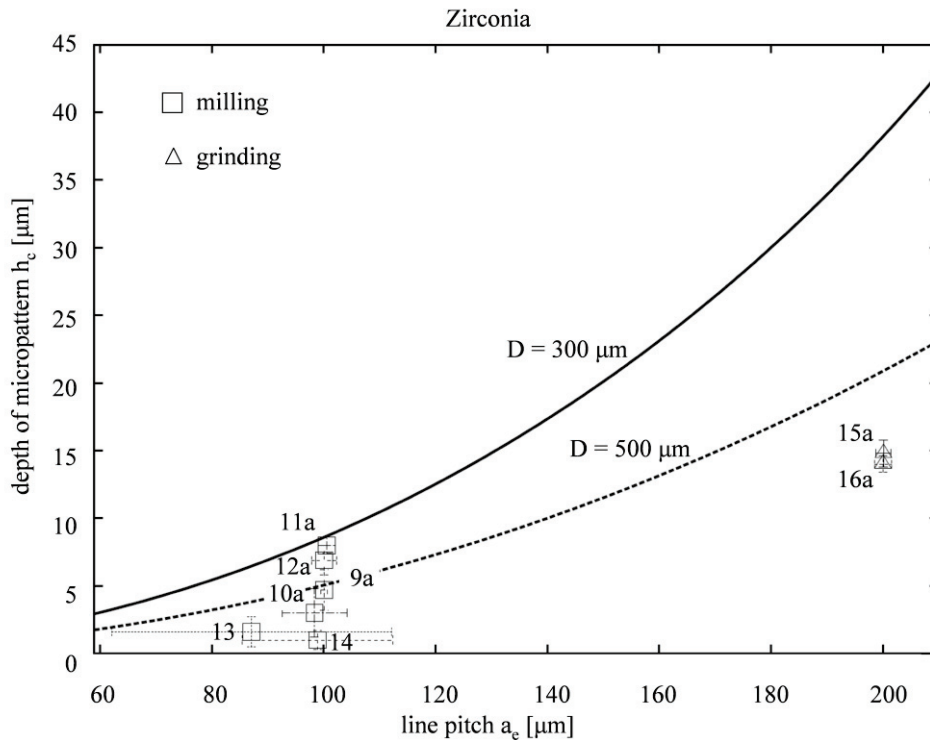


Fig. 59: Micropattern depths (h_c) according to eq. 14 for two different cutting tool diameters (D) versus the line pitch (a_e). Points show the experimentally obtained results for zirconia. Error bars show the standard deviation. Descriptions of the samples are given in Tab. 6.

Milling with a tool of $300\ \mu\text{m}$ and a feed velocity of $125\ \text{mm/min}$ yielded an overlap of the measured values and the predicted cusp heights. Here, a divergence of 8% between mean value and predicted cusp height was observed. At a feed velocity of $250\ \text{mm/min}$ the deviation was 20%.

Independently of the feed velocity, milling of zirconia ($1350\ ^\circ\text{C}$) showed no overlap between the measured cusp heights and the predicted ones, with deviations of more than 50%. For the grinding of zirconia the predicted cusp heights clearly exceeded the measured values, with deviations of more than 60%.

Wear residues and abrasive wear

In order to evaluate the effect of abrasion on the tool tips, SEM micrographs were taken before and after the machining procedures. Wear due to abrasion was noticeable for both fabrication methods (**Fig. 60**). EDS and XRF analysis were performed for hydroxyapatite and zirconia in order to investigate if wear residues could be found on the surface of the micromachined samples. Although both surface analyses were conducted on two different spots, no significant differences within the detection limit could be observed, neither before nor after micromachining the ceramic surfaces.

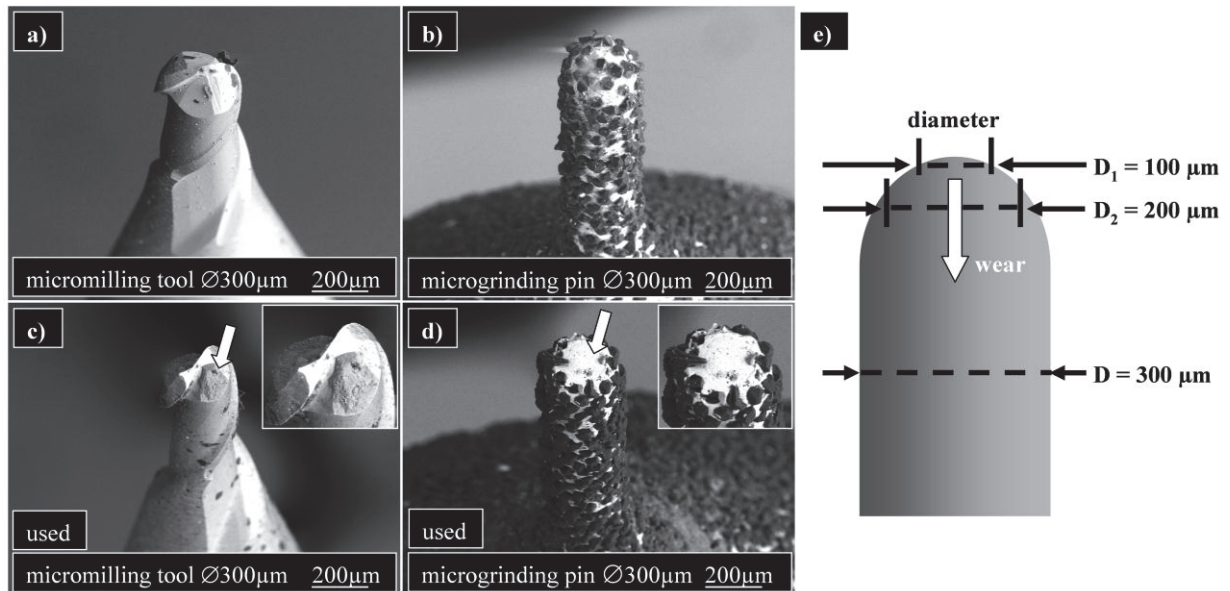


Fig. 60: SEM micrographs of tools for micromilling (left) and microgrinding (right). The cutting tools before use are shown in a) and b); c) and d) show wear due to abrasion (white arrow and magnification box); e) illustrates an increase in the tool tip diameter from the effective cutting diameter D_1 to D_2 due to abrasive wear.

Cutting tool stiffness

The measured tool stiffness was 323 N/mm for ball end milling tools with a diameter of 500 μm . The ball end mills with tool diameters of 300 μm had a stiffness of 163 N/mm. The lowest stiffness of 27 N/mm was measured for the grinding pins (**Fig. 61**).

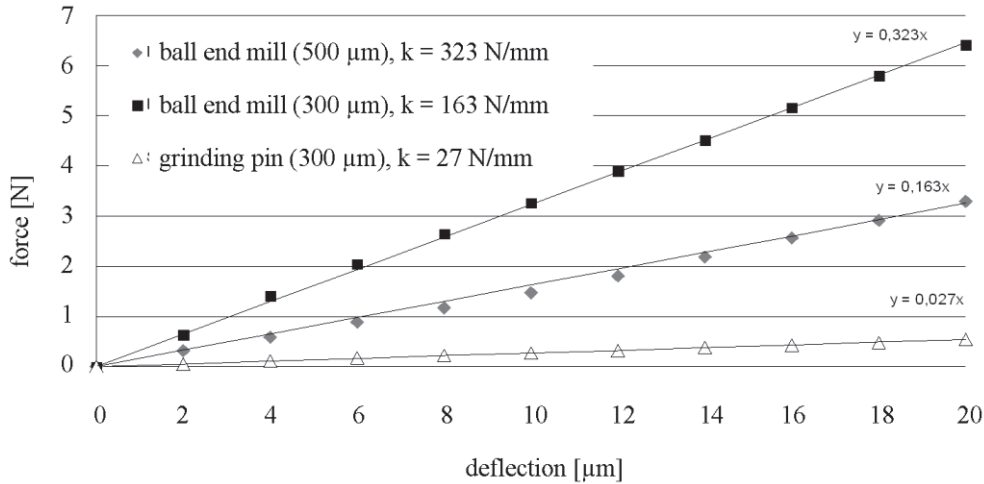


Fig. 61: The tips of the clamped cutting tools were moved into feed direction against a dynamometer. The tool deflection and the resulting forces were recorded. The stiffness of the whole system was calculated by the slope of force vs. deflection.

Discussion

Topographical characteristics

The U-shaped surface produced by milling of zirconia and slow milling of HA resembled the kind of topography found in earlier studies for ball-end shaped milling tools (Lazoglu, 2003). In the case of the higher feed velocity for milling of HA (1200 $^{\circ}\text{C}$), we assume that chipping occurs during the process and causes a sharply edged V-shaped surface topography. During this process, also microcracks might appear at the machined surface. The influence of these microcracks after machining on the strength of a ceramic has already been described. Thus, Griffith et al. and Gogotsi and Andrievski stated that the strength of ceramics in brittle condition is defined by surface and by volume defects in the material. The strength decreases with the presence of strong surface relief on sintered ceramic samples or due to microcracks appearing after electro-machining or diamond cutting (Griffith et al., 1921, Gogotsi and Andrievski, 1999). Hence, the occurrence of chipping depicts a loss of quality of the microstructure and is very likely to decrease the sample's overall strength.

The rectangle profile caused by grinding of both materials cannot be explained on the basis of fracturing or chipping of the machined surface. More likely, the rectangular surface profiles were caused by the instantaneous abrasive wear and thus flattening of the grinding pin tip. This hypothesis is supported through the results from pre-testing. Therefore, a pre-selected micropattern width of 100 μm only patterns with insufficient cusp heights were ground. As the height of the tool tip was fixed during the machining process, the low cups heights are caused by immediately wearing down the tool tip (**Fig. 60**). Therefore, by selecting the machining method the user is able to predetermine the surface relief topography. Regarding the process efficiency, the limiting factor is the short economic life time of the grinding tools. This circumstance makes the grinding method disadvantageous concerning costs and machining time. Consequently, we suggest instead the use of novel CVD diamond-coated shaft tools.

In the SEM micrographs, the circular tool marks are clearly visible (**Fig. 57**). These circular defects occur when cutting conditions are subject to local changes. Cutting the material is temporarily inhibited because of an increased mechanical resistance. The surface is too hard on these specific positions to be removed homogenously by the cutting tool. Thus, the cutting tool cannot progress that fast and is slowed down for a few turns on these positions, which in turn results in a circular removal of the material. This causes a formation of circular tool marks. We therefore assume that the selected cutting speed is too low and the feed velocity too high on the positions where the tool marks occur.

The ground HA samples displayed a smoother microchannel surface as compared to the non-patterned reference sample. This decrease of roughness is caused by large micron-sized grains, which are pulverized into smaller submicron-sized grains within the grinding contact region. These submicron grains then act as a fine powder filling the irregularities of the ground groove. Due to the generated heat of the grinding process the grains re-sinter, which fosters a smoothing of the surface (Marinescu et al., 1999). Compared to the roughness of the untreated samples, milling of HA increased the surface roughness. This increase is in accordance with the findings of Chelule et al. For a larger order of magnitude, Chelule et al. showed that the surface of milled HA was highly porous. They suggested that a removal of grains during the milling process causes unevenness and thus an increase in the surface roughness (Chelule et al., 2003). We for our part suppose that a similar effect in combination with surface fracturing/microcracking - which causes unevenness, too - was responsible for our measured increase of HA surface roughness.

Additionally, we measured a more distinctive roughness for the samples milled with the higher feed velocity of 250 mm/min. The SEM micrographs revealed a larger degree of fracturing on these samples. The higher roughness was caused by a more distinct peak-to-valley topography. Grinding of HA is therefore more suitable to achieve highly defined patterns with smooth surfaces. If an application requires rougher channel surfaces, milling of HA seems to be the better choice.

Similar to the findings for hydroxyapatite, the SEM micrographs of the ground zirconia samples showed a smoother surface structure as compared to the milled ones. Roughness measurements yielded, however, that the differences were not significant. Nevertheless, all zirconia samples exhibited a similar surface roughness after exposure to the milling or grinding process. SEM micrographs showed no fracturing of zirconia (1100 °C) for both processing methods. We thus suppose that this is caused by the lower hardness compared to HA (1200 °C). Due to the absence of fracturing/microcracking on zirconia, roughness was not influenced by the machining method. In contrast to the results concerning HA, with zirconia the machining method can only be used to influence the surface relief topography but not the surface roughness inside the micropatterns.

Tool tip wear residues

No residues from the tools were found on the ceramic samples after machining. We assume that loose particles debris from the tool tips were centrifuged away from the sample during the machining process. In addition, remaining wear particles were fully removed from the samples in the course of three washing processes in double deionised water in an ultrasound cleaner. Thus, no contamination of the ceramic surfaces with cutting tool particles took place.

Process parameters

Due to the lowered stiffness, the resilience of the grinding pins was six to twelve times higher than that of the applied micro milling tools, which was caused by two tool properties. Firstly, the milling tool material (tungsten carbide) has a three times higher elastic module than the grinding pin material (steel). Secondly, the milling tools have a higher area moment of inertia than the grinding pins.

The cutting forces were not measured in this study. In general, the average cutting force is mainly dominated by the machining parameters and the workpiece material properties. If all boundary conditions are kept constant, the maximum cutting force can be assumed to be

lower for grinding pins, due to the shape of the cutting tool. The removal of material takes place on a large area – thus, at an undefined number of cutting edges – as compared to two defined active cutting edges when using a milling tool.

For all used tools a certain amount of tool deflection occurs during the machining of ceramics. In ball end milling of straight grooves, this effect is not that important since the minor inclination of the cutting edge causes only small differences in the cutting conditions. So, no differences in the cutting widths are expected. Due to tool deflection the cutting depth would be marginally lower as adjusted, whereas the cusp height (h_c) would not be influenced by the tool deflection. The tool deflection seems to be negligible in all experiments. As can be seen from the SEM micrographs of the tools, the worn-out tip surfaces are nearly flat instead of conical, as expected for strong deflected cutting tools. The tool's hardness seems to be a more influencing factor for the surface patterning. Due to different tool materials, the tools have different levels of hardness and distinct wear characteristics. So, TiAlN coated tungsten carbide mills have a hardness of about 2212 ± 105 HV, measured via Vickers indentation test (HV0.2). Thus, the mills are harder than the sintered ceramics, but the mills may abrade due to abrasive wear during the cutting process.

The grinding pins were made of a solid steel body electroplated with diamond grains. The hardness of the steel body measured nearly 960 ± 68 HV, thus being much lower than e.g. zirconia samples sintered at 1350°C with a hardness of about 1300 HV. The hardness of diamonds is about 9000 HV (according to manufacturer data), which is many times higher than the ceramic's hardness. The diamonds are galvanically bonded to the steel body. The strength of such bonding is very important, though unknown. The embedding depth of the diamond grains is lower on strongly curved parts of the ball-end tool. Therefore, loss of grains is likely to occur in these curved areas. If such a loss of grains occurs at the tool tip, the bare steel shaft is exposed to the sample. Consequently, an ongoing abrasive flattening of the steel tool is to be expected, whereas the tool length decreases continuously (**Fig. 60**). This assumption could be affirmed through SEM micrographs, where a loss of single grains after short-time cutting became visible (**Fig. 62**). This unintentional flattening of the tool shaft is probably the main reason for the rectangular ceramic micropatterns, instead of the V and U-shaped profiles as fabricated with the milling tools.

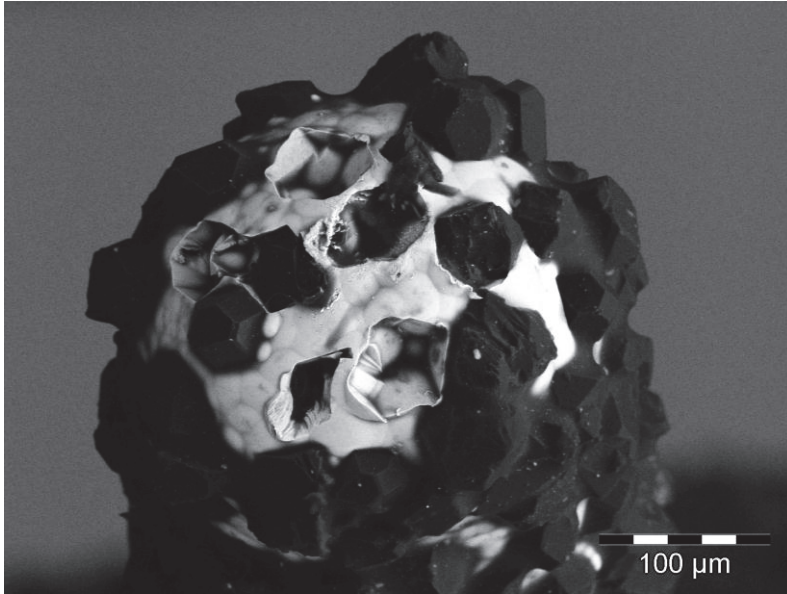


Fig. 62: SEM micrograph of a short-time used grinding pin with partially loss of diamond grains at the tool tip

An analysis of the machining processes has revealed that the feed velocity has nearly no impact on the machined pattern widths for both materials. Only for milling of HA (1200 °C) with a tool of 500 μm, slightly different widths were detected. In contrast, the determination of the feed velocity had a significant influence on the majority of the machined cusp heights. This was found for HA as well as for zirconia, for both processing methods. For all setups that showed a significant difference the higher feed velocity caused lower cusp heights. This suggests that a higher feed velocity increases the wear and fracture of the tool or an increased mechanical resistance causes tool deflection, which leads to lower penetration depth. In consequence, the depth of indentation of the tool and therefore the machined cusp heights decrease.

The milling tool diameter and sintering temperatures showed no clear and distinct influence on the machined micropattern widths and depths for HA. Likewise for zirconia, the milling tool diameter and the sintering temperature had no significant influence on the machined pattern widths, either. A variation of the sintering temperature, however, caused a distinct difference in the cusp heights. The machined cusp heights on zirconia 1350 °C were remarkable low. These results unveil the impossibility to operate micromilling accurately and repeatedly. Therefore, the difference in cusp heights for the two sintering temperatures might be due to the high hardness of zirconia (1350 °C). Although the sintering temperature has no significant influence on the pattern geometries, it is responsible for the high abrasive wear of the tool tips. To guarantee a machinability of the two ceramic surfaces, the sintering

temperature needs to be chosen carefully so as to adjust a proper material hardness. For milling of zirconia the sintering temperature should not exceed 1100 °C in order to minimize tool wear. A temperature of maximally 1200 °C, or even lower, is suggested for the milling of HA. As in this study high abrasive wear was observed in the grinding of both materials, an optimized sintering temperature for this process lies considerably below the used temperatures.

Model prediction

The model given in **eq. 14** assumes an ideal machining process. However, effects like tool wear, vibration, chipping or fracturing are not taken into account. This deficiency of the model became manifest in the comparison between the predicted and the measured cusp heights. The occurring deviations demonstrated that **eq. 14** does not describe a suitable model for the cusp heights of the two machining processes. Particularly all grinding setups exhibited strong deviations of a minimum of 58% for both materials. The pre-selected micropattern widths could be machined with good accuracy for both ceramic materials and processing methods. In most of the cases the deviation was less than 3%.

Conclusions

Hydroxyapatite and zirconia surfaces could be micropatterned successfully by using CNC precision machining. Milling of HA caused two different kinds of micropatterns: a U-shaped or a V-shaped topography, depending on the feed velocity. Milling of zirconia caused a U-shaped topography. Grinding generated edgy rectangular patterns for both materials. When compared to the milled HA samples, all ground HA samples exhibited a smoother surface roughness at the bottom area along the feed direction of the micromachined groove-like patterns. No difference in the surface roughness was observed for zirconia.

The sintering temperature has a major influence on the sample's Vickers hardness and has therefore a strong impact on the machinability. This aspect was found to be heavily influencing in terms of abrasive tool wear, which in turn altered significantly the fabricated pattern depth. Neither the sintering temperature nor the choice of different tool diameters, however, had a distinct influence on the obtained micropattern width. This was found for both processing methods as well as for both materials. Although stiffness was strongly different comparing milling and grinding tools, this property seems to have a negligible effect for all cutting processes. By contrast, the different wear characteristics of the tools were mainly

responsible for the varying pattern topographies. In this context the increased unintentional flattening of the grinding tool is supposedly the main reason for the rectangular ceramic micropatterns. Our results also indicated that the feed velocity had no distinct influence on the produced micropattern width. For both machining processes the preset line pitch of 100 μm was perfectly reached without exception. Concerning the cusp heights, lower feed velocities caused deeper micropatterns. A precise theoretical prediction with regard to the processed cusp height was not possible. The re-sintering of the machined samples led in all cases to a distinct shrinkage of the patterns. Taking all our findings into account, it can be said that the optimal production scenario depends on the required properties of the processed micropatterns. Although abrasive wear occurred at the tool tips no unintentional contamination of the samples' surfaces could be found.

3.3.2 Monitoring osteoblast viability on hydroxyapatite with adjusted submicron and micron surface roughness by using proliferation reagent WST-1

The following results have been partially submitted to the “Journal of Materials Science: Materials in Medicine” in 2011 by Marzellus grosse Holthaus, Laura Treccani and Kuroschi Rezwan (University of Bremen, Advanced Ceramics) (Holthaus et al., 2011c).

Abstract

The dependency of human osteoblast viability on hydroxyapatite submicron and micron surface roughness has hitherto not been clarified yet. Therefore, we investigated in this study the effects of hydroxyapatite substrates with different well-adjusted levels of surface roughness on human osteoblast proliferation by using colorimetric reagent WST-1. By grinding we obtained hydroxyapatite surfaces with six levels of well-defined surface roughness ranging from $S_a = 3.36 \mu\text{m}$ down to $0.13 \mu\text{m}$, which resulted in hydrophilic contact angles of 11° to 27° . Energy dispersive X-ray spectroscopy, X-ray diffraction and X-ray fluorescence measurements confirmed that neither grinding paper residues nor changes in the crystal structure were introduced to the hydroxyapatite substrate during the grinding process. The application of this simple surface treatment allowed the effects of the surface roughness to be independent from surface chemistry, crystal structure, and relative density. The osteoblast proliferation and collagen type I expression on the fabricated surfaces was investigated in-vitro after 1, 3, and 7 days. All surface-treated samples caused a good cell attachment, as flat and spread cell morphologies with lamellipodiae and filopodiae were present after one day already. The cell proliferation obtained through WST-1 assay differed insignificantly for samples of varying roughness. The semi-quantitative assessment of collagen type I yielded the same amounts for all samples on days 3 and 7. From the obtained results we can clearly conclude that significant differences in the osteoblast proliferation are not detectable via WST-1 assay on HA micron and submicron surface roughness in-vitro within the first seven days.

Introduction

Micropatterned and roughened ceramic surfaces are of great interest in biological and medical research fields (Kim et al., 2006; Mustafa et al., 2005). Compared to metals or polymers, the advantages of oxidic ceramics consist in their chemical resistance and inertness, their high

hardness as well as temperature resistance (Lemons, 1996; Munz and Fett, 1999). The use of calcium phosphate ceramics in medical applications is very common due to the chemical similarities to biological apatite in bone or teeth (Dorozhkin, 2009; Wang et al., 2005). One of these important apatites is hydroxyapatite (HA), which is used e.g. as a coating on titanium (Ti) implants or as bone-replacing material (Boyan et al., 1996; Mangano et al., 2010). The interface between cells and the implant surface exhibits a strong influence on the tissue response and the overall success of the incorporation of an implant (Boyan et al., 1996, Curtis and Wilkinson, 1998; Kieswetter et al., 1996; Thomas and Cook, 1985). Thereby, the interaction strongly depends on a variety of surface properties such as chemistry, free energy, and topography. The effects on the surface topography or, in particular, the surface roughness, have been thoroughly investigated for titanium. In most studies, osteoblasts and osteoblast-like cells prefer rougher Ti surfaces as compared to smoother ones by comparing roughness values ranging from $R_a = 0.60 \mu\text{m}$ to $5.70 \mu\text{m}$ (Bowers et al., 1993, Boyan et al., 2002; Keller et al., 2003; Kunzler et al., 2007; Schneider et al., 2003).

Osteoblast viability is indirectly assessable via various indications such as measured cell proliferation, cell attachment, cell spreading, and collagen type I or alkaline phosphatase production. A few studies correlated osteoblast or osteoblast-like cell viability to different levels of hydroxyapatite surface roughness. Deligianni et al. investigated the influence of three different HA roughness values ($R_a = 0.73 \mu\text{m}$; $R_a = 2.86 \mu\text{m}$; $R_a = 4.68 \mu\text{m}$) on bone marrow stromal cells. The roughness of HA had no impact on the cell morphology or alkaline phosphatase activity (ALP) (Deligianni et al., 2001). Ball et al. found no significant differences in the ALP activity of osteoblasts on HA-coated implant materials when comparing roughness values of $R_a = 0.49 \mu\text{m}$ and $R_a = 1.75 \mu\text{m}$, yet the cell shapes looked different after 48 hours (Ball et al., 2008). From in-vivo experiments with implant surfaces in bone tissue, Hayashi et al. reported no differences in interface shear strength of two different HA surfaces with roughness values of $R_a = 0.88 \mu\text{m}$ and $R_a = 3.38 \mu\text{m}$ (Hayashi et al., 1994). In addition to the above-mentioned studies, we have used more levels of well-defined surface roughness and included cell proliferation quantification in order to assess impacts on cell behaviour. Apart from the measured osteoblast proliferation via WST-1 assay, the expression of collagen I type was semi-quantified. In our study, we focused on the hypothesis that HA roughness has an influence on osteoblast viability.

Sample fabrication

Cylindrical plane samples were made of 1.1 g of commercially available calcium phosphate hydroxyapatite powder (HA, $(\text{Ca}_{10}(\text{PO}_4)_6(\text{OH})_2)$, Prod.-No. 04238, Lot: 8345A, Sigma-Aldrich Chemie GmbH, Munich, Germany). The powder had a primary particle size of 151 ± 0.235 nm (unimodal distribution) and a density of 3.03 ± 0.04 g/cm³. It was uni-axially die-pressed by means of metal plungers and a hydraulic press (Weber Maschinen- und Apparatebau GmbH, Remshalden, Germany), applying a compressive force of 15 kN. The sample diameter was 23 ± 0.1 mm with a thickness of 2.8 ± 0.2 mm. The die-pressed samples were sintered in a furnace (LHT08/17, Nabertherm GmbH, Lilienthal, Germany) at ambient conditions at 1200 °C for two hours with a heating rate of 50 °C/h and a cooling rate of 100 °C/h.

Fabrication of defined surface roughness

The sintered platelets were treated with SiC grinding papers (WS Flex, Hermes Abrasives Ltd., Virginia Beach, USA) with the aim to generate a controlled surface roughness. For the grinding process, the ceramic platelets were pressed manually on the rotating grinding paper for 45 seconds, with a rotation speed of 150 rpm (Phoenix Alpha, Buehler GmbH, Duesseldorf, Germany). During the treatment process, the position of the samples was altered in order to achieve a randomized surface texture. The treatment processes were truncated after selected stages so as to process samples with final grits of p80, p120, p180, p320, p600, and p4000. Water was used as a lubricant to remove the excessive material and to avoid a heating of the samples during the grinding process. After polishing, each platelet was washed three times for five minutes with double deionised water (Synergy[®], Millipore, resistivity 18 MΩcm, Schwalbach, Germany) in an ultrasonic cleaner (1510 Branson[®], Branson Ultraschall, Dietzenbach, Germany). After cleaning with double deionised water, all samples were dried at ambient conditions and then sterilised at 180 °C for two hours.

Imaging of surface texture, measurement of surface roughness and surface area

SEM images were taken at 20 kV (Camscan Series 2, Obducat CamScan Ltd., Cambridgeshire, United Kingdom). Prior to imaging, the samples were sputtered with gold (K550, Emitech, Judges Scientific plc, West Sussex, UK).

The imaging of the surface texture as well as the measurement of the surface roughness and surface area was performed with an optical profilometer (Plu2300, Sensofar, Schaefer

Technology GmbH, Langen, Germany) with 420-folds magnification. Measurements in triplicate have been conducted on fifteen ceramic samples for each treatment. The size of each single measurement area was $477 \times 636 \mu\text{m}^2$ containing 442,368 measurement data points from which the average surface roughness S_a , the maximum heights of the surfaces S_z (from highest peak to lowest valley), and the surface area were calculated according to ISO25178. The arithmetical mean height of the surface (S_a) is defined in **eq. 15** according to ISO25178-2, with A being the domain of definition and $z(x,y)$ the height of the surface at position x, y (ISO25178, 2007).

$$S_a = \frac{1}{A} \int_A |z(x,y)| dx dy$$

eq. 15

All 3D data analysis was performed using SensoMap Plus software (Sensofar), version 5.0.3.4995. A commercially available hydroxyapatite-coated dental implant (Tapered HA, Nobel Biocare™, Yorba Linda, USA) and a commercially available standard titanium dental implant (Dentsply Friadent, Ankylos®) were measured as reference materials for the surface characterisation. Here, the average surface roughness between two screw threads was measured on three different positions according to ISO25178. The surface curvature was compromised by use of the SensoMap Plus software. In addition, plastic coverslips (Thermanox®, Nalge NUNC, Rochester, New York, USA), generally used as cell culture substrate material, were measured as a reference material.

Crystal structure analysis

X-ray diffraction measurements (XRD, C3000, Seifert, Ahrensburg, Germany) of sintered (1200 °C) hydroxyapatite samples were made for all roughness values in order to determine the crystal structure and to monitor possible changes in the crystal structure due to the grinding processes. Moreover, scans with 2θ ranging from 15° to 70° were taken.

Detection of grinding wear residues

Energy Dispersive Spectroscopy (EDS, Camscan Series 2, Obducat CamScan Ltd., Cambridgeshire, United Kingdom) with a detection limit of about 0.1% of the element's mass was used to avoid possible wear residues originating from the grinding papers. The

measurements were taken on treated and sintered HA (p4000, 1200 °C) for two different spots with an area of $27 \times 17 \mu\text{m}^2$ each.

X-ray Fluorescence analysis (XRF) was performed to detect residues such as Si from the grinding papers (detection limit of approximately 10 ppm). XRF measurement was carried out using a low pass filter and a main filter (0-40 keV, XL3t900 AnalytiCON Instruments GmbH, Rosbach, v.d. Hoehe, Germany). XRF was conducted on two different circular spots with an area of 7.1 mm^2 each. Prior to the EDS and XRF analysis, the samples were washed three times for five minutes in deionised water in an ultrasonic cleaner.

Density measurements

The density of non-sintered hydroxyapatite particles was measured by a helium pycnometry system (Accu Pyc 1330, Micromeritics, Aachen, Germany). Ten measurements were made and the relative density of the samples after sintering was calculated according to the geometrical approach, comparing theoretical and experimental (mass/geometrical volume) densities.

Contact angle measurements

The contact angles (Θ) between sessile drops (20 μL) of double deionised water and the ceramic surfaces were measured on three samples for each roughness value; as a reference material, Thermanox[®] was used. Side view images of the droplets were taken via an aligned (45°) mirror with a microscope (Axio Imager M.1, Carl Zeiss GmbH, Jena, Germany). The contact angles were analysed with the help of Software ImageJ (version 1.39u, National Institutes of Health, USA).

Cell culturing

Prior to cell testing, all samples were rinsed with double deionised water containing 1% antibiotics/antimycotics and dried in air in ultraviolet light for one hour. Human osteoblast cells (HOB, cryovial, Cat.-No.: 121 0311, Provitro GmbH, Berlin, Germany) with a doubling time of 120 hours cultivated in their fourth-culture generation for the in-vitro testing. One sample was put into one polystyrene culturing dish (12-well multidish, Nalge NUNC, Rochester, New York, US). Then the samples were fully immersed into 2 ml of complete DMEM media with high glucose (Dulbecco's Modified Eagle's Medium) and stored at 37 °C, 10% CO₂ and 94.5% RH in an incubator (C200, Labotect Labor-Technik-Göttingen GmbH,

Goettingen, Germany) for 30 minutes. The media contained 10% fetal calf serum (FCS) and 1% antibiotics/antimycotics. Afterwards, the media was removed with a sterile pipette and then discarded. Approximately 8×10^4 cells, homogenously dispersed in 2 ml DMEM media, were added to each well containing the wet samples. The cells were incubated on the various substrates in the same incubator for a period of seven days under static conditions. Sampling points were taken after 24 hours (day 1), 72 hours (day 3), and after 168 hours (day 7). As cell culture reference materials, plastic coverslips (Thermanox[®]) with a diameter of 15 mm were used. The cell relevant chemicals were purchased from Invitrogen GmbH, Darmstadt, Germany.

Cell proliferation measurements via WST-1 assay

The proliferation of the HOB cells was analysed via a plate reader (Cameleon, HIDEX, Turku, Finland) using a colorimetric WST-1 assay (WST-1, Roche Diagnostics GmbH, Mannheim, Germany) for the non-radioactive quantification of the cell proliferation via the measurement of the formazan product in living cells. Supernatants were quantified spectrometrically (OD) at 450 nm with a reference wavelength of 650 nm. Proliferation measurements of three samples of each roughness level per sampling day were applied. The same volume of culture medium and cell proliferation reagent WST-1 was used in the experiment as a background control (absorbance of culture medium plus WST-1 in the absence of cells) for the plate reader. Due to different sample sizes the measured proliferation values of Thermanox[®] were normalised to the sample area of the ceramic samples.

Cell imaging

Fluorescence staining of cell components was accomplished with different fluorescent dyes. Thus, Alexa Fluor[®] 488 Phalloidin was used for the cytoskeletons; 4'6'- Diamidino-2-phenylindol (DAPI) was taken for the cell nuclei, mouse anti-human-collagen as primary antibody, and conjugated anti-mouse-IgG (Alexa Fluor[®] 546) as secondary antibody was used for the specific collagen type I staining. Cells were observed and visualized with a fluorescence microscope (Axio Imager M.1, Carl Zeiss GmbH, Jena, Germany). Further, imaging of three samples of each roughness value was realised. The chemicals for cell staining were purchased from Invitrogen GmbH, Darmstadt, Germany.

Statistical analysis

The statistical analysis was performed with the aid of MiniTab 16. Also, a one-way ANOVA using Tuckey's Multiple Comparison test was performed. In so doing, a p-value ≤ 0.05 was considered statistically significant for the comparison of the absorbance values from the proliferation measurement. Data is shown as mean values including standard deviation.

Results of surface characterisation

Surface texture

The grinding processes of hydroxyapatite with SiC grinding papers resulted in a range of micro and submicron roughness values between $S_a = 3.36 \mu\text{m}$ and $S_a = 0.13 \mu\text{m}$. Grinding with a grit of p80 resulted in a surface roughness of $S_a = 3.36 \pm 0.54 \mu\text{m}$. The surface was matt finished with an apparent, randomly grooved and craggy topography. A variety of depths having either rounded U-shaped or V-shaped profiles or cavities in the sample surface could be distinguished. Comparable results in surface texture were achieved with grits of p120, p180, and p320, though with less salient characteristics. In doing so, the treatment with p120 resulted in a surface roughness of $S_a = 1.41 \pm 0.18 \mu\text{m}$. With p180, a surface roughness of $S_a = 0.92 \pm 0.24 \mu\text{m}$ was achieved and grinding with p320 caused a surface roughness of $S_a = 0.50 \pm 0.10 \mu\text{m}$. The grinding procedure with a grit of p600 resulted in a half-matt surface with a craggy topography and with U and V-shaped profiles in the submicron range. Grooves were partially present on the surface but were smaller and less intense when compared to p320. A surface roughness of $S_a = 0.24 \pm 0.05 \mu\text{m}$ was fabricated using a grid of p600. The polishing with p4000 resulted in a surface roughness of $S_a = 0.13 \pm 0.03 \mu\text{m}$. The surface was glossy with a very smooth topography, albeit a few tiny grooves in the submicron range were visible. Likewise, a small amount of defects was detectable on the surface (**Fig. 63**)

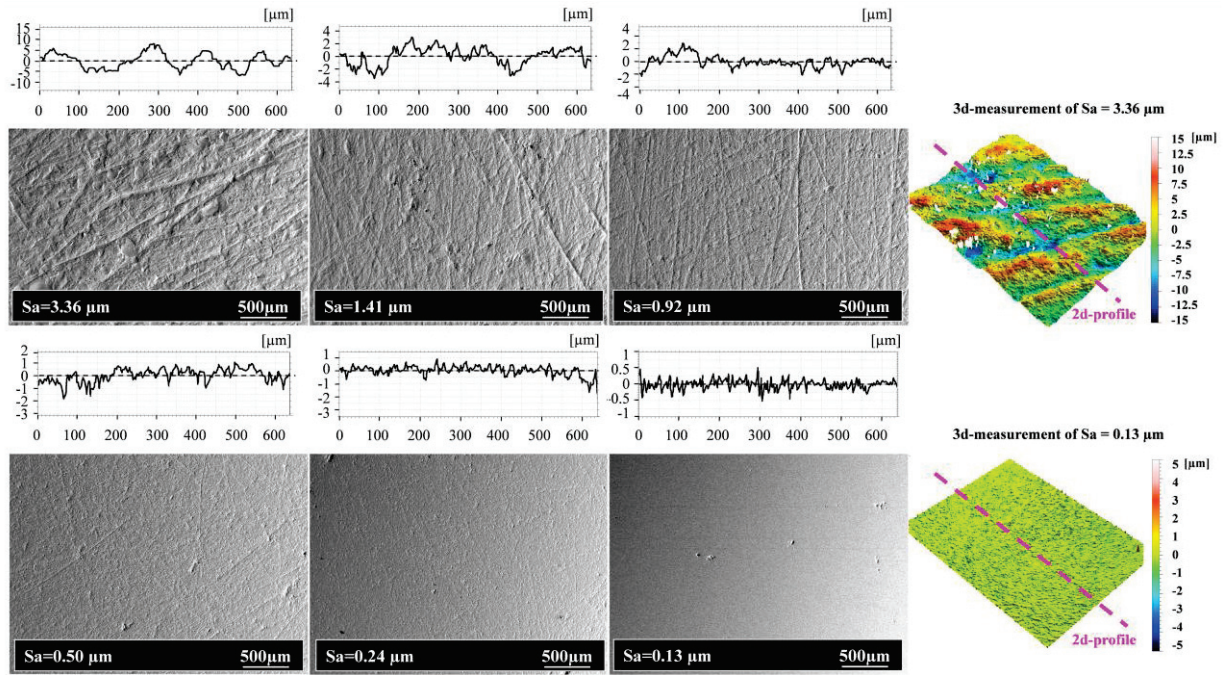


Fig. 63: SEM micrographs of HA surfaces with different surface roughness values (S_a). The white insets show representative 2D surface profile of the treated HA surfaces. The obtained 3D surface topography of two treated HA samples is exemplarily shown on the right hand side. The dashed lines (pink) show the position of the 2D profile sections.

The reference hydroxyapatite-coated titanium implant had an average roughness of $S_a = 4.23 \pm 0.28 \mu\text{m}$. The reference standard titanium implant had a roughness of $S_a = 2.06 \pm 0.11 \mu\text{m}$. Both implant surfaces were matt and rough. The reference material Thermanox[®] had a roughness level of $S_a = 0.03 \pm 0.00 \mu\text{m}$ and was shiny and transparent (**Tab. 7**).

Total surface area

The field of view for the measurement of the total surface area was of $477 \times 636 \mu\text{m}^2$, which results in a geometrically ideal surface area of $303,372 \mu\text{m}^2$. The measurements on treated HA showed an increase in total surface area with increasing roughness (**Tab. 7**).

Sample density and sample size

The ceramic platelets were $17 \pm 0.3 \text{ mm}$ in diameter and $2.4 \pm 0.2 \text{ mm}$ in thickness after sintering at 1200°C . Thus, a total shrinkage of 26% was measured due to sintering.

The relative density was at 94.5% for all HA samples ($p_{\text{rel}} = 0.945 \pm 0.017 \text{ g/cm}^3$) resulting thus in a porosity of 5.5%. Further, there was no significant difference between the densities of the samples with different roughness values.

Tab. 7: Roughness, contact angles, and total surface area for ground HA surfaces, Thermanox[®], and dental implants

Surface	Arithmetical mean height of the surface (Sa) (μm)	Maximum height of the surface (Sz) (μm)	Mean contact angle (Θ) (°)	Mean surface area (μm ²)	total
HA p80	3.36 ± 0.54	39.94 ± 8.67	11 ± 1	342,635	
HA p120	1.41 ± 0.18	29.46 ± 6.25	12 ± 1	323,166	
HA p180	0.92 ± 0.24	24.90 ± 7.47	24 ± 2	320,126	
HA p320	0.50 ± 0.10	21.04 ± 5.76	20 ± 1	313,638	
HA p600	0.24 ± 0.05	10.26 ± 4.49	27 ± 1	307,394	
HA p4000	0.13 ± 0.03	5.40 ± 2.03	24 ± 3	306,793	
Thermanox [®]	0.03 ± 0.00	5.05 ± 3.22	58 ± 2	-	
HA-coated dental implant	4.23 ± 0.28	36.41 ± 3.34	-	-	
Titanium dental implant	2.06±0.11	24.46 ± 3.68	-	-	

Crystal structure

The crystal structure of hydroxyapatite samples sintered at 1200 °C proved to be identical to pure and non-sintered HA and did not change due to grinding processes. No traces of other calcium phosphate structures, e.g. β-tri-calcium phosphate, were detectable, either.

Contact angle

Hydroxyapatite with a surface roughness of 3.36 μm (p80) resulted in a contact angle of 11 ± 1° with double deionised water. The HA surfaces with a roughness of 1.41 μm (p120) had a mean contact angle of 12 ± 1°. Contact angles of 24 ± 2° and 20 ± 1° were measured on HA surfaces with roughness values of 0.92 μm (p180) and 0.50 μm (p320), respectively. A surface roughness of 0.23 μm (p600) resulted in a mean contact angle of 27 ± 1°. An angle of 24 ± 3° was measured on HA surfaces with a roughness of 0.13 μm (p4000). The reference material Thermanox[®] had a contact angle of 58 ± 2° (**Tab. 7**).

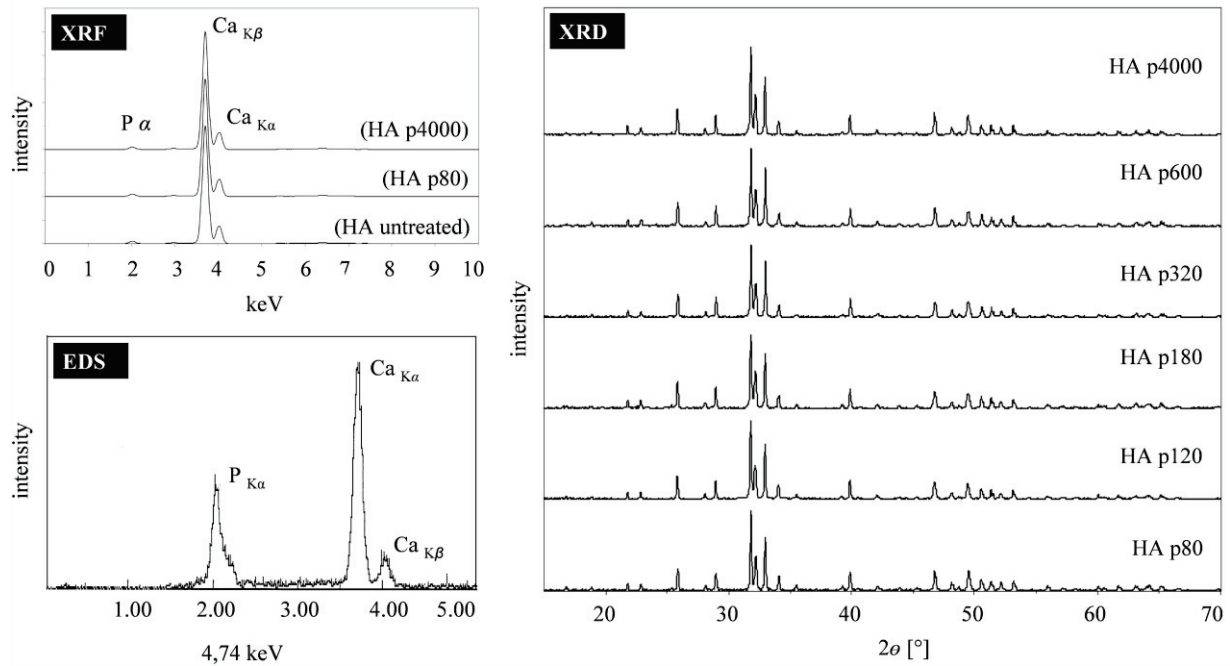


Fig. 64: Upper left: XRF analysis of surface-treated HA and untreated HA; lower left: EDS measurement of surface-treated HA (p4000); right: XRD measurement of treated HA surfaces

Grinding wear residues

No residues of silicon from the grinding processes with SiC grinding papers could be found in the analysis of elements with EDS or XRF (**Fig. 64**).

Results of cell experiments

Cell proliferation

The proliferation of the human osteoblast cells steadily increased on each surface-treated HA sample with prolonging period from day 1 to day 7 due to the proliferation kinetics of the osteoblasts. After day 1, the measured cell proliferation varied from $OD = 0.024 \pm 0.013$ on the roughest HA surfaces to $OD = 0.041 \pm 0.011$ on the smoothest hydroxyapatite surfaces.

After day 3, the measured absorbance varied from $OD = 0.057 \pm 0.009$ on the roughest HA surfaces to $OD = 0.093 \pm 0.006$ on the smoothest hydroxyapatite surfaces. Finally, after day 7, the two roughest (p80 and p120) HA surfaces showed the highest tendency towards a high proliferation with $OD = 0.149 \pm 0.023$ (p80) and $OD = 0.153 \pm 0.010$ (p120). The two smoothest surfaces, i.e. p600 and p4000, showed lower proliferation with $OD = 0.122 \pm 0.006$ (p600) and $OD = 0.134 \pm 0.020$ (p4000) (**Fig. 65**).

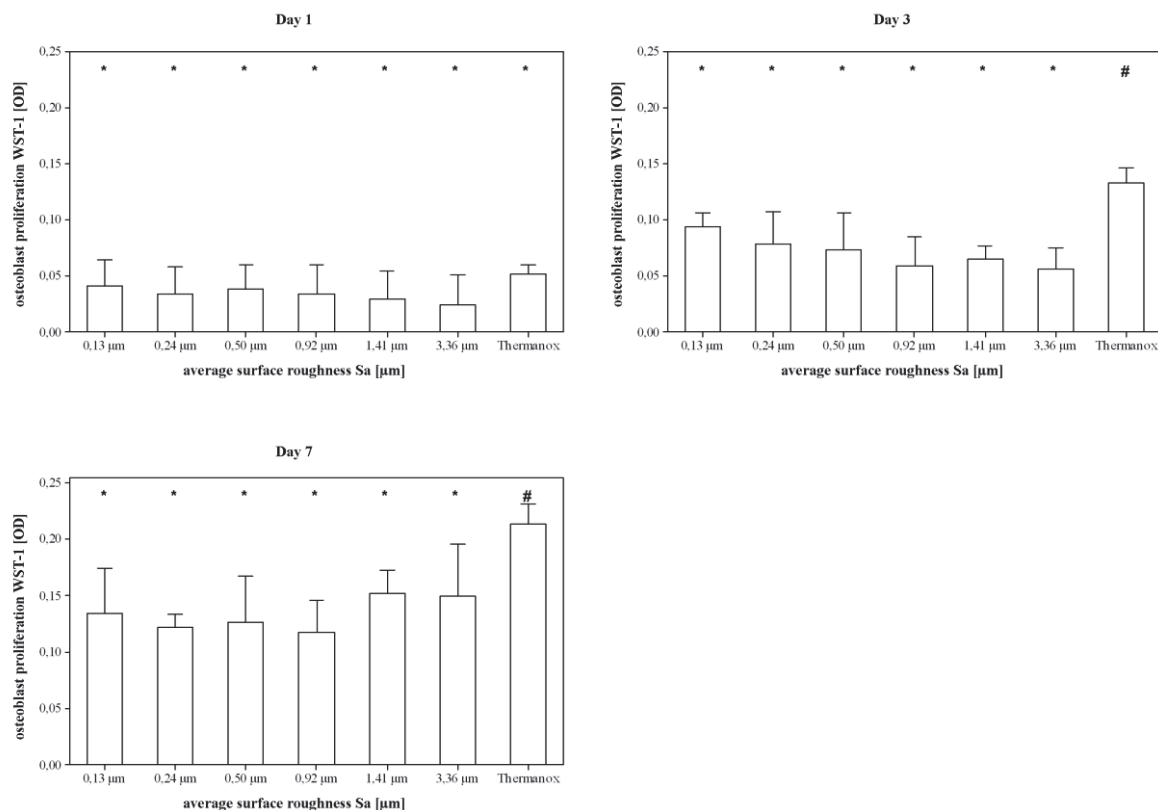


Fig. 65: Proliferation (WST-1 assay) of human osteoblasts grown on hydroxyapatite prepared with different roughness values after days 1, 3, and 7. The standard tissue culture support material Thermanox® was used as a reference (ref. 0.03). Mean values that share a symbol (*/#) are not significantly different (ANOVA: post-hoc Tuckey's Multiple Comparison Method, $p < 0.05$; error bars show the 95% confidence interval for the mean).

The results for all three sampling points were evaluated in a statistical analysis, which has shown that the cell proliferation does not depend on the sample roughness, since a value of $p > 0.05$ was found for all three sampling points (day 1: $p = 0.742$ / day 3: $p = 0.057$ / day 7: $p = 0.243$).

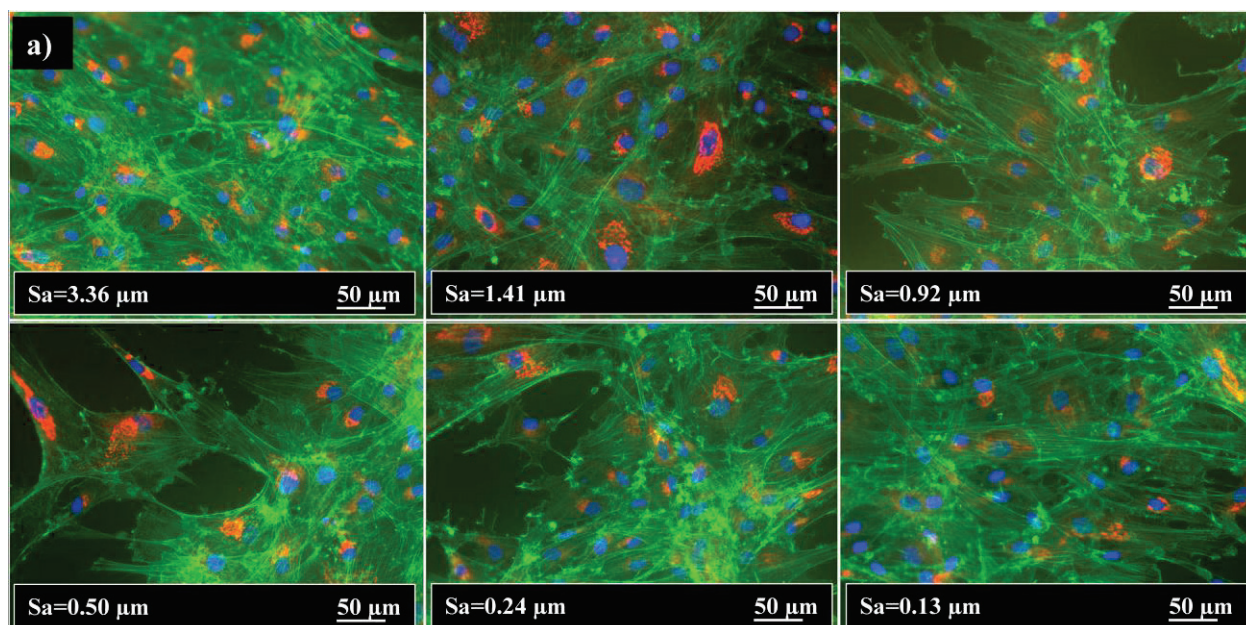
Cell morphology and production of collagen type I

On day 1, the osteoblasts showed the same flat and spread morphologies with lamellipodiae and filopodiae on all treated samples. Non-attaching cells with spherical morphologies could be found on any HA sample. Thereby, the cells grew interconnected and actin fibres were clearly visible on all samples. No signal of collagen type I staining could be detected on any sample that day. By contrast, on Thermanox[®] a weak signal of the collagen type I staining became apparent (**Fig. 66** and **Tab. 8**).

Tab. 8: Collagen type I production in osteoblasts: (-) = no signal, (+) = low signal, (++) = strong signal.

Surface	Arithmetical mean height of the surface (Sa) (µm)	Collagen type I		
		day	day 3	day 7
HA p80	3.36	-	++	++
HA p120	1.41	-	++	++
HA p180	0.92	-	++	++
HA p320	0.50	-	++	++
HA p600	0.24	-	++	++
HA p4000	0.13	-	++	++
Thermanox [®]	0.03	+	+	+

On day 3, on all HA surfaces with a roughness between $Sa = 3.36 \mu\text{m}$ and $Sa = 0.13 \mu\text{m}$ the osteoblasts showed a flat and widely spread morphology with lamellipodiae and filopodiae. The cells were still intercellularly connected on all samples.



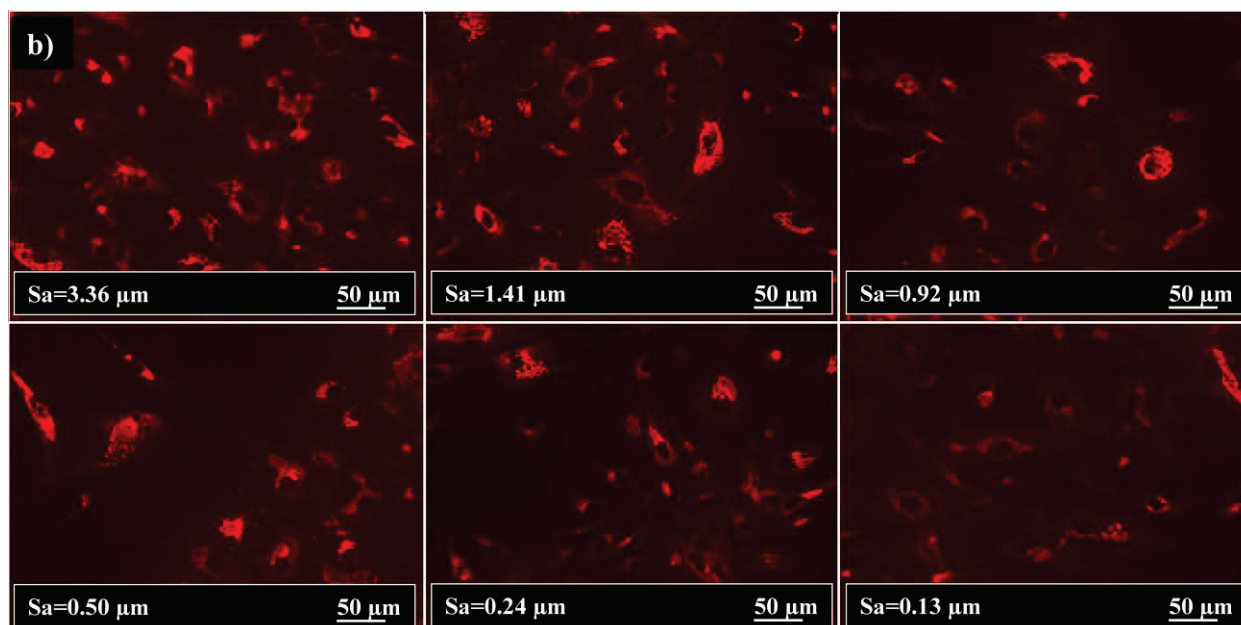


Fig. 66: a) Fluorescence images of human osteoblasts grown on surface-treated hydroxyapatite with different roughness values S_a . The images were taken after seven days of in-vitro proliferation. Blue: nucleus, Green: cytoskeleton, Red: collagen type I. b) The identical fluorescence images of a) are shown without the staining signals of cytoskeletons or nuclei, showing only collagen type I.

Clearly visible actin fibres in the cytoskeleton and a strong signal of collagen type I staining could be detected in the cells. No spherical cells could be found on any sample. Likewise, no evident differences between the visualized strength of the high collagen type I signal could be perceived between samples with different roughness values on day 3. However, a weak signal of the collagen type I staining was present on Thermanox[®] (**Fig. 66** and **Tab. 8**).

On day 7, eventually, neither a difference in the cell morphologies, nor in the visualized strength of the high collagen type I signal was noticeable between samples of varying roughness. Likewise, no difference in the collagen type I production could be observed between days 3 and 7. On Thermanox[®] a weak signal of collagen type I staining was detectable. On all samples a confluent cell layer was detected as well (**Fig. 66** and **Tab. 8**).

Discussion

Diverse surface treatments or machining processes can result in similar roughness values, but exhibit different topographies and textures, which may affect cells during in-vitro experiments. In our experiments, we focused on the hypothesis according to which HA submicron and micron roughness has an influence on osteoblast viability. Accordingly, we

produced six different surface roughness levels on hydroxyapatite samples through a traditional grinding technique. The roughness of a surface can be defined by measuring a single 2D profile (Ra) according to DIN EN ISO4287 or else a 3D area (Sa) according to ISO25178 (ISO25178, 2007; ISO4287, 1997). In our tests, the surface roughness was evaluated using a 3D area. The maximum height of the surface (Sz) was measured in order to account for the spread of the cells. The results obtained clearly demonstrated that a reproducible and very homogenous fabrication of levels of roughness between $Sa = 3.36 \pm 0.54 \mu\text{m}$ and $Sa = 0.13 \pm 0.03 \mu\text{m}$ was possible for hydroxyapatite. The same reproducible results were found for the maximum height of the surfaces ranging from $Sz = 39.94 \mu\text{m}$ down to $5.05 \mu\text{m}$. The fabricated average roughness values (Sa) as well as the maximum heights (Sz) for the HA samples were comparable to the roughness of two commercially available dental implants analysed by us. Thus, the reference HA-coated titanium implant from Nobel BiocareTM ($Sa = 4.23 \mu\text{m}$ / $Sz = 36.41 \mu\text{m}$) showed a slightly higher surface roughness but similar maximum surface heights as compared to the fabricated HA samples. The reference standard titanium implant from Dentsply Friadent ($Sa = 2.06 \mu\text{m}$ / $Sz = 24.46 \mu\text{m}$) was in the range of the fabricated HA surface roughness values and maximum surface heights, which emphasizes the relevance of the examined HA surface roughness levels. The surface chemistry and the mechanical properties of the commercially available dental implants might be different from the fabricated HA surfaces, yet these properties were not of interest for this study.

As already anticipated, an increase of the total surface area on HA was clearly measurable due to an increased surface roughness. An increased surface area means a larger contact area for the binding of important and relevant proteins, growth factors or interaction with cells. The importance of proteins and growth factors for the adhesion of osteoblasts has been reviewed in detail by Anselme (2000). Although the total surface area of the HA samples increased due to an increase in surface roughness, no significant differences in the osteoblast cell proliferation or shape were detectable.

Contact angles were measured as an indication for surface wettability in our study. Contact angles of less than 30° were measured on all hydroxyapatite samples, independently of roughness. The lowest contact angles were measured for the two roughest HA samples, i.e. p80 and p120. The highest angles were measured for the two smoothest HA samples, which were p600 and p4000. As a tendency, the contact angles decreased in correlation with an increase in surface roughness, indicating thus an increase also in surface wettability as well as in free surface energy. Schakenraad et al. reported wettability to be one important factor for

cell adhesion and proliferation of human fibroblasts on polymer materials (Schakenraad et al., 1986). The results from our study showed that all tested surfaces were clearly hydrophilic ($\Theta < 90^\circ$) and that no significant differences in the wettability of all fabricated HA samples could be found. Significantly higher contact angles were measured on Thermanox[®].

Changes in the surface porosity and relative density of HA have influence on the metabolic activities, such as ALP activity of rat bone marrow cells (Rosa et al., 2003). The density was the same for all treated HA surfaces in our study. Different crystal structures of calcium phosphate, such as tri-calcium phosphate (TCP) versus hydroxyapatite, may alter the osteoblast-like cell response (Detsch et al., 2008). Nevertheless, neither the crystal structure nor the relative density changed throughout our experiments. Thus, the influence of the relative density and crystal structure on the osteoblast cells should be identical for all HA samples.

After cleaning the treated HA samples in double deionised water, no particles or residues of the SiC papers were detected by XRF and EDS. This indicates that no residues could have influenced the cell proliferation or morphology during the in-vitro cell testing.

In our study, the osteoblasts showed flat and well-spread morphologies with lamellipodiae and filopodiae at their periphery on all treated samples on day 1. This indicates a good adhesion between the hydroxyapatite surfaces and the cells, yet no influence of the different roughness levels on the osteoblasts was detectable. Additionally, they showed clearly visible actin fibres (stress fibres) in the cytoskeleton, which is often associated with strong cell adhesion; however, as the occurring processes are very complex, the role of these stress fibres in relation to adhesion is still not fully understood (Huang et al., 2005; Huang et al., 2006; Lim et al., 2005; Matsuda et al., 1998; Thian et al., 2008; Thian et al., 2006; Yamakura et al., 2001; Zhu et al., 2004b; Zhu et al., 2004). The attachment and proliferation of the HOB was good on all treated HA surfaces. Collagen type I was produced after day 1. This indicates that the cell adapted to their environment and showed normal metabolic activity. No abnormal cell phenotypes like blebbed plasma membranes (blebbing) were detected which might give an indication of low cell adhesion or even apoptotic mechanisms within the cells (Fackler and Grosse, 2008; Hagmann et al., 1999; Panupinthu et al., 2007).

A minor role of the surface roughness on cell behaviour and metabolic activity was demonstrated in the studies by Hayashi et al. and Ball et al. Thus, Hayashi et al. reported no differences in interface shear strength of a dense sintered HA surface with $R_a = 0.88 \mu\text{m}$ and a rougher HA-coated Ti surface with $R_a = 3.38 \mu\text{m}$ from in-vivo experiments on bone tissue (Hayashi et al., 1994). Other results were found, for instance, by Deligianni et al., who

investigated the influence of three different roughness values of HA ($R_a = 0.73 \mu\text{m}$; $R_a = 2.86 \mu\text{m}$; $R_a = 4.68 \mu\text{m}$) fabricated via grinding papers of p180, p600, and p1200. It turned out that the roughness of HA had no impact on the bone marrow stromal cells morphology or alkaline phosphatase activity. However, the proliferation after 14 days was higher on rougher HA than on smoother ones (Deligianni et al., 2001). The higher proliferation is similar to our results with HOB after seven days in-vitro. Altogether, a period of seven days may be too short to detect significant differences in the proliferation of HOB on HA. This assumption is confirmed by the slightly higher (but statistically insignificant) proliferation values of the two roughest HA surfaces (p80 and p120) on day 7. The measurement of the proliferation via WST-1 assay might also be not sufficiently sensitive or specific to detect differences in osteoblast metabolism between the evaluated HA roughness levels. Likewise, Ball et al. reported no significant differences in the ALP activity of osteoblasts after 48 hours on HA-coated implant materials when comparing roughness levels of $R_a = 1.75 \mu\text{m}$ (grit blasted) and $R_a = 0.49 \mu\text{m}$ (treated p240). Though cell shapes were different, collagen type I appeared present and was similar on all samples after seven days (Ball et al., 2008), which is in accordance with our results.

In contrast, our findings for osteoblasts grown on HA surfaces with various roughness values are different to results obtained from osteoblasts or osteoblast-like cells grown on Ti surfaces. On Ti, it has been reported that osteoblasts prefer rougher surfaces to smoother ones. For example, Kunzler et al. stated a significant increase in the number of osteoblasts (RCO) with increasing surface roughness of titanium. Thereby, the cells were seeded on titanium with roughness gradients ranging from $R_a = 1.12 \mu\text{m}$ to $R_a = 5.70 \mu\text{m}$. The osteoblasts morphology changed continuously following the gradient of roughness from smooth to rough. Boyan et al. reported a decrease in the number of cells (FRC) with increasing Ti surface roughness, albeit the alkaline phosphatase activity of the osteoblast-like cells was increasing (Boyan et al., 2002). Schneider et al. (2003) and Bowers et al. (1993) found a higher mineralisation ratio of osteoblasts (RCO) on sandblasted Ti compared to ground titanium. Mangano et al. (2010) reported a faster osteo integration by the differentiation of human dental pulp stem cells on laser-sintered titanium (SLS) as compared to acid-etched Ti surfaces. Comparing these results for Ti surfaces from the literature to our findings, it may be suggested that in contrast to Ti the treatment of HA surfaces does not improve the cell proliferation (WST-1 assay) and collagen type I production of osteoblasts within the first seven days.

Conclusions

With a simple and low-cost surface treatment technique we produced homogenous and reproducible hydroxyapatite surface roughness values between $Sa = 3.36 \mu\text{m}$ and $Sa = 0.13 \mu\text{m}$ for in-vitro osteoblast experiments. No residues of silicon from the grinding process and no changes in the crystal structure of the hydroxyapatite samples were detected. Applying only a simple surface treatment technique allowed the effects of the surface roughness to be isolated from differences in surface chemistry, crystal structure as well as relative density. The changes of the osteoblast proliferation (WST-1 assay) on these differently roughened hydroxyapatite surfaces after seven days turned out insignificant ($p > 0.05$), evaluated by one-way ANOVA and Tuckey's Multiple Comparison Method. The results from this study thus have shown that all roughened HA surfaces, regardless of the microtopography, are biocompatible and allow for osteoblast attachment, proliferation, and collagen type I production. The comparison with surface roughness values of Ti has revealed that for HA no finishing process is necessary in order to ensure a sound HOB cell proliferation in-vitro.

3.4 Laser treatment

3.4.1 Laser ablation of hydroxyapatite surfaces

The following results were partially published in the “Proceedings of the 2008 International Manufacturing Science and Engineering Conference in Evanston, IL, USA (MSEC2008)” by Marzellus grosse Holthaus and Kuroschi Rezwan (University of Bremen, Advanced Ceramics) (Holthaus and Rezwan, 2008).

In the beginning of the experimental work for this thesis, laser ablation was used to fabricate micropatterns. The HA powder introduced at the beginning of this chapter was die-pressed uni-axially with 3.5 kN so as to generate plane cylindrical platelets with diameters of 10 millimetre. Afterwards, the platelets were sintered in a furnace at 1200 °C for two hours with a heating rate of 50 °C/h and a cooling rate of 100 °C/h. The thus sintered platelets were micropatterned by using a Nd:YAG laser with a wavelength of 1064 nm and a pulse duration of 100 ns for the ablation processes. The micropatterns had a length of 3 mm and varied in width from approximately 40 µm to a maximum of 220 µm (**Fig. 67**). The laser power amounted to 3.5 watts, at a feed motion of 16 mm/s.

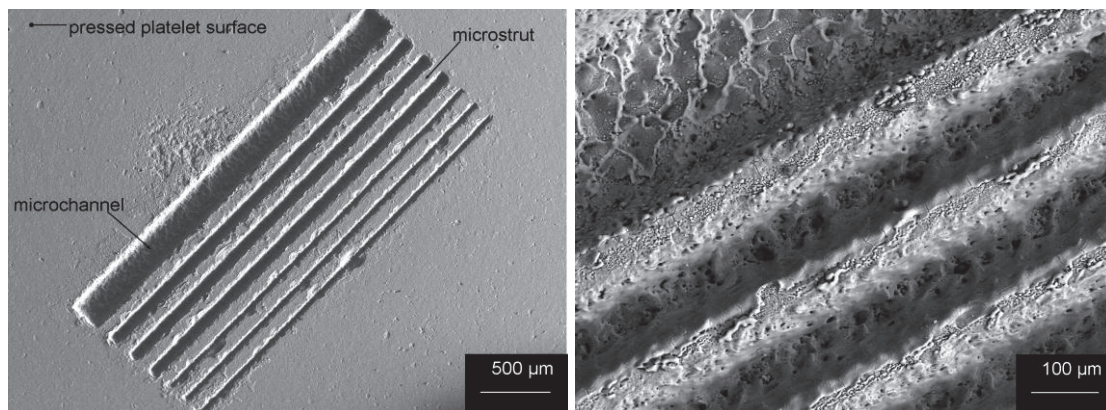


Fig. 67: Left: laser-ablated microchannels with different widths between 220 µm, 80 µm, and 40 µm; right: magnification of the molten surface of a 220 µm wide channel (upper left) and 80 µm wide channels

The surface inside of the laser-ablated microchannels was rougher than non-laser-structured areas in SEM images. Therefore, the area of microchannels with 40 µm and 80 µm in widths seemed to be partially molten through the laser treatment and subsequently solidified quickly. The surface of microchannels with 220 µm width looked molten as well, but also seemed to be rougher and craggy. Same occurrence was noticed next to the microchannels and on the

struts. The depth of the laser-ablated micropatterns varied unintentionally between 30 to 110 μm (**Fig. 68**). The microstruts between the microchannels had a width of approximately 100 μm .

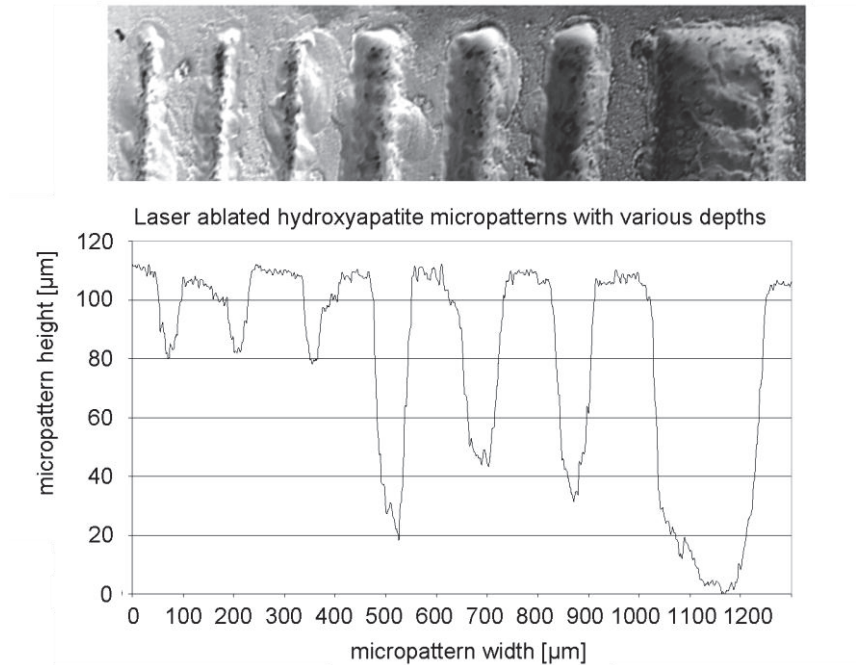


Fig. 68: SEM image (top view) and 2D profile of laser-ablated microchannels. Microchannels were generated by use of NdYAG laser on a plane hydroxyapatite surface.

A problem in this was the difficult selection of laser power to get a constant ablation quality. Furthermore, it was not possible to generate microchannels smaller than 30 to 40 μm on these pressed HA platelets without quality loss on defined micropattern edges. An XRD analysis of a laser-ablated hydroxyapatite sample showed no traces of β -tri calcium phosphate (β -TCP) on the surface, though amorphous fractions had been expected.

Within these first tests it could be demonstrated that laser ablation is suitable for the fabrication of calcium phosphate micropatterns. These preliminary results with laser-ablated patterns and osteoblast-like osteosarcoma cells (MG-63) were published in Holthaus and Rezwan 2008. Laser treatment was further investigated in another study using laser interference patterning, which is described in the following chapter.

3.4.2 Laser interference patterning of hydroxyapatite surfaces

The following results were published in the journal “Applied Surface Science” in 2011 by Jana Berger^a, Marzellus grosse Holthaus^b, Nicola Pistillo^c, Teja Roch^a, Kurosch Rezwan^b, Andrés Fabián Lasagni^a (^aFraunhofer Institute for Material and Beam Technology, Dresden; ^bUniversity of Bremen, Advanced Ceramics; ^cPolitecnico di Bari, Department of Mechanical and Management Engineering, Bari) (Berger et al., 2011).

Abstract

Direct laser interference patterning (DLIP) was used to produce periodic patterns on hydroxyapatite. An Nd:YAG laser operating at 266 and 355 nm wavelengths and with a pulse duration of 10 ns was used in these experiments. Line and cross-like patterns with periodical distances of 10 and 20 μm were fabricated with energy densities between 0.6 and 2.4 J/cm^2 and pulse numbers from 1 to 100. In the low/middle laser intensity range it could be observed that the structure depth increased with the pulse number. However, for higher energies the patterns smudged due to thermal effects. For single pulse laser experiments, an increase in laser fluence did not produce deeper structures. In addition, the best results were obtained when using low-medium laser intensities ($\sim 0.6\text{--}1.2 \text{ J}/\text{cm}^2$) and moderate numbers of laser pulses (20–50), depending on the laser wavelength. Moreover, at a wavelength of 355 nm only patterns with 20 μm periods presented a good quality structure. In contrast, wavelengths of 266 nm improved resolution up to periods of 10 μm due to a higher photochemical contribution to the ablation process. An X-ray Photoelectron Spectroscopy (XPS) analysis showed that there were no significant changes in the chemical composition of laser-treated hydroxyapatite.

Introduction

There are several circumstances in which it may turn out necessary to repair or replace a considerable part of lost bone tissue. Now, one of the advantages of substituting lost bone tissue with artificial material is that a removal of healthy tissue is not necessary. On the other hand, there is an imminent danger of immune reaction and subsequent rejection of the implant (Queiroz et al., 2004; Blindow et al., 2009; Rodriguez-Lorenzo et al., 2003; Holthaus and Rezwan, 2008; Holthaus et al., 2010; Heule et al., 2003). Therefore, ideally, artificial bone replacement materials should present a similar structure and composition as compared to human bone, presenting thus bone function. One of the most widely used materials in this

field is hydroxyapatite (HA), $\text{Ca}_5(\text{PO}_4)_3(\text{OH})$. This ceramic has often been used in bone implants thanks to its chemical composition being very similar to bone tissue as well as its excellent biocompatibility. Apart from chemical composition and mechanical properties of the artificial materials, a suitable modification of the surface topography can increase the bioactivity and may achieve a stronger bone-implant fixation (Dearnley et al., 1999; Jaffe et al., 1996; Brunette et al., 1999; de Groot et al., 1998). It has also been reported that a proper surface topography may not only improve the implant's bone integration (Buser et al., 1991) but is also able to influence cell organization (Thomas et al., 1999; Perizzollo et al., 2001). In this manner, it is possible to organize bone tissue structure (which is mechanically anisotropic), so that a strong implant/bone interface can be achieved. Within the techniques recently used to create micropatterns to influence bone cell growth, several techniques can be mentioned including Aerosol-Jet[®] printing of aqueous ceramic suspensions, laser ablation, and microcontact printing of aqueous ceramic suspension (Holthaus and Rezwan, 2008; Holthaus et al., 2010) using microstructured PDMS stamps. These surface patterning technologies have already been tested and proved to influence tumorous bone cell growth (MG-63) on micropatterned hydroxyapatite surfaces (Holthaus and Rezwan, 2008). Until now, the techniques previously deployed consist in rather time-consuming processes or require several processing steps. For example, in Aerosol-Jet[®] printing (Holthaus and Rezwan, 2008, Hedges et al., 2005, Zöllmer et al., 2006), an aqueous hydroxyapatite ceramic slurry is used first to print micropatterns on the substrate, which are subsequently sintered by a laser radiation. Through this technique, it was possible to obtain micropatterns ranging from 20 to 140 μm in width. For microcontact printing, it is necessary first to produce a stamp of PDMS (polydimethylsiloxane) by replicating a microstructured silicon wafer. After plasma treatment with oxygen, the stamp becomes covered with hydroxyapatite ceramic slurry and pressed on the ceramic samples where it dries for 24 hours. The ceramic micropatterns remain on the surface after removal of the PDMS stamp. To reach the final stability, the samples are sintered at 1200 °C. With this technique, ceramic micropatterns with widths up to 10 μm could be fabricated (Holthaus and Rezwan, 2008, Heule et al., 2003). Another approach that has been used for this purpose is based on laser ablation using a scanning system to sequentially pattern an array of lines, for example. Yet, this is a time-consuming procedure, too, and due to limitations on focusing diameter of the laser beam, the microstructures obtained are generally not smaller than 30 μm . In addition, patterning on curved surfaces requires a precise control of the focusing distance. An alternative method for the fabrication of periodic arrays consists in Direct Laser Interference Patterning (DLIP). In this procedure,

the laser beam is split up into two or more coherent laser beams which interfere on the sample surface producing an interference pattern on the irradiated area. Depending on the irradiated materials, only one single laser pulse is necessary to process a surface area of several square millimetres at once. Further, different structures in the micrometer scale are producible. Moreover, a wide range of two-dimensional micrometer arrays can be fabricated by just controlling the geometrical configuration of the interference setup (e.g. number of utilized laser beams) (Lasagni et al., 2007; D'Alessandria et al., 2008). Compared to other laser-assisted methods, variable geometries with controlled feature sizes are producible in a significantly shorter time. In addition, since the interference patterns result from the overlapping of different laser beams, no masks are necessary in this technique. Moreover, there is no particular need for controlled environment (such as vacuum or special gases), and as the interference patterns are produced in the volume at which the beams overlap, curved surfaces are treatable as well. In this study, we describe first the results from Direct Laser Interference Patterning of hydroxyapatite using a two-beam configuration. Also 2D arrays with cross-like patterns were fabricated using a positioning stage with controlled rotation angles. The topography and chemical structure of the fabricated arrays was determined by means of an optical profilometer and an X-ray Photoelectron Spectroscopy (XPS), respectively.

Materials and methods

Sample fabrication

Hydroxyapatite substrates were prepared through biaxial die-pressing of calcium phosphate powder ($\text{Ca}_{10}(\text{PO}_4)_6(\text{OH})_2$) (04238, Lot: 8345A, Sigma–Aldrich) to plane cylindrical platelets with a diameter of 10 and 23 mm and a thicknesses of about 2.8 mm. The particle size was about 150 nm. Afterwards, the green bodies were sintered at 1200 °C at ambient atmosphere for 2 hours with a heating rate of 50 °C/h and a cooling rate of 100 °C/h. To reduce surface roughness the platelets were polished manually with SiC paper (grit p4000, WS Flex Hermes).

Laser interference patterning

An Nd:YAG laser (Spectra Physics) with a pulse duration of 10 ns providing a fundamental wavelength of 1064 nm was used for the laser interference experiments. Shorter wavelengths (532, 355, and 266 nm) can be obtained through harmonic generation. In our case, the

substrates were irradiated with wavelengths of 266 and 355 nm. The laser fluence (energy per unit of area) was measured with a power meter (Newport model 842 PE). As it can be seen in **Fig. 69**, the laser beam was split into two coherent beams which interfere on the sample surface.

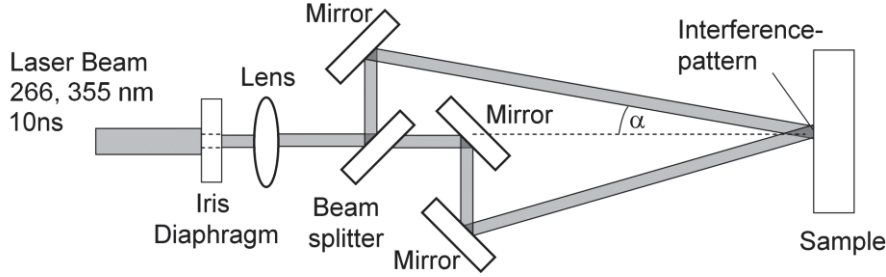


Fig. 69: Experimental setup for the interference experiments; the laser beam was split into two individual laser beams interfering at the sample with an angle 2α .

In this way, a line-like interference pattern is obtained with an intensity distribution given by:

$$I = 2I_0 \cos(kx \sin \alpha)^2$$

eq. 16

with I_0 marking the laser intensity of each laser beam and α the half angle between the laser beams. The periodic distance of the interference pattern (period) can be controlled by modifying the incident angles of the beams, and is given in **eq. 17** below:

$$p = \frac{\lambda}{2 \sin \alpha}$$

eq. 17

with λ being the laser wavelength. For applying periodical distances of 10 and 20 μm , an angle of incidence (α) of 0.5 and 1.0° was adjusted, respectively for 355 nm wavelengths. For the 266 nm radiation, an angle of incidence of 0.76° permitted to fabricate periods of 10 μm . In order to produce cross-like structures, the samples were rotated utilising angles of 60° or 90°, and with a second laser pulse additional lines were produced. The influence of pulse frequency and laser fluence was investigated in the range from 1 to 100 pulses and from 0.6 to 2.4 J/cm², respectively.

Surface characterization

The surface topography of the samples was examined through optical microscope (OM), and SEM images were taken at 20 kV with a Camscan Series 2, Cambridge Instruments. The

surface profile was measured with an optical profilometer (Plμ 2300, Sensofar). These measurements were also used to calculate the structure depth, defined as the depth of the gratings within the pattern. The 3D data analysis was performed with the help of SensoMap Plus software (Sensofar), version 5.0.3.4995. A photoelectron spectrometer AXIS ULTRA (Kratos Analytical, UK) was utilised to investigate possible chemical changes on the surface due to the laser treatment.

Results and discussion

Different periodic arrays including line and cross-like structures have been fabricated on hydroxyapatite using DLIP. Depending on the interference pattern period, laser fluence as well as pulse number, different effects have been observed. Firstly, the polished HA substrates were irradiated with 355 nm laser radiation. Starting from a period of 20 μm, well defined structures developed even using one laser pulse (**Fig. 70 a and b**). Small regions of the original surface remained unchanged at the interference minima positions (**Fig. 70 b**).

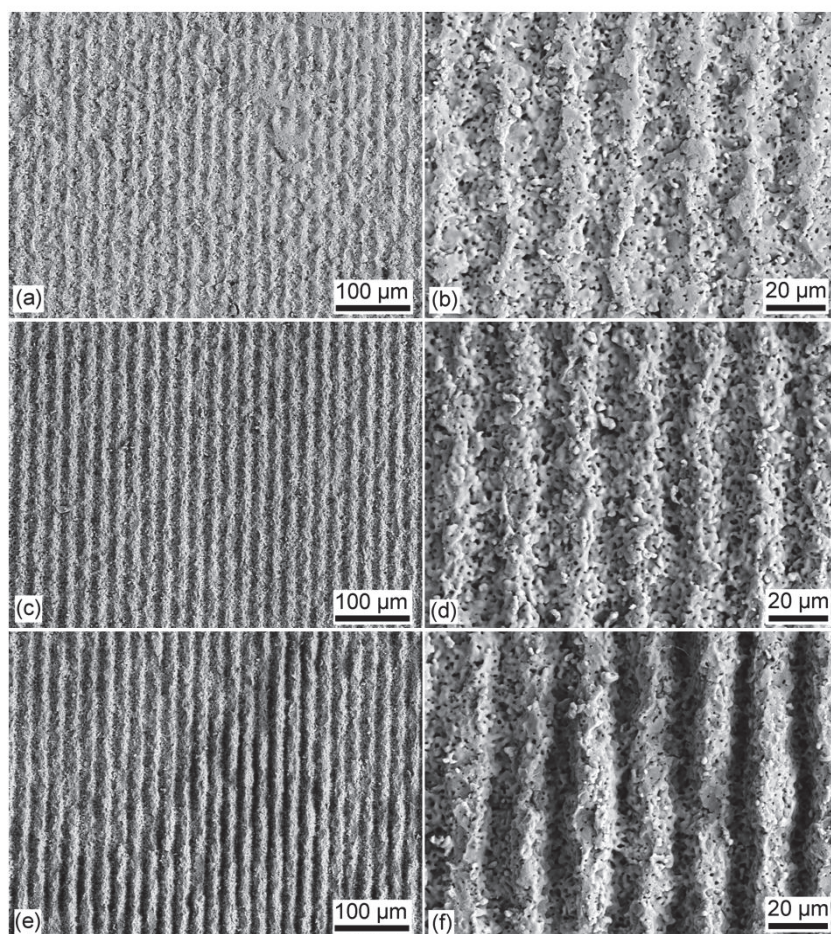


Fig. 70: SEM-micrographs of periodic line-like patterns fabricated on hydroxyapatite with 355 nm laser radiation, 20 μm period and 1.2 J/cm² of laser fluence with: (a and b) 1 pulse, (c and d) 10 pulses and (e and f) 50 laser pulses

At interference maxima positions, the material was molten and ablated, and also several pores ranging from 0.4 to 1.5 μm were recognizable. A laser fluence of 1.2 J/cm^2 was necessary to obtain a homogenous surface structure using a single laser pulse. The increase in laser fluence from 1.2 to 2.4 J/cm^2 produced straighter and clearer lines. Furthermore, for values higher than 2.4 J/cm^2 , even the walls of the structures corresponding to the interference minima positions were modified. However, the variation of laser fluence did not necessarily lead to obtain deeper structures, as shown in **Fig. 71** for 20 μm periodic arrays (e.g. 2.64 and 2.71 μm) for 1.2 and 1.8 J/cm^2 , respectively. On the other hand, variation of the number of laser pulses permitted a better control of the structure depth.

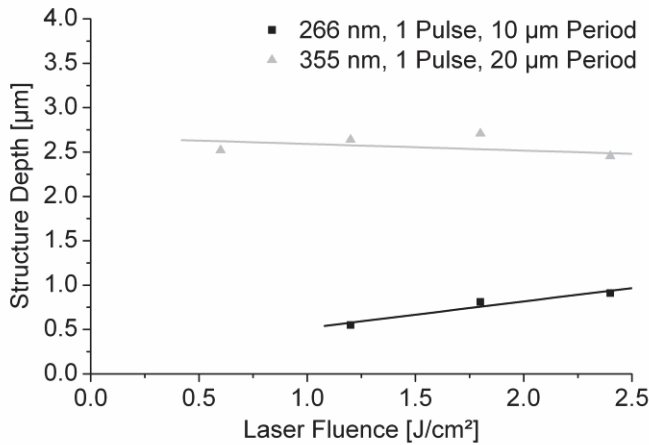


Fig. 71: Structure depth as a function of laser fluence for 355 and 266 nm laser radiation. In all cases one laser pulse was utilized. For 355 nm radiation, the period was 20 μm while for arrays irradiated with a wavelength of 266 nm 10 μm patterns were realized.

From **Fig. 72** (left) it can be seen that structures become deeper with increasing laser pulse number, up to a certain point, for all the studied laser intensities (0.6–2.4 J/cm^2). This effect can be observed in the Scanning Electron Microscope images of **Fig. 70** for HA substrates irradiated with 1.2 J/cm^2 and different number of laser pulses (1 and 10). On the other hand, a high number of laser pulses resulted in a partial destruction of the pattern at several positions. This effect is shown in **Fig. 70 e** for a 20 μm periodic array produced with 50 laser pulses at 1.2 J/cm^2 . In consequence, such processing parameters are not adequate for producing stable micropatterns. This behaviour is even more evident with higher laser fluence rates. The information depicted in **Fig. 72** corresponds to experimental data where the partial destruction of the micropatterns was not observed.

In another set of experiments, HA substrates were irradiated with the same wavelength (355 nm) but using interference patterns with 10 μm periods. In the whole studied range of laser intensities (0.6–2.4 J/cm^2) and pulse numbers (1–100), periodic structures presenting a totally modified surface were observed (even with only one laser pulse). In addition, the structure lines are much less pronounced and, in general, surface patterns could be hardly recognized.

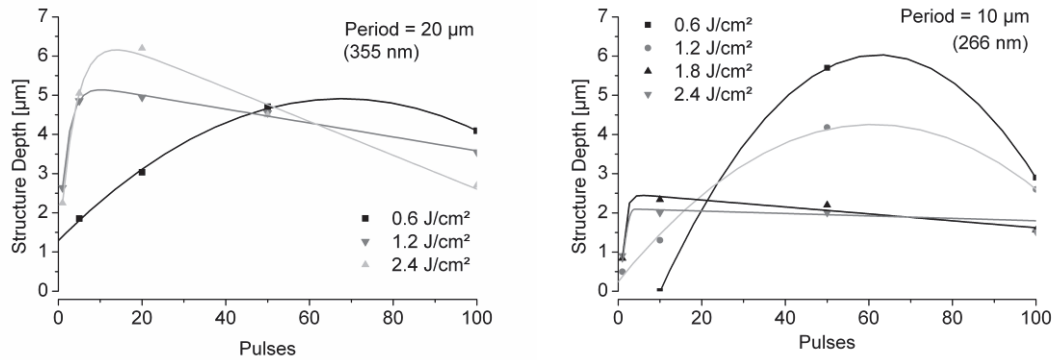


Fig. 72: Structure depth as a function of pulse number for 355 (left) and 266 nm (right) laser wavelength and laser fluence rates ranging from 0.6 to 2.4 J/cm^2

This situation can be clearly observed looking at the 3D surface profiles depicted in **Fig. 73** a and b. The effects mentioned above can be explained with the following process. Firstly, the temperature difference within the wall and the untreated material lead to significant thermal stresses that can partially destroy the pattern, especially when using several laser pulses (**Fig. 70** e and f) (Amer et al., 2005). For 355 nm laser pulses interacting with HA, an important contribution of photo-thermal processes is expected (Wheeler et al., 2003). This means that the material at the interference maxima positions is strongly heated during the laser pulse interaction. Moreover, due to the low thermal conductivity of the material, temperature differences even higher than 2000 to 3000 K are expected between interference maxima and minima positions (Bieda et al., 2010; D'Alessandria et al., 2008). In addition, the porosity of the ceramic material caused by the sintering process enhances such stresses due to disruption of the heat flow. In this way, the temperature is locally increased at the pore borders (Chivel et al., 2007). For smaller periods, the heat can be faster evacuated to the interference minima, thus also modifying substantially the material at those positions (melting and even vaporization). As a consequence, the pattern may get destroyed.

Fig. 73 show a comparison of 10 and 20 μm pattern profiles. For the 10 μm structures (**Fig. 73** a), the patterns are less pronounced and practically not recognizable. By contrast,

patterns with a 20 μm period showed a better morphology (**Fig. 73 b**). Using a wavelength of 266 nm, the HA substrates were also irradiated with different laser fluence rates as well as number of laser pulses.

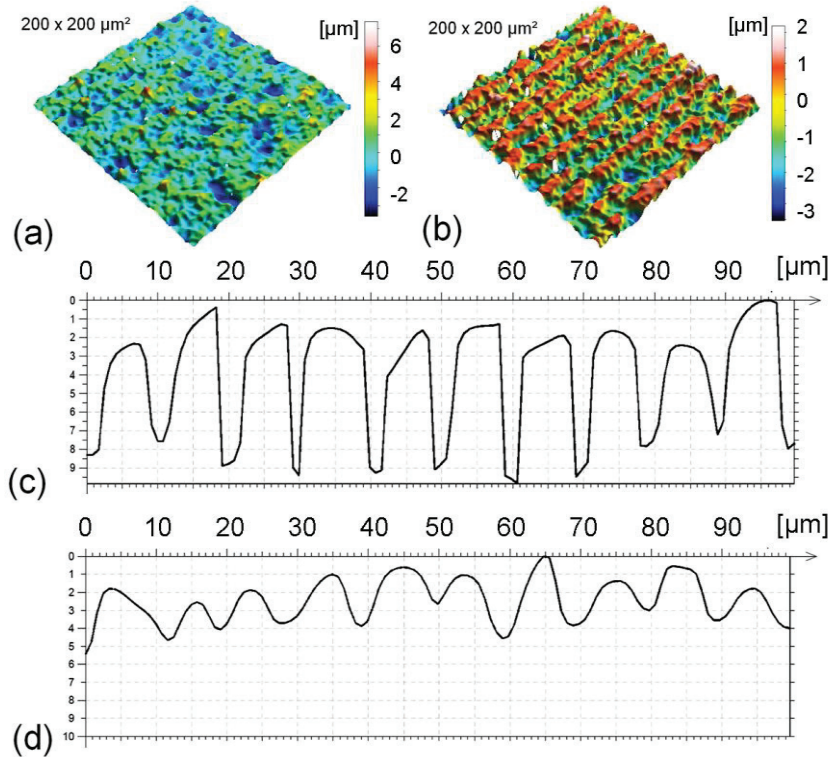


Fig. 73: (a, b) 3D and (c, d) 2D surface profiles of different periodic arrays fabricated with 266 and 355 nm laser pulses; (a) 1.2 J/cm², 1 pulse, 355 nm, 10 μm period; (b) 1.2 J/cm², 1 pulse, 355 nm, 20 μm period; (c) 0.6 J/cm², 50 pulses, 266 nm; (d) 1.8 J/cm², 50 pulses, 266 nm

As can be deduced from **eq. 17**, shorter wavelengths produce smaller periodic arrays at the same incident angle. In order to fabricate 20 μm periodic arrays, an intercepting angle of 0.381° is necessary. Due to geometrical restrictions of the setup utilized for the laser interference experiments, the minimal possible separation between the beam splitter and the first mirror is about 20 mm. This means that the sample should be located at least 300 cm from the beam splitter. In consequence, smaller periodic structures (10 μm pattern periods) have to be fabricated. **Fig. 74 a–c** show SEM micrographs of different 10 μm periodic arrays fabricated with 0.6 J/cm² and different numbers of laser pulses (1–50). Similarly to the 355 nm pulses, more laser pulses produced deeper structures up to a certain value, from which the structure was partially destroyed (**Fig. 72 right**). This effect is stronger for more energetic laser pulses and, as explained before, results from thermal stresses which become more relevant at higher laser fluence rates as well as at large numbers of laser pulses (**Fig. 74 d**).

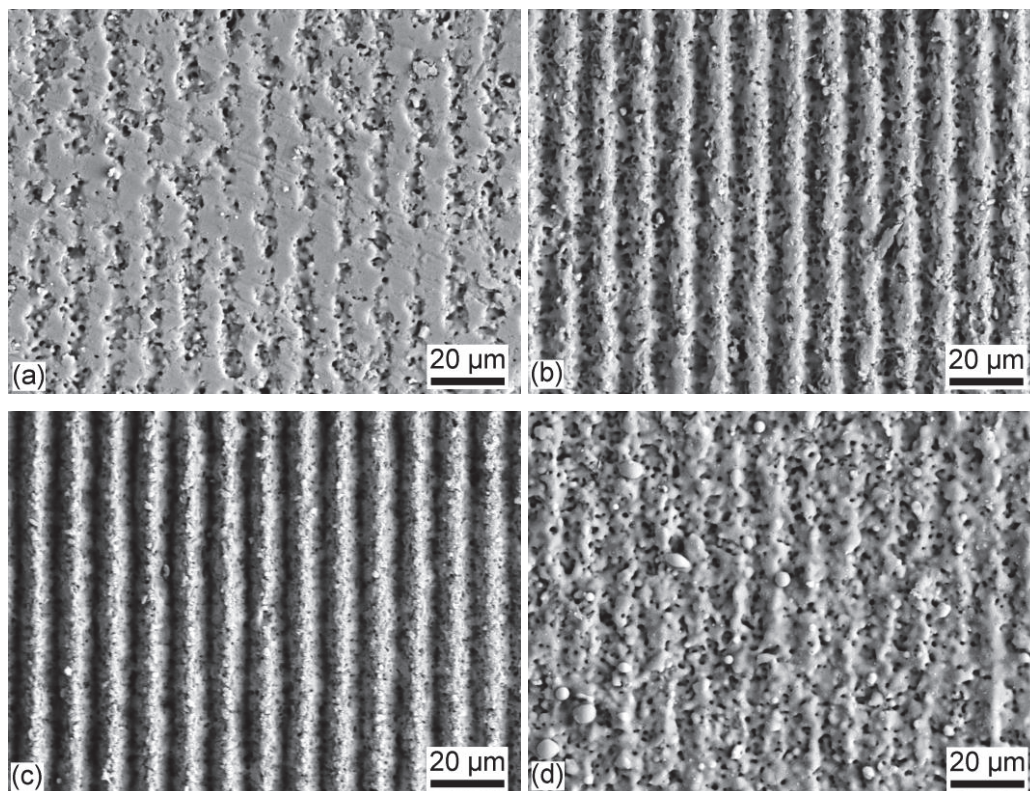


Fig. 74: SEM micrographs of periodic line-like patterns fabricated on hydroxyapatite with 266 nm laser radiation and 10 µm pattern period; (a–c) 0.6 and (d) 2.4 J/cm² per pulse; (a) 1 pulse; (b and d) 10 pulses; (c) 50 pulses

On the other hand, patterns with 10 µm period were homogenous for several combinations of number of pulses and laser fluence rates in comparison to the structures fabricated with 355 nm of wavelength (e.g. **Fig. 74 a–c**). In particular, substrates irradiated with 0.6 J/cm² and 50 pulses showed a structure depth of 5.5 µm (**Fig. 74 c**). A 2D profile of this structure is shown in **Fig. 73 c**. Furthermore, even in substrates irradiated with only one laser pulse, well defined line-like structures could be observed (**Fig. 74 a**). In the latter case, and similarly to 355 nm laser pulses, the structure depth almost did not change when increasing laser fluence for single laser pulse experiments (**Fig. 71**). Moreover, for both studied wavelengths, the thermal diffusion length of HA substrates irradiated with 10 ns laser pulses was much smaller than the obtained structure depth (~0.5 and 2.5 µm for 266 and 355 nm, respectively). Thus, the ablation process is mainly controlled via the absorption coefficient, which means that at 266 nm the smaller structure depth can be related to the higher absorption of the HA substrates (Nakata et al., 2007; Dahotre et al., 2008; Laude et al., 1998; Samant et al., 2009).

Also the width of the modified regions at the interference maxima was smaller than with 355 nm pulses. With short UV wavelengths, absorption of photons can result in transitions

between different electronic energy levels. Thus, the excited ceramic can decompose directly into different products without significant increment of temperature (photochemical ablation) (Nakata et al., 2007). However, we also cannot neglect for this wavelength a significant photothermal contribution, which is especially true for high laser fluence rates (e.g. 1.8–2.4 J/cm²), as depicted in **Fig. 74 d**. In addition to 10 μ m, also 5 μ m patterns were fabricated with 266 nm wavelength. However, in this case, throughout the whole studied range of laser fluence and pulse number, the surface was partially destroyed and no well-defined structure was obtained (not shown). The reason for this behaviour can also be found in thermal stresses induced by the laser treatment. Nevertheless, since for 266 nm wavelengths a higher contribution of photochemical effects is expected, significant thermal stresses are only expected for shorter periods than for 355 nm irradiation. This behaviour is very different to periodic arrays fabricated with this technique on metals (Lasagni et al., 2007; D'Alessandria et al., 2008). In this case, even periodic arrays with periodic distance in the sub-micrometer range could be fabricated.

When comparing **Fig. 72** left and right, and even for the different periodic distances studied, there is a clear shift of the maximal number of laser pulses necessary to obtain deeper structures without distorting the pattern. While for 355 nm and 20 μ m arrays less than 20 pulses must be utilized to preserve the structure, for 266 nm and 10 μ m patterns the number of laser pulses can be increased of up to 50. This effect can be also attributed to a stronger photochemical process for 266 nm wavelengths.

In addition to line-like shaped arrays, also other geometries can be fabricated using the same two-beam setup. Cross-like surface structures, for instance, can be produced by rotating the sample a specific angle as shown in **Fig. 75 a** and **b**, for wavelengths of 355 and 266 nm, and rotation angles of 60° and 90°, respectively. As expected, cross-like patterns fabricated with shorter wavelengths (266 nm) present a better structure quality (**Fig. 75 b**). For 355 nm pulses, in all cases no original (i.e. untreated) surface was observed after irradiation, and the whole surface seemed to be molten and/or ablated. This behaviour was generally observed independently of laser intensity and number of laser pulses. However, and especially for small periods and large number of laser pulses (>50), since thermal stresses are produced when fabricating the line-like arrays during the first irradiation step, at some stage in the second irradiation step after rotation of the substrate, the first structure may be partially destroyed due to the cumulated stresses (**Fig. 75 c**).

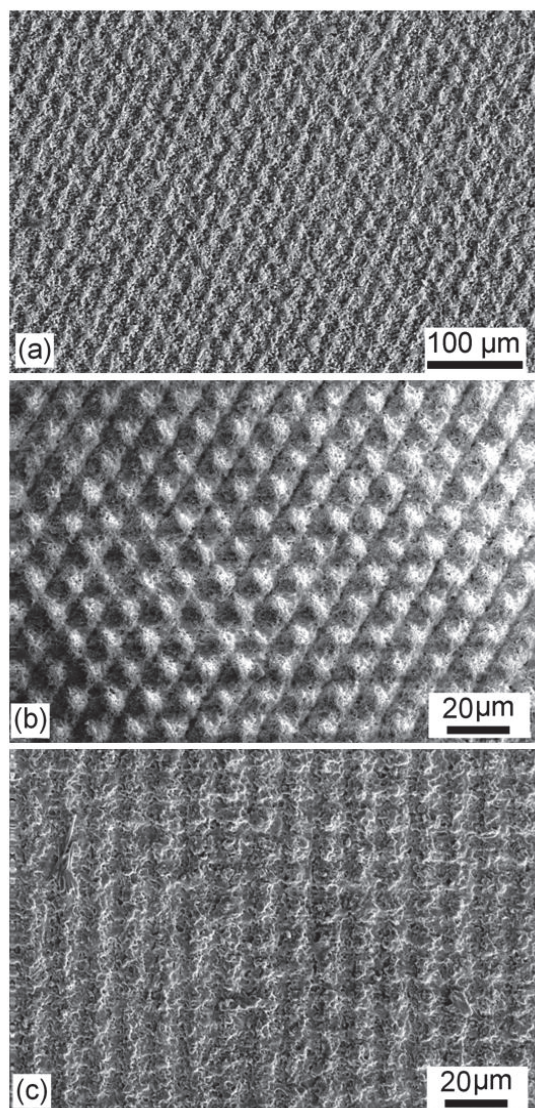


Fig. 75: SEM micrographs of periodic cross-like structures fabricated with (a) 355 and (b, c) 266 nm laser radiation. The period in (a) was 20 μm and the sample was rotated 60° between irradiation steps. In (b) and (c), the period was 10 μm and the sample was rotated 60 and 90°, respectively. The laser fluence and number of laser pulses per irradiation step were: (a) 1.8 J/cm², 1 laser pulse; (b) 0.8 J/cm², 25 pulses; (c) 0.8 J/cm², 75 laser pulses.

As shown in **Fig. 70** and **Fig. 74**, for 355 and 266 nm wavelengths, the modified regions corresponding to the interference maxima positions present several pores. It is very well known that interaction of ns-pulsed lasers with materials may induce different photothermal effects. One of these effects is the formation of pores due to local evaporation of the material at high temperatures. Another reason to explain this phenomenon is given in the high affinity of water and HA. Water is absorbed at the surface as well as at the pores of the ceramic material. Then, it evaporates during the laser interaction process, forming bubbles of gas that

move towards the surface and thus produce the μm pores (Corno et al., 2009; Santos et al., 2002).

In order to determine the chemical surface composition of hydroxyapatite after laser treatment, the samples were analyzed using X-ray Photoelectron Spectroscopy (XPS) (Amrah-Bouali et al., 1994). **Fig. 76** shows XPS spectra of untreated (not irradiated) and treated HA substrates with a laser fluence of 4.8 J/cm^2 and 10 laser pulses for both utilized wavelengths (266 and 355 nm).

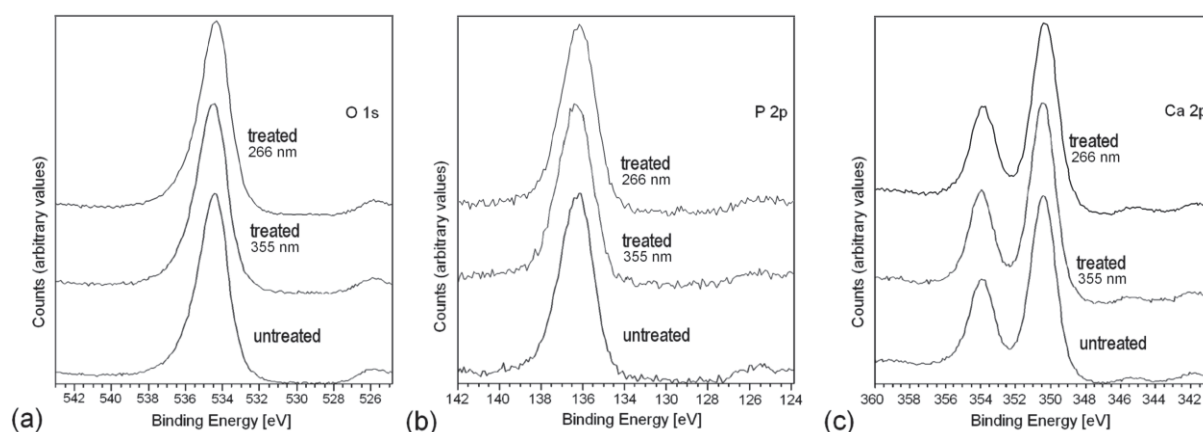


Fig. 76: XPS spectra of untreated (not irradiated) and treated samples (4.8 J/cm^2 , 10 laser pulses) at laser wavelengths of 266 and 355 nm

This laser intensity is clearly higher than the maximal energy densities utilized in the interference experiments. **Fig. 76 b** shows that the phosphorus peaks (P 2p) in the irradiated and not irradiated HA samples do not show any substantial changes. This indicates that no additional phosphate phase is formed during laser irradiation. Also the calcium peaks (Ca 2p, **Fig. 76 c**) for the irradiated and not irradiated samples corresponding to Ca $2p_{3/2}$ ($\sim 348 \text{ eV}$) and Ca $2p_{1/2}$ (351 eV) are very similar to peak ratios ranging from 1.44 to 1.50. The evolution of the oxygen peaks (O 1s, **Fig. 76 a**) corroborates the behaviour observed in the phosphorus and calcium peaks, and, in conclusion, we can confirm that even when using a large number of laser pulses and high laser intensities, no substantial changes in the chemical composition have been produced on the studied materials. Similar results were obtained for other samples irradiated with 1 to 10 laser pulses and 2.4 J/cm^2 of laser fluence (not shown). The obtained results are in accordance with the findings of other researchers describing irradiation of HA substrates with UV lasers (Amrah-Bouali et al., 1994; Ferraz et al., 1999; Sivakumar et al., 2008).

Conclusions

Single and multi-pulse laser interference experiments have been conducted on hydroxyapatite. Using different interference patterns such as line and cross-like arrays, the effects of laser fluence, periodic distance, pulse number, and wavelength were investigated. It was found that there is a range of laser fluence rates and pulse numbers where homogenous structures develop. In addition, larger periods (e.g. 20 and 10 μm for 355 and 266 nm wavelengths, respectively) allow for better patterns. In consequence, a compromise between laser fluence and number of laser pulses must be found to obtain well-defined and stable structures.

By increasing the pulse number (5–50) deeper structures could also be fabricated, especially at moderate laser fluence rates (e.g. 0.6 J/cm^2 for 266 nm wavelength). For single pulse laser experiments, an increase in laser fluence did not produce deeper structures after certain laser fluence. The smaller structure depth of HA substrates irradiated with 266 nm wavelength result from a higher absorption than when using 355 nm laser radiation.

At high laser fluence rates (1.8–2.4 J/cm^2) as well as with several laser pulses (~ 20), the periodic arrays become partially destroyed due to significant thermal stresses between interference maxima and minima positions. On the other hand, using shorter wavelengths (266 nm) the ablation is also conducted by photochemical processes. Hence, smaller periodic arrays as well as deeper structures could be fabricated since thermal stresses are reduced. In the case of 266 nm laser radiation, patterns with periodic distance smaller than 10 μm were partially destroyed in the whole studied range of laser fluence and pulse numbers, while for 355 nm radiation the limit was 20 μm .

XPS analyses have shown that there are no chemical changes in the irradiated hydroxyapatite surface, due to the laser irradiation, not even at high laser fluence rates (4.8 J/cm^2). However, since HA substrates are locally molten and evaporated, it is also possible that amorphous HA has been formed due to the fast interaction of the laser beam with the material. This behaviour has been reported for HA substrates irradiated with ArF, KrF, and XeF lasers (193, 248 and 351 nm, respectively), where a thin layer of amorphous HA (of some nanometres) was formed after evaporation of the material from an ablated hole and posterior deposition around that hole (Nakata et al., 2007).

The size and scale of the structures reported here are appropriate for controlling cell adhesion, promoting cell alignment, and improving biocompatibility. Further studies to evaluate biological response of cells are being conducted and will be reported in the future.

4. Comparison of micropatterning methods for ceramic surfaces

The following results were submitted to the Journal of the European Ceramic Society by Marzellus grosse Holthaus, Laura Treccani and Kurosch Rezwan in 2011 (University of Bremen, Germany).

Abstract

The fabrication of defined ceramic micropatterns smaller than 100 μm is, due to the hardness and brittleness of ceramic materials, still very challenging. However, in recent years micropatterned ceramic surfaces have become highly interesting for biomedical applications or the fabrication of energy-converting devices, such as solid oxide fuel or solar cells. In this study, we will evaluate six modern techniques for ceramic pattern fabrication with feature sizes ranging from 5 to 100 μm . Ceramic materials such as alumina, zirconia, silica, and hydroxyapatite will be discussed herein. Advantages and disadvantages for each process are highlighted and compared to other techniques. Three of these techniques, namely microtransfer molding, modified micromolding, and Aerosol-Jet[®] printing generate patterns starting with aqueous ceramic suspensions. The other three techniques, i.e. micromachining and two different types of laser treatment, produce micropatterns through the removal of material from solid ceramic substrates. The detailed analysis yields that properties such as the desired micropatterning size, shape, or the production time are strongly dependent on the chosen technique.

Introduction

Micropatterned surfaces are gaining ever more interest in the field of material research and industrial manufacture. They have become state of the art and opened new fields of potential applications for the fabrication of, for example, micromolds with modulated micro-topographies (Brinksmeier et al., 2008), or for the modification of micro-bio-interfaces in order to guide interactions between cell tissue and medical implant surfaces (Kirmizidis and Birch, 2009; Lim and Donahue, 2007). The development and improvement of surface micro and nanopatterning have been in the focus of materials research for the last twenty years. In doing so, various techniques for the fabrication of patterned surfaces have been developed. These techniques have been reviewed by a large number of research groups (Gates et al., 2005; Geissler and Xia, 2004; Heule et al., 2003; ten Elshof et al., 2010; Xia and Whitesides,

1998). Ceramic materials are of great interest for micropatterning processes, because they exhibit highly advantageous properties compared to polymers and metals, advantages such as high thermal resistance, chemical inertness, high hardness, and biocompatibility. However, obtaining ceramic micropatterns with high accuracy, e.g. precise edge contours, is very challenging due to the particular hardness and typically brittle behaviour of ceramic materials. For the surface patterning of ceramic materials mainly two different strategies can be applied. First of all, there is the possibility of machine-aided ceramic micropatterning with a strong need for technical equipment. Examples of it are laser surface treatment, injection molding of microparts, slip pressing or casting of microdevices, and micromachining of surfaces through CNC machining, for instance (Computer Numerical Control). Beyond doubt, the results of the machine-aided methods are quite convincing. Bauer et al. reported the reliable fabrication of microparts with highly accurate edge contours and surface details by use of ceramic slip pressing. Thereby, alumina arrays of more than a thousand columns could be fabricated with smooth sidewalls and sharp edges. The thus fabricated patterns were 455 μm high and 115 μm wide (Bauer et al., 1999). Other groups reported reproducible results from the fabrication of microdevices via ceramic injection molding (CIM), in particular with low pressure injection molding (LPIM) of ceramic feedstocks. Various ceramic materials such as alumina, hydroxyapatite, and zirconia have been used to reliably produce micropatterned components of a few cm^2 in size (Fanelli et al., 1989; Knitter et al., 2001; Piottter et al., 2003). Some of these machine-aided processes yielded remarkable results in terms of micropattern edge contours und process reliability. One main advantage of this is the potential fabrication of high numbers of items per time. The limiting factor, however, is the difficulty in obtaining micropatterns or components smaller than 100 μm . A different approach to fabricate highly defined ceramic patterns is the possibility of using low-cost methods such as soft-lithography techniques (Xia and Whitesides, 1998). Soft-lithography is able to fabricate micropatterns with low technical efforts and yet very high accuracy - even smaller than 100 μm - at the same time.

In this study, we evaluate the results of six different micropatterning techniques for ceramic materials for obtaining structural features of less than 100 μm . Non-oxide ceramic hydroxyapatite and at least one oxide material, such as alumina or zirconia, were used as material to be patterned. The following techniques will be evaluated: microtransfer molding (μTM), modified micromolding (m- μM), Aerosol-Jet[®] printing, CNC-micromachining as well as two types of laser treatment. Each technique was tested and evaluated for ceramic micropatterning size features ranging from 5 to 100 μm .

Experimental procedures

Six different processing techniques were applied to fabricate micropatterned ceramic surfaces. For CNC micromachining and two types of laser treatment, solid ceramic substrates were deployed. From these samples, material was removed in order to form micropatterned surfaces. For the other three techniques, namely, microtransfer molding, modified micromolding, and Aerosol-Jet[®] printing, the micropatterns were obtained by starting with aqueous ceramic suspensions.

Fabrication of non-patterned substrates

Plane cylindrical, non-patterned platelets were fabricated through uni-axially die-pressing with 15 kN of 1.7 g commercially available calcium phosphate hydroxyapatite powder (HA, $\text{Ca}_{10}(\text{PO}_4)_6(\text{OH})_2$, Prod.-No. 04238, Lot: 8345A, Sigma-Aldrich Chemie GmbH, Munich, Germany). The HA powder had a theoretical density of $3.03 \pm 0.04 \text{ g/cm}^3$ and particle sizes of $151 \pm 0.24 \text{ nm}$. After die-pressing, all samples were sintered for two hours at 1200 °C in a furnace at ambient conditions (LHT08/17, Nabertherm GmbH, Lilienthal, Germany). The heating rate was at 50 °C/h, the cooling rate at 100 °C/h. Except for modified micromolding, the non-patterned samples were used for all patterning processes.

Fabrication of aqueous ceramic suspensions for molding and printing

Three different ceramic suspensions were used for the patterning processes. One suspension contained 11.15 g of HA particles. The HA powder was stirred (RW20, IKA Werke GmbH, Staufen, Germany) into 20 g of double deionised water (Synergy[®], Millipore, resistivity 18 MΩ*cm, Schwalbach, Germany) so as to obtain a suspension of 15 vol.% solid loading. The ceramic suspension was adjusted to pH 9-10 through the addition of ammonia solution (25 %), which served the aim to achieve electrostatic stability and to prevent agglomeration of the particles. This ceramic suspension was used as a stamping liquid for the microtransfer molding (μTM) process. Another ceramic suspension was utilised as a ceramic “ink” for Aerosol-Jet[®] printing processes. It was similar to the first suspension, yet it was diluted to a solid loading of 6.6 vol.%. The third suspension was used for modified micromolding. Its composition was similar to the one used for liquid stamping, but, additionally, a polyacrylic acid-based dispersant/binder was added (12 mg/g ceramic powder). Prior to micropatterning, all ceramic suspensions were homogenised through ultrasonic treatment (Sonifier 450,

Branson Ultraschall, Dietzenbach, Germany) for three minutes in order to disperse potential agglomerates.

Micropatterning techniques

Microtransfer molding

For the microtransfer molding (μ TM) process, a ceramic suspension was pipetted onto the micropatterned area of a soft mold (PDMS, Sylgard[®] 184 silicone elastomer, Dow Corning, Wiesbaden, Germany). Excessive suspension was carefully removed with a doctor's blade. Subsequently, the filled mold was deposited on a plane ceramic substrate. After drying, the mold was lifted carefully. The patterned thin film remained on the substrate during the removal of the mold (**Fig. 77 a**). Hereafter, the ceramic substrate and ceramic patterns were sintered. A more detailed description of this method is published in Holthaus and Rezwan 2008. Generally speaking, adjustable parameters for microtransfer molding are, for example, drying conditions, dispersants and binders, particle sizes, and solid loadings of used ceramic suspensions.

Modified micromolding

Similar to the microtransfer molding process, micropatterned soft PDMS master molds were deployed for modified micromolding (m- μ M). The cylindrical molds were sealed with polyethylene tubes and aqueous ceramic suspension was pipetted into the molding chamber. During the drying process the ceramic particles sank down to the bottom of the mold, while water was continuously evaporating. After drying, the mold could be lifted with care from the micropatterned solid ceramic sample. Afterwards, sintering was performed as mentioned above. Additional details about this method are described in Holthaus et al. 2010 (**Fig. 77 b**). Adjustable parameters for modified micromolding are e.g. drying conditions, binders and dispersants, solid loading of the ceramic suspensions and particle size.

Aerosol-Jet[®] printing

Aerosol-Jet[®] printing (Optomec Inc., Albuquerque, USA), also known as maskless mesoscale materials deposition (M³D), was used for directly printing ceramic aerosols on non-patterned ceramic substrates. The aerosol of a ceramic suspension was generated with an ultrasonic transducer. The printing device is computer-aided and was used to deposit the ceramic

particles on specific positions onto the plane substrate. The particles were carried by a gas and deposited by a nozzle onto the substrate. Subsequent sintering of the printed microstructures by means of an NdYAG laser (Newport Spectra-Physics, Darmstadt, Germany) was proceeded. Further information about this experiment is provided in Holthaus and Rezwan (2008) (**Fig. 77 c**). Adjustable parameters for Aerosol-Jet[®] printing are related to the used ceramic suspensions, e.g. dispersants and binders, particle sizes, and solid loading. Additionally, process parameters such as the feed motion of the print head, the distance between nozzle and substrate, the repetition of printing cycles on identical locations, and the power of the laser are important parameters for the outcome of the patterning process.

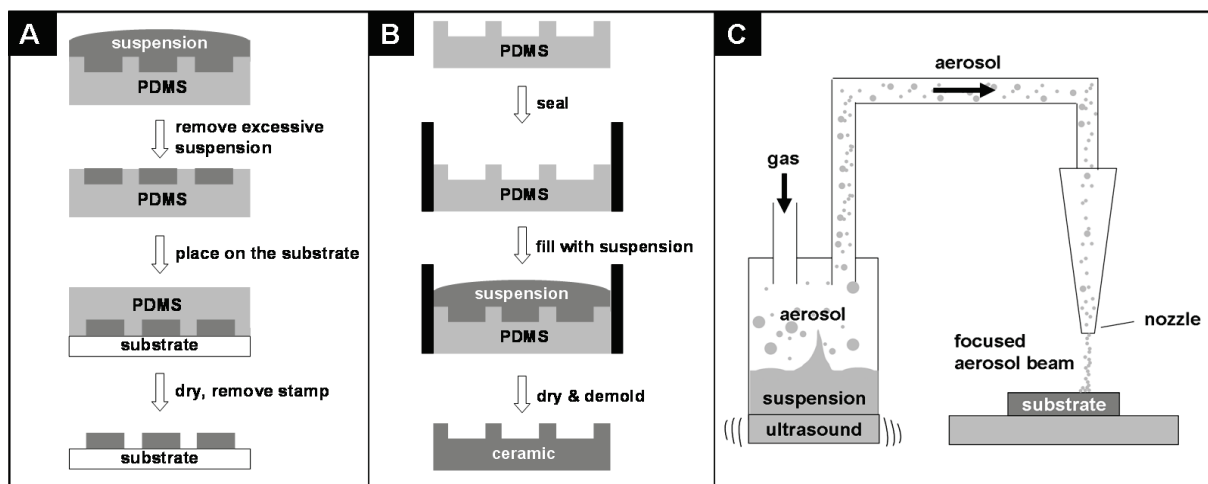


Fig. 77: Illustrations of micropatterning techniques using aqueous ceramic suspension. **A:** microtransfer molding (μTM). **B:** modified micromolding ($m\text{-}\mu\text{M}$). **C:** Aerosol-Jet[®] printing (M^3D)

CNC micromachining

Automated CNC milling and grinding (Ultrasonic 20 linear, DMG Sauer GmbH, Stipshausen, Germany) was applied on solid ceramic substrates. During the cutting process, the workpiece was held stationary as the rotating cutting tool moved along a programmed path in order to cut the material. Machining was operated with so-called end milling cutters, namely, with ball-nose end mills. The tools cut with their sides as well as with their tips, while the contact force during machining removed particles from the surface layer of the ceramic substrate (**Fig. 78 a**). Altogether, the rotational speed (n), the feed velocity (v_f), and the diameter of the cutting tool (D) are important adjustable parameters which influence the machining results.

Laser treatment

Two different laser treatment processes were applied. By use of the first laser treatment ceramic particles were directly removed from the solid ceramic substrate through thermal laser ablation at ambient conditions via an Nd:YAG laser (Newport Spectra-Physics) at a wavelength of 1064 nm. Thereby, ceramic particles were removed by the laser beam from a flux zone in the irradiated area (**Fig. 78 b**). A more detailed description of this treatment is given in Holthaus and Rezwan (2008).

The second laser treatment technique was the direct laser interference patterning (DLIP). In this procedure, the laser provides a fundamental wavelength of 1064 nm (Nd:YAG, Newport Spectra-Physics). An applied wavelength of 266 nm was obtained by harmonic generation via a shutter. The laser beam was split into two coherent laser beams which interfered on the ceramic substrate surface. This interference process, then, produced micropatterns on the irradiated area of several square millimetres (**Fig. 78 c**). Further details of this method can be found in Berger et al. (2011). Various parameters such as the laser power, the laser beam wave length, the number of laser pulses, or the pulse duration are important parameters for the adjustment of both laser treatment processes.

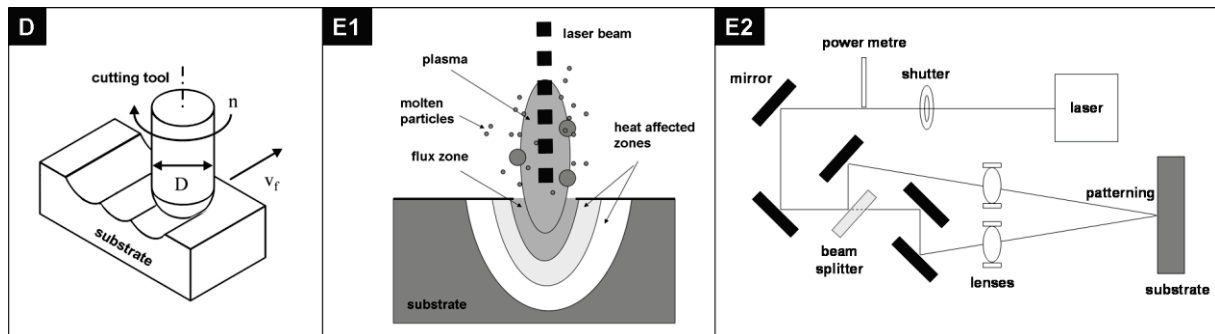


Fig. 78: Illustrations of different micropatterning techniques. D: CNC micromachining via a cutting tool with a diameter (D), rotational speed (n), and feed velocity (v_f). E1: laser ablation process. E2: setup of direct laser interference patterning (DLIP)

Imaging of surface texture and analysis of surface roughness

Micrographs were taken at 20 kV through scanning electron microscopy (SEM) with a Camscan Series 2 (Obducat CamScan Ltd., Cambridgeshire, United Kingdom). Prior to imaging, the samples were sputtered with gold (K550, Emitech, Judges Scientific plc, West Sussex, UK).

3D measurements of fabricated ceramic micropatterns were taken via a confocal optical profilometry system (Plμ 2300, Sensofar Technology, Terrassa, Spain) at 420-fold magnification. Measurements in triplicate were conducted on $n = 3$ samples each. In doing the profilometry analysis, the average surface roughness (R_a) of micropatterned areas was determined. The measurement length was $l_c = 4$ mm according to ISO4287 (ISO 4287, 1997). These measurements were applied to evaluate the influence of each micropatterning process on the surface roughness in the patterning region. In addition, virtual cross sections (2D surface profiles) were exemplarily measured for one sample of each micropatterning method.

Determination of crystal structure and analysis of surface properties

The samples of all applied patterning methods were analysed via X-ray diffraction measurements (XRD, C3000, Seifert, Ahrensburg, Germany) in order to determine possible changes in the crystal structure due to the patterning technique.

Two methods were used to detect possible wear residues from, for instance, tools from the patterning process. Firstly, energy-dispersive spectroscopy (EDS, Camscan Series 2, Obducat CamScan Ltd., Cambridgeshire, UK) with a detection limit of about 0.1% of the elements mass was used, and two different spots with an area of $27 \times 17 \mu\text{m}^2$ each were measured. Secondly, X-ray Fluorescence analysis (XRF) was conducted so as to detect residues from the patterning process (detection limit of approximately 10 ppm). XRF measurement was carried out using a low and a high pass filter (0-40 keV, XL3t900 AnalytiCON Instruments GmbH, Rosbach, v.d. Hoehe, Germany). The measurements were taken on two different circular spots with an area of 7.1 mm^2 each. Prior to the EDS and XRF analysis, the samples were washed three times for five minutes respectively with deionised water in an ultrasonic cleaner.

Results

Micropatterned ceramic thin films stamped via microtransfer molding (μTM)

The drying of microtransfer-molded ceramic surfaces took about two to three days at ambient conditions ($\sim 21^\circ\text{C}$, 30-40% r.h.) and up to six days at 4°C . Although it was possible to fabricate ceramic samples without any cracks after the drying process, all samples showed very fine micron sized cracks after sintering. The cracks occurred throughout the whole sample surface. However, accurate micropatterns with vertical sidewalls were clearly visible. Various pattern geometries such as microcylinders, channels, and struts have been successfully transfer-molded. Although excessive ceramic suspension was removed from the

mold, a layer of suspension below the patterns was always transferred to the substrate surface. The thickness of the transferred thin films varied from 20 to 110 μm . The accuracy in height of some transferred patterns was homogenous after drying ($\pm 1 \mu\text{m}$). The smallest transferred HA patterns were 10 μm in width featuring heights of 10 μm . All patterned areas looked craggy and fissured after sintering, whereas microchannels and microstruts were still accurate and had defined contours on edges. Due to big cracks the accuracy of pattern heights was strongly reduced ($\pm 4 \mu\text{m}$) after sintering. The accuracy of sintered patterns varied about $\pm 2 \mu\text{m}$ in width. The average surface roughness inside sintered transfer-molded HA microchannels was of $R_a = 2.9 \mu\text{m}$.

The microtransfer-molded ZrO_2 patterns shown in **Fig. 79 a** were fabricated using a suspension of 15 vol.%. The patterns dried at ambient conditions. XRD analysis of transfer-molded and sintered HA samples showed no detectable changes in crystal structure, e.g. peaks of β -tricalcium phosphate (β -TCP). Other ceramic suspensions, such as alumina, have been transfer-molded with similar results.

Micropatterned solid ceramic bodies fabricated via modified micromolding (m- μM)

Solid micropatterned ceramic samples were fabricated via modified micromolding and were dried for a period of up to five days at ambient conditions. This drying period could be decreased to two days by means of a climate chamber at 30 °C and 30% r.h. The crack-free fabrication of patterned solid ceramic samples was feasible with various ceramic suspensions. Thereby, different geometries such as cylinders, struts, and microchannels with widths and depths ranging from 5 to 200 μm could be successfully produced. The molded micropatterns featured very accurate edge contours after drying and sintering. Molded patterns measured on different samples varied about $\pm 1.4 \mu\text{m}$ in height and $\pm 1.2 \mu\text{m}$ in width after sintering.

The molded patterns shown in **Fig. 79 b** were fabricated using a SiO_2 suspension of 10 vol.% with 12 mg Syntran[®]/ g ceramic. The samples were then dried at 25 °C with 25% r.h. and sintered at 1400 °C. The average roughness inside and outside patterned areas was identical. For example, a roughness of $R_a = 0.2 \mu\text{m}$ was measured inside sintered molded HA patterns. XRD analysis of a modified micromolded and sintered HA sample showed no changes in crystal structure.

Aerosol-Jet[®]-printed ceramic micropatterns on ceramic substrates

The complete Aerosol-Jet[®] patterning of a ceramic sample as shown in **Fig. 79 c** took roughly three hours. The printed micropatterns showed a grainy surface and did not feature vertical sidewalls and accurate edge contours. Single ceramic particles or agglomerates were visible on top of the fabricated patterns as well as next to the patterned regions. The Aerosol-Jet[®]-printed patterns dried within seconds, thus a controlled drying process was not applicable. Various pattern geometries such as circles and lines could be successfully printed. After the laser treatment, the ceramic particles were not fully sintered and partially showed only sinter neck formation. A few fine cracks were distinguished within the generated structures. The sintering quality varied strongly, with some regions of the micropatterns having been more sintered than others and some being already molten. The micropattern size was limited by the size of a single printed line. The smallest adjustable printed lines ranged from 10 to 15 μm in width and height. The heights of printed micropatterns on different samples varied between $\pm 4 \mu\text{m}$ and $\pm 3 \mu\text{m}$ in width. It was possible to print multi-layers in order to fabricate, for instance, micropatterns with widths of 50 μm and heights of almost 30 μm . The average roughness on aerosol-printed regions was $R_a = 4.1 \mu\text{m}$. The focused aerosol beam had often to be re-adjusted, which was due to an inconstant aerosol flow.

The patterns shown in **Fig. 79 c** were fabricated by printing single lines of HA suspension (6.6 vol.%), using a feed motion of the printer nozzle at 0.5 mm/s. Afterwards, the patterns were sintered with an Nd:YAG laser (1064 nm) with a power of 0.25 W. The lateral laser movement was at 0.5 mm/s. An XRD analysis of a laser-sintered, aerosol-printed HA sample showed no changes in crystal structure.

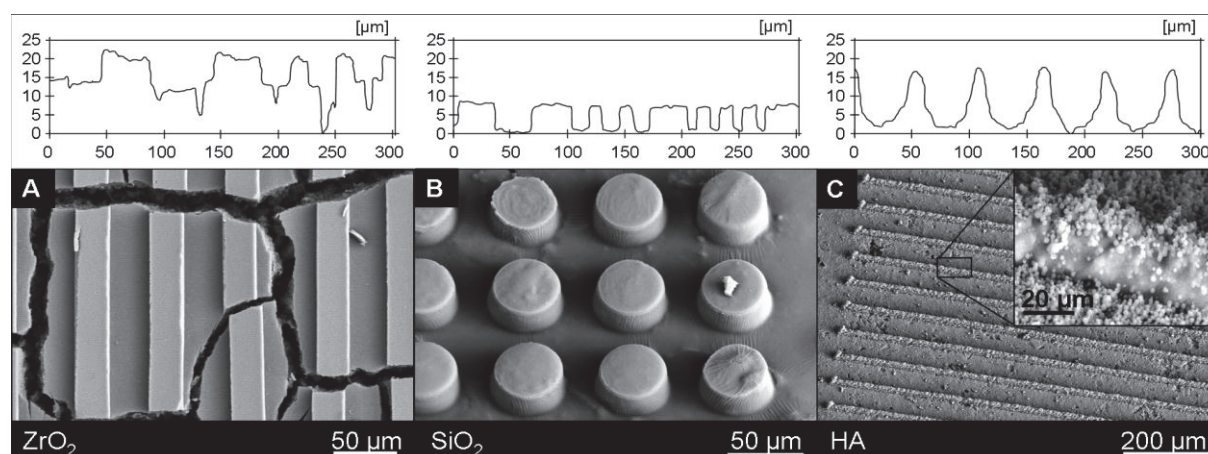


Fig. 79: SEM micrographs of micropatterned ceramic surfaces. A: microtransfer-molded 30 μm wide zirconia channels; B: modified micromolded 50 μm wide SiO_2 cylinders; C: Aerosol-Jet[®]-printed, 10 μm wide HA struts. The inset shows the magnification of a printed and sintered line. The 2D profiles show representative profiles of fabricated ceramic patterns.

CNC-micromachined solid ceramic samples

By using grinding pins or milling tools in the micromachining process it was possible to fabricate large ceramic micropatterns of several cm². The complete machining of each ceramic sample took about sixty minutes. In both cases, periodic groove-like micropatterns were machined. In addition, other pattern geometries such as pyramid-like patterns were successfully machined in preliminary tests. Milled HA samples exhibited U and V-shaped topographies, with their surface being chipped and rough. In contrast, grinding delivered sharply edged grooves (rectangle profile) with pattern sidewalls almost vertical and perpendicular to the bottom area. Microgrinding resulted in smoother surface roughness as compared to milling. However, the surface roughness of all CNC-machined regions ranged from Ra = 0.3 to 0.8 µm. The smallest machined patterns were of 100 µm in width with a maximum pattern depth of about 10 µm. Smaller patterns of 75 µm in width were achieved by re-sintering micromachined ceramic green bodies due to shrinkage. In comparing the identically machined samples, the accuracy in pattern width was of ± 3 µm and ± 2 µm in depth. The ZrO₂ micropatterns illustrated in **Fig. 80 d** were machined using a ball-end grinding pin with a tool diameter of 500 µm, a feed velocity of 125 mm/min, and a rotational speed of 40.000 rpm. An XRD analysis of the thus machined HA samples showed no alterations in crystal structure. Although strong defects due to abrasive wear were found on the machine tools, no residues from the tools were detectable via XRF analysis or EDS after three washing processes with double deionised water in an ultrasound cleaner.

Laser-treated ceramic surfaces

The ablation process of a ceramic sample took about ten minutes. The fabricated microchannels showed U/V-shaped profiles. The surface of these ablated patterns looked rough and bumpy. Thereby, the surface of microchannels with widths of 40 µm and 80 µm seemed to be partially molten. The surface of microchannels with widths of 220 µm looked molten as well, but also rough and craggy. Moreover, the contours of ablated pattern edges were inaccurate and rough. The surface roughness inside microchannels of 220 µm in width was of Ra = 14.8 µm. Rough surfaces with drop-shaped bumps were noticed next to laser-ablated regions, e.g. on the struts between the channels. It seemed like molten ceramic particles solidified subsequently after ablation. The depth of the laser-ablated micropatterns varied from 30 to 110 µm, whereas the depth increased with increasing channel width. The accuracy in pattern height was about ± 10 µm and the accuracy in pattern width about ± 8 µm.

The adjustment of laser power in order to get constant ablation quality turned out somewhat difficult. Furthermore, it was not feasible to generate micropatterns smaller than $\sim 30 \mu\text{m}$ on die-pressed ceramic substrates without a significant loss of micropattern edge contour. The HA micropatterns shown in **Fig. 80 e1** were laser-ablated using an Nd:YAG laser with a wavelength of 1064 nm and a pulse duration of 100 ns. The laser power was of 3.5 W, and a feed motion of 16 mm/s was used. The XRD analysis of laser-ablated HA samples showed no change in crystal structure, though amorphous fractions due the massive heat impact are most likely to appear. The oxide ceramic alumina was patterned in initial tests.

Direct laser interference patterning (DLIP) conducted on plane ceramic surfaces resulted in periodic patterns with U/V-shaped pattern profiles. The effects of laser fluence, periodic distance, pulse number, and wavelength were investigated, from which it was found that there is a range of laser fluence rates and pulse frequencies at which homogenous ceramic patterns can be developed. Different interference patterns such as line-like and cross-like arrays were fabricated using single laser or multi-laser pulses. The generation of large area patterning with distinct patterns of several mm^2 was realisable by using only one single laser pulse. The patterning of all sample surfaces took a few minutes. The interference patterns showed a distinct geometry, but their surfaces looked rough and partially molten. The contour on pattern edges was inaccurate and rough, while the measured surface roughness inside patterns was of $R_a = 2.1 \mu\text{m}$. The smallest producible line-like patterns were of $10 \mu\text{m}$ in width. Pattern depths ranging from $0.5 \mu\text{m}$ to $6 \mu\text{m}$ could be fabricated controllably.

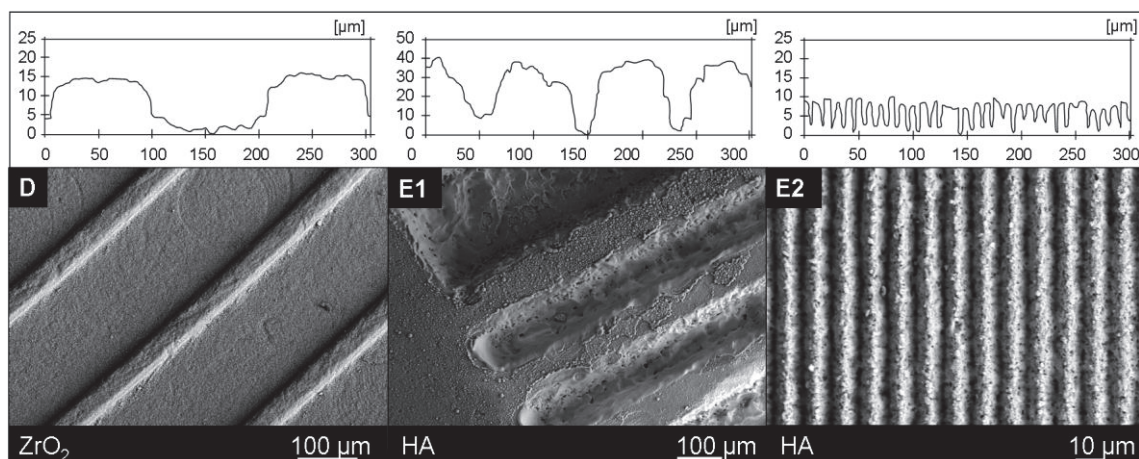


Fig. 80: SEM micrographs of micropatterned ceramic surfaces. D: micromachined (grinding) $200 \mu\text{m}$ wide ZrO_2 channels; E1: laser-ablated HA microchannels with widths of $40 \mu\text{m}$ (centre); E2: laser-interference patterned $10 \mu\text{m}$ wide HA channels. 2D profiles show representative profiles of fabricated ceramic patterns.

The accuracy of pattern width as well as pattern depth was about $\pm 1 \mu\text{m}$, comparing various samples. The HA patterns shown in **Fig. 80 e2** were generated at a wavelength of 266 nm, a laser fluence of 0.6 J/cm^2 , and 50 pulses with durations of 10 ns each. Other materials such as oxide ceramics alumina and zirconia were patterned in initial tests. No significant changes were detectable in the XPS analysis of untreated and DLIP-treated HA substrates with a laser fluence of 4.8 J/cm^2 and ten laser pulses.

Discussion

Microtransfer molding was applied in order to fabricate micropatterned thin films with various pattern geometries as small as $10 \mu\text{m}$ with very high accuracy on edge contours. Even suspensions containing, for instance, fluorescently labelled biomolecules such as protein BSA (bovine serum albumin) have been successfully patterned to ceramic surfaces and glass slides (**Fig. 25**). The deviations of $\pm 4 \mu\text{m}$ in pattern height and of $\pm 2 \mu\text{m}$ in width on different ceramic transfer-patterned samples seemed promising. A disadvantage of it consists in the production time, which is of some days due to the drying process. On the other hand, one advantage can be seen in the relatively low costs for equipment. The occurrence of cracks is strongly dependent on processing parameters such as the substrate surface, the sintering process, or the amount of stamped material. The lower the amount of stamped material, the lower will be the probability of cracks. The maximum success rate for crack-free drying on glass slides was about 70%, whereas the maximal crack-free drying on a ceramic (HA) surface was only 15%. In the end, though, all sintered samples showed cracks. However, until the occurrence of cracks is not fully evitable, the μTM process is not applicable for large area patterning of ceramic surfaces.

Overall, it was possible to fabricate micropatterned solid ceramic samples via modified micromolding. In doing so, various materials and geometries have been successfully used. The smallest fabricated patterns were only $5 \mu\text{m}$ in width and height, whereas the edge contours were still very high. Smaller patterns have not been fabricated with any other tested technique. The deviations of molded patterns on different samples were $\pm 1 \mu\text{m}$ in height and width. One big disadvantage is the long production time of a few days. A clear advantage of m- μM consists in the joint processing of the substrate/device and the micropatterns at once. The success rates for crack-free drying with subsequent sintering were different for the used ceramic materials and strongly depended on process parameters. However, success rates of 88% were reached for HA and even 100% for zirconia and alumina. The main advantage,

without doubt, can be seen in the high output of crack-free ceramic micropatterns. Other advantages are the relatively low costs for equipment and the possibility of local deposition of molecules on patterned regions by the use of the μ TM method. This has successfully been tested with BSA on micromolded HA and alumina patterns with widths of 50 μm (**Fig. 25**). One property which differentiated m- μM from all other tested patterning techniques was the identical surface roughness on patterned and non-patterned regions. Except for the etching of the master molds, no complex devices or machines were needed for this soft-lithographic-based technique, which makes this method accessible to a wide range of users.

Using Aerosol-Jet[®] printing it was possible to generate patterns of 10 μm in width. The contour of edges and the achieved deviations of $\pm 4 \mu\text{m}$ in pattern height and of $\pm 3 \mu\text{m}$ in width on different samples were not that high when compared to m- μM . A big advantage lies in the possibility to print maskless patterns of various materials onto the same substrate. Even the printing of different materials onto the same sample thus becomes feasible. Aerosol-Jet[®] printing is a useful, automated, fast processing method, through which samples can be patterned within hours. A disadvantage of it is the occurrence of molten areas in the patterning regions due to the uncontrollable sintering temperature by the adjustment of the laser power. Amorphous phases or change in crystal structure cannot be excluded, either. However, this is avoidable by sintering in a furnace at controlled conditions. Big disadvantages of it are the high costs for equipment.

Using CNC micromachining the limit in pattern width was at 100 μm , which was much larger than in all the other techniques. Although smaller geometries of 75 μm in width could be realized by re-sintering, these patterns were still larger than those from the remaining techniques. The shape of the machined ceramic patterns depended on the chosen machine tool, where U and V-shaped as well as rectangular pattern profiles could be successfully fabricated on oxide and non-oxide ceramic surfaces. The contour on pattern edges was high, though still lower in comparison to m- μM . The deviations of the machined samples were about $\pm 2 \mu\text{m}$ in pattern depth, but were always at least 12% lower than the predicted (calculated) pattern depth. Deviations of $\pm 3 \mu\text{m}$ were achieved in pattern width on different samples. The surface roughness ($R_a = 0.3$ to $0.8 \mu\text{m}$) of the machined regions was lower than in other techniques, e.g. in laser treatment. Some disadvantages of it were strong wear of the cutting tools tip, the size of the smallest producible patterns, and the relatively high costs for

equipment. Its advantages lie in the automated, fast, and maskless manufacture of solid patterned samples within hours.

The use of laser ablation resulted in patterns with a minimum width of 30 μm , tested on oxide and non-oxide ceramics. This is not as small as fabricated via m- μM or Aerosol-Jet[®] printing, yet much smaller than through micromachining. Ablated pattern edges looked inaccurate, with the pattern surface either being rough and craggy, or even molten. In molten regions, amorphous phases or changes in crystal structure cannot be excluded. The deviations between patterns of ablated samples were of $\pm 10 \mu\text{m}$ in height and $\pm 8 \mu\text{m}$ in width. These values were the largest measured deviations of all tested techniques. Likewise, the average roughness on ablated regions ($R_a = 14.8 \mu\text{m}$) was the highest R_a value measured in our experiments. A clear disadvantage of this technique can be seen in the high costs for equipment. On the other hand, laser ablation is a fast and maskless method for the fabrication of micropatterned solid ceramic samples.

Direct laser interference patterning resulted in various shaped micropatterns with minimum widths of only 10 μm on oxide and non-oxide ceramics. The accuracy on pattern edges was lower than with m- μM , but much higher in comparison to common laser ablation. The deviations of interference patterned structures on different samples were of $\pm 1 \mu\text{m}$ in height and width, which was as low as with m- μM . The average roughness on DLIP-patterned regions ($R_a = 2.1 \mu\text{m}$) was similarly low as obtained through Aerosol-Jet[®] printing. The most palpable disadvantage consists in the high costs for equipment and regions with molten surfaces. Important advantages of DLIP are a maskless processing and the very fast patterning of large areas by using only a few laser pulses.

Highly accurate microgeometries with vertical sidewalls generated via molding could be used e.g. for biological applications such as fluidic chambers, sensor surfaces, for fundamental cell-surface research, or for novel types of energy conversion cells. Because of its ability to print various materials into the same pattern, Aerosol-Jet[®] printing could be useful e.g. for applications where different materials have to be integrated into the same processing step, such as layer-wise printing of conductive metallic paths and isolating ceramic parts for sensor applications. Moreover, CNC micromachining is applicable for the patterning of ceramic implant surfaces or even for the manufacture of whole ceramic implants with inline-processing of specific surface patterning in order to mediate the implant in-growth into the

body. Laser treatment of ceramic surfaces could be applied to pattern ceramic implant surfaces, too, or else to modulate surfaces of ceramic bearings so as to optimize friction and wear. In summary, all tested patterning techniques proved to be very useful for the fabrication of ceramic micropatterns smaller than 100 μm . The thus fabricated micropattern surfaces and geometries all turned out somewhat different from each other, depending on the method applied, which in turn enables a wide range of potential usages. An overview of the properties of all these patterning techniques is given in **Tab. 9**.

Tab. 9: Overview on properties of micropatterning techniques for ceramic materials

Method	stamping via microtransfer molding (μ TM)	modified micromolding (m- μ M)	Aerosol-Jet [®] printing with laser sintering (M^3D)	micro-machining via CNC	laser ablation	direct laser interference patterning (DLIP)
Properties						
Smallest pattern size in x/y (*)	10 μ m	5 μ m	10 μ m	100 μ m	30 μ m	10 μ m
Are various pattern geometries producible?	yes	yes	yes	yes	yes	yes
Contour accuracy on edges	very high	very high	middle	high	middle	middle
Surface roughness (Ra) of patterned regions (*)	$\sim 3 \mu$ m	$\sim 0.2 \mu$ m	$\sim 4 \mu$ m	$\sim 0.3-0.8 \mu$ m	$\sim 15 \mu$ m	$\sim 2 \mu$ m
Tolerances in height/depth (z) (*#)	$\pm 4 \mu$ m	$\pm 1 \mu$ m	$\pm 4 \mu$ m	$\pm 2 \mu$ m (> 12 %)	$\pm 10 \mu$ m	$\pm 1 \mu$ m
Tolerances in width (x,y) (*)	$\pm 2 \mu$ m	$\pm 1 \mu$ m	$\pm 3 \mu$ m	$\pm 3 \mu$ m	$\pm 8 \mu$ m	$\pm 1 \mu$ m
final product	μ -patterned thin film on substrate	μ -patterned solid ceramic sample	μ -patterned thin film on substrate	μ -patterned solid ceramic sample	μ -patterned solid ceramic sample	μ -patterned solid ceramic sample
Is joint processing of substrate & pattern possible?	no	yes	no	no	no	no
Was there a change in crystal structure detectable after patterning?	no	no	no	no	No. However, localized amorphous phases very likely.	No. However, localized amorphous phases very likely.
Is there possible contamination by residues from e.g. tools?	no	no	no	yes	no	no
Is in situ deposition of other particles/biomolecules possible with this method?	yes	yes (via μ TM)	yes	no	no	no
Is the method applicable for oxide and non-oxide ceramics alike?	yes	yes	yes	yes	yes	yes
Production time from raw material to final product	days	days	hours	hours	hours	hours
Is sintering required after patterning?	yes	yes	yes	no	no	no
Are masks/templates needed?	yes	yes	no	no	no	no
Is industrial up-scaling possible?	yes	yes	yes	yes	yes	yes
Costs for equipment	low	low	high	high	high	high
(*) Measurements in triplicate of neighbouring patterns were taken on n = 3 final micropatterned products made of HA.						
(#) Machined depths turned out at least 12% lower than predicted pattern depths, which were calculated before machining.						

Conclusions

All tested patterning techniques proved to be useful for the production of ceramic micropatterns, but each tested process, naturally enough, has its respective advantages and disadvantages. However, general properties, such as the costs for equipment, may affect the choice of a certain patterning technique more strongly than other aspects. On the other hand, in deciding thus, one has to bear in mind that the desired kind of micropattern geometry, accuracy, or size are also affected by the choice, which limits the number of suitable patterning methods in situations, for instance, in which a specific surface finish turns out indispensable. So, micropatterns as small as 5 μm with vertical sidewalls can be achieved through modified micromolding. These patterns feature very high accuracy and low technical effort at the same time. However, the production time from the raw material to the final patterned product takes some days. A considerably faster processing method consists in Aerosol-Jet[®] printing, but there the accuracy is lower and the costs for equipment are higher. Further, via micromachining it is not possible to fabricate ceramic patterns smaller than 100 μm , and the costs for the equipment are high, too. On the other hand, it is a fast process for the patterning of various ceramic solid materials. Laser treatment processes still imply high costs for technical equipment, though the production time required is comparatively low. Especially direct interference patterning offers a fast and accurate patterning of ceramic surfaces.

5. Conclusion

Different patterning techniques for the fabrication of ceramic micropatterns have been investigated. In doing so, it has been found that all tested methods are capable to generate ceramic patterns smaller than 100 μm . On the one side, the choice for a patterning technique was found to be limited by factors such as the costs for equipment or the production time from raw material to the final product. On the other hand, the kind of micropattern the geometry, the accuracy as well as the size of the micropattern required are also factors that may come to play a significant role in this choice. This in turn limits the number of suitable patterning methods, i.e. especially if specific surface finish requirements are obligatory. Via microtransfer molding (μTM) it was possible to fabricate ceramic patterns of 10 μm in width, though in most cases these patterns were very craggy and fissured after sintering. At that time, this technique showed the least suitability for the fabrication of ceramic patterns. However, μTM could be used, in combination with modified micromolding (m- μM), in order to locally functionalise non-patterned and patterned surfaces with proteins. Modified micromolding has been introduced during this thesis as a new patterning technique. Because of its low technical effort and the low costs for equipment, m- μM has probably the highest potential to get optimized. Although it is rather a slow and non-automated processing route, pattern sizes of 5 μm could already be fabricated with very high accuracy on micropattern edge contours. Additional testing has revealed that scratches of several tens of microns in length and only one micron in height and width could be molded with ceramic suspensions, which indicates a very high potential for further downsizing. In addition, this process showed a very high potential to become fully automated.

Automated Aerosol-Jet[®] printing was able to pattern surfaces in shorter periods of time compared to μTM and m- μM . The accuracy on pattern edge contours was lower and the pattern surface was much rougher. The costs for equipment were very high. Nevertheless, it provided the possibility to pattern differently shaped ceramic surfaces with various materials down to 10 to 15 μm in size.

CNC micromachining resulted in the biggest pattern sizes, i.e. in sizes of 100 μm in width, which shrank down to 75 μm after re-sintering the machined samples. The use of smaller tool diameters and other tool materials might result in much smaller machined ceramic patterns in the future. Besides, this processing route was automated and should be easily capable of being integrated into industrial processes. Both tested laser treatment processes imply high costs for technical equipment, but their big advantage consists in the short production time from raw

material to the final patterned product. Direct interference patterning (DLIP) offers, due to its higher accuracy as compared to direct laser ablation, a very fast and accurate patterning of ceramic surfaces. The patterns were less accurate and much rougher than with modified micromolding, but pattern widths of 10 μm were already feasible within one laser pulse. In addition, this technique has high potentials to get fully automated and integrated into industrial processes.

In total, we can conclude that in this study we have highlighted and compared the advantages and disadvantages of all the above-mentioned methods. The detailed analysis has yielded that properties such as the desired micropatterning size, shape or production time strongly depend on the chosen patterning technique. Randomized hydroxyapatite surface roughness with a roughness of $R_a = 3.36 \mu\text{m}$ to $0.13 \mu\text{m}$ has no significant influence on the human osteoblast viability (WST and collagen type I production) within the first 7 days in-vitro. Different hydroxyapatite-based micropatterns ranging from 16 μm to 77 μm have been used for in-vitro cell studies on human osteoblasts. The results thereof have shown that a distinct osteoblast alignment is already caused by patterns of only 16 μm in width. Most cells oriented between orientation angles from 0 to 15° in reference to the micropattern direction. Very similar results were achieved with patterns of 30 μm in width. Contrary to this, larger pattern widths such as from 45 to 76 μm caused much lower cell orientation. We have further shown that, in our experiments, more osteoblasts grew on top of the micropatterns instead of inside the microchannels. This effect increased with decreasing pattern widths. Overall, it was found that less viable cells grow on patterned compared to non-patterned HA-based surfaces.

6. Outlook

All tested patterning techniques offer many possible fields for further studies. Microtransfer molding (μ TM) as well as modified micromolding (m- μ M) can be improved in terms of crack-free drying and sintering. Therefore, the effect of binder contents or binder systems, such as silica-based or polymer based binders, could be further investigated. In addition, drying processes could be varied. Probably, drying processes with continuing ramps of different temperatures and humidity rates may deliver better results. Likewise, the stamping of proteins and ceramic nanoparticles into molded ceramic patterns via pre-structured PDMS molds could be of interest in order to mediate surface-chemistry-dependent cell growth. Although patterns of 5 μ m in width were fabricated, especially modified micromolding should be studied to achieve even smaller patterns with high accuracy at the same time. The main aim, however, should be the achievement of reproducible high success rates for large area patterning of several cm². Aerosol-Jet[®] printing, for example, could be used to deposit various proteins into microchannels or to realize an inline printing of cells and protein-doped ceramic suspensions. Those printed patterned samples could be used, then, as bone-grafting material - without sintering - for the fabrication of patient-adapted scaffolds with immobilized viable cells. In addition, the effect of different bio-functionalizations on patterned surfaces could be tested by combining Aerosol-Jet[®] printing and m- μ M. Tools smaller than 300 μ m in diameter could be tested for their ability to fabricate smaller ceramic patterns by using CNC micromachining. Therefore, tools such as CVD diamond-coated shaft tools could be used. A possible re-sintering effect of ceramic particles was assumed in the grinding region. This effect could be of interest for further experiments since a similar effect has already been reported for metals. The systematic investigation of process parameters using laser treatment processes could be expanded to other oxide ceramics such as alumina and zirconia. These materials could be of interest for load-bearing applications such as hip-joints or friction-type bearings. Therefore, the influence of laser-treated ceramic patterns on the surfaces' friction and wear behaviour could be of high interest. Furthermore, other laser treatment methods, such as microlense array patterning, should be studied so as to achieve smaller patterns with higher pattern edge contours. The effect of large-area laser treatment of hydroxyapatite or zirconia on HOB cells could be interesting for dental applications. Further, in-vitro testing with HOB cells, e.g. on molded ceramic patterns, should be conducted. There are still many unanswered questions. For example, what happens exactly on patterns in the range between 30 and 45 μ m, and what occurs on patterns larger than 76 μ m? Do the HOB cells then still recognize that a surface is micropatterned? Which pattern depth is still effective enough to

guide HOB cells and at which depth do the HOBs grow inside as well as on top of the micropatterns? Micromolding certainly provides a versatile tool to get answers for these questions.

7. References

Adams, D. P., Vasile, M. J. and Krishnan, A. S. M., "Microgrooving and microthreading tools for fabricating curvilinear features," *Precision Engineering*, 24(4) 347-56 (2000).

Ahn, S. J., Min, J. H., Kim, J. and Moon, J., "Process mechanism for vacuum-assisted microfluidic lithography with ceramic colloidal suspensions," *J Am Ceram Soc*, 91(7) 2143-49 (2008).

Amer, M. S., El-Ashry, M. A., Dosser, L. R., Hix, K. E., Maguire, J. F. and Irwin, B., "Femtosecond versus nanosecond laser machining: comparison of induced stresses and structural changes in silicon wafers," *Appl Surf Sci*, 242(1-2) 162-67 (2005).

Amrah-Bouali, S., Rey, C., Lebugle, A. and Bernache, D., "Surface modifications of hydroxyapatite ceramics in aqueous media," *Biomaterials*, 15(4) 269-72 (1994).

Anselme, K., "Osteoblast adhesion on biomaterials," *Biomaterials*, 21(7) 667-81 (2000).

Bailey, R. C., Stevenson, K. J. and Hupp, J. T., "Assembly of Micropatterned Colloidal Gold Thin Films via Microtransfer Molding and Electrophoretic Deposition," *Adv Mater*, 12(24) 1930-34 (2000).

Ball, M., Grant, D. M., Lo, W. J. and Scotchford, C. A., "The effect of different surface morphology and roughness on osteoblast-like cells," *Journal of Biomedical Materials Research Part A*, 86(3) 637-47 (2008).

Bauer, W., Ritzhaupt-Kleissl, H. J. and Hausselt, J., "Micropatterning of ceramics by slip pressing," *Ceramics International*, 25(3) 201-05 (1999).

Bäuerle, D., "Laser processing and chemistry," pp. 788 3 ed. Springer: Berlin, (2000).

Beck, C., "Dreidimensionale Beschreibung technischer Oberflächen- Quo vadis Rauheitsmessung?," pp. 40-45. in Messen und Prüfen, Vol. 54. Messen und Prüfen, München, 2009.

Beh, W. S., Xia, Y. N. and Qin, D., "Formation of patterned microstructures of polycrystalline ceramics from precursor polymers using micromolding in capillaries," *J Mater Res*, 14(10) 3995-4003 (1999).

Beh, W. S., Kim, I. T., Qin, D., Xia, Y. and Whitesides, G. M., "Formation of Patterned Microstructures of Conducting Polymers by Soft Lithography, and Applications in Microelectronic Device Fabrication," *Adv Mater*, 11(12) 1038-41 (1999).

Berger, J., Grosse Holthaus, M., Pistillo, N., Roch, T., Rezwan, K. and Lasagni, A. F., "Ultraviolet laser interference patterning of hydroxyapatite surfaces," *Appl Surf Sci*, 257(7) 3081-87 (2011).

Bernard, A., Renault, J. P., Michel, B., Bosshard, H. R. and Delamarche, E., "Microcontact printing of proteins," *Adv Mater*, 12(14) 1067-70 (2000).

Berry, C. C., Campbell, G., Spadicino, A., Robertson, M. and Curtis, A. S. G. A. S. G., "The influence of microscale topography on fibroblast attachment and motility," *Biomaterials*, 25(26) 5781-88 (2004).

Bertsch, A., Renaud, P., Vogt, C. and Bernhard, P., "Rapid prototyping of small size objects," *Rapid Prototyping J*, 6(4) 259-66 (2000).

Bieda, M., Beyer, E. and Lasagni, A. F., "Direct Fabrication of Hierarchical Microstructures on Metals by Means of Direct Laser Interference Patterning," *Journal of Engineering Materials and Technology*, 132(3) 031015-6 (2010).

Blindow, S., Pulkin, M., Koch, D., Grathwohl, G. and Rezwan, K., "Contents: (Adv. Eng. Mater. 11/2009)," *Adv Eng Mater*, 11(11) 867-72 (2009).

Bowers, K., Keller, J., Randolph, B., Wick, D. and Michaels, C., "Optimization of surface micromorphology for enhanced osteoblast responses in vitro," *Implant Dentistry*, 2(2) 131 (1993).

Boyan, B. D., Bonewald, L. F., Paschalis, E. P., Lohmann, C. H., Rosser, J., Cochran, D. L., Dean, D. D., Schwartz, Z. and Boskey, A. L., "Osteoblast-mediated mineral deposition in

culture is dependent on surface microtopography," *Calcified Tissue International*, 71(6) 519-29 (2002).

Bradt, R. C., Munz, D., Sakai, M. and White, K. W., "Fracture Mechanics of Ceramics," pp. 636 Vol. 1. Springer: Berlin, (2005).

Brinksmeier, E., Gläbe, R., Riemer, O. and Twardy, S., "Potentials of precision machining processes for the manufacture of micro forming molds," *Microsyst Technol*, 14(12) 1983-87 (2008).

Brunette, D. M. and Chehroudi, B., "The Effects of the Surface Topography of Micromachined Titanium Substrata on Cell Behavior in Vitro and in Vivo," *Journal of Biomechanical Engineering*, 121(1) 49-57 (1999).

Buser, D., Schenk, R. K., Steinemann, S., Fiorellini, J. P., Fox, C. H. and Stich, H., "Influence of surface characteristics on bone integration of titanium implants. A histomorphometric study in miniature pigs," *Journal of Biomedical Materials Research*, 25(7) 889-902 (1991).

Catrin, R., Lasagni, A. F., Gachot, C., Schmid, U. and Mücklich, F., "Microstructural Design of Advanced Architectures in Titanium/Platinum Thin Films by Laser Interference Metallurgy," *Adv Eng Mater*, 10(5) 466-70 (2008).

Cavallini, M., Murgia, M. and Biscarini, F., "Patterning a Conjugated Molecular Thin Film at Submicron Scale by Modified Microtransfer Molding," *Nano Lett*, 1(4) 193-95 (2001).

Cawley, J. D., "Solid freeform fabrication of ceramics," *Current Opinion in Solid State and Materials Science*, 4(5) 483-89 (1999).

Cesarano, J., "A review of robocasting technology," *Solid Freeform and Additive Fabrication*, 542 133-39 (1999).

Cesarano, J. I., Baer, T. A. and Calvert, P., "Recent developments in freeform fabrication of dense ceramics from slurry deposition," pp. Medium: ED; Size: 10 p. in Conference: 8. solid

freeform fabrication conference, Austin, TX (United States), 11-13 Aug 1997; Other Information: PBD: (1997). **1997**.

Chelule, K. L., Coole, T. J. and Cheshire, D. G., "An investigation into the machinability of hydroxyapatite for bone restoration implants," *J Mater Process Tech*, 135(2-3) 242-46 (**2003**).

Chichkov, B. N., Momma, C., Nolte, S., von Alvensleben, F. and Tünnermann, A., "Femtosecond, picosecond and nanosecond laser ablation of solids," *Applied Physics A: Materials Science & Processing*, 63(2) 109-15 (**1996**).

Chivel, Y., Petrushina, M. and Smurov, I., "Influence of initial micro-porosity of target on material ejection under nanosecond laser pulses," *Appl Surf Sci*, 254(4) 816-20 (**2007**).

Clem, P. G., Jeon, N.-L., Nuzzo, R. G. and Payne, D. A., "Monolayer-Mediated Deposition of Tantalum(V) Oxide Thin Film Structures from Solution Precursors," *J Am Ceram Soc*, 80(11) 2821-27 (**1997**).

Corno, M., Busco, C., Bolis, V., Tosoni, S. and Ugliengo, P., "Water Adsorption on the Stoichiometric (001) and (010) Surfaces of Hydroxyapatite: A Periodic B3LYP Study," *Langmuir*, 25(4) 2188-98 (**2009**).

Curtis, A. S. G. and Wilkinson, C. D. W., "Reactions of cells to topography," *Journal of Biomaterials Science, Polymer Edition*, 9 1313-29 (**1998**).

D'Alessandria, M., Lasagni, A. and Mücklich, F., "Direct micro-patterning of aluminum substrates via laser interference metallurgy," *Appl Surf Sci*, 255(5, Part 2) 3210-16 (**2008**).

Dahotre, N. B. and Harimkar, S. P., "Laser Fabrication and Machining of Materials." Springer: Berlin, (**2007**).

Dahotre, N. B. and Samant, A. N., "Laser machining of structural ceramics--A review," *J Eur Ceram Soc*, 29(6) 969-93 (**2009**).

de la Fuente, J. M., Andar, A., Gadegaard, N., Berry, C. C., Kingshott, P. and Riehle, M. O., "Fluorescent aromatic platforms for cell patterning," *Langmuir*, 22(13) 5528-32 (**2006**).

Dearnley, P., "A review of metallic, ceramic and surface-treated metals used for bearing surfaces in human joint replacements," *Proceedings of the Institution of Mechanical Engineers, Part H: Journal of Engineering in Medicine*, 213(2) 107-35 (**1999**).

Delamarche, E., Bernard, A., Schmid, H., Michel, B. and Biebuyck, H., "Patterned Delivery of Immunoglobulins to Surfaces Using Microfluidic Networks," *Science*, 276(5313) 779-81 (**1997**).

Deligianni, D. D., Katsala, N. D., Koutsoukos, P. G. and Missirlis, Y. F., "Effect of surface roughness of hydroxyapatite on human bone marrow cell adhesion, proliferation, differentiation and detachment strength," *Biomaterials*, 22(1) 87-96 (**2001**).

Detsch, R., Uhl, F., Deisinger, U. and Ziegler, G., "3D-Cultivation of bone marrow stromal cells on hydroxyapatite scaffolds fabricated by dispense-plotting and negative mould technique," *J Mater Sci-Mater M*, 19(4) 1491-96 (**2008**).

Dormer-Tools, "Technical Handbook - Dormer Tools," pp. 1-148. in, Vol. 1. Edited by Dormer-Tools. Dormer-Tools, Sheffield, UK, **2005**.

Dorozhkin, S. V., "Bioceramics based on calcium orthophosphates (Review)," *Glass Ceram+*, 64(11-12) 442-47 (**2007**).

Dorozhkin, S. V., "Calcium orthophosphate-based biocomposites and hybrid biomaterials," *J Mater Sci*, 44(9) 2343-87 (**2009**).

Ducy, P., Schinke, T. and Karsenty, G., "The Osteoblast: A Sophisticated Fibroblast under Central Surveillance," *Science*, 289(5484) 1501-04 (**2000**).

Dusseiller, M. R., Schlaepfer, D., Koch, M., Kroschewski, R. and Textor, M., "An inverted microcontact printing method on topographically structured polystyrene chips for arrayed micro-3-D culturing of single cells," *Biomaterials*, 26(29) 5917-25 (**2005**).

Elliott, J. C., "Structure and chemistry of the apatites and other calcium orthophosphates," pp. 387. Elsevier: New York, (1994).

Elssner, G., Hoven, H., Kiessler, G., Wellner, P. and Wert, R., "Analysis of hardness testing indentations," pp. 144-58. in *Ceramics and Ceramic Composites*. Elsevier Science, New York, 1999.

Fackler, O. T. and Grosse, R., "Cell motility through plasma membrane blebbing," *Journal of Cell Biology* (2008).

Fanelli, A. J., Silvers, R. D., Frei, W. S., Burlew, J. V. and Marsh, G. B., "New Aqueous Injection Molding Process for Ceramic Powders," *J Am Ceram Soc*, 72(10) 1833-36 (1989).

Ferraz, M. P., Monteiro, F. J. and Santos, J. D., "CaO-P₂O₅ glass hydroxyapatite double-layer plasma-sprayed coating: In vitro bioactivity evaluation," *Journal of Biomedical Materials Research*, 45(4) 376-83 (1999).

Filiz, S., Xie, L., Weiss, L. E. and Ozdoganlar, O. B., "Micromilling of microbarbs for medical implants," *Int J Mach Tool Manu*, 48(3-4) 459-72 (2008).

Friedrich, C. R. and Vasile, M. J., "Development of the micromilling process for high-aspect-ratio microstructures," *J Microelectromech S*, 5(1) 33-38 (1996).

Gates, B. D., Xu, Q., Stewart, M., Ryan, D., Willson, C. G. and Whitesides, G. M., "New Approaches to Nanofabrication: Molding, Printing, and Other Techniques," *Chemical Reviews*, 105(4) 1171-96 (2005).

Geissler, M. and Xia, Y., "Patterning: Principles and Some New Developments," *Adv Mater*, 16(15) 1249-69 (2004).

Gogotsi, Y. G. and (Eds.), R. A. A., "Materials Science of Carbides, Nitrides and Borides," pp. 380 Vol. 68. Kluwer: Dordrecht (NL), (1999).

Greulich, M., Greul, M. and Pintat, T., "Fast, functional prototypes via multiphase jet solidification," *Rapid Prototyping J*, 1(1) 20-25 (1995).

Griffith, A. A., "The Phenomena of Rupture and Flow in Solids," Philosophical Transactions of the Royal Society of London. Series A, Containing Papers of a Mathematical or Physical Character, 221(582-593) 163-98 (1921).

Groot, K., Wolke, J. and Jansen, J., "Calcium phosphate coatings for medical implants," *Proceedings of the Institution of Mechanical Engineers, Part H: Journal of Engineering in Medicine*, 212(2) 137-47 (1998).

Grunwald, I., Groth, E., Wirth, I., Schumacher, J., Maiwald, M., Zoellmer, V. and Busse, M., "Surface biofunctionalization and production of miniaturized sensor structures using aerosol printing technologies," *Biofabrication*, 2(1) (2010).

Ha, S. W., Mayer, J., Koch, B. and Wintermantel, E., "Plasma-sprayed hydroxylapatite coating on carbon fibre reinforced thermoplastic composite materials," *Journal of Materials Science: Materials in Medicine*, 5(6) 481-84 (1994).

Hagmann, J., Burger, M. M. and Dagan, D., "Regulation of plasma membrane blebbing by the cytoskeleton," *J Cell Biochem*, 73(4) 488-99 (1999).

Hansch, R., Chowdhury, M. R. R. and Menzler, N. H., "Screen printing of sol-gel-derived electrolytes for solid oxide fuel cell (SOFC) application," *Ceramics International*, 35(2) 803-11 (2009).

Hayashi, K., Inadome, T., Tsumura, H., Nakashima, Y. and Sugioka, Y., "Effect of surface roughness of hydroxyapatite-coated titanium on the bone-implant interface shear strength," *Biomaterials*, 15(14) 1187-91 (1994).

Hedges, M., Renn, M. and Kardos, M., "Mesoscale Deposition Technology for Electronics Applications," pp. 53-57 in *Polymers and Adhesives in Microelectronics and Photonics*, Polytronic, 2005. Polytronic 2005. 5th International Conference on.

Heule, M. and Gauckler, L. J., "Gas sensors fabricated from ceramic suspensions by micromolding in capillaries," *Adv Mater*, 13(23) 1790-93 (2001).

Heule, M., Vuillemin, S. and Gauckler, L. J., "Powder-Based Ceramic Meso- and Microscale Fabrication Processes," *Adv Mater*, 15(15) 1237-45 (2003).

Heule, M., Schonholzer, U. P. and Gauckler, L. J., "Patterning colloidal suspensions by selective wetting of microcontact-printed surfaces," *J Eur Ceram Soc*, 24(9) 2733-39 (2004).

Holthaus, M. and Rezwan, K., "Comparison of Three Microstructure Fabrication Methods for Bone Cell Growth Studies," *ASME Conference Proceedings*, 2008(48524) 483-90 (2008).

Holthaus, M. G., Treccani, L. and Rezwan, K., "Monitoring osteoblast viability on hydroxyapatite with adjusted submicron and micron surface roughness by using proliferation reagent WST-1," *Biomed Mater*, submitted (2011).

Holthaus, M. G., Kropp, M., Treccani, L., Lang, W. and Rezwan, K., "Versatile Crack-Free Ceramic Micropatterns Made by a Modified Molding Technique," *J Am Ceram Soc*, 93(9) 2574-78 (2010).

Hu, J. M., Deng, T., Beck, R. G., Westervelt, R. M. and Whitesides, G. M., "Fabrication of arrays of Schottky diodes using microtransfer molding," *Sensor Actuat a-Phys*, 75(1) 65-69 (1999).

Huang, J., Jayasinghe, S., Best, S. M., Edirisinghe, M. J., Brooks, R. A., Rushton, N. and Bonfield, W., "Novel deposition of nano-sized silicon substituted hydroxyapatite by electrostatic spraying," *J Mater Sci-Mater M*, 16(12) 1137-42 (2005).

Huang, J., Jayasinghe, S. N., Su, X., Ahmad, Z., Best, S. M., Edirisinghe, M. J., Brooks, R. A., Rushton, N. and Bonfield, W., "Electrostatic atomisation spraying: A novel deposition method for nano-sized hydroxyapatite," *Bioceramics*, Vol 18, 309-311(18) 635-38 (2006).

Hull, C., "Apparatus for production of three-dimensional objects by stereolithography." in U.S. Patent Office, Vol. U.S. Patent 4575330. USA, 1986.

Ihleemann, J., Scholl, A., Schmidt, H. and Wolff-Rottke, B., "Nanosecond and femtosecond excimer-laser ablation of oxide ceramics," *Applied Physics A: Materials Science & Processing*, 60(4) 411-17 (**1995**).

ISO6344-1:1998, "Coated abrasives ". in Grain size analysis - Part 1: Grain size distribution test. Beuth, **2000**.

ISO25178-6 (2007), C. D., Geometrical product specification (GPS)-Surface texture: areal - Part 6: classification of methods for measuring surface texture, International Organization for Standardization, 2007.

ISO 4287 (1997), G. p. s. G., Surface texture: profile method-terms, definitions and surface texture parameters, International Organization for Standardization, 1997. in.

Jaffe, W. L. and Scott, D. F., "Current Concepts Review - Total Hip Arthroplasty with Hydroxyapatite-Coated Prostheses," *J Bone Joint Surg Am*, 78(12) 1918-34 (**1996**).

Kaiser, J.-P., Reinmann, A. and Bruinink, A., "The effect of topographic characteristics on cell migration velocity," *Biomaterials*, 27(30) 5230-41 (**2006**).

Keller, J. C., Schneider, G. B., Stanford, C. M. and Kellogg, B., "Effects of Implant Microtopography on Osteoblast Cell Attachment," *Implant Dentistry*, 12(2) 175-81 (**2003**).

Khan, S. U., Göbel, O. F., Blank, D. H. A. and ten Elshof, J. E., "Patterning Lead Zirconate Titanate Nanostructures at Sub-200-nm Resolution by Soft Confocal Imprint Lithography and Nanotransfer Molding," *Acs Appl Mater Inter*, 1(10) 2250-55 (**2009**).

Kieswetter, K., Schwartz, Z., Dean, D. D. and Boyan, B. D., "The Role of Implant Surface Characteristics in the Healing of Bone," *Critical Reviews in Oral Biology & Medicine*, 7(4) 329-45 (**1996**).

Kim, E., Xia, Y. and Whitesides, G. M., "Micromolding in Capillaries: Applications in Materials Science," *J Am Chem Soc*, 118(24) 5722-31 (**1996**).

Kim, P., Kwon, K. W., Park, M. C., Lee, S. H., Kim, S. M. and K.Y., S., "Soft Lithography for Microfluidics: a Review," *Biochip Journal*, Vol. 2(No. 1) 1-11 **(2008)**.

Kim, Y., Yamashita, J., Shotwell, J. L., Chong, K.-H. and Wang, H.-L., "The comparison of provisional luting agents and abutment surface roughness on the retention of provisional implant-supported crowns," *The Journal of Prosthetic Dentistry*, 95(6) 450-55 **(2006)**.

Kirmizidis, G. and Birch, M. A., "Microfabricated Grooved Substrates Influence Cell-Cell Communication and Osteoblast Differentiation In Vitro," *Tissue Eng Pt A*, 15(6) 1427-36 **(2009)**.

Knitter, R., Bauer, W., Göhring, D. and Haußelt, J., "Manufacturing of Ceramic Microcomponents by a Rapid Prototyping Process Chain," *Adv Eng Mater*, 3(1-2) 49-54 **(2001)**.

Kunzler, T. P., Drobek, T., Schuler, M. and Spencer, N. D., "Systematic study of osteoblast and fibroblast response to roughness by means of surface-morphology gradients," *Biomaterials*, 28(13) 2175-82 **(2007)**.

Lam, M. T., Clem, W. C. and Takayama, S., "Reversible on-demand cell alignment using reconfigurable microtopography," *Biomaterials*, 29(11) 1705-12 **(2008)**.

Lange, F. F., "Powder Processing Science and Technology for Increased Reliability," *J Am Ceram Soc*, 72(1) 3-15 **(1989)**.

Lasagni, A., Holzapfel, C. and Mücklich, F., "Periodic Pattern Formation of Intermetallic Phases with Long Range Order by Laser Interference Metallurgy," *Adv Eng Mater*, 7(6) 487-92 **(2005)**.

Lasagni, A., Holzapfel, C. and Mücklich, F., "Production of two-dimensional periodical structures by laser interference irradiation on bi-layered metallic thin films," *Appl Surf Sci*, 253(3) 1555-60 **(2006)**.

- Lasagni, A., D'Alessandria, M., Giovanelli, R. and Mücklich, F., "Advanced design of periodical architectures in bulk metals by means of Laser Interference Metallurgy," *Appl Surf Sci*, 254(4) 930-36 (2007).
- Laude, L. D., Ogeret, C., Jadin, A. and Kolev, K., "Excimer laser ablation of Y-SiAlON," *Appl Surf Sci*, 127-129 848-51 (1998).
- Lazoglu, I., "Sculpture surface machining: a generalized model of ball-end milling force system," *International Journal of Machine Tools and Manufacture*, 43(5) 453-62 (2003).
- Lee, J. H., Kim, C. H., Ho, K. M. and Constant, K., "Two-Polymer Microtransfer Molding for Highly Layered Microstructures," *Adv Mater*, 17(20) 2481-85 (2005).
- Lee, J. Y., Shah, S. S., Yan, J., Howland, M. C., Parikh, A. N., Pan, T. and Revzin, A., "Integrating Sensing Hydrogel Microstructures into Micropatterned Hepatocellular Cocultures," *Langmuir*, 25(6) 3880-86 (2009).
- LeGeros, R. Z., "Properties of Osteoconductive Biomaterials: Calcium Phosphates," *Clin Orthop Relat R*, 395 81-98 (2002).
- Lemons, J. E., "Ceramics: Past, present, and future," *Bone*, 19(1, Supplement 1) S121-S28 (1996).
- Liao, C.-J., Lin, F.-H., Chen, K.-S. and Sun, J.-S., "Thermal decomposition and reconstitution of hydroxyapatite in air atmosphere," *Biomaterials*, 20(19) 1807-13 (1999).
- Lide, D. R., "Handbook of Chemistry and Physics," pp. 2544. CRC Press Inc.: Boca Raton, USA, (2005).
- Lim, J. Y. and Donahue, H. J., "Cell sensing and response to micro- and nanostructured surfaces produced by chemical and topographic patterning," *Tissue Eng*, 13(8) 1879-91 (2007).

Lim, J. Y., Hansen, J. C., Siedlecki, C. A., Hengstebeck, R. W., Cheng, J., Winograd, N. and Donahue, H. J., "Osteoblast adhesion on poly(L-lactic acid)/polystyrene demixed thin film blends: Effect of nanotopography, surface chemistry, and wettability," *Biomacromolecules*, 6(6) 3319-27 (2005).

Liu, Y., Sun, S., Singha, S., Cho, M. R. and Gordon, R. J., "3D femtosecond laser patterning of collagen for directed cell attachment," *Biomaterials*, 26(22) 4597-605 (2005).

Lu, J., Descamps, M., Dejou, J., Koubi, G., Hardouin, P., Lemaitre, J. and Proust, J.-P., "The biodegradation mechanism of calcium phosphate biomaterials in bone," *Journal of Biomedical Materials Research*, 63(4) 408-12 (2002).

Lu, X. and Leng, Y., "Quantitative analysis of osteoblast behavior on microgrooved hydroxyapatite and titanium substrata," *Journal of Biomedical Materials Research Part A*, 66A(3) 677-87 (2003).

Lu, X. and Leng, Y., "Comparison of the osteoblast and myoblast behavior on hydroxyapatite microgrooves," *Journal of Biomedical Materials Research Part B: Applied Biomaterials*, 90B(1) 438-45 (2009).

Lucht, U., "Absorption of peroxidase by osteoclasts as studied by electron microscope histochemistry," *Histochemistry and Cell Biology*, 29(4) 274-86 (1972).

Maiwald, M., Werner, C., Zoellmer, V. and Busse, M., "INKtelligent printed strain gauges," *Sensors and Actuators A: Physical*, 162(2) 198-201 (2010).

Mangano, C., De Rosa, A., Desiderio, V., d'Aquino, R., Piattelli, A., De Francesco, F., Tirino, V., Mangano, F. and Papaccio, G., "The osteoblastic differentiation of dental pulp stem cells and bone formation on different titanium surface textures," *Biomaterials*, 31(13) 3543-51 (2010).

Marinescu, I., Rowe, B., Ling, Y. and Wobker, H. G., "Abrasive Processes," pp. 94-189. in *Handbook of Ceramic Grinding & Polishing*. Edited by D. M. Ioan, K. T. Hans, and I. Ichiro. William Andrew Publishing, Norwich, NY, 1999.

Martin, C. R. and Aksay, I. A., "Submicrometer-Scale Patterning of Ceramic Thin Films," *J Electroceram*, 12(1) 53-68 **(2004)**.

Matsuda, N., Yokoyama, K., Takeshita, S. and Watanabe, M., "Role of epidermal growth factor and its receptor in mechanical stress-induced differentiation of human periodontal ligament cells in vitro," *Arch Oral Biol*, 43(12) 987-97 **(1998)**.

Mette, A., Richter, P. L., Hörteis, M. and Glunz, S. W., "Metal aerosol jet printing for solar cell metallization," *Progress in Photovoltaics: Research and Applications*, 15(7) 621-27 **(2007)**.

Miotello, A. and Kelly, R., "Laser-induced phase explosion: new physical problems when a condensed phase approaches the thermodynamic critical temperature," *Applied Physics A: Materials Science & Processing*, 69(7) S67-S73 **(1999)**.

Mott, M. and Evans, J. R. G., "Solid Freeforming of Silicon Carbide by Inkjet Printing Using a Polymeric Precursor," *J Am Ceram Soc*, 84(2) 307-13 **(2001)**.

Mücklich, F., Lasagni, A. F. and Daniel, C., "Laser Interference Metallurgy - : using interference as a tool for micro/nano structuring," pp. 8 Vol. 97. Hanser: Munich, ALLEMAGNE, **(2006)**.

Munz, D. and Fett, T., "Ceramics- Mechanical Properties, Failure Behaviour, Materials Selection," pp. 298 Vol. 26. Springer: Berlin, **(1999)**.

Mustafa, K., Odén, A., Wennerberg, A., Hulténby, K. and Arvidson, K., "The influence of surface topography of ceramic abutments on the attachment and proliferation of human oral fibroblasts," *Biomaterials*, 26(4) 373-81 **(2005)**.

Nakata, K., Umehara, M. and Tsumura, T., "Excimer laser ablation of sintered hydroxyapatite," *Surface and Coatings Technology*, 201(9-11) 4943-47 **(2007)**.

Odom, T. W., Love, J. C., Wolfe, D. B., Paul, K. E. and Whitesides, G. M., "Improved Pattern Transfer in Soft Lithography Using Composite Stamps," *Langmuir*, 18(13) 5314-20 **(2002)**.

Oh, Y., Kim, J., Yoon, Y. J., Kim, H., Yoon, H. G., Lee, S.-N. and Kim, J., "Inkjet printing of Al₂O₃ dots, lines, and films: From uniform dots to uniform films," *Curr Appl Phys*, In Press, Corrected Proof **(2010)**.

Olabi, A., Béarée, R., Gibaru, O. and Damak, M., "Feedrate planning for machining with industrial six-axis robots," *Control Engineering Practice*, 18(5) 471-82 **(2010)**.

Panupinthu, N., Zhao, L., Possmayer, F., Ke, H. Z., Sims, S. M. and Dixon, S. J., "P2X7 Nucleotide Receptors Mediate Blebbing in Osteoblasts through a Pathway Involving Lysophosphatidic Acid," *J Biol Chem*, 282(5) 3403-12 **(2007)**.

Perizzolo, D., Lacefield, W. R. and Brunette, D. M., "Interaction between topography and coating in the formation of bone nodules in culture for hydroxyapatite- and titanium-coated micromachined surfaces," *Journal of Biomedical Materials Research*, 56(4) 494-503 **(2001)**.

Piconi, C., Maccauro, G., Muratori, F. and Brach Del Prever, E., "Alumina and zirconia ceramics in joint replacements," *J Appl Biomater Biomech*, 1(1) 19-32 **(2003)**.

Piotter, V., Gietzelt, T. and Merz, L., "Micro powder-injection moulding of metals and ceramics," *Sadhana*, 28(1) 299-306 **(2003)**.

Pla-Roca, M., Fernandez, J. G., Mills, C. A., Martinez, E. and Samitier, J., "Micro/nanopatterning of proteins via contact printing using high aspect ratio PMMA stamps and NanoImprint apparatus," *Langmuir*, 23(16) 8614-18 **(2007)**.

Queiroz, A. C., Santos, J. D., Vilar, R., Eugénio, S. and Monteiro, F. J. F. J., "Laser surface modification of hydroxyapatite and glass-reinforced hydroxyapatite," *Biomaterials*, 25(19) 4607-14 **(2004)**.

Rahaman, M. N., "Ceramic Processing and Sintering," Vol. Second Edition: New York, **(2003)**.

Reed, J. S., "Principles of Ceramic Processing," pp. 658 2 ed. Vol. 2. John Wiley & Sons: New York, **(1995)**.

Reichert, J., Brukner, S., Bartelt, H. and Jandt, K. D., "Tuning cell adhesion on PTFE surfaces by laser induced microstructures," *Adv Eng Mater*, 9(12) 1104-13 (2007).

Rodríguez-Lorenzo, L. M., Hart, J. N. and Gross, K. A., "Influence of fluorine in the synthesis of apatites. Synthesis of solid solutions of hydroxy-fluorapatite," *Biomaterials*, 24(21) 3777-85 (2003).

Rosa, A. L., Beloti, M. M. and van Noort, R., "Osteoblastic differentiation of cultured rat bone marrow cells on hydroxyapatite with different surface topography," *Dent Mater*, 19(8) 768-72 (2003).

Roy, M. E. and Whiteside, L. A., "Clinical Comparison of Polyethylene Wear with Zirconia or Cobalt-Chromium Femoral Heads," *Clin Orthop Relat R*, 468(2) 624-25 (2010).

Salmang, H., Scholze, H. and Telle, R., "Keramik," Vol. 7. Springer: Berlin, (2006).

Samant, A. N. and Dahotre, N. B., "Laser machining of structural ceramics--A review," *J Eur Ceram Soc*, 29(6) 969-93 (2009).

Santos, C., Clarke, R. L., Braden, M., Guitian, F. and Davy, K. W. M., "Water absorption characteristics of dental composites incorporating hydroxyapatite filler," *Biomaterials*, 23(8) 1897-904 (2002).

Schakenraad, J. M., Busscher, H. J., Wildevuur, C. R. H. and Arends, J., "The influence of substratum surface free energy on growth and spreading of human fibroblasts in the presence and absence of serum proteins," *Journal of Biomedical Materials Research*, 20(6) 773-84 (1986).

Schmid, H. and Michel, B., "Siloxane Polymers for High-Resolution, High-Accuracy Soft Lithography," *Macromolecules*, 33(8) 3042-49 (2000).

Schneider, G. B., Perinpanayagam, H., Clegg, M., Zaharias, R., Seabold, D., Keller, J. and Stanford, C., "Implant Surface Roughness Affects Osteoblast Gene Expression," *J Dent Res*, 82(5) 372-76 (2003).

Sears, J., Colvin, J. and Carter, M., "Fabricating Devices Using Nano-Particulates with Direct Write

Technology," *Materials Science Forum*, 534-536 1385-88 (2007).

Segawa, H., Adachi, S., Arai, Y. and Yoshida, K., "Fine Patterning of Hybrid Titania Films by Ultraviolet Irradiation," *J Am Ceram Soc*, 86(5) 761-64 (2003).

Semlyen, J. A., Wood, B. R. and Hodge, P., "Cyclic polymers: past, present and future," *Polymers for Advanced Technologies*, 5(9) 473-78 (1994).

Sivakumar, M., Eugenio, S., Vilar, R. and Oliveira, V., "KrF laser treatment of human dentin," pp. 71311M-7. Vol. 7131 Edited by R. Vilar, O. Conde, M. Fajardo, L. O. Silva, M. Pires, and A. Utkin.

Somiya, S., "Handbook of Advanced Ceramics," pp. 1320 Vol. 1. Elsevier, Academic Press Inc.: Amsterdam, (2004).

Song, J. H. and Nur, H. M., "Defects and prevention in ceramic components fabricated by inkjet printing," *J Mater Process Tech*, 155-156 1286-92 (2004).

Su, B., Zhang, D. and Button, T. W., "Micropatterning of fine scale ceramic structures," *J Mater Sci*, 37(15) 3123-26 (2002).

Su, B., Dhara, S. and Wang, L., "Green ceramic machining: A top-down approach for the rapid fabrication of complex-shaped ceramics," *J Eur Ceram Soc*, 28(11) 2109-15 (2008).

Subramanian, P. K. and Marcus, H. L., "SELECTIVE LASER SINTERING OF ALUMINA USING ALUMINUM BINDER," *Mater Manuf Process*, 10(4) 689-706 (1995).

Suchanek, W., Yashima, M., Kakihana, M. and Yoshimura, M., "Processing and mechanical properties of hydroxyapatite reinforced with hydroxyapatite whiskers," *Biomaterials*, 17(17) 1715-23 (1996).

Suh, K.-Y., Park, M. C. and Kim, P., "Capillary Force Lithography: A Versatile Tool for Structured Biomaterials Interface Towards Cell and Tissue Engineering," *Adv Funct Mater*, 19(17) 2699-712 (2009).

Sundh, A. and Sjögren, G., "A study of the bending resistance of implant-supported reinforced alumina and machined zirconia abutments and copies," *Dent Mater*, 24(5) 611-17 (2008).

Takacs, M., Vero, B. and Meszaros, I., "Micromilling of metallic materials," *J Mater Process Tech*, 138 152-55 (2003).

Talei Franzesi, G., Ni, B., Ling, Y. and Khademhosseini, A., "A Controlled-Release Strategy for the Generation of Cross-Linked Hydrogel Microstructures," *J Am Chem Soc*, 128(47) 15064-65 (2006).

Tan, J. and Saltzman, W. M., "Biomaterials with hierarchically defined micro- and nanoscale structure," *Biomaterials*, 25(17) 3593-601 (2004).

Tang, M. D., Golden, A. P. and Tien, J., "Molding of Three-Dimensional Microstructures of Gels," *J Am Chem Soc*, 125(43) 12988-89 (2003).

Tari, M. J., Bals, A., Park, J., Lin, M. Y. and Thomas Hahn, H., "Rapid prototyping of composite parts using resin transfer molding and laminated object manufacturing," *Composites Part A: Applied Science and Manufacturing*, 29(5-6) 651-61 (1998).

Tay, B. Y., Evans, J. R. G. and Edirisinghe, M. J., "Solid freeform fabrication of ceramics," *Int Mater Rev*, 48 341-70 (2003).

Teitelbaum, S. L., "Bone Resorption by Osteoclasts," *Science*, 289(5484) 1504-08 (2000).

ten Elshof, J. E., Khan, S. U. and Göbel, O. F., "Micrometer and nanometer-scale parallel patterning of ceramic and organic-inorganic hybrid materials," *J Eur Ceram Soc*, 30(7) 1555-77 (2010).

Thian, E. S., Ahmad, Z., Huang, J., Edirisinghe, M. J., Jayasinghe, S. N., Ireland, D. C., Brooks, R. A., Rushton, N., Bonfield, W. and Best, S. M., "The role of electrosprayed apatite nanocrystals in guiding osteoblast behaviour," *Biomaterials*, 29(12) 1833-43 (2008).

Thibault, C., Severac, C., Trévisiol, E. and Vieu, C., "Microtransfer molding of hydrophobic dendrimer," *Microelectron Eng*, 83(4-9) 1513-16 (2006).

Thomas, C. H., Lhoest, J. B., Castner, D. G., McFarland, C. D. and Healy, K. E., "Surfaces Designed to Control the Projected Area and Shape of Individual Cells," *Journal of Biomechanical Engineering*, 121(1) 40-48 (1999).

Thomas, K. A. and Cook, S. D., "An Evaluation of Variables Influencing Implant Fixation by Direct Bone Apposition," *Journal of Biomedical Materials Research*, 19(8) 875-901 (1985).

Tian, J., Zhang, Y., Guo, X. and Dong, L., "Preparation and characterization of hydroxyapatite suspensions for solid freeform fabrication," *Ceramics International*, 28(3) 299-302 (2002).

Tiaw, K. S., Goh, S. W., Hong, M., Wang, Z., Lan, B. and Teoh, S. H., "Laser surface modification of poly(ϵ -caprolactone) (PCL) membrane for tissue engineering applications," *Biomaterials*, 26(7) 763-69 (2005).

Tien, J., Nelson, C. M. and Chen, C. S., "Fabrication of aligned microstructures with a single elastomeric stamp," *P Natl Acad Sci USA*, 99(4) 1758-62 (2002).

Treccani, L., Maiwald, M., Zöllmer, V., Busse, M., Grathwohl, G. and Rezwan, K., "Antibacterial and Abrasion-Resistant Alumina Micropatterns," *Adv Eng Mater*, 11(7) B61-B66 (2009).

Tseng, A. A. and Tanaka, M., "Advanced deposition techniques for freeform fabrication of metal and ceramic parts," *Rapid Prototyping J*, 7(1) 6-17 (2001).

Tuttle, B. A., Smay, J. E., Cesarano, J., Voigt, J. A., Scofield, T. W., Olson, W. R. and Lewis, J. A., "Robocast Pb(Zr_{0.95}Ti_{0.05})O₃ Ceramic Monoliths and Composites," *J Am Ceram Soc*, 84(4) 872-74 (2001).

von Allmen, M. and Blatter, A., "Laser-Beam Interactions with Materials - Physical Principles and Applications," pp. 205 2 ed. Springer: Berlin, (1995).
Walboomers, X. F., Croes, H. J. E., Ginsel, L. A. and Jansen, J. A., "Contact guidance of rat fibroblasts on various implant materials," *Journal of Biomedical Materials Research*, 47(2) 204-12 (1999).

Wang, H., Gerbaudo, V. H., Hobbs, L. W. and Spector, M., "Quantitation of osteoblast-like cell mineralization on tissue culture polystyrene and Ti-6Al-4V alloy disks by Tc-99m-MDP labeling and imaging in vitro," *Bone*, 36(1) 84-92 (2005).

Wang, L., Wu, Z.-Z., Xu, B., Zhao, Y. and Kisaalita, W. S., "SU-8 microstructure for quasi-three-dimensional cell-based biosensing," *Sensors and Actuators B: Chemical*, 140(2) 349-55 (2009).

Wheeler, C. R., Fried, D., Featherstone, J. D. B., Watanabe, L. G. and Le, C. Q., "Irradiation of dental enamel with Q-switched $\lambda = 355$ -nm laser pulses: Surface morphology, fluoride adsorption, and adhesion to composite resin," *Laser Surg Med*, 32(4) 310-17 (2003).

Wintermantel, E. and Ha, S. W., "Medizintechnik mit biokompatiblen Werkstoffen und Verfahren," Vol. 3. Springer-Verlag Berlin, (2002).

Wittel, H., Muhs, D., Jannasch, D. and Voßiek, J., "Roloff/Matek: Maschinenelemente-Normung, Berechnung, Gestaltung," Vol. 19. Vieweg + Teubner: Wiesbaden, (2009).

Wozniak, M., Graule, T., de Hazan, Y., Kata, D. and Lis, J., "Highly loaded UV curable nanosilica dispersions for rapid prototyping applications," *J Eur Ceram Soc*, 29(11) 2259-65 (2009).

Xia, Y. N. and Whitesides, G. M., "Soft lithography," *Annu Rev Mater Sci*, 28 153-84 (1998).

Xu, X. W. and Newman, S. T., "Making CNC machine tools more open, interoperable and intelligent--a review of the technologies," *Computers in Industry*, 57(2) 141-52 (2006).

Yamakura, K., Watanabe, H., Abe, S. and Yanagisawa, T., "Ultrastructural changes in calvarial osteoblast cytoskeleton after prostaglandin E-2 administration in rats," *Anat Histol Embryol*, 30(5) 301-07 (2001).

Yin, L., Jahanmir, S. and Ives, L. K., "Abrasive machining of porcelain and zirconia with a dental handpiece," *Wear*, 255(7-12) 975-89 (2003).

Yu, M.-C., Young, W.-B. and Hsu, P.-M., "Micro-injection molding with the infrared assisted mold heating system," *Materials Science and Engineering: A*, 460-461 288-95 (2007).

Zhang, D., Su, B. and Button, T. W., "Preparation of concentrated aqueous alumina suspensions for soft-molding microfabrication," *J Eur Ceram Soc*, 24(2) 231-37 (2004).

Zhang, D., Su, B. and Button, T. W., "Improvements in the structural integrity of green ceramic microcomponents by a modified soft moulding process," *J Eur Ceram Soc*, 27(2-3) 645-50 (2007).

Zhang, Y., Lo, C.-W., Taylor, J. A. and Yang, S., "Replica Molding of High-Aspect-Ratio Polymeric Nanopillar Arrays with High Fidelity," *Langmuir*, 22(20) 8595-601 (2006).

Zhang, Y., Yu, K., Ouyang, S. and Zhu, Z., "Selective-area growth and field emission properties of Zinc oxide nanowire micropattern arrays," *Physica B: Condensed Matter*, 382(1-2) 76-80 (2006).

Zhao, X., Evans, J. R. G., Edirisinghe, M. J. and Song, J. H., "Formulation of a ceramic ink for a wide-array drop-on-demand ink-jet printer," *Ceramics International*, 29(8) 887-92 (2003).

Zhao, X. M., Xia, Y. N. and Whitesides, G. M., "Fabrication of three-dimensional microstructures: Microtransfer molding," *Adv Mater*, 8(10) 837-& (1996).

Zhu, X. L., Chen, J., Scheideler, L., Reichl, R. and Geis-Gerstorfer, J., "Effects of topography and composition of titanium surface oxides on osteoblast responses," *Biomaterials*, 25(18) 4087-103 (**2004a**).

Zhu, X. L., Chen, J., Scheideler, L., Altebaeumer, T., Geis-Gerstorfer, J. and Kern, D., "Cellular reactions of Osteoblasts to micron- and submicron-scale porous structures of titanium surfaces," *Cells Tissues Organs*, 178(1) 13-22 (**2004b**).

Zöllmer, V., Müller, M., Renn, M., Busse, M., Wirth, I., Godlinsky, D. and Kardos, M., "Printing with aerosols : A maskless deposition technique allows high definition printing of a variety of functional materials," *European coatings journal*, 7-8 46-50 (**2006**).

8. Appendices

8.1 Fabrication of micropatterned freestanding ceramic films through m- μ M

m- μ M of freestanding ceramic films:

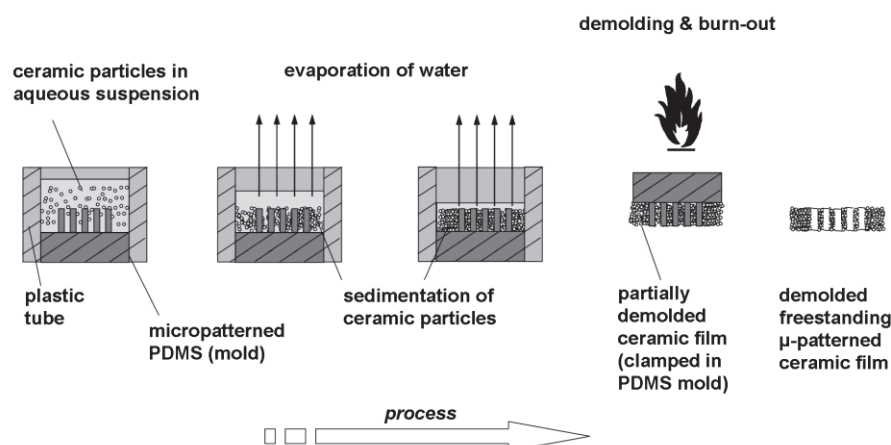


Fig. 81: Drying process of freestanding ceramic micropatterned films made through modified micromolding (m- μ M). At the beginning, the ceramic particles are homogenously dispersed in the aqueous suspension. It is important that the micropatterns are not or only slightly covered by the suspension. Due to gravity the particles sink down to the microstructured bottom of the mold (PDMS stamp) while water evaporates. The evaporation of water is finished within one day and the dried ceramic films with open micropatterns can be removed from the mold by burn-out.

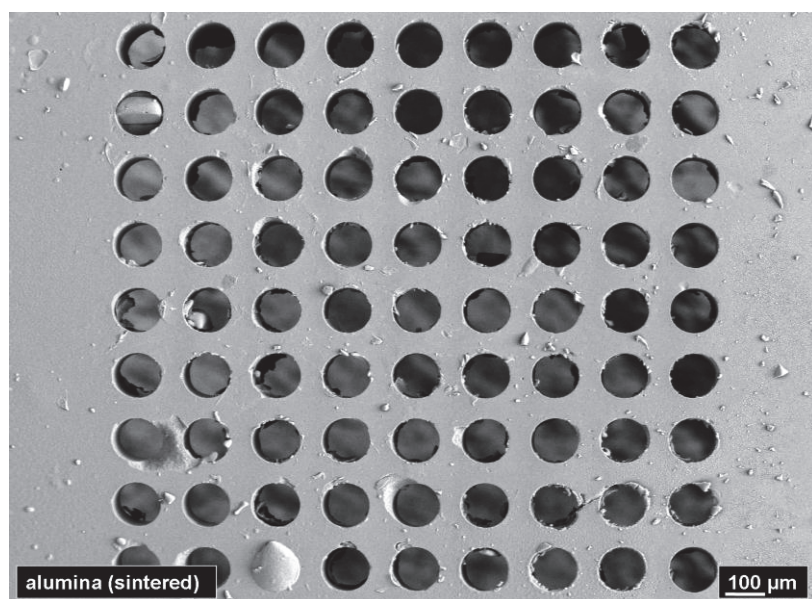


Fig. 82: SEM micrograph of a sintered crack-free ceramic film (Al₂O₃) with open micropatterned holes. The holes have a diameter of about 86 μ m. Some microholes contain loose residual ceramic particles from the demolding. One microhole in the lowest row is closed due to a defect in the PDMS mold.

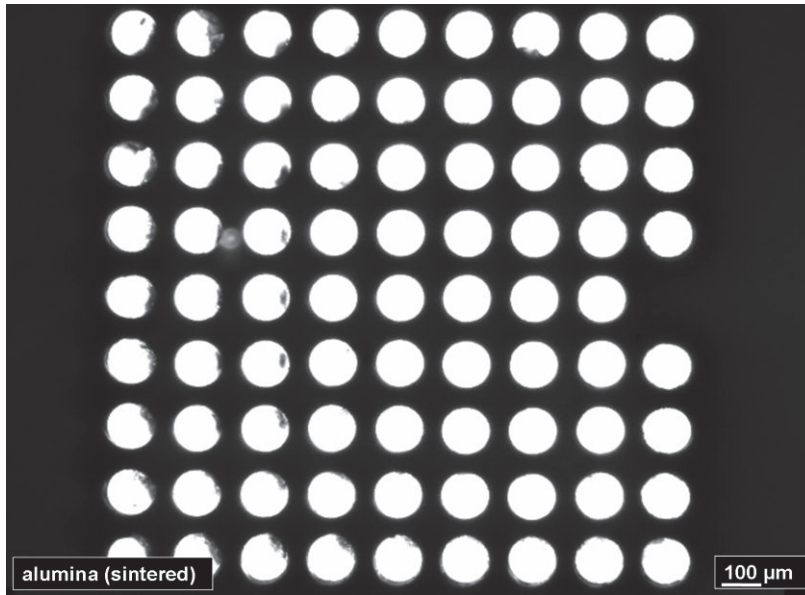


Fig. 83: Bright field image with backlight of a sintered freestanding ceramic film (Al_2O_3) with open micropatterned holes. The holes have a diameter of about $86\ \mu\text{m}$. One microhole in the last column on the right hand side is closed due to a defect in the PDMS mold.

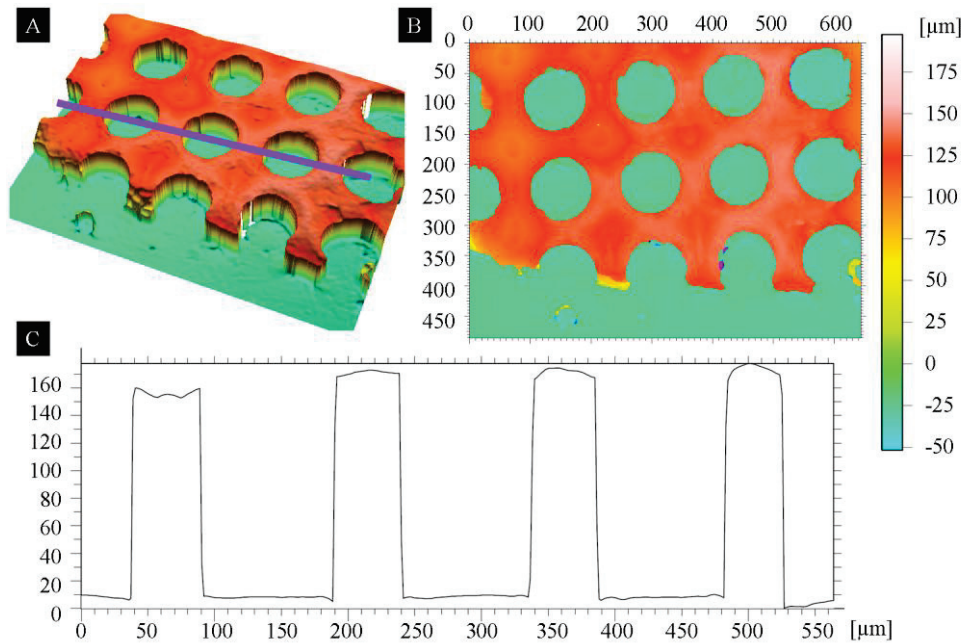


Fig. 84: Profilometry measurements of a non-sintered micropatterned ceramic film (Al_2O_3). The microholes have a diameter of $89.0 \pm 3.1\ \mu\text{m}$. The ceramic film has a thickness of $156.3 \pm 1.9\ \mu\text{m}$. A: 3D image of the fabricated ceramic film. The purple line shows the 2D profile in C. B: 2D top view with heights and dimensions. C: 2D profile measurement of three microholes. Due to the geometry of the molds the maximum sizes of the thin ceramic films were 5 mm in diameter with a micropatterned area of $1 \times 1\ \text{mm}^2$ in the middle.

8.2 Supporting data for 3.1.1 Versatile crack-free ceramic micropatterns made through m- μ M:

Table 3.1.1: Sintering shrinkages and success rates for crack-free drying and demolding of various ceramic suspensions with three different solid contents filled into 200 μ L molds. (a) demolding of any crack-free dried sample was not possible without destroying the sample.

Material	particle size (nm)	solids content (vol%)	BET surface area of non-sintered powder (m ² /g)	zeta potential of suspension + 12 mg PAA/g ceramic at pH 9-10 (mV)	Hamaker-constant (*10-20 J)	success rate for crack-free drying of 200 μ L fillings (%)	success rate for crack-free demoulding of 200 μ L fillings (%)
Hydroxyapatite	150	10	68.3	-16	6 (1)	88	100
		15				71	100
		20				4	100
Alumina	150	10	12.8	-16	6.7 (2)	54	100
		15				96	100
		20				100	100
Silica	150	10	22.6	-13	1.6 (2)	75	94
		15				100	88
		20				96	91
Zirconia	26	10	15.1	-12	13 (2)	0	0
		15				25	100
		20				25	100
Zirconia	150	10	9.7	-18	13 (2)	100	100
		15				100	100
		20				100	100
Zirconia	360	10	6.8	-25	13 (2)	100	100
		15				100	100
		20				100	100
Titania	150	10	13.1	-33	26 (2)	29	0 (a)
		15				71	0 (a)
		20				67	0 (a)

(1) Tian et al., 2002

(2) Rezwan et al., 2005

Success rates for molded samples with diameters of 15 mm (24 NUNC-Well). Volumes of 800 μ L and 400 μ L were used for the molding processes. For each process, n = 12 samples were fabricated.

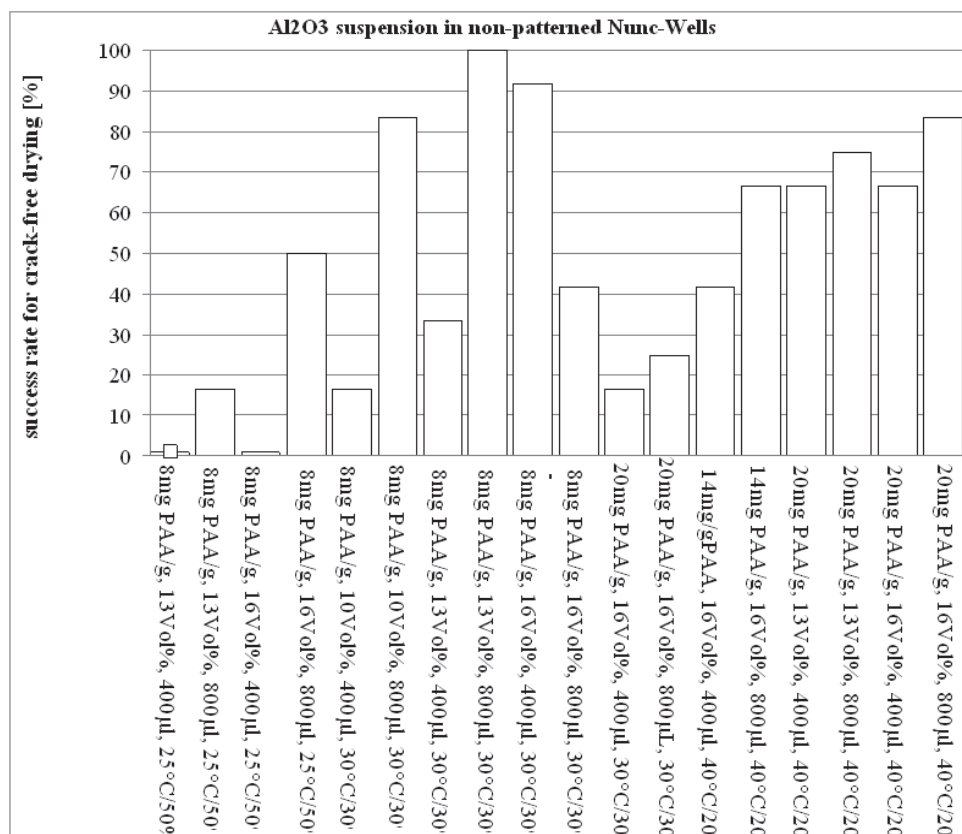


Fig. 85: Alumina (150 nm) suspension filled into non-patterned NUNC-wells

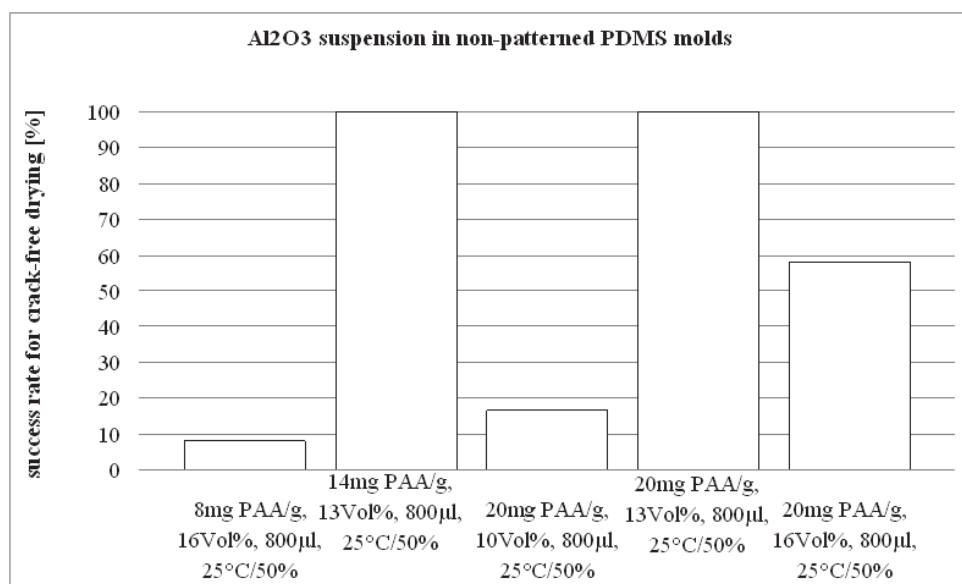


Fig. 86: Alumina (150 nm) suspension filled into NUNC-wells. Non-patterned PDMS was used as the bottom of each mold.

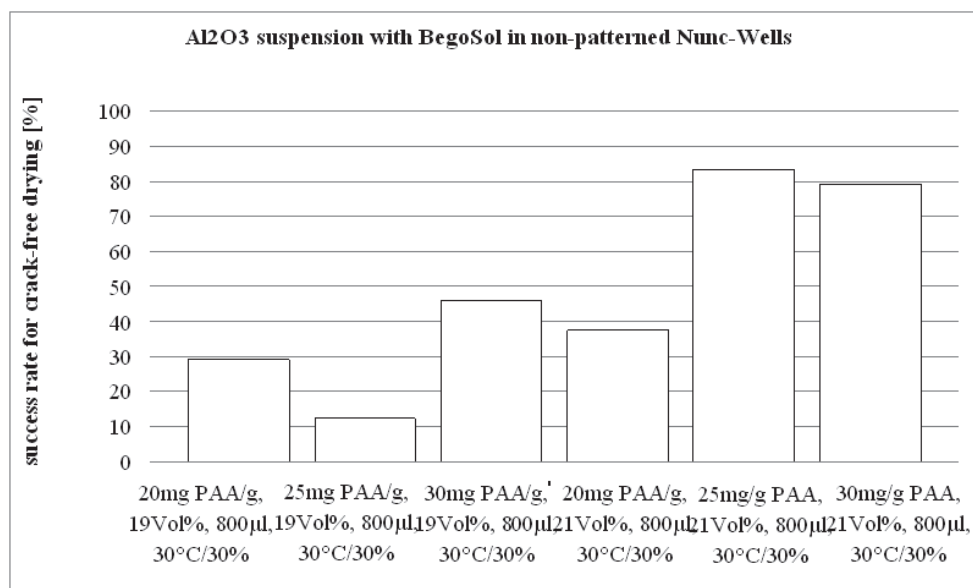


Fig. 87: Alumina (150 nm) suspension with BegoSol K filled into non-patterned NUNC wells

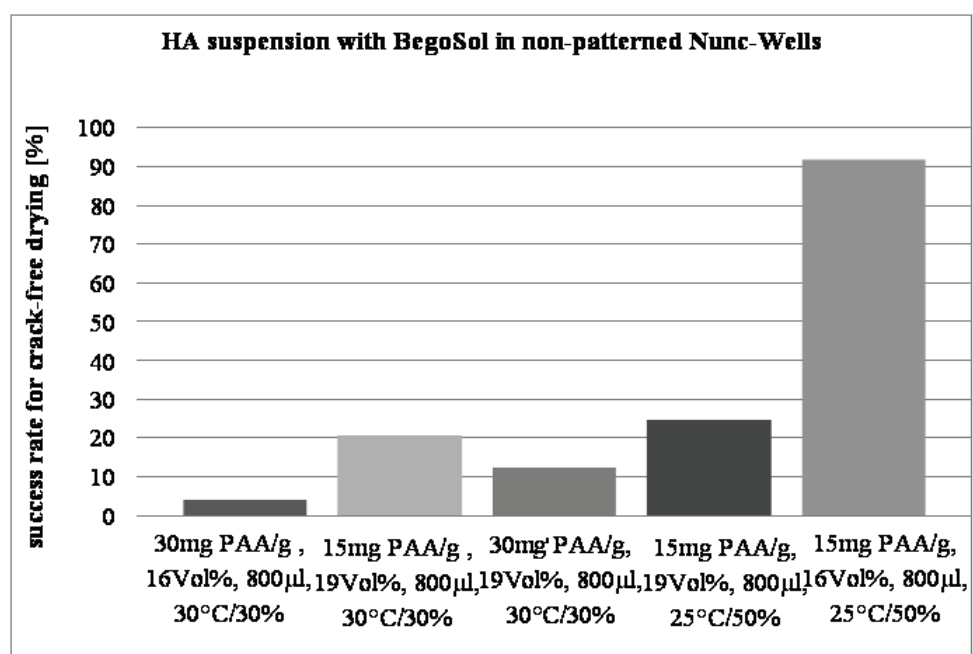


Fig. 88: Hydroxyapatite (150 nm) suspension with BegoSol K filled into non-patterned NUNC wells

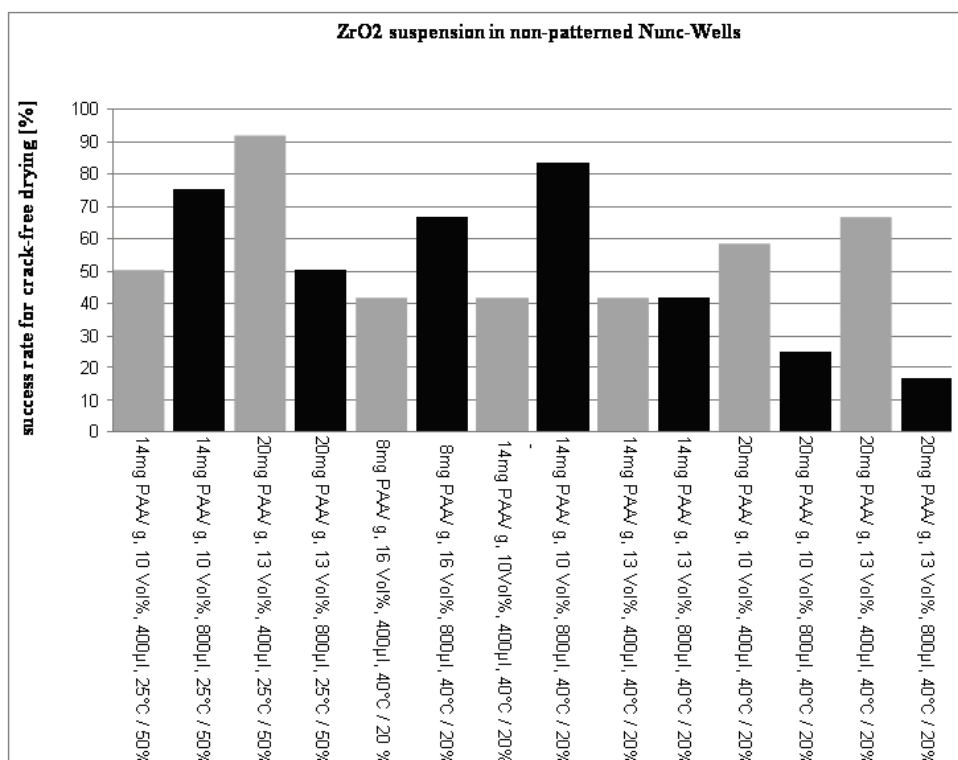


Fig. 89: Zirconia (360 nm) suspension filled into non-patterned NUNC wells

8.3 Supporting data for “Orientation of Osteoblasts on hydroxyapatite-based micropatterns”

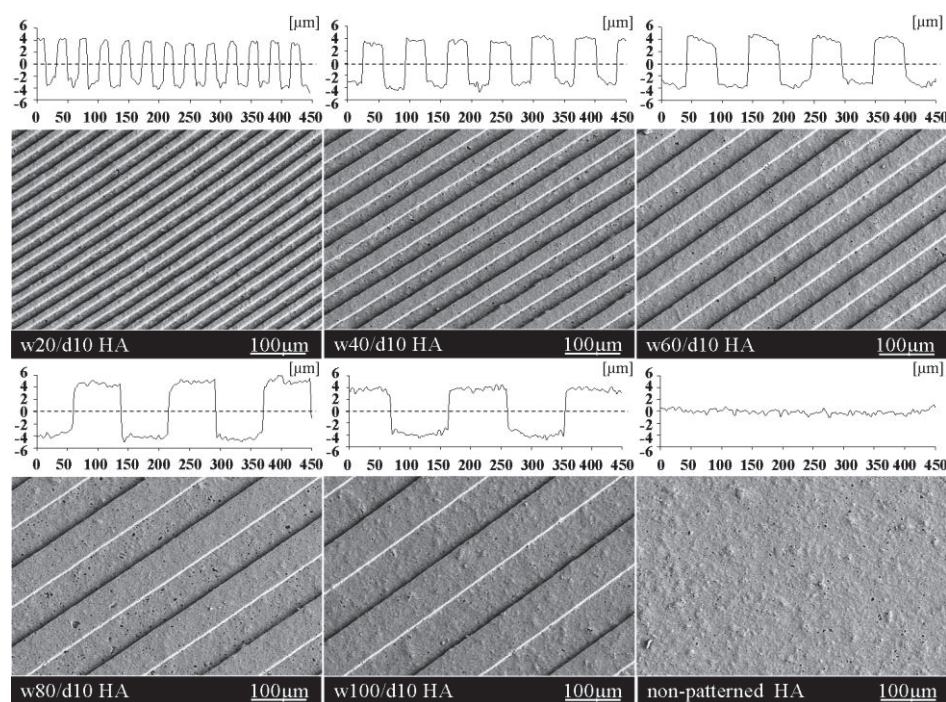


Fig. 90: SEM micrographs and measured 2D profiles of the surface cross section (insets) of micromolded, sintered hydroxyapatite. „w“ and „d“ refer to width and depth, respectively, of each micropattern.

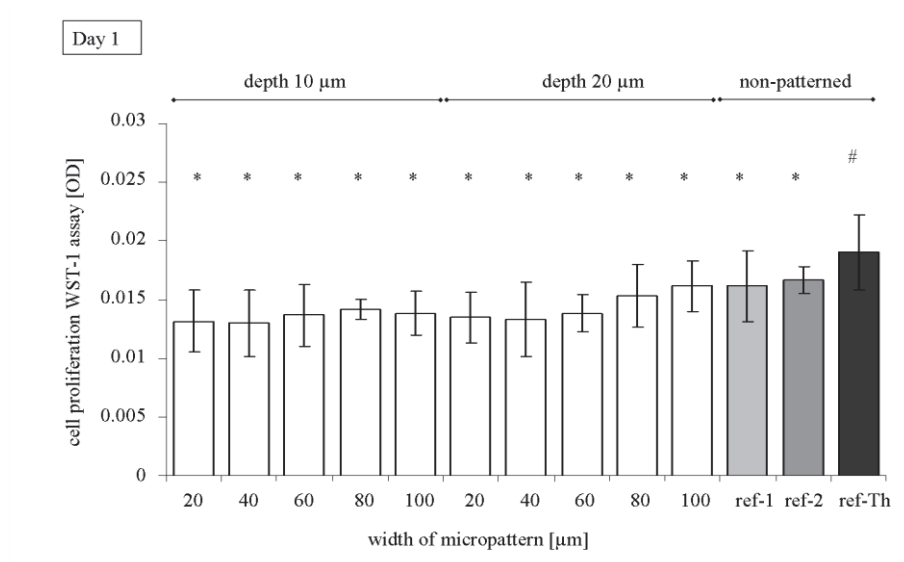


Fig. 91: Dependency of width and depth of micropatterns on the osteoblast WST-1 proliferation measured after one day. Ref.-1: molded hydroxyapatite, ref.-2: die-pressed pure hydroxyapatite, ref.-Th: Thermanox®. Mean values that share a symbol (*/#) are not significantly different (ANOVA: Tukey's Multiple Comparison Test).

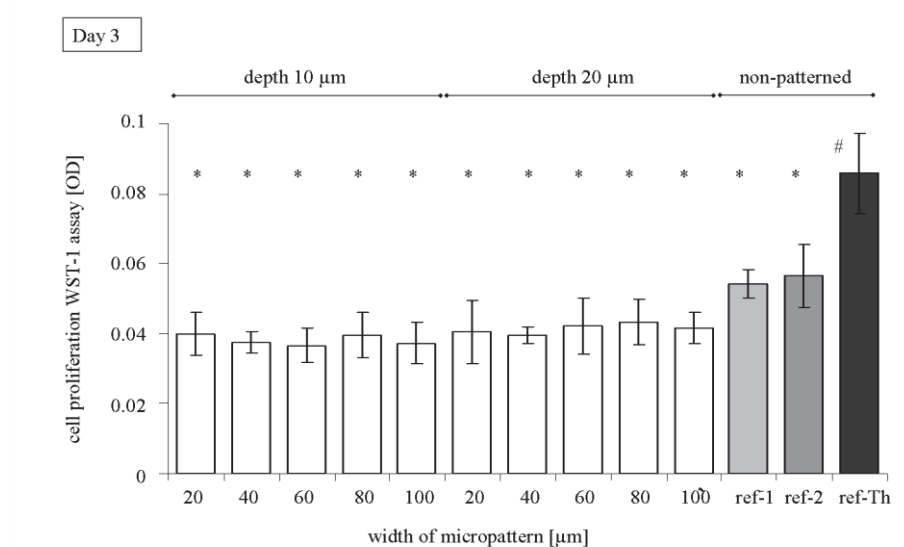


Fig. 92: Dependency of width and depth of micropatterns on the osteoblast WST-1 proliferation measured after three days. Ref.-1: molded hydroxyapatite, ref.-2: die-pressed pure hydroxyapatite, ref.-Th: Thermanox®. Mean values that share a symbol (*/#) are not significantly different (ANOVA: Tukey's Multiple Comparison Test).

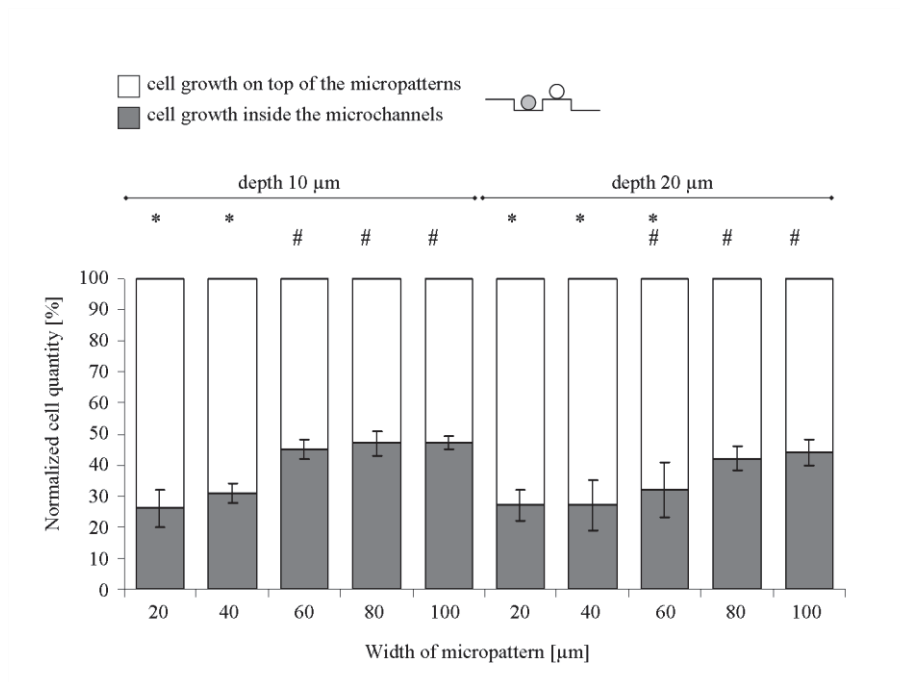


Fig. 93: Distribution of osteoblast cells on different micropatterns in-vitro after one day. Cells adhered either "inside" the microchannels or "on top" of the molded hydroxyapatite micropatterns. Cells on $n =$ three samples were analysed on an area of 2.35 mm^2 each. Mean values that share a symbol (*/#) are insignificantly different (ANOVA: Tukey's Multiple Comparison Test).

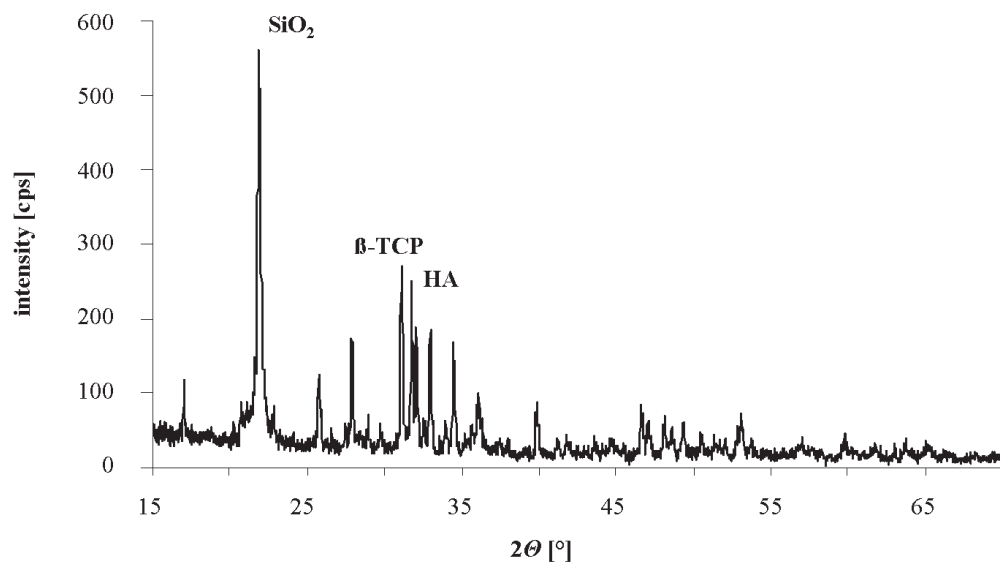


Fig. 94: crystal structure analysis via XRD of a sintered molded HA-based sample (ref.-1).

8.4 Supporting data for 3.3.1 “Micromachining of ceramic surfaces: hydroxyapatite and zirconia”

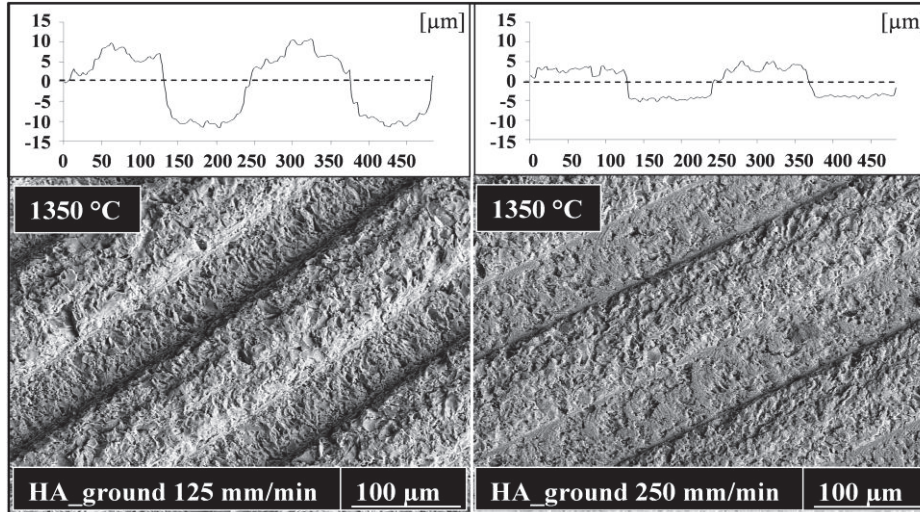


Fig. 3.3.1: SEM micrographs and 2D-profile cross section measurements (white insets) of hydroxyapatite sintered at 1350 °C. Samples were ground with a tool diameter of 300 μm.

Tab.3: Significance of process parameters (Mann-Whitney, U test) for hydroxyapatite (HA)

Observed parameter	Fixed settings	Milling		Grinding	
		Depth of micropattern	Width of micropattern	Depth of micropattern	Width of micropattern
Feed velocity	D=300 μm 1200 °C	p>0.05	p>0.05	*	p>0.05
	D=300 μm 1350 °C	-	-	*	p>0.05
	D=500 μm 1200 °C	*	*	-	-
Tool diameter	v _f =125 mm/min 1200 °C	*	*	-	-
	v _f =250 mm/min 1200 °C	*	p>0.05	-	-
Sinter temp.	D=300 μm v _f =125 mm/min	-	-	p>0.05	p>0.05
	D=300 μm v _f =250 mm/min	-	-	*	p>0.05
(*) significant (-) not applicable					

Tab.4: Significance of process parameters (Mann-Whitney, U test) for zirconia ($Y_2O_3:ZrO_2$)

Observed parameter	Fixed settings	Milling		Grinding	
		Depth of micropattern	Width of micropattern	Depth of micropattern	Width of micropattern
Feed velocity	D=300 μm 100 °C	*	p>0.05	*	p>0.05
	D=500 μm 1100 °C	*	p>0.05	-	-
	D=500 μm 1350 °C	p>0.05	p>0.05	-	-
Tool diameter	v_f =125 mm/min 1100 °C	*	p>0.05	-	-
	v_f =250 mm/min 1100 °C	*	p>0.05	-	-
Sinter temp.	D=500 μm v_f =125 mm/min	*	p>0.05	-	-
	D=500 μm v_f =250 mm/min	*	p>0.05	-	-
(*) significant (-) not applicable					

8.5 Additional micrographs

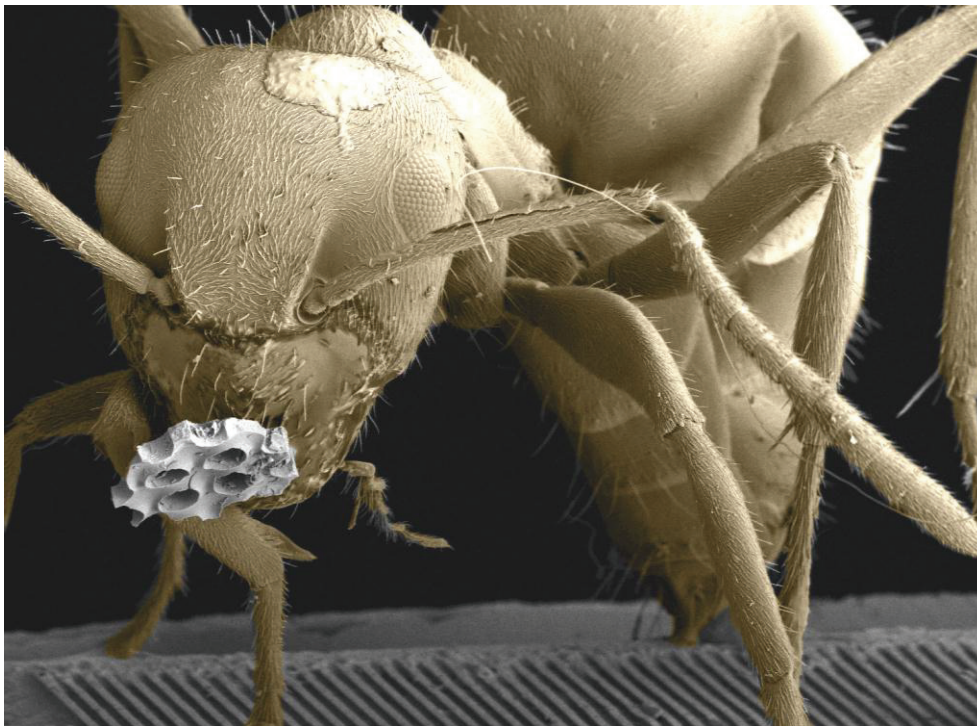


Fig. 95: “Ameise”, Photographic competition 2010, *Focus - Bilder der Forschung*, this image won the 2nd place in an online voting. SEM micrograph of an ant with a fractured piece of a ceramic micropatterned mask (alumina) in its mouth.

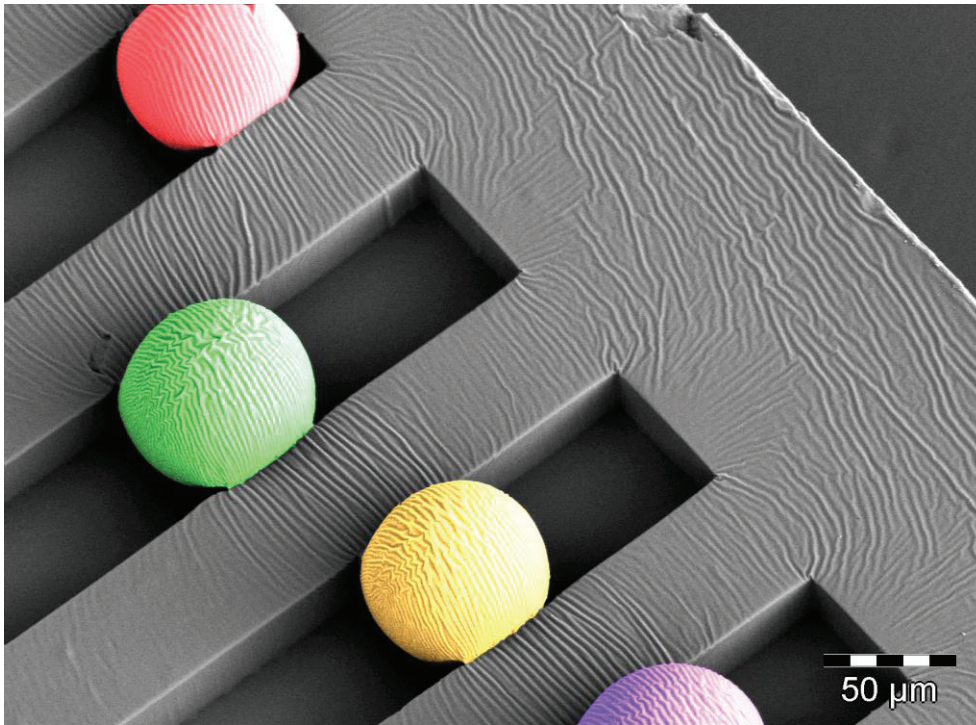


Fig. 96: SEM micrograph of ceramic microspheres in ceramic microchannels. The width of the channels is about 50 μm, the depth is 30 μm. The sample was made of an alumina suspension and fabricated via modified micromolding.

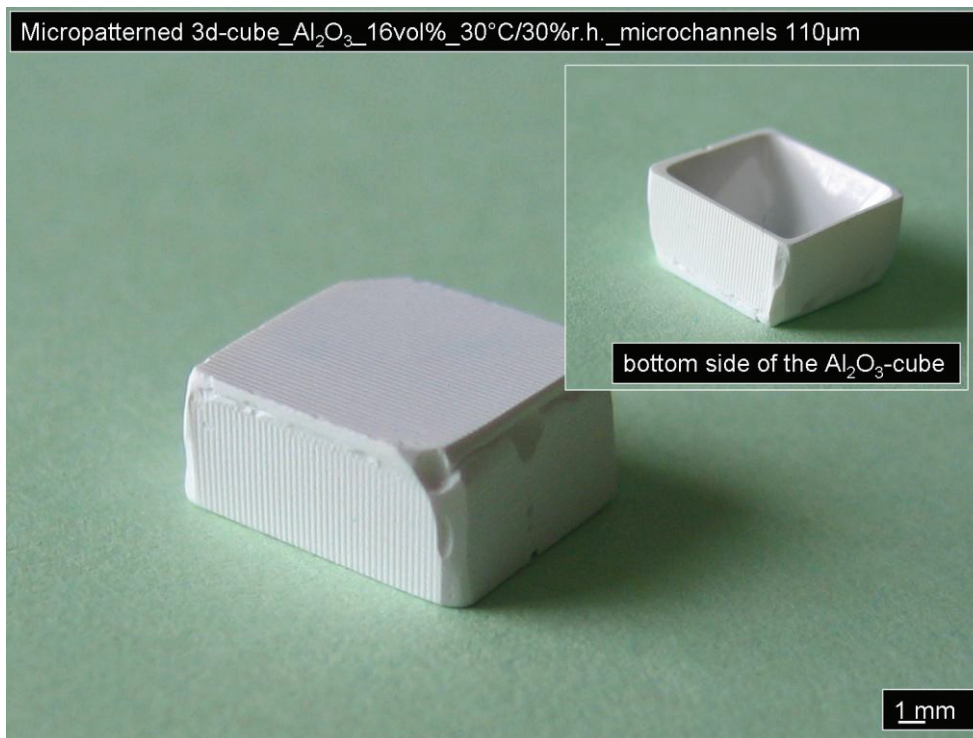


Fig. 97: Micropatterned three-dimensional cube made of an alumina suspension via modified micromolding. All surfaces are patterned with 110 μm wide and 10 μm deep microchannels.

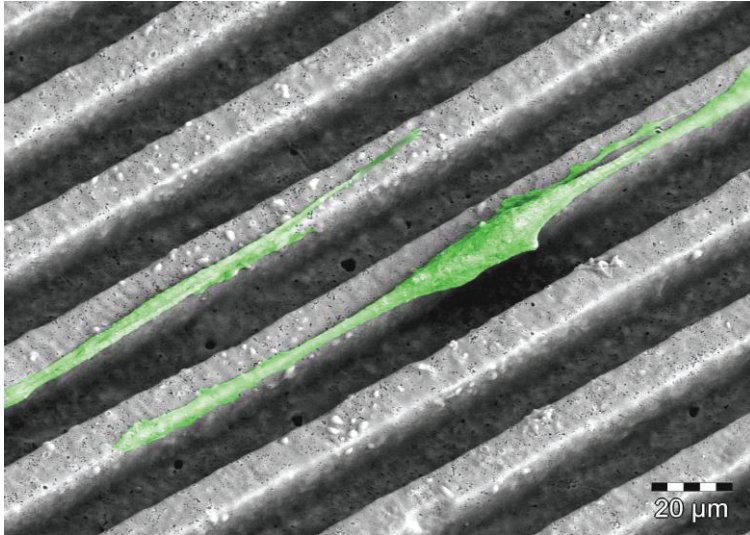


Fig. 98: SEM micrograph of human osteoblast cells (HOB) on molded ceramic micropatterns with widths of 20 μm and depth of 20 μm after one day of proliferation.

ACKNOWLEDGEMENTS

I would like to thank Prof. Dr.-Ing. Kurosch Rezwan for his valuable mentoring and his trust in me during the last four years. He has always trusted me and always left me the freedom to run own ideas and start new collaborations. I further thank Dr. Laura Treccani for co-advising me and the discussion of the concepts and results. I am also grateful to Prof. Dr.-Ing. Lutz Mädler, who agreed to be the co-examiner of my PhD defence and who provided me a very effective collaboration.

Further, I want to thank all collaboration partners, namely, Sven Twardy (LFM), Marcus Maiwald & Veronika Ruttkowski (IFAM), Dr. Andrés Lasagni and Jana Berger (IWS), Andreas Stephen (BIAS), Miron Kropp, Claudia Garcia (IMSAS), and Dr. Huanjun Zhang (IWT) for helping me with everything and particularly for the good results.

I want to thank all of my students who helped me succeed in this research project.

Moreover, I would like to thank all of my colleagues for kindly discussing a lot of research aspects to me during my work and for creating a nice and comfortable working ambiance.

I also want to thank the kicker team for many nice “17 o’clock meetings”.

I would like to thank my parents for their support, for their understanding, and particularly for their great patience with me.

Also very special thanks go out to Svea and Prof. Mücke for their endless supportiveness, enormous patience, and their companionship, which made not only my PhD research more enjoyable.

Thank you,
Marzellus

CURRICULUM VITAE

Marzellus große Holthaus was born in 1979 in Bremerhaven, Germany. After graduation from a German high school in 1999 he studied medical engineering at the University of Applied Sciences Bremerhaven where he received his diploma (Dipl.-Ing.(FH)) in the middle of 2005. In his diploma thesis, he characterised the adhesion of polymers and their interfaces for use in neuroprothetic implants.

At the end of 2005, he started studying biomedical engineering in Muenster, receiving his diploma (Master of Science) in May 2007. In his Master Thesis, he investigated antimicrobial titan and stainless steel surfaces for use in medical implants.

In June 2007, he joined the Bioceramics Group at the Department of Process and Industrial Engineering at the University of Bremen as a PhD student.

PUBLICATIONS

Peer-reviewed articles

M. Grosse Holthaus and K. Rezwan, Comparison of Three Microstructure Fabrication Methods for Bone Cell Growth Studies, Proc. of ASME Int. Manuf. Sci. Eng. Conf. 2 (2008), pp. 483–490.

M. Grosse Holthaus, M. Kropp, L. Treccani, W. Lang and K. Rezwan, Versatile Crack-Free Ceramic Micropatterns Made by a Modified Molding Technique, J. Amer. Ceram. Soc. (2010), pp. 2574–2578.

J. Berger, M. Grosse Holthaus, N. Pistillo, T. Roch, K. Rezwan and A. F. Lasagni, Ultraviolet laser interference patterning of hydroxyapatite surfaces, Appl. Surf. Sci. (2011), pp. 3081–3087

M. Grosse Holthaus, S. Twardy, J. Stolle, L. Treccani, O. Riemann, E. Brinksmeier, K. Rezwan, “Micromachining of Ceramic Surfaces: Hydroxyapatite and Zirconia”, Journal of Materials Processing Technologies, accepted, 2011

M. Grosse Holthaus, L. Treccani, K. Rezwan, “Monitoring osteoblast viability on hydroxyapatite with adjusted submicron and micron surface roughness by using proliferation reagent WST-1”, submitted, 2011

M. Grosse Holthaus, L. Treccani, K. Rezwan, “Orientation of Osteoblasts on Hydroxyapatite-based Micropatterns”, submitted, 2011

M. Grosse Holthaus, L. Treccani, K. Rezwan, “Comparison of micropatterning methods for ceramic surfaces”, submitted, 2011

Non-peer-reviewed articles

M. Grosse Holthaus, V. Ruttkowski, V. Zöllmer, M. Busse, K. Rezwan, “Keramische Mikrostrukturen für Knochenzellwachstumsstudien“, Proceedings of 7th Thüringer Biomaterialien-Kolloquium, Thüringer Grenzflächen- und Oberflächentagen ThGOT (2009), pp. 293–298

J. Berger, M. Grosse Holthaus, K. Rezwan and A. F. Lasagni, Surface modification by Laser Interference Patterning of hydroxyapatite substrates, Proceedings of 24th Surface Modification Technologies Conference (SMT24), Dresden, 2010

Selected talks

M. Grosse Holthaus, “Effect of Ceramic Microstructures on Bone Cell Growth”, Materials Science and Engineering, Nuremberg, 2008

M. Grosse Holthaus, K. Rezwan, “Comparison of Three Microstructure Fabrication Methods for Bone Cell Growth Studies”, Proceedings of the International Manufacturing Science And Engineering Conference, MSEC2008, Evanston, Illinois (USA), 2008

M. Grosse Holthaus, “Effect of Ceramic Microstructures on Bone Cell Growth”, 4. Regionaltagung Nord, Bremen, November, 2008

M. Grosse Holthaus, K. Rezwan, “Keramische Mikrostrukturen für Knochenzellwachstumsstudien- Wechselwirkungen von MG-63 Zellen mit Aerosol-Jet-gedruckten Kalziumphosphat-Mikrokanälen“, 7. Thüringer Biomaterialien-Kolloquium bei den Thüringer Grenzflächen- und Oberflächentagen (ThGOT), 2009

M. Grosse Holthaus, K. Rezwan, “Ceramic Micropatterning for Bone Cell Growth Studies“, Fachausschuss Biomaterialien, Arbeitskreis Grenzflächen (DGM), 2009

M. Grosse Holthaus, L. Treccani, K. Rezwan, “Versatile Crack-free Ceramic Micropatterns Made by a Modified Molding Technique”, Materials Science and Engineering (MSE), Darmstadt, 2010

Selected posters

M. Grosse Holthaus, “Interaction of Cells with Ceramic Microstructures”, Biomaterials: Fundamentals and Clinical Applications, BioMat2008, Essen, 2008

J. Berger, M. grosse Holthaus, K. Rezwan, A. F. Lasagni, “Ultraviolet Laser Interference Patterning of Hydroxyapatite Surfaces”, Surface Modification Technologies Conference (SMT24), Dresden, 2010

Awards

Photographic competition „Publikumspreis: Focus - Bilder der Forschung 2010“, Micrograph title: „Ameise“, 2nd place in an online voting